An Investigation into the Imager Pointing Accuracy and Stability for a CubeSat Using a CubeADCS in Sun-synchronous Low Earth Orbits

by

Luke Hans van der Stokker

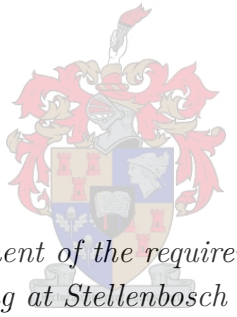

Thesis presented in partial fulfilment of the requirements for the degree of Master of Engineering at Stellenbosch University

Supervisor:

Prof. W.H. Steyn

Department of Electrical and Electronic Engineering

December 2021

Declaration

By submitting this thesis electronically, I declare that the entirety of the work contained therein is my own, original work, that I am the owner of the copyright thereof (unless to the extent explicitly otherwise stated) and that I have not previously in its entirety or in part submitted it for obtaining any qualification.

Date: December 2021

Abstract

The past decade has seen a rapid increase in investment and interest into the CubeSatellite industry, with a particular rise in interest seen from the commercial sector. The demand for miniaturised satellite technology has further fuelled the need for miniaturised attitude determination and control systems, without which, most mission objectives would be unattainable. Few companies exist whose sole purpose is to provide CubeSatellite mission designers with the control system they need to achieve their mission objectives. One such company which has emerged, is the South African born CubeSpace Satellite Systems RF (Pty) Ltd. whose CubeADCS does exactly this.

This thesis sought to investigate the imager pointing accuracy that can be achieved by a CubeSatellite in a sun-synchronous low Earth orbit, equipped with a CubeADCS. An initial investigation found that components such as star trackers and reaction-wheels are critical to high accuracy pointing, and that other systems in industry have been able to achieve arcsecond pointing accuracies. An in-depth investigation was conducted into the underlying components of the CubeADCS, consisting of both a theoretical study and practical hardware investigation, which aimed to understand the inner workings of each component, in addition to identifying and characterising their primary sources of error. An accurate simulation space environment reflective of that experienced by a CubeSatellite in low Earth orbit was constructed. A model of the CubeADCS model was additionally developed from the results of the subcomponent investigation to be tested by means of comprehensive simulations.

The CubeADCS was investigated in its ability to track a constant reference, in addition to its ability to perform an accurate target tracking manoeuvre in an attempt to image a location on Earth's surface. Several scenarios were investigated, which aimed to observe the effects of changing various size, orientation, star tracker placements, and attitude estimator parameters. Simulation results revealed that the CubeADCS is capable of achieve pointing accuracies of within $32''$ when following a constant reference, and within $31''$ during target tracking manoeuvres in Sun-synchronous orbits. A stability analysis revealed that the CubeADCS would be acceptable for the likes of stellar observation missions, making it more than adequate to satisfy Earth observation stability requirements.

Samevatting

Die afgelope dekade is gekenmerk deur aansienlike groei in belangstelling en beleggings in die CubeSat industrie, spesifiek vanuit die kommersiële sektor. Hierdie aanvraag na miniatuur sateliet tegnologie het die behoefte aan miniatuur orientasie bepalers en bedryfstelsels, 'n voorvereiste vir komplekese satelliet missies, aangevuur. Daar bestaan slegs 'n beperkte aantal maatskappye wat uitsluitlik fokus op die verskaffing van beheerstelsels aan CubeSat missies. Een van hulle is die Suid Afrikaans gebaseerde privaat kommersiële maatskappy, CubeSpace Satellite Systems RF (Pty) Ltd, wat met 'n innoverende CubeADCS stelsel oplossings bied aan CubeSat missie ontwerpers om hulle doelwitte te behaal.

Hierdie tesis het ten doel om die optimale kamera rigakkuraatheid wat 'n CubeSat, toegerus met 'n CubeADCS substelsel, in 'n sonsinkrone lae-aarde wentelbaan kan bereik te bepaal. 'n Aanvanklike ondersoek het bevind dat spesifieke CubeSat onderdele soos sterkameras en reaksiewiele, 'n kritiese rol speel in optimale rigakkuraatheid, en dat akkuraatheidsvlakke van boogsekondes deur kompeterende satellietstelsels bereik word. 'n Indiepte ondersoek van die onderliggende komponente van die CubeADCS stelsel is uitgevoer. Die ondersoek, bestaande uit 'n teoretiese analise en 'n praktiese ondersoek van die hardware, is uitgevoer om die individuduele funksionaliteite van elke komponent te verstaan. Elke onderliggende komponent se werkverrigting foutdrywers en die grootte daarvan is ook geïdentifiseer en beskryf. 'n Akkurate ruimte simulasie omgewing wat die invloed van 'n lae-aarde wentelbaan op 'n CubeSat implementeer is ontwikkel. 'n Model van die CubeADCS stelsel is ontwikkel, gebasseer op die bevindinge van die subkomponent ondersoek, en in omvattende simulasies in die ruimte simulasie omgewing getoets.

Die CubeADCS stelsel is getoets vir sy vermoë om 'n konstante verwysingspunt te volg sowel as om 'n akkurate teiken volging uit te voer tydens die neem van 'n foto van 'n teiken op die aardoppervlak. Verskeie scenarios is geanaliseer om die effek van veranderinge in groottes, orientasie, posisionering van sterkameras, asook verandering in orientasie afskatter parameters te evalueer. Simulasie resultate het getoon dat CubeADCS rig akkuraathede van minder as 32 boogsekondes behaal tydens volging van konstante verwysingspunte en beter as 31 boogsekondes gedurende teikenvolging. 'n Stabiliteitsanalise het aangetoon dat die CubeADCS stelsel voldoen aan die vereistes vir sterrekundige waarnemingsmissies, en dus heeltemal geskik is vir aardwaarneming satellietstelsels.

Acknowledgements

I would like to acknowledge the following persons:

- Professor WH Steyn for his immense patience, guidance, willingness to help, and timely edits.
- CubeSpace Satellite Systems RF (Pty) Ltd. for generously offering their time, knowledge and assistance to me throughout this process.
- My ESL colleagues for their support and invaluable discussions.
- Hendrik Burger for his help, understanding and mentorship throughout the past year.
- My family and friends, and in particular my mother, for their never ending support and motivation.
- My partner Amy Wardle for her infinite patience, emotional support, and for always believing in me.
- Sandy Wardle for her plethora of advice and support with the editing process of this research.

SCS Space (Pty) Ltd. and the THRIP bursary programme are lastly acknowledged for their financial assistance contributing to this research.

Contents

List of Tables

List of Figures

List of Algorithms

List of Abbreviations and Acronyms

ADC	Analogue to Digital Converter
ADCS	Attitude Determination and Control System
ADEV	Allan Deviation
AME	Absolute Measurement Error
AME	Absolute Pointing Error
ARL	Army Research Laboratory
ARW	Angle Random Walk
aSGP4	Augmented Simplified General Pertubations 4
ASTERIA	Arcsecond Space Telescope Enabling Research in Astrophysics
AU	Astronomical Unit
AVAR	Allan Variance
BCT	Blue Canyon Technology
BI	Bias Instability
BLDC	Brushless Direct Current
BMSP	Body-Mounted Solar Panels
BRITE	BRIght-star Target Explorer
BS	Boresight
BST	Berlin Space Technology
BW	Bandwidth
CANOE	Canadian Advanced Nanospace Operating Environment
CC	CubeComputer
CCD	Charge-Coupled Device
CF	Coordinate Frame
CL	CubeControl
CMOS	Complementary MetalOxideSemiconductor
CoM	Centre of Mass
CoP	Centre of Pressure
COTS	Commercial Off The Shelf

CS	CubeSense
CSS	Coarse Sun Sensor
CT	CubeStar
CW	CubeWheel
DC	Direct Current
DCM	Direction Cosine Matrix
DR	Detection Range
DSP	Deployed Solar Panels
ECEF	Earth-Centred Earth-Fixed
ECI	Earth-Centred Inertial
EKF	Extended Kalman Filter
EM	Engineering Model
EO	Earth Observation
ESA	European Space Agency
ESL	Electronic Systems Laboratory
FEKF	Full Extended Kalman Filter
FFT	Fast Fourier Transform
FIR	Finite Impulse Response
FM	Flight Model
FORTRAN	Formula translation
FOV	Field Of View
FSS	Fine Sun Sensor
GEKF	Gyro Extended Kalman Filter
GMST	Greenwich Mean Sidereal Time
GNB	Generic Nanosatellite Bus
GPS	Global Positioning System
GS	Ground Station
GST	Greenwich Sidereal Time
IAGA	International Association of Geomagnetism and Aeronomy
ICRS	International Celestial Reference System
ID	Identification
IEEE	Institute of Electrical and Electronics Engineers
IGRF	International Geomagnetic Reference Field
IMU	Inertial Measurement Unit
IPA	Imager Pointing Accuracy
IPE	Imager Pointing Error

IRC	Inertial-Referenced Coordinate
ISS	International Space Station
JD	Julian Date
JPL	Jet Propulsion Laboratory
LASP	Laboratory for Atmospheric and Space Physics
LEO	Low Earth Orbit
LOBF	Line of Best-Fit
LQR	Linear Quadratic Regulator
MCU	Micro-Controller Unit
MEMS	Micro-ElectroMechanical Systems
MIT	Massachusetts Institute of Technology
MM	Magnetometer
NASA	National Aeronautics and Space Administration
NORAD	North American Aerospace Defense Command
NRCSD	Nanoracks CubeSat Deployer
NRO	National Reconnaissance Office
OASYS	On-orbit Attitude System Software
OBC	On-Board Computer
ORC	Orbit-Referenced Coordinate
PCB	Printed Circuit Board
PCS	Pointing Control Subsystem
PD	ProportionalDerivative
PI	ProportionalIntegral
PID	ProportionalIntegralDerivative
PNS	Piezoelectric Nanopositioning Stage
PWM	Pulse-Width Modulation
QN	Quantization Noise
QUEST	Quaternion Estimation Algorithm
RA	Right Ascension
RAAN	Right Ascension of the Ascending Node
RMS	Root-Mean-Square
RMSE	Root-Mean-Square Error
RPM	Revolutions Per Minute
RPY	Roll-Pitch-Yaw
RR	Rate Ramp
RRW	Rate Random Walk

SBC	Satellite Body Coordinate
SF	Scale Factor
SFL	Space Flight Laboratory
SGP	Simplified General Perturbations
SGP4	Simplified General Perturbations 4
SP	Sun Point
SPI	Serial Peripheral Interface
SPM	Simplified Perturbation Models
SSDL	Space Systems Development Laboratory
SSO	Sun-Synchronous Orbit
SSP	Sub-Satellite Point
SSTL	Surrey Satellite Technology
ST	Star Tracker
STEM	Sience Technology Engineering Mathematics
TLE	Two-Line Element
TT	Terrestrial Time
UC	University of Colorado
US	University of Stellenbosch
USA	United States of America
UT1	Universal Time 1
WGS72	World Geodetic System '72
WOD	Whole Orbit Data

Chapter 1

Introduction

1.1 Problem Statement

An attitude determination and control system (ADCS) is responsible for providing satellites in orbit with the ability to accurately and stably orientate itself in space to achieve various mission objects, such as Earth observation (EO) or improving global telecommunication systems. It is a fundamental subsystem aboard a satellite, as without it, nearly no mission objectives (scientific or otherwise) would be achievable. The last decade has seen an exponential growth in the need to design and manufacture miniaturised satellites, at a lower cost and a shorter lead time as was traditionally the norm prior to 2003, after which marked the beginning of the CubeSatellite (CubeSat) era.

The rising demand in miniaturised satellites has subsequently resulted in the need for miniaturised and relatively inexpensive ADCSs. The challenge for ADCS design engineers is to create a system which can compete with larger more powerful ADCSs in its ability to control a miniaturised spacecraft at a fraction of the price. The added challenge is that these systems must be able to control satellites with incredibly low mass moments of inertia, operating in low-Earth orbits (LEO) which are known to harbour a space environment that induces some of the largest disturbance torques on a satellite. Companies such as CubeSpace Satellite Systems RF (Pty) Ltd. (CubeSpace) have risen to the challenge, and have been officially designing and building minaturised ADCSs (CubeADCS) from commercial-off-the-shelf (COTS) components since 2015. It is valuable for ADCS manufacturers to gain meaningful feedback on their systems so that they may verify their system's performances and make possible improvements. At present, very little research exists which aims to prove the imager pointing accuracy (IPA) of the CubeADCS as it is a relatively new system.

1.2 Objectives of this Study

This research seeks to investigate and verify the accuracy of the CubeADCS in its ability perform in EO missions whose goal is to point a CubeSat towards a desired Earth target reference or to follow and track a constant attitude reference. The aim is to determine how a CubeSat in a Sun-synchronous LEO, equipped with an imaging payload, would perform if it were controlled by a CubeADCS – revealing its IPA.

In order to achieve this goal, the research aims to

- investigate existing systems currently suited to control CubeSats,
- to perform an in-depth investigation into the CubeADCS's underlying hardware subsystems to better understand the theory behind their operation,
- to construct an accurate simulation model which mimics the space environment experienced by satellites in LEO,
- to model the CubeADCS's individual subcomponent functionalities and error characteristics and,
- to assess the performances of CubeSpace's attitude control and estimation software algorithms in

their ability to perform in the constructed simulation model.

The research hopes to gain a better understanding of the CubeADCS's expected IPA and stability in comparison to existing systems designed for CubeSats, by achieving the aforementioned objectives. Lastly, this research seeks to gain meaningful insight into the CubeADCS as a whole, in order to provide feedback to CubeSpace on the findings, which may contribute to the system's future improvements.

1.3 Document Outline

This section provides a summarised overview of the chapters contained in this research and their focusses. The document contains a total of eight chapters.

Chapter 1: Introduction

This chapter presents the problem statement to be addressed by this research, the objectives of this research, and to provide an overview of the entire document.

Chapter 2: Literature Review

The literature review examines existing literature to gain a better understanding of CubeSat concepts and trends and miniaturised ADCS trends. The chapter concludes with an in-depth analysis into previous CubeSat missions known ADCS accuracies and sets a benchmark for the CubeADCS.

Chapter 3: The CubeADCS

This chapter takes a broad look into the CubeADCS as a whole, where specific focus is placed on the theory behind the operation of the various CubeADCS subcomponents and outlining the key performance parameters of each such component.

Chapter 4: Satellite Orbit and ADCS Concepts

This chapter discusses fundamental satellite orbit theory and ADCS concepts which lay the groundwork to construct an accurate simulation environment in which to accurately test the performance of the CubeADCS.

Chapter 5: CubeSat Simulation Environment

A realistic simulation environment is defined and modelled here based on the theory laid out in chapter 4. Important sources of disturbance torques reflective of those found in LEO are analysed which creates a realistic environment in which to investigate the expected accuracy of a satellite equipped with a CubeADCS.

Chapter 6: CubeADCS Hardware Investigation and Modelling

This chapter builds onto chapter 3 by investigating the CubeADCS hardware in greater detail and identifying each individual component's error characteristics. Each section investigates a different subcomponent and finishes with a simulated model of that component aimed at reflecting its performance.

Chapter 7: Simulation Investigations

The simulation environment and CubeADCS hardware models are combined in this chapter to finally investigate the expected pointing accuracy and stability of the CubeADCS as a whole. Several scenarios are investigated which seek to test the system under different environmental conditions with different satellite sizes, orientations and star tracker configurations.

Chapter 8: Conclusions and Recommendations

Conclusions are drawn from the results of the simulations in chapter 7, where various system triumphs and shortfalls are identified. Finally, further conclusions and recommendations based on the entire research is given, where possible improvements to future research of the CubeADCS are offered.

Chapter 2

Literature Review

2.1 Overview

This chapter analyses existing literature pertaining to CubeSats and CubeSat ADCS performances. The CubeSat standard is first defined and further expanded on by discussing a brief history of the CubeSat. Following this, various CubeSat trends including size, organisations involved in CubeSat development, mission applications and ADCS components are discussed. The chapter then concludes with a more in-depth examination of some of the more recent studies and CubeSat missions conducted, which analyse the performances of miniaturised ADCSs. Key factors influencing the pointing accuracy and stability provided by CubeSat and NanoSats are identified, with reference to recent satellite missions which have set up an additional benchmark for the expected performances that miniaturised ADCSs can achieve.

2.2 CubeSats

The CubeSat is a miniaturised type of spacecraft which was originally developed to create an affordable way for universities worldwide to gain access into space predominantly for research purposes. The concept has additionally helped to develop the skills of students, researchers and aspiring satellite engineers in the design and manufacturing of small satellites. This concept was developed in 1999 as a collaboration between two professors: Jordi Puig-Suari from California Polytechnic State University (Cal Poly) and Bob Twiggs from Stanford Universitys Space Systems Development Laboratory (SSDL) [1].

2.2.1 The CubeSat Standard

Small satellites (SmallSats) are defined by the National Aeronautics and Space Administration (NASA) to have a mass no larger than 180 kg [2]. They can be further sub-divided into five categories based on their mass ranges, as seen in table 2.1.

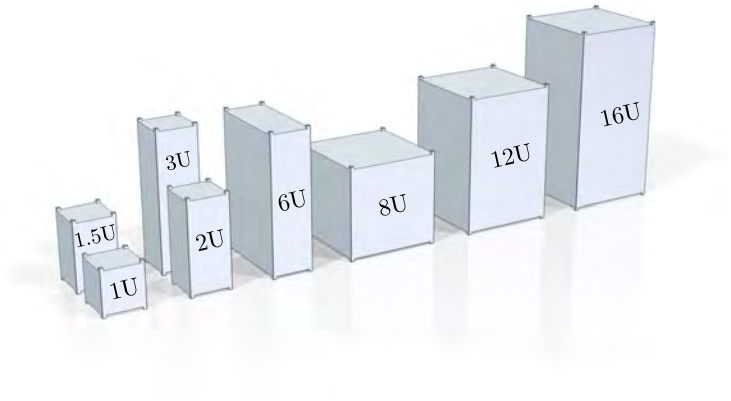

Figure 2.1: Common CubeSat Sizes [3]

The CubeSat however, is primarily categorised by its volume as opposed to its mass. As initially laid

out by Cal Poly and SSDL, a CubeSat's volume is defined in terms of a fixed CubeSat unit (1U) with volumetric dimensions 10 cm × 10 cm × 11.35 cm, where each unit has a mass limit of $m_{1U} \leq 1.33\,\text{kg}$ originally designed to fit into the Poly Picosatellite Orbital Deployer (P-POD) which can hold up to three CubeSat units. Since this time, however, multiple new deployment mechanisms have been developed to suit variations in CubeSat sizes and mission requirements. Combinations of the 1U CubeSat can be used to define smaller or larger CubeSats, where the most common configurations (launched and currently in development) can be seen in fig. 2.1 which places CubeSats predominantly in the Microsatellite and Nanosatellite (NanoSat) mass categories.

Table 2.1: SmallSat Mass Categories [2]

SmallSat Category	Mass Range
Minisatellite	$100\,\text{kg} \leq m_{sat} < 180\,\text{kg}$
Microsatellite	$10\,\text{kg} \leq m_{sat} < 100\,\text{kg}$
Nanosatellite	$1\,\text{kg} \leq m_{sat} < 10\,\text{kg}$
Picosatellite	$0.01\,\text{kg} \leq m_{sat} < 1\,\text{kg}$
Femtosatellite	$0.001\,\text{kg} \leq m_{sat} < 0.01\,\text{kg}$

The first CubeSats built consisted of five 1U CubeSats and one 3U CubeSat, namely: AAU CubeSat, developed by Aalborg University; CanX-1, developed by University of Toronto Institute for Aerospace Studies; Cubesat XI-IV, developed by the University of Tokyo; CUTE-1, developed by the Tokyo Institute of Technology; DTUsat, developed by the Technical University of Denmark and QuakeSat, the world's first 3U CubeSat developed by Stanford University. Each CubeSat mission took approximately two years to develop, where the satellites were later launched together on 30 June 2003 aboard a Russian Eurorockot [4] from Plesetsk, Russia [5]. The CubeSat's widely popular small size and standardisation has since resulted in an exponential growth in CubeSat development and launches. The standardisation of the CubeSat has additionally made it possible for multiple companies to mass-produce mechanical and electronic COTS components to be used by satellite engineers and developers at a far reduced cost [1].

2.2.2 CubeSat Trends

Since the launch of the first CubeSats, the industry has seen various trends and developments. Figs. 2.2 to 2.4 are all adapted from a predominantly NanoSat and CubeSat database created by Erik Kulu [3]. Kulu has grouped CubeSats, NanoSats, Picosatellites (PicoSats), PocketQubes, TubeSats and ThinSats under the NanoSat umbrella term – where the author of this thesis shall do the same when referring to the entire set of data adapted from Kulu for the remainder of this subsection. Fig. 2.2 shows the number of NanoSats launched and planned to be launched from 1998 up until 2023 – last updated in April 2020. The data shows, that in the last decade, that there has been a significant increase in the number of CubeSats launched, where the most popular size is clearly 3U and is followed in close contention by 1U and 6U CubeSat sizes.

In addition to CubeSat type trends, the types of orbits that CubeSats are injected into is also of interest for this study. Since their inception in 2003, the vast majority of CubeSats has been injected into low-Earth orbits (LEOs), where the European Space Agency (ESA) defines a satellite to be in LEO if it has an orbit altitude of less than 1000 km [6] – which is also used to define LEOs in this study. Fig. 2.4 shows typical LEOs selected by NanoSat mission designers required to complete their desired mission objectives. The data shows that the two most common mission orbit types selected, are from NanoSats released from the International Space Station (ISS) at an approximate altitude of 400 km and SSOs at an altitude of 500 km. NanoSats in the same orbit as the ISS can be seen to decay at a much faster rate than NanoSats in the 500 km altitude orbit due to a larger atmospheric drag felt by CubeSats orbiting closer to Earth's surface.

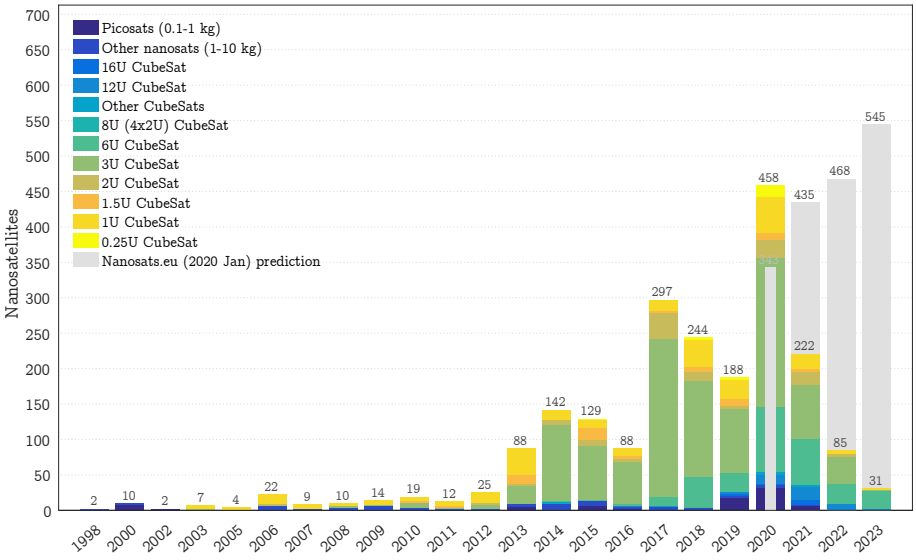

Figure 2.2: NanoSat Launches by Type [3]

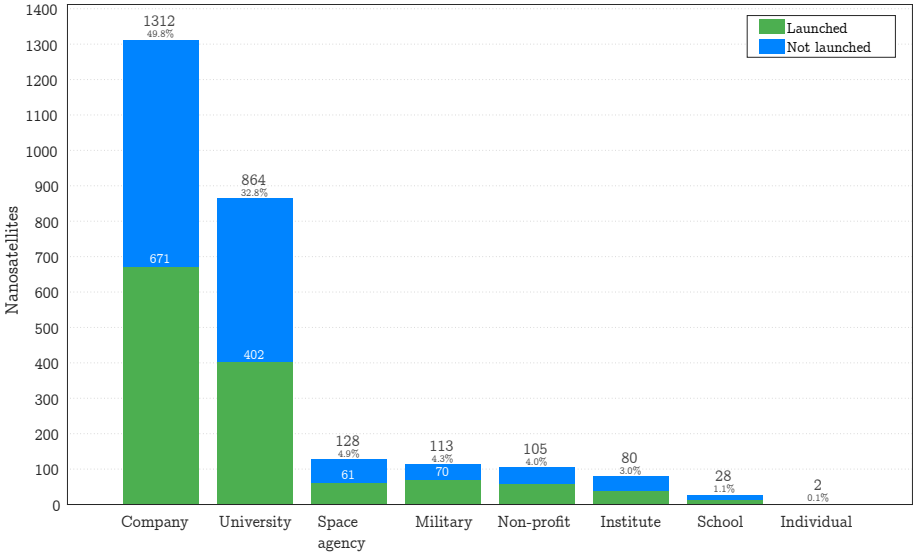

Figure 2.3: NanoSats Developed by Organisations [3]

The popularity of the CubeSat standard has attracted large numbers of commercial companies to invest in their own CubeSat development for scientific investigation, technology demonstration or, as of recently, the development of CubeSat constellations for telecommunication applications – such as internet of things (IoT) services and global internet coverage [4]. This is illustrated in fig. 2.3 which clearly shows how the commercial industry has now overtaken academia in NanoSat development, thus broadening the CubeSat concept and its applications into a whole new industry.

The types of CubeSat applications have also been evolving since the CubeSat's inception. Brazilian researchers Villela et al. [7] conducted a study in 2019 producing a statistical overview of the CubeSat industry between 2005 and 2018. Amongst many other categories, the researchers analysed trends within CubeSat applications to assess the direction of industry's progression. As seen in fig. 2.5, they found that there has been a sharp spike in CubeSats being implemented in remote sensing applications since 2013. The spike also seems to increase hand-in-hand with an enhanced interest in technology development applications of which the miniaturisation of CubeSat subsystems is a likely component.

There have been significant capital injections into CubeSat missions and component development – especially within the commercial sector, which further fuels competition and innovation. The increased contention and complexity in CubeSat mission design, fuelled by a relatively recent interest in EO or

remote sensing applications, has created a demand for compact and lightweight ADCSs with greater levels of performance which can be used to carry out accurate pointing manoeuvres to suit more stringent mission requirements as the industry grows. The next section will analyse the trends in ADCS components utilised by CubeSats which have complemented the advancement of CubeSats into new and innovative streams.

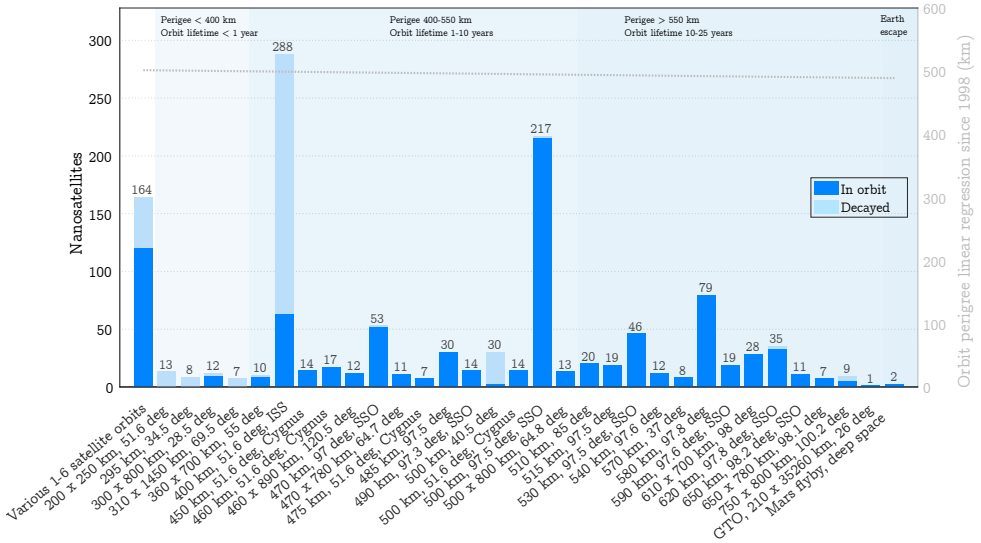

Figure 2.4: NanoSat Orbit Types [3]

2.3 CubeSat ADCS Trends

In 2016, Xia et al. [8] conducted a survey of the ADCSs used by over 350 different NanoSats, where the vast majority of the satellites analysed were CubeSats. The survey revealed that before 2008, over 50% of successfully launched CubeSats and NanoSats employed passive control techniques or no control at all, where the remaining satellites employed active magnetic control with or without a momentum-biased wheel. This had limited CubeSat control accuracies to a minimum of approximately 5° [8], [9] during this time, which is not suitable for achieving fine precision pointing but which was more than adequate for ground station (GS) communications and educational mission purposes.

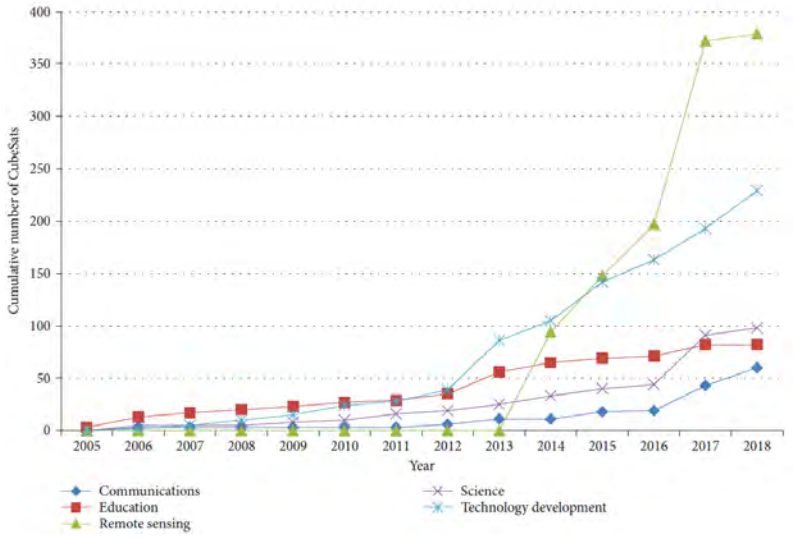

Figure 2.5: CubeSat Cumulative Application Trends [7]

In 2012, Selva and Krejci [9] produced an exhaustive survey of the capabilities of CubeSats for EO applications. The study aimed to identify whether CubeSats could be used for more than just educational

purposes and if so, what those capabilities would extend to and what limitations would arise. Selva and Krejci had found that (at the time of writing), CubeSats designed for EO applications had primary been used to conduct space weather measurements or used modest resolution optical cameras to capture images of Earth [9].

The researchers analysed the most important factors limiting CubeSat EO capabilities such as: on-board data handling, communications, mass and dimensions, power, propulsion, thermal control and most relevant to this study – the attitude determination and control limiting factors. They found that the attitude determination was limited to the performance of miniaturised sun sensors usually combined with magnetometers with accuracies stated to be less than 2° in the CanX-2 CubeSat mission (the successor to one of the first CubeSats injected into orbit) [9], [10]. They added that with the development of miniaturised star trackers for utilisation by CubeSat ADCSs, attitude determination accuracies could be as low as 0.01° for a CubeSat's cross star tracker boresight axes and 0.05° for a CubeSat's about star tracker boresight axis orientation [9].

To achieve a favourable control accuracy, Selva and Krejci [9] stated that an integration of fine sun sensors and magnetometers combined with active magnetorquers and reaction wheels is the optimal choice, drawing attention to the payload pointing performance of CanX-2 being as good as 2° [9], [10]. They proceed to quote certain integrated ADCS suppliers (Pumpkin CubeSatKit and Satellite Services Ltd) who stated their overall pointing accuracies to potentially be within 1° [9], which had yet to be proven at the time.

Fig. 2.6 is adapted from the data presented by Xia et al. [8] in their survey, which shows that it was not until 2013 that reaction wheel-based attitude control started to become the dominant scheme of choice to be implemented by CubeSat mission designers. Between 2008 and 2016, the researchers showed that over 50% of successful CubeSat and NanoSat missions (from the provided data) had employed a reaction wheel-based control scheme. This seems to complement Selva and Krejci's [9] prior research which concluded that CubeSats could indeed be used to perform more complex EO missions achieving higher pointing accuracies, provided that CubeSats employ integrated ADCS systems which utilise reaction wheel-based control schemes with miniaturised star trackers – which appeared to only become commercially available by 2011 [11]. This is further supported by Villela et al.'s [7] research as presented in fig. 2.5, which shows the rapid increase in remote sensing CubeSat applications.

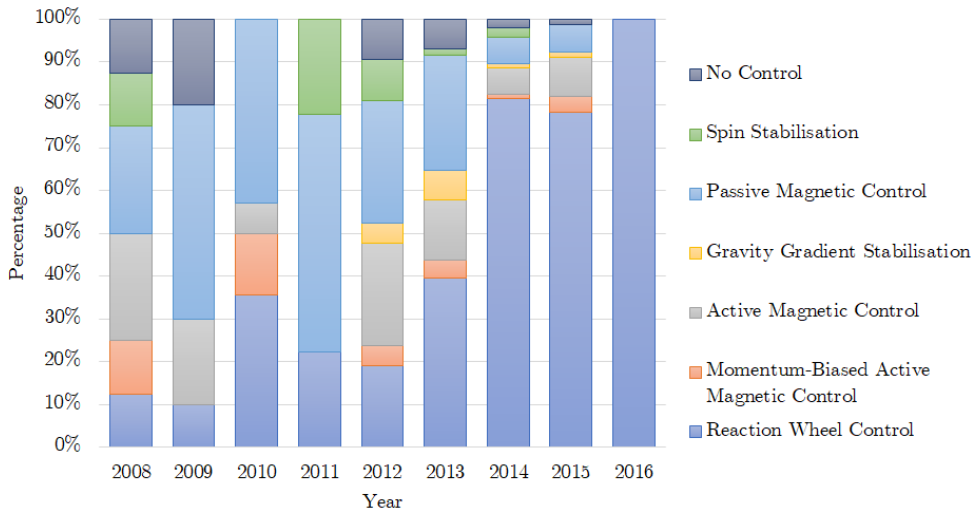

Figure 2.6: Control Scheme Proportions [8]

2.4 CubeSats ADCS Pointing Performance

It is clear that there has been a movement towards achieving higher accuracy payload pointing and that it is necessary to analyse the different performances of CubeSat ADCSs in achieving these requirements.

Guo and Han [12] conducted a study in 2016 which aimed to analyse the limit of CubeSat ADCS performances. The researchers identified six integrated ADCS systems which could provide 3-axis reaction wheel-based control (in which the CubeADCS is included) after investigating 15 different CubeSats from recent missions at the time. They indicated that the majority of the identified CubeSat mission designers opted to use integrated ADCSs as a whole package, as opposed to using a combination of different sensors and actuators from multiple suppliers [12]. A tabulated summary of the six integrated ADCSs is shown in table 2.2, in which the provided information is taken exactly as presented by the researchers in their paper [12].

Table 2.2: Summary of ADCS Configurations of a Selection of Launched CubeSats [12]

ADCS Unit	Developer Country	Attitude Knowledge (°)	Reaction Wheel Performance		Year of 1st Flight
			Momentum mN m s	Max Torque mN m	
TUD ADCS Unit	The Netherlands	0.4	1.56	0.006	2013
iADCS-100	Germany	0.008	1.5	0.087	2016 (expect)
CubeADCS	South Africa	0.2	1.7	0.23	2013
Prometheus	USA	Unknown	Unknown	Unknown	2013
XACT	USA	0.002	15	4	2016
MAI-400	USA	0.013 (MAI-400SS)	9.351	0.635	2013

The researchers' summary presents the integrated ADCS units' attitude knowledge performances as provided by supplier datasheets or statements, and does not discuss the actual determination and payload pointing performances from CubeSats in orbit. This can be attributed to the fact that at the time of those researchers' writing, the ADCS performance results from the relevant CubeSat missions utilising the aforementioned integrated units were not yet available or had restricted access, and so the attitude knowledge predictions were largely limited to speculation.

For the remainder of the article, Guo and Han [12] singled out the TUD ADCS unit to conduct an analysis of its short- and long- term performances as the ADCS controls a 3U CubeSat with body mounted solar panels in a 600 km altitude SSO. The simulation model was set up to be as realistic as possible with both the ADCS sensors and actuators performances conforming to empirical data obtained through ground or in-orbit tests [12]. The researchers include a modelled GPS in addition to an NST-1 nano star tracker from TY-Space as part of the ADCS sensor suite, with a quoted 3σ accuracy of $7''$ and $70''$ for the sensors cross boresight and about boresight respectively [12]. A seven state gyro EKF is used for the attitude estimation of the satellite, where the attitude control is implemented with a system linearisation and LQR [12].

The simulated CubeSat's orbit is propagated by the SGP4 model, which is further used to simulate the International Geomagnetic Reference Field (IGRF) model to calculate the various magnetic torques on a CubeSat with an assumed (and optimistic) residual magnetic dipole of $0.5\,\mathrm{mA\,m^2}$ [12]. Finally, the resultant solar radiation, gravitational and aerodynamic environmental disturbance torques are simulated. The results of the simulation can be seen in fig. 2.7, from which it was concluded that the TUD ADCS (equipped with an accurate star tracker) can obtain a 1σ absolute pointing error (APE) and attitude measurement error (AME) of $74.46''$ and $22.40''$ respectively whilst pointing nadir – calculated within a 60 s window [12]. The results from the TUD ADCS simulation imply that a high ADCS estimation and pointing accuracy could be achieved provided that the unit's sensors and actuators are correctly characterised before the launch of the CubeSat [12].

The researchers briefly discuss the CubeADCS in their survey, with a specific reference to Strand-1 CubeSat developed by Surrey Satellite Technology (SSTL) and two South African QB50 initiative precursor CubeSats – ZA-AeroSat and nSight-1, developed in partnership between CubeSpace and SCS Space (Pty) Ltd. (SCS Space). According to the EO satellite missions database maintained by ESA [13], Strand-1 was launched in 2013 and was equipped with one of the first versions of the CubeSense (a sun and nadir sensor). The CubeSense was originally developed by Loubser [14] at the Electronic Systems Laboratory (ESL) at Stellenbosch University and later adapted to form part of the CubeSpace sensor

suite. The two QB50 CubeSats were developed in the years that followed and were later deployed from the ISS in 2017, making them the first integrated CubeADCS units to be released into orbit.

Strand-1 was developed in the premature days of CubeSpace and did not use any other CubeSpace sensors (excluding the CubeSense) or actuators and so its performance is ignored in this thesis. The latter two QB50 CubeSats were equipped with a Y-Momentum configured CubeADCS which performed their specified mission requirements with distinction, but which did not provide the satellites with highly accurate pointing capabilities. It follows that the two QB50 CubeSats serve as poor examples when discussing the potential imager pointing accuracy (IPA) which could be provided by a 3-axis reaction wheel controlled CubeADCS equipped with a full suite of CubeSpace sensors. The attitude knowledge accuracy seen in table 2.2 is likely quoted from the stated CubeSense accuracy at the researcher's time of writing, and is thus not a true reflection of the CubeADCSs performance.

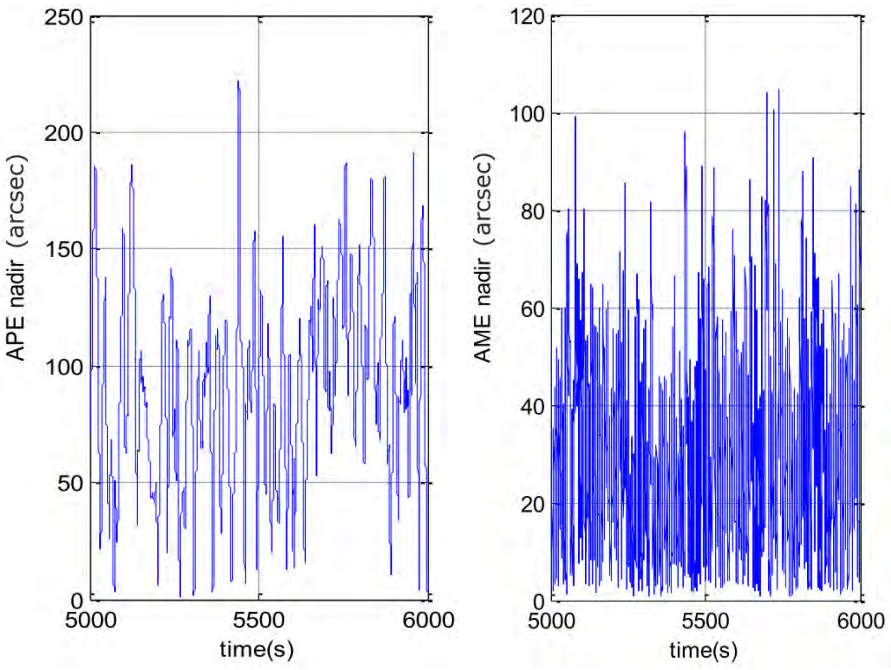

(a) Absolute Pointing Error [12] **(b)** Attitude Measurement Error [12]

Figure 2.7: TUD ADCS Simulated ADCS Performance Errors

Unfortunately, much is still unknown about the performances of both the Prometheus and MAI-400 ADCSs as the missions were commanded and overseen by the US military or National Reconnaissance Office (NRO), making data about the missions classified. The iADCS-100 is developed as a joint system by Berlin Space Technology (BST) and Hyperion Technologies based in Germany and the Netherlands respectively. The system had its maiden flight aboard Aalto-1 CubeSat, pioneered by students at Aalto University in Finland. An article written about the CubeSat's first months in orbit indicated that a software issue on the iADCS resulted in the systems inability to detumble the satellite [15]. This malfunction lasted for almost a year after Aalto-1 was injected into orbit, until finally the system was able to receive a firmware update resulting in the detumbling of the satellite. Precise information about the pointing accuracy of the iADCS has not been made public, however, the system developers have stated that the iADCS-100 should be able to achieve a pointing accuracy of within 1° [16].

2.5 CubeSat ADCS Performances from Recent CubeSat Missions

The remaining ADCS listed in table 2.2 is the integrated XACT ADCS (XACT-15 to be precise) developed by Blue Canyon Technology (BCT) based in Colorado, USA. A substantial amount of information is

known about the in-orbit performances of this system – making it valuable to discuss in this chapter. Two known CubeSats which have previously flown with the XACT ADCS are initially investigated (a 3U and 6U CubeSat) in this section. Additionally, a NanoSat mission which utilised different miniaturised ADCS sub-components is analysed in order gain a wider perspective about other known NanoSat ADCS performances from genuine reported in-orbit data.

2.5.1 MinXSS Mission

The Miniature X-ray Solar Spectrometer (MinXSS) is a 3U CubeSat which was designed, built and operated by students and staff at the University of Colorado's (UC) Laboratory for Atmospheric and Space Physics (LASP) [17]. The MinXSS project consisted of two separate satellites of which the first (MinXSS-1, discussed in this section and is shown in fig. 2.8a as FM1) was deployed from the ISS in May 2016. As the name of the satellites suggests, the primary mission objective was scientific, with the aim of measuring the soft x-ray energy distribution from the Sun [17] with the intention of training students in the STEM fields. MinXSS-1 was intended to last a mere three months in orbit, however, the CubeSat continued to operate for just under a year before deorbiting naturally [17].

MinXSS-1 was fitted with two 3U deployable solar panels consisting of seven solar cells on each panel as well as one body-mounted solar panel with five solar cells to handle the satellite's power generation requirements. The solar panel array was developed at UC and was able to achieve a maximum power output of 23.41 W which was used to recharge the system's COTS lithium-polymer battery pack [17]. Additionally, the satellite's nominal orbital attitude configuration was defined to point its long body axis in the ram direction to minimise the effects of atmospheric drag, whilst keeping the solar panels pointed towards the Sun.

The MinXSS-1 was the first satellite in the world to be equipped with BCT's XACT ADCS [17] – seen in fig. 2.8b. The system integrated a set of three highly precise reaction wheels as well as three magnetorquer rods for momentum dumping to handle the CubeSat's actuation [17]. The sensor suite in the ADCS consisted of a combination of one highly accurate star tracker, a fine sun sensor (FSS) with an FOV of 110°, a set of coarse sun sensors (CSS), a three-axis magnetometer (MM) and a three axis inertial measurement unit (IMU) [17]. MinXSS-1 did not use a GPS which could have been provided with the XACT ADCS, where its orbit was instead propagated using uploaded ephemeris [17]. The entire integrated system fits into a space of 0.5U and consumes an average power of 1.9 W according to a presentation [18] given by James Mason (one of the students which headed up the project). The system is able to process ~70 telecommands and to generate ~300 telemetry items at 5 Hz [17].

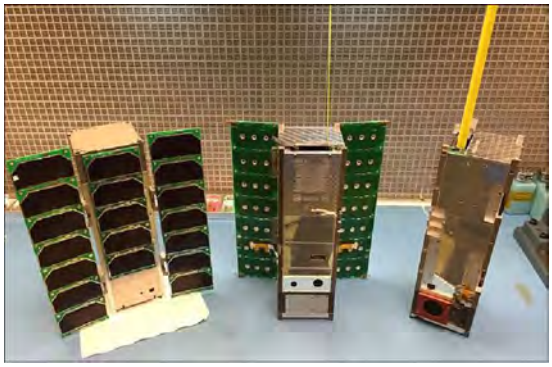

(a) MinXSS family (left to right): Engineering Model (EM), FM1 (Flight Model 1), and FM2 (image credit: LASP/University of Colorado) [13]

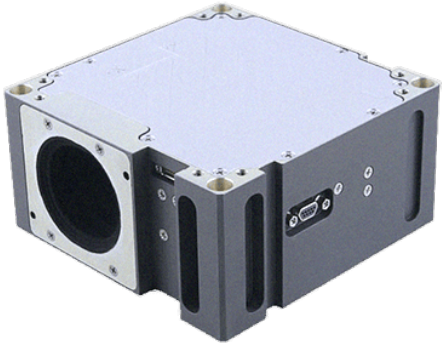

(b) XACT-15 ADCS [19]

Figure 2.8: MinXSS Family of CubeSats and BCT XACT-15 ADCS

An article written by Mason et al. [17] presents the performance of the XACT ADCS in its capacity to control MinXSS-1. The performance of the ADCS is discussed separately in terms of pointing

performance, attitude stability, momentum dumping, agility, orbit propagation, sensor degradation and edge cases – of which the first two categories are primarily focussed on in this section. The agility aspect is not looked at as the satellite was not required to perform any slew manoeuvres for target tracking purposes.

2.5.1.1 Pointing Accuracy and Stability

Prior to MinXSS-1's deployment from the ISS, BCT specified that the XACT ADCS would be able to achieve a theoretical 3σ accuracy of 0.009° about satellite's x and z axes and 0.021° about its y-axis [17]. The star tracker boresight is aligned primarily along the satellite's y-axis canted by 10° towards the satellite zenith direction [17] which explains why accuracies about the y-axis are twice as bad in this case. The MinXSS mission only required a 3σ pointing accuracy about all three axes of 2° and an attitude knowledge of 0.05° to achieve its scientific objectives, making the XACT ADCS a more than suitable choice for the mission. From this, it likely follows that the MinXSS mission was primarily advantageous to BCT to gain flight heritage and prove the accuracy for their XACT ADCS.

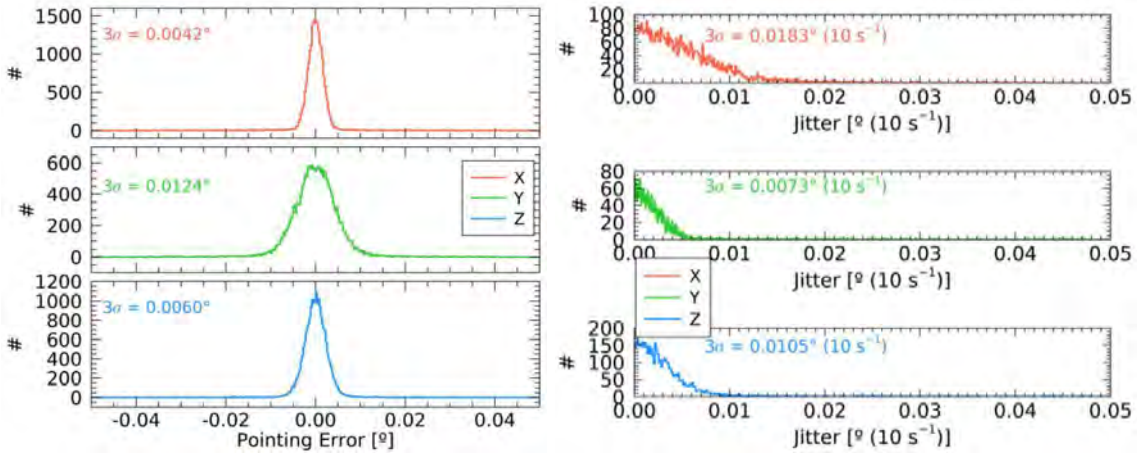

(a) MinXSS XACT ADCS Pointing Accuracy Histograms [17]

(b) MinXSS XACT ADCS Jitter Histograms [17]

Figure 2.9: MinXSS Pointing Accuracy and Stability

The best pointing requirements were needed during the satellite's science mode, which required the XACT ADCS to point the satellite's solar spectrometer payload towards the Sun. The pointing error histograms for all three of the satellite's axes are adopted from Mason et al.'s article [17] and presented in fig. 2.9a. The accuracy that was achieved by the XACT ADCS is reported to be 0.0042°, 0.0117° and 0.006° for the satellite's x, y and z axes respectively [17] – performing nearly twice as well as was specified by BCT and a few hundred times better that what was required for the mission. The stated control errors were obtained from two independent sources: the XACT star tracker and the MinXSS fine Sun Position Sensor with 2″ dark noise [18]. A full width half max computation of each error histogram divided by a 2.355 conversion factor was multiplied by 3 to obtain the 3σ accuracies.

Early in the satellite's mission, commands to bias the XACT's momentum were sent in order to keep the reaction wheel speeds from reaching zero RPM. The system was able to adequately dump the momentum buildup caused by environmental disturbance torques for the majority of the MinXSS-1 mission until the satellite decayed to an altitude of 174 km. At this altitude, the extreme external disturbance torques resulted in the reaction wheels reaching their maximum momentum storage capacity where they were finally idled.

The solar spectrometer payload instrument has an FOV of 3° and requires an integration time of 10 s, from which a required maximum jitter in the satellites y and z axes was calculated to be a 3σ maximum of 0.3 °$(10s^{-1})$ [17]. The data from the histogram errors shown in fig. 2.9a was placed into 10 s bins

from which the peak-to-peak differences were calculated in each bin to compute the maximum attitude fluctuation over each integration period [17].

The resultant attitude stability histograms are shown in fig. 2.9b where the 3σ attitude stability values were calculated to be $0.0183\,°(10s^{-1})$, $0.0073\,°(10s^{-1})$ and $0.0105\,°(10s^{-1})$ for the satellite x, y and z axes respectively [17]. The 3σ values were calculated by using the bin which contained more than 66% of the data and multiplying this value by 3 [17]. The attitude stability values are found to be larger than the pointing accuracy errors due to the fact that the attitude stability was calculated from peak-to-peak values, where the pointing accuracy errors were centred around zero [17].

The performance of the XACT ADCS on MinXSS-1 serves as an excellent benchmark for the potential performance which can be achieved by 3U CubeSats in a LEO. Its performance far exceeded the expectations of the mission requirements as well as BCT's estimations prior to the mission. Recommendations by Mason et al. with regards to bettering the XACT's ADCS performance include functional ground testing of the ADCS on an air bearing table prior to launch, integrating a GPS into the ADCS (especially for LEO missions) and running simulations which determine if and when bright objects will come into the star trackers FOV [17].

2.5.2 ASTERIA Mission

The Arcsecond Space Telescope Enabling Research in Astrophysics (ASTERIA) is a 6U CubeSat which conforms to a new dimension specification of 12 cm × 24 cm × 36 cm presented by Twiggs et al. [20] and deployed from the Nanoracks CubeSat Deployer (NRCSD) – which has been in operation since 2014 [21],[22]. ASTERIA was designed, built and operated by the Jet Propulsion Laboratory (JPL) at NASA [23] in collaboration with Massachusetts Institute of Technology (MIT) [13]. The satellite was also deployed from the ISS in November 2017 where it later stopped transmitting and responding to commands in December 2019 [3]. The primary mission objective was to demonstrate cutting edge technologies for enabling photometry on small satellites by possibly discovering exoplanets orbiting Sun-like stars nearest the solar system [23].

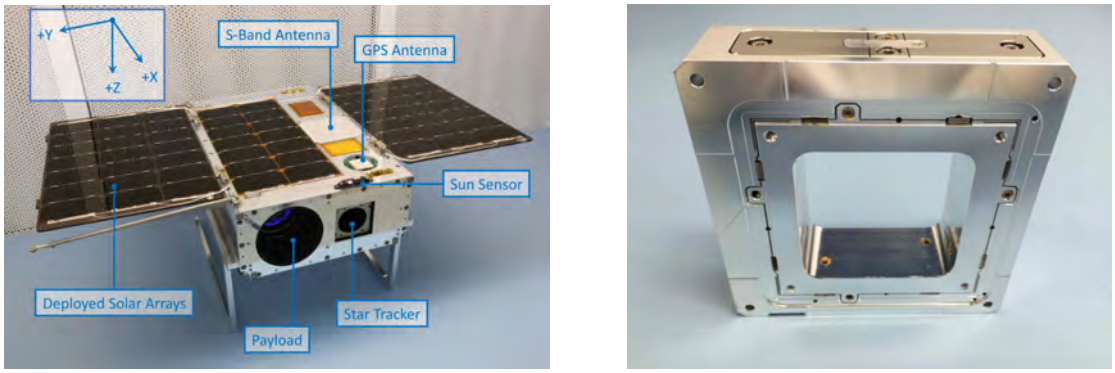

(a) ASTERIA Final Assembly [23]

(b) ASTERIA Piezoelectric Nanopositioning Stage [23]

Figure 2.10: ASTERIA Assembly and Custom Imager Pointing Stage

As seen in fig. 2.10a, ASTERIA was fitted with two 3U by 3U deployable solar panels as well as one 2U by 3U body-mounted solar panel on the satellite's zenith facet. Each 3U by 1U solar panel conforms to the more traditional dimension specifications stipulated in sec. 2.2 (which explains the size discrepancy seen in the figure). The panels each consist of seven cells amounting to a total of 56 cells on the CubeSat which are capable of generating a beginning of life power of 48 W to charge the satellite's 47 W h battery assembly [24]. In ASTERIA's safe mode, the satellite is placed into a sun pointing mode which holds the Sun normal to the solar panels during the sunlit portion of the orbit [24]. During the eclipse portion of the orbit, the satellite's nominal orientation is defined to align the long body axis in the satellite's ram

direction [24].

As mentioned in the beginning of this section, ASTERIA was additionally equipped with the XACT-15 ADCS developed by BCT – differing to MinXSS-1 only by the added integration of a GPS unit. Unfortunately, however, the GPS was not powered on in space following complications with a flight harness discovered during integration on the ground exceedingly close to the satellite's launch date [23]. As such, the satellite had to rely on ephemeris which needed to be uploaded by the spacecraft operators at regular intervals, making the system almost identical to the ADCS aboard MinXSS-1.

The nature of the mission required ASTERIA to precisely point the on-board imager at a target star to within an accuracy of less than $5''$. As such, the XACT ADCS was intended to only execute the satellite's coarse pointing where the fine pointing of the payload was further improved by a pointing control subsystem (PCS) developed by JPL which consisted of a lens assembly, a piezo stage and an imager [23] (all three form the components of the payload). The piezoelectric nanopositioning stage (PNS) can be seen in fig. 2.10b. The PNS was custom built by Physik Instrumente but controlled with algorithms developed by JPL [23] and was able to accurately control the imager's position along ASTERIA's x and z axes. Additionally, the 2592×2192 pixel Fairchild monochrome CMOS image sensor was used to perform a star centroiding algorithm which computed a commanded quaternion which was fed to the XACT ADCS at 5 Hz [23] acting as a second star tracker to assist the ADCS in its attitude estimation and control.

2.5.2.1 Pointing Accuracy and Stability

Christopher Pong [23] analysed the pointing performance that was achieved by both the XACT ADCS and PCS (as they worked together) in addition to the pointing performance of the XACT ADCS acting alone. Only the latter will be discussed in this subsection as only the performances of ADCSs aboard CubeSats is of interest in this thesis, due to the fact that the addition of a PCS will greatly improve any payload's pointing accuracy aboard a CubeSat.

To measure the accuracy of the XACT ADCS's ability to point the imaging payload on its own, the feedback from the imaging payload was disabled and the piezo stage was locked into its nominal position [23]. The XACT ADCS was commanded to point the payload at the Alpha Centauri star field using Alpha Centauri A (HIP 71683) as the target star (seen in fig. 2.11) to determine the XACT ADCS's pointing accuracy. It is noted that the payload and the XACT's star tracker FOV's did not overlap but that their boresights are only separated by 10° [23].

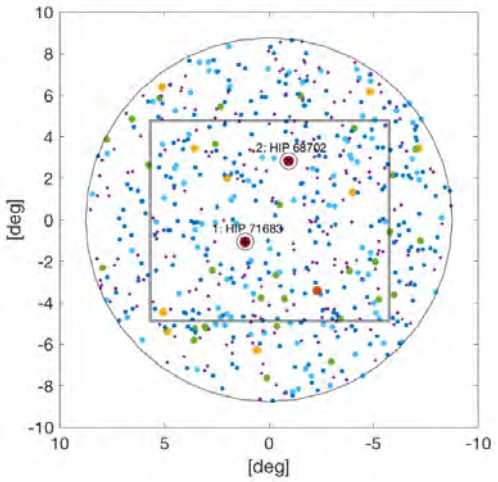

Figure 2.11: ASTERIA Alpha Centauri Star Field [23]

Fig. 2.12a shows the cross-boresight payload pointing error from the XACT ADCS, where fig. 2.12b shows the about boresight (roll) payload pointing error. Both errors are measured relative to the payload's axes and not the satellite's axes, however, as the XACT is the only system being used to point at the star

field, it is representative of the satellite's attitude pointing error. The results indicate a low-frequency bias drift dominating the y-axis errors which Pong suggests is due to changes in the alignment between the star tracker and payload caused by changes in temperature experienced between the two different structures made of different materials holding the star tracker and payload respectively. This is shown in Fig. 2.12a where the y-axis error has an initial alignment bias of around $15''$ and drifts by nearly $20''$ over the 20 min observation period [23].

Pong points out the increase in high-frequency pointing errors which he attributes to the larger gains which were used to reject environmental disturbance torques [23]. Overall, the average error about the x-axis is $-10''$ with a 1σ error of $1.75''$ and the average error about the y-axis is $-31.22''$ with a 1σ error of $4.57''$ over a 20 min observation. Finally, the roll pointing error (seen in fig. 2.12b) measured over the same 20 min period of observation was shown to drift over time by $30''$ and had a mean bias of $-110.9''$ with a 1σ accuracy of $9''$.

The pointing and stability performances achieved by ASTERIA have been the best known for a CubeSat to date [23]. This can be largely attributed to the both the XACT ADCS and PCS working together to achieve this milestone. The XACT ADCS aboard ASTERIA performed slightly worse than the XACT ADCS aboard MinXSS-1, which can be largely attributed to the large low-frequency bias drift in the y-axis caused by thermal gradients as previously mentioned. Nevertheless, both missions prove the high degree of accuracy of the XACT ADCS in its ability to point and stabilise CubeSats.

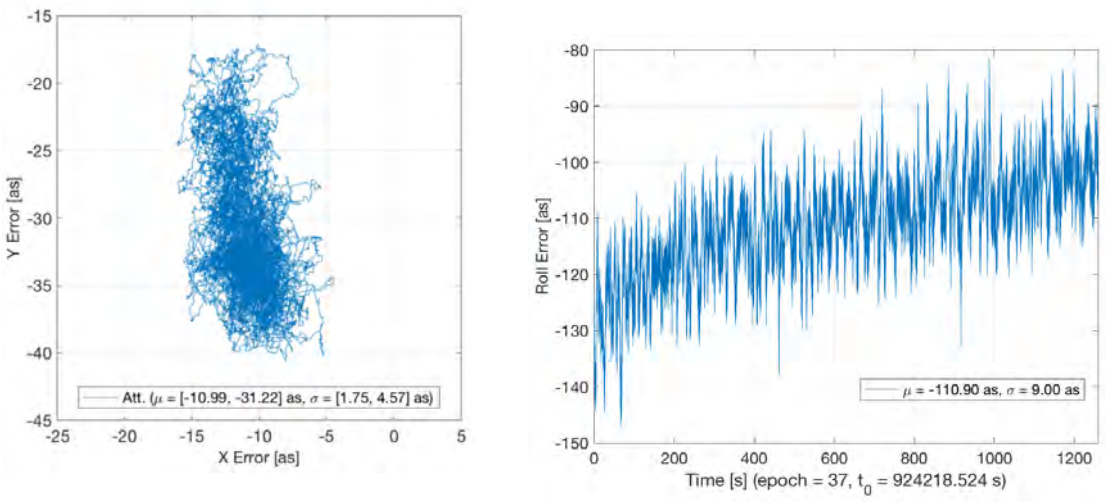

(a) ASTERIA XACT ADCS Cross-Boresight [23]

(b) ASTERIA XACT ADCS Roll Error [23]

Figure 2.12: ASTERIA XACT ADCS Pointing Error

2.5.3 BRITE Mission

The BRIght-star Target Explorer (BRITE) mission was conceptualised and developed by the University of Toronto Institute for Aerospace Studies Space Flight Laboratory (UTIAS-SFL) in partnership with organisations from Austria and Poland. The mission is made up of a constellation of six NanoSats whose primary objective is to make photometric observations of some of the brightest stars in the night sky [11]. The mission entails observing several of the most massive stars thought to be responsible for producing some of the heavier elements in the known universe [11]. To achieve this, focus was placed on massive stars with a visual magnitude of 3.5 or brighter [11]. Measuring variations in the brightness of these stars would help scientists involved in the mission to deduce their internal behaviour – where the mission aimed to measure these variations to within an accuracy of 0.1% [11].

Four separate launches between February 2013 and August 2014 contributed to the deployment of the BRITE constellation [25]. The NanoSats were all intended to be injected into low-Earth SSOs at altitudes greater than 600 km [25]. The two Canadian satellites (BRITE-Toronto and BRITE-Montréal) were

launched in June 2014, where BRITE-Montréal is thought to have unfortunately not detached from the third stage of the Dnepr launch vehicle [25]. The remaining five NanoSats were successfully deployed into their respective approximately circular orbits – with the exception of one Polish NanoSat (Lem) whose Depnr rocket deployed it into an eccentric 600 km × 890 km orbit. All six of the satellites use the modular Generic Nanosatellite Bus (GNB) platform developed at UTIAS-SFL with cubic dimensions of 20 cm × 20 cm × 20 cm [11] where their masses vary between 6 kg and 10 kg [3]. An annotated component view of the GNB platform as well as the final assembly of one of the BRITE NanoSats (UniBRITE) can be seen in fig. 2.13.

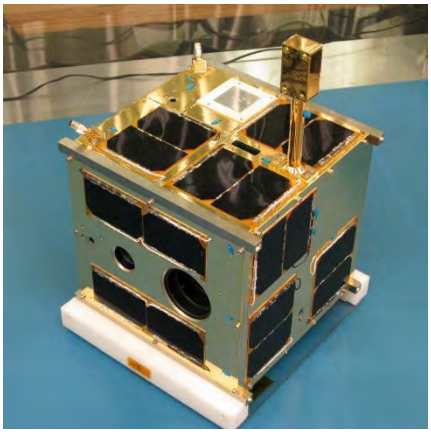

(a) UniBRITE NanoSat [26]

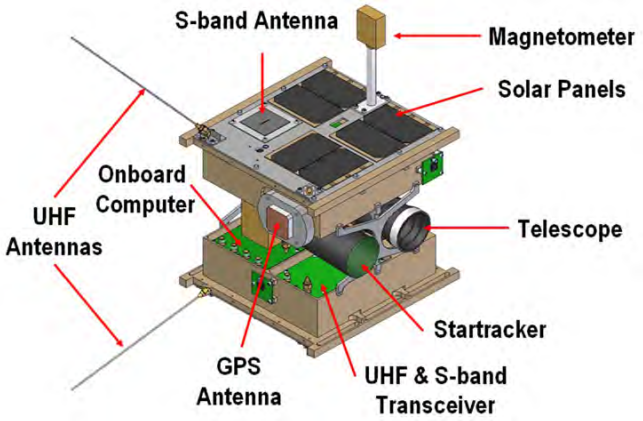

(b) GNB Components for BRITE NanoSats [27]

Figure 2.13: Final Assembly and Components for the BRITE NanoSat GNB Platform

The payload aboard each BRITE NanoSat consists of a wide angle telescope with an FOV of 24° × 19° and a CCD imager which utilised a region of 4008 × 2672 pixels, translating to a resolution of around 30″ per pixel [11]. A point spread function over the CCD's pixels is achieved by slightly defocussing the lens assembly which distributes the stars' light over a small number of pixels, thus improving the photometric accuracy and avoiding undersampling [11]. The challenging scientific objectives of the mission meant that each NanoSat needed to be capable of stabilising itself to hold the centre of the point spread to within 78″ (1σ) or 3 pixels RMS [28]. Minor fluctuations in attitude were desired during imaging in order to slightly smear and effectively smooth the image on each exposure – provided that these fluctuations were radially symmetric over these exposures [11].

The standard GNB offers GPS capabilities with a sensor suite comprised of a 3-axis magnetometer and rate sensor and coarse sun sensors on each face of the cube [28]. The actuators are comprised of three orthogonal Sinclair-SFL reaction wheels (developed in 2006/07) and three magnetic torque coils for momentum dumping [28]. To achieve the fine pointing requirements set out by the ambitious mission objectives, the BRITE ADCSs utilise additional miniaturised star trackers. The first two BRITE NanoSats launched are equipped with a ComTech Aero Astro Miniature Star Tracker (AA-MST), where the remaining four NanoSats use the Sinclair Interplanetary-Ryerson University-SFL Star Tracker (ST-16) [28].

2.5.3.1 Pointing Accuracy and Stability

Grant et al. [28] published an article in 2014 which discusses the on-orbit performance of the BRITE constellation, in which the authors highlight that the high degree of pointing accuracy and stability of the BRITE NanoSats can be attributed to the on-board star tracker and reaction wheel performances as well as the implementation of accurate estimation and control algorithms [28]. Both types of star trackers implemented in the NanoSats were tested on the ground before the full constellation launch. These initial tests indicated that the AA-MST had a 1σ error of 23″ and 114″ around the star tracker cross and about boresight axes respectively, where the ST-16 star tracker performed substantially better with a 1σ error

of 7″ and 70″ over the same respective axes [28]. To reduce the effects of thermal misalignments between the star trackers and the imager payloads, the pair were mounted to the same bracket at the centre of the GNB – where the smallest temperature fluctuations are observed [28].

Each Sinclair-SFL reaction wheel is balanced to less than 0.5×10^{-6} kg m which amounts to an estimated imbalance error of less than 1″ [28], meaning that the greatest source of jitter would not be caused by the pure spin of the reaction wheels themselves. The largest source of jitter is rather attributed to the wheels' drive electronics and control software which causes the reaction wheels to imperfectly track commanded torque references [28]. During initial ground tests, an FFT was applied to the wheels' measured torque error revealing a 6.5 Hz oscillation which was causing an unacceptable amount of jitter [28]. This oscillation was removed by adjusting the wheels' control gains which greatly reduced the amount of control jitter caused by the wheels' drive electronics and thus improving the control stability and accuracy of the satellites [28].

Running on each NanoSat's OBC is the Canadian Advanced Nanospace Operating Environment (CANOE). The CANOE multi-threaded operating system has multiple responsibilities – the most important of which is to execute attitude cycles at fixed intervals. Each attitude cycle is conducted over a relatively long 2.5 s period which incorporates a sensor-measurement collection period, an execution of SFL's On-orbit Attitude System Software (OASYS) estimation and control algorithms, an actuator commanding period and a waiting period [28]. The main contributor to the large attitude cycle period is the AA-MST star tracker which can take up to 2 s to return a solution [28].

OASYS incorporates the system's cascade-EKF responsible for state estimation as well as the required set of control laws which govern the spacecraft's attitude [28]. As the name suggests, the cascade-EKF sensor update steps are implemented in the same order of received measurements. The satellites have two primary estimation modes, namely: coarse and fine estimation modes. The fine estimation mode only makes use of the on-board star tracker for sensor measurements, where the coarse estimation mode only uses the CSSs and magnetometer measurements [28].

Of all the terms characterised and accounted for in Euler's dynamic equations of motion governing the spacecrafts' attitude, the external and internal satellite disturbance torques were identified by Grant et al. [28] to be the most vital to precision pointing. The relatively low orbits of each BRITE NanoSat highlighted that the main source of disturbance would be magnetic. The integral term in the well-tuned PID 3-axis controller was fed back into the system's state equation during state propagation to track the steady-state pointing errors (i.e. net disturbance torques), instead of empirically calculating the disturbance torques in orbit [28]. Grant et al. additionally mentioned that accurately measuring residual magnetic dipoles of the BRITE satellites during ground tests are difficult and unreliable. This prompted the engineers to choose the aforementioned PID integral term feedback method to determine the primarily magnetic disturbance torques [28] – the results of which can be seen in fig. 2.14.

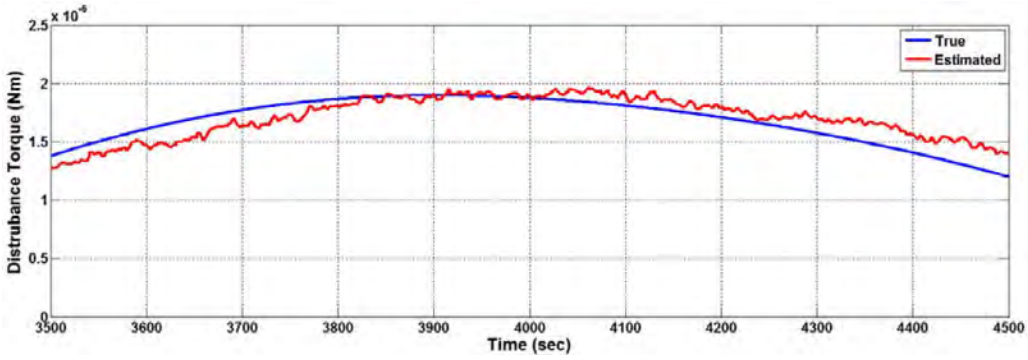

Figure 2.14: BRITE Estimated Disturbance Torque [28]

The feedback of each satellite's wheel torque is from the system's commanded torque values as opposed to using wheel speed telemetry to work out the corresponding torque. This was done so as to minimise

the large errors which would result from differentiating noisy telemetry data [28]. The choice is justified by the authors who stipulate that the reaction wheels are able to deliver the torque with a low enough error [28]. The authors lastly mentioned that all wheel momentum management is disabled during the BRITE NanoSats' fine-pointing modes, in order to disable the integrated magnetorquers and remove the possible effects caused by applied currents and magnetic field measurements.

The spacecrafts' state variables are well estimated during sensor update steps due to the high accuracy of each star tracker. The possible errors which could have arisen due to the relatively long propagation period of up to 2 s are minimised through the accurate tracking of disturbance torques and through stringent characterisation of the remaining terms in Euler's equation. According to the authors, only the satellites' mass moments of inertias were characterised on the ground before launch to within an accuracy of 5% using a horizontal pendulum [28].

The performance of the Austrian BRITE NanoSats was simulated before launch by characterising the on-board sensors and actuators, and simulating the predicted satellite orbit environment. Fig. 2.15a shows the results of the simulation, where the centroid of a star was observed over a 15 min period and was predicted to vary on the imager pixel array by approximately 2.1 pixels RMS (53.6″) – significantly lower than the required 3 pixels RMS (78″) [28]. The two Austrian satellites were launched in February 2013, where UniBRITE and BRITE-Austria further underwent a six and eight month commissioning period respectively [28]. Following this, the satellites completed their scientific goal of consistently observing the Orion constellation over a seven-month period [28]. The data obtained from the mission was used to assess each satellite's pointing accuracy and stability by observing how the centroid of a target star varied over the imager payload's pixel array over time. The actual measured in-orbit accuracy of the same simulated observation period exhibited by UniBRITE, not only outperformed the required accuracy, but was in fact better than the predicted simulated results – measuring at slightly less than 2 pixels RMS (45″) [28].

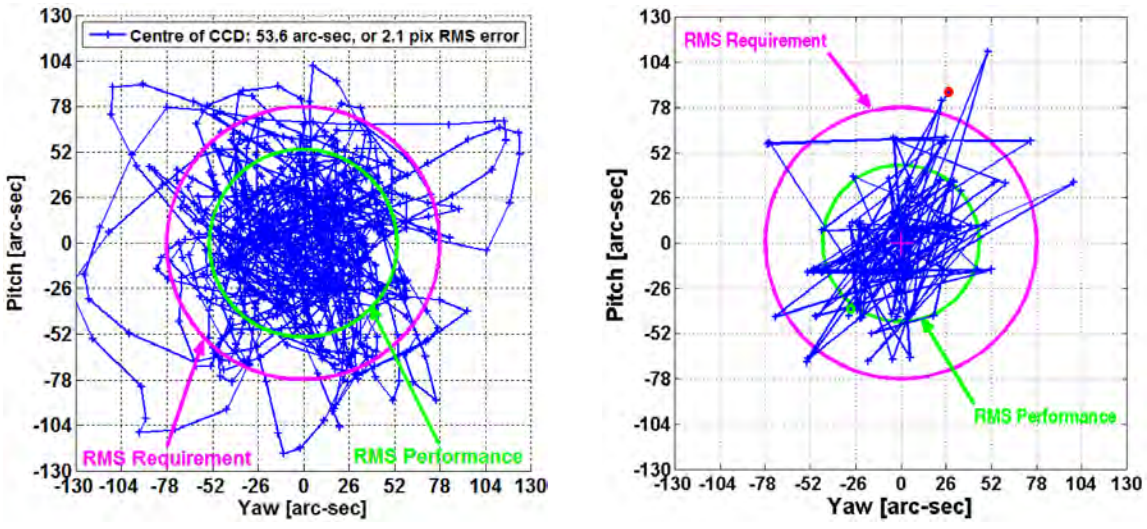

(a) UniBRITE ADCS Fine Pointing Accuracy and Stability Predicted Performance [28]

(b) UniBRITE ADCS Fine Pointing Accuracy and Stability Actual Performance [28]

Figure 2.15: BRITE ADCS Fine Pointing Accuracy and Stability Performance

2.6 Summary

The above literature aids in creating a general understanding of CubeSats and assists in identifying the key ADCS factors, which allow CubeSats to achieve good IPAs. Firstly, the CubeSat was defined before going into the prominent trends since its discovery. These trends included the popular types of CubeSats, types of orbits, and the organisations that fund development. Following on, three missions were discussed to gain further perspective as to why CubeSats are being increasingly developed as well as to learn from

the process in order to increase future CubeSat IPA. The missions were MinXSS-1, ASTERIA, and the BRITE constellation. Particular focus was placed on the pointing accuracy and stability reached in each mission, and factors which lead to the high level of performances, which can be achieved by miniaturised ADCSs. The miniaturisation of high accuracy ADCS sensors, such as star trackers, allowed each satellite to achieve ambitious arc-second pointing accuracy and attitude stability. The above provided context and useful information that will assist in this research that aims to investigate the IPA which can be achieved by a CubeADCS operating in very similar conditions to the aforementioned missions.

Chapter 3

The CubeADCS

3.1 Overview

CubeSat trends combined with the expected CubeSat ADCS performances have been discussed in the previous chapter. Sec. 2.3 briefly touched on the performance of the CubeADCS, but this was decidedly not a true reflection of the CubeADCS's potential IPA. This chapter discusses the CubeADCS and its subcomponents in greater detail. The chapter mainly focusses on the underlying theory behind the inner workings and design of the various sensors and actuators, whilst additionally outlining each subsystem component's various key performance parameters as stipulated by CubeSpace and relevant subcomponent supplier datasheets. Sources of errors and component limitations are analysed, to assist with sensor and actuator modelling in chapter 6. Additional focus is placed on sensors which provide the CubeADCS with more precise environmental and attitude estimates, such as the Earth and Sun sensors, and CubeSpace's star tracker – the CubeStar.

3.2 An Integrated System

The CubeADCS is an integrated ADCS consisting of up to four separate PCBs (conforming to the CubeSat dimension standards) and multiple peripheral components. Certain combinations of these PCBs and peripheral components make up the various modules aboard the CubeADCS as shown in fig. 3.1. These modules can be customised to integrate less or more sensors and actuators in order to achieve the unique goals and mission requirements set out by various clients purchasing the system.

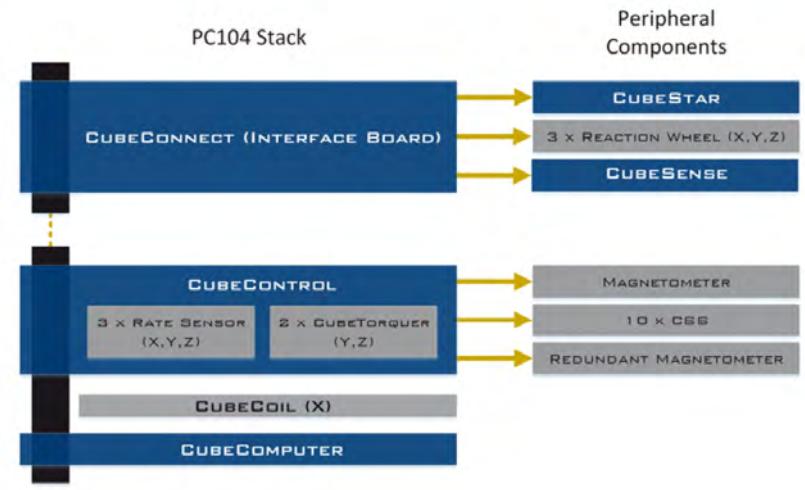

Figure 3.1: CubeADCS Modules and Peripheral Components [29]

A summary of all possible components included in the integrated CubeADCS and their pertaining modules are presented in table 3.1, which includes all relevant ADCS sensors and actuators. The component manufacturers are also stipulated in the table, of which the majority are designed and manufactured by

CubeSpace themselves. The magnetometer (MM) and redundant magnetometer (RMM) sensing devices are sourced externally, however, the incorporated structure (including the deployment mechanism of the primary MM) and internal PCB designs are designed and produced by CubeSpace.

There are two standard CubeADCS integrated solutions, namely: Y-Momentum and 3-Axis. The default Y-Momentum solution offers three primary control modes which include: detumbling a satellite, stabilising a satellite's attitude in its orbit and performing satellite pitch manoeuvres in its orbital plane [30]. The standard Y-Momentum bundle (seen in fig. 3.2a – with an additional CubeSense upgrade) comes equipped with a CubeComputer, a CubeControl, a small CubeWheel, a deployable MM, ten coarse sun sensors (CSS), two CubeTorquer rods and a CubeTorquer coil [30]. Both magnetometers and CSSs are not shown for both configurations in fig. 3.2.

Table 3.1: CubeADCS Sensor and Actuator Summary

No.	Component	Manufacturer	Module
1	MEMS Gyro	Silicon Sensing® Systems (UK) Ltd.	CubeControl
2	Magnetometer	Honeywell International Inc.	CubeControl
3	Redundant Magnetometer	Honeywell International Inc.	CubeControl
4	Coarse Sun Sensor	Silonex Inc.	CubeControl
5	Fine Sun Sensor	CubeSpace	CubeSense
6	Earth Sensor	CubeSpace	CubeSense
7	Star Tracker	CubeSpace	CubeStar
8	Reaction Wheels	CubeSpace	CubeWheel
9	Y-Momentum Wheel	CubeSpace	CubeControl
10	Magnetorquers	CubeSpace	CubeControl
11	On-Board Computer	CubeSpace	CubeComputer

The 3-axis solution (seen in fig. 3.2b) comes standard with all the previously mentioned components with the addition of CubeSense sun and earth sensors to provide more precise attitude estimation capabilities and two extra small CubeWheels to provide the full 3-axis stability [31]. The 3-axis solution can provide the satellite with the same three control modes with the added advantage of being able to perform more complex pointing manoeuvres and target tracking. Finally, both solutions can be upgraded to suit a client's specific needs. This includes the addition of an RMM, CubeSense sun and nadir sensors (if not already included) and a CubeStar for missions which require high accuracy pointing. Actuators can also be upgraded to larger sizes depending on the mass of the satellite and its moments of inertia.

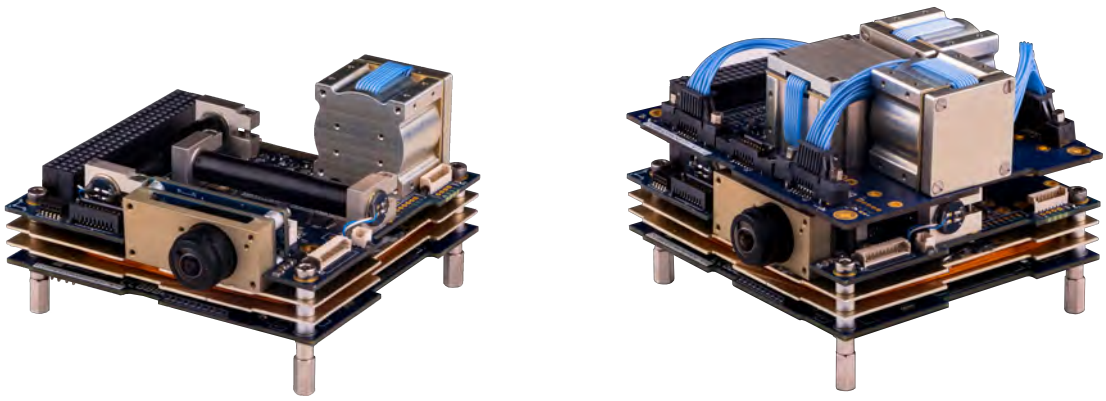

(a) CubeADCS Y-Momentum [30]

(b) CubeADCS 3-Axis [31]

Figure 3.2: Typical CubeADCS Bundle Configurations

The design and operation of each sensor and actuator will be briefly discussed in the context of its interfacing module, where focus will be placed on the high accuracy sensors and actuators vital to a good IPA.

3.3 CubeComputer

The CubeComputer (CC) module is based on the ARM Cortex-M3 architecture which can be configured as a general purpose NanoSat OBC or as an ADCS OBC. It is responsible for executing the CubeADCS's attitude control program (ACP), executing estimation and control algorithms [32] and providing data storage for various logged telemetries and captured images. The CC is also responsible for all intermodule communication and for processing all external commands. The CC's ICD [33] specifies that it has:

- a 32-bit ARM Cortex-M3 processor which has a clock frequency of up to 48 MHz at 1.25 DMIPS/MHz,
- internal and external watchdogs,
- 32 kB of EEPROM storage,
- 4 MB of flash memory for code storage,
- 1 MB of SRAM for data storage,
- a MicroSD socket for greater storage requirements up to 2 GB,
- I2C, UART, CAN V2.0B and SPI communication interfaces and
- a piggyback utility expansion header for mission specific extensions.

The CC physical characteristics indicate that it is low in mass (< 70 g), it has an operating temperature of between -10 °C and 70 °C and a typical power consumption of 200 mW on average [33].

3.4 CubeControl

The CubeControl (CL) module is used to control the three on-board CubeTorquers and can be used to control one small Y-momentum wheel. It is also used to interface with the 3-axis MM and the RMM (if included in the assembly), three single axis MEMS gyros (placed orthogonally to each other) and up to 10 CSSs (four redundant). The CL module can additionally be configured to support the integration of a GPS unit, however, the actual GPS must be supplied externally and does not come standard with a CubeADCS.

3.4.1 MEMS Gyro

A satellite's gyroscopes are responsible for measuring a satellite's inertial rates about its respective axes. An accurate gyro will provide more precise rate measurements and thus lead to a good IPA – making the gyros important to analyse. The gyros implemented on the CubeADCS are three orthogonally mounted single axis PinPoint® CRM100 vibrating ring gyros (VRGs) designed and manufactured by Silicon Sensing® Systems Ltd. The gyro can be used in either an analogue or digital mode (SPI), where the CL uses the latter to interface with the gyros.

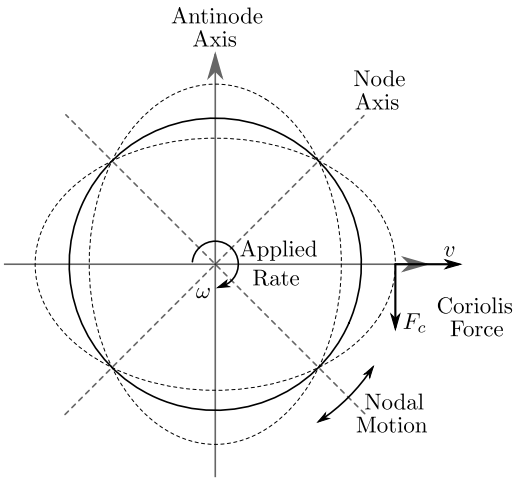

Figure 3.3: Vibrating Ring Gyroscope

As illustrated in fig. 3.3, VRGs work by driving a thin silicon ring into resonance, which allows the transducers in the sensor to detect radial motion caused by the Coriolis effect when the gyro is rotating about its centre axis [34].

A gyro's measured output rate, ω_{out}, would ideally be equal to its applied input rate, ω_{in}. In reality however, there are multiple sources of errors effecting the measured output rate – as illustrated in fig. 3.4. The resulting measured output angular rate of a single axis sensor can be modelled with [35]

$$\omega_{out} = k_{SF}\omega_{in} + N_{MA}\omega_{in} + \omega_{bias} + \omega_{noise}, \tag{3.1}$$

where k_{SF} and N_{MA} represent the scale factor and the misalignment error of the sensor respectively [35]. The additive terms ω_{bias} and ω_{noise} denote the offset bias and stochastic noise of the sensor respectively [35].

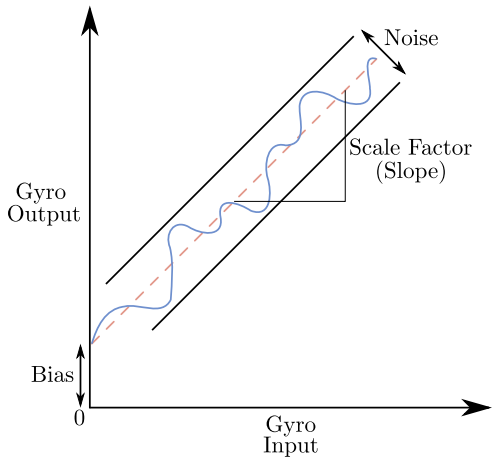

Figure 3.4: Gyro Errors

3.4.1.1 Scale Factor

The scale factor of a gyro is the ratio between the applied rate and the output rate. The scale factor of a gyro can have a thermal variation as well as a non-linear variation with respect to an applied rate.

3.4.1.2 Misalignment

The misalignment error (or cross-axis error) of a gyro is caused by imperfections in the manufacturing of a sensor or by imperfect mounting on the respective satellite body axes. In MEMS sensors, this misalignment can also be effected by thermal variation. Intuitively, both scale factor and misalignment errors have the greatest impact at high angular rates.

3.4.1.3 Bias

The bias is the measured output of the gyro when it is stationary (the offset). The bias of a gyro can be decomposed into three main parts, namely: thermal bias drift, switch on bias repeatability and bias instability (BI) [36]. The switch on repeatability describes a gyro's ability to have the same bias offset at device start-up, assuming the same temperature and rate input conditions. The BI is a stochastic error and can only be modelled for and not removed [35] – which more aptly forms part of the ω_{noise} noise term. Temperature gradients causing the thermal bias drift are typically significant in MEMS sensors and can fortunately be compensated for in most cases.

3.4.1.4 Noise

The remaining stochastic errors are determined from the Allan variance method (BI included), which is used to identify fundamental noise terms caused by underlying random processes. This method is discussed in greater detail in chapter 5 together with thermal bias drift compensation.

3.4.1.5 CRM100 Gyro Performance

The CRM100 gyro datasheet [37] states that the sensor has:

1. measurement sensitivity ranges of $\pm 75\,^\circ\,s^{-1}$, $\pm 150\,^\circ\,s^{-1}$, $\pm 300\,^\circ\,s^{-1}$ and $\pm 900\,^\circ\,s^{-1}$,
2. a worst-case scale factor variation over a temperature range of $-40\,^\circ C$ to $85\,^\circ C$ of between -1.5% to 1.5%,
3. a worst-case scale factor non-linearity of 0.15%,
4. a nominal bias of $0.5\,^\circ\,s^{-1}$ at a sensitivity range of $\pm 75\,^\circ\,s^{-1}$ measured at $25\,^\circ C$,
5. a bias switch on repeatability of $0.14\,^\circ\,s^{-1}$ (RMS),
6. a bias drift with time of $0.05\,^\circ\,s^{-1}\,min^{-1}$ after switch on from 250 s onwards (usually due to self-heating),
7. a typical BI of $24\,^\circ\,h^{-1}$,
8. a typical angular rate noise density of $0.018\,^\circ\,s^{-1}\,Hz^{-0.5}$,
9. an ARW of $0.28\,^\circ\,h^{-0.5}$,
10. a maximum misalignment error of 0.63° and
11. an operating temperature range of $-40\,^\circ C$ to $105\,^\circ C$.

3.4.2 Magnetometer and Redundant Magnetometer

A magnetometer is responsible for measuring Earth's magnetic field components as the satellite propagates along its orbit trajectory. This is important for both attitude estimation and feedback for the required magnetic control torques to be applied by a satellite's magnetorquers. Both magnetometers used by the CubeADCS are low-cost COTS 3-axis HMC1053 magnetoresistive sensors developed by Honeywell. The MM is sampled digitally via SPI, where the RMM is sampled via an analogue signal.

The Honeywell sensors take advantage of the anisotropic magnetoresistive (AMR) effect which causes the resistance of certain ferromagnetic materials to change with a varying magnetic field (B-field). As such, this changes the amount of current permitted to flow through the material, which enables the magnitude of each respective B-field to be calculated about each sensing axis.

Significant magnetometer errors can be attributed to a combination of:

- errors caused by temperature gradients on the magnetometer measurement,
- errors due to satellite magnetic bus disturbances on the measurement (such as unshielded currents in harnesses),
- errors due to the spin of the satellite which create alternating currents and current loops in the solar panels, leading to magnetic disturbances (during in-orbit calibration),
- linearity, orthogonality and hysteresis errors, and
- stochastic magnetometer measurement noise.

Sensitive sensor biases affected by temperature gradients requires that both magnetometers be calibrated on the ground to assist with commissioning calibration during the start of a satellite's mission in orbit.

Specifications, according to the Honeywell datasheet [38], indicate that the sensor has:

1. a B-field measurement range of $\pm 600\,\mu T$,
2. a typical measurement sensitivity of $10\,\mu V/V_{bus}/\mu T$ and a minimum of $8\,\mu V/V_{bus}/\mu T$,
3. a typical noise density, $e_{n_{1\,Hz}}$ of $50\,nV\,Hz^{-0.5}$ and e_n of $5\,nV\,Hz^{-0.5}$ after 50 Hz,
4. an orthogonality error of ±3% FS over a $100\,\mu T$ range,
5. a maximum linearity error of 0.5% FS when operating in B-field strengths in the range of $\pm 300\,\mu T$,

6. a resolution of 12 nT at a 50 Hz filter bandwidth with a bridge voltage of 5 V and
7. an operating temperature range of −40 °C to 125 °C.

3.4.3 Coarse Sun Sensors

The CSSs are made up of a combination of SLCD-61N8 planar photodiode cells developed by Silonex Inc. Photodiodes work by the same principle as solar panels, where they convert light energy (photons) into electrical current. The CubeADCS comes with a total of ten photodiodes to be mounted, where six cells are typically placed on the exterior panels of a satellite's body and four are for redundancy. A coarse sun vector can be calculated from the respective light intensities on each exterior panel as the total amount of current varies in correspondence with the light intensities. As such, the CubeADCS is always able to calculate a sun vector regardless of the satellite's orientation – provided that it is in the sunlit part of the orbit.

The CSS Sun vector components are measured by the short circuit currents of the three CSSs mounted on the facets of a satellite, which are illuminated during the sunlit portion of an orbit. The measured vector components are each proportional to the cosine of the Sun angle to the specific CSS normal-to-surface vector, and can subsequently be represented by

$$\hat{\mathbf{S}}_b = \begin{bmatrix} S_{bx} \\ S_{by} \\ S_{bz} \end{bmatrix} = \begin{bmatrix} \cos\theta_{az}\cos\theta_{el} \\ \sin\theta_{az}\cos\theta_{el} \\ \sin\theta_{el} \end{bmatrix} \tag{3.2}$$

The main errors in CSS measurements come from reflection errors of light off of the photodiodes, modelling errors and errors caused by imperfect mounting of the photodiodes on each satellite face. The datasheet [39] for the photodiodes indicate:

1. a typical spectral sensitivity of 550 mA W^{-1} at light wavelengths of 940 nm,
2. a typical short circuit current, $I_{sc} = 170$ µA at a flux density of 25 mW cm^{-2},
3. a sensitivity spectral range of 400 nm to 1100 nm and
4. an operating temperature range of −40 °C to 125 °C.

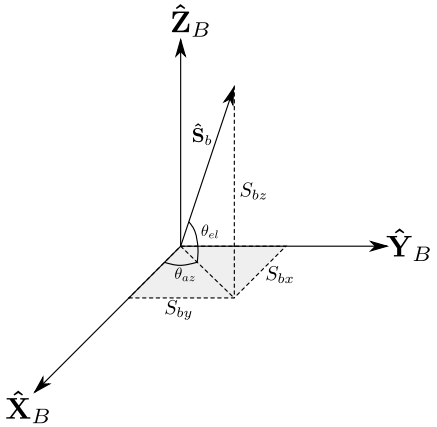

Figure 3.5: CSS Sun Vector with Azimuth and Elevation

3.4.4 CubeTorquers

The final components discussed which form part of the CL are the magnetorquer rods (CubeTorquers) which typically consists of two small CubeRods (CR) and a CubeCoil (CO). The illustration in fig. 3.6a shows the basic concept behind the workings of a magnetorquer, where the resultant magnetic torque vector, $\mathbf{N}_{mt}$, generated by a magnetorquer can be described by

$$\mathbf{N}_{mt} = \mathbf{M}_{mt} \times \mathbf{B}_{\oplus}, \tag{3.3}$$

where $\mathbf{M}_{mt}$ represents the magnetic moment vector induced by current loops flowing around a ferromagnetic core and $\mathbf{B}_{\oplus}$ is the Earth's instantaneous B-field vector.

The main use of magnetorquers is typically to assist in the detumbling of a satellite, placing the satellite into a controlled spin, or to use them in conjunction with a Y-momentum wheel for steady state control – allowing for pitch manoeuvres (as mentioned in sec. 3.2). In a 3-axis control system however, magnetorquers play an important role in dumping angular momentum build-up in reaction wheels, ensuring that the wheels do not saturate and cause possible damage to themselves or to the satellite's attitude stability. The configuration of the CubeTorquers can be seen in fig. 3.6b, where the CRs are ferromagnetic rods with cylindrical coils which are physically mounted to the CL, and the CO is a coil wire loop with an air core, which is wedged between the CC and CL modules.

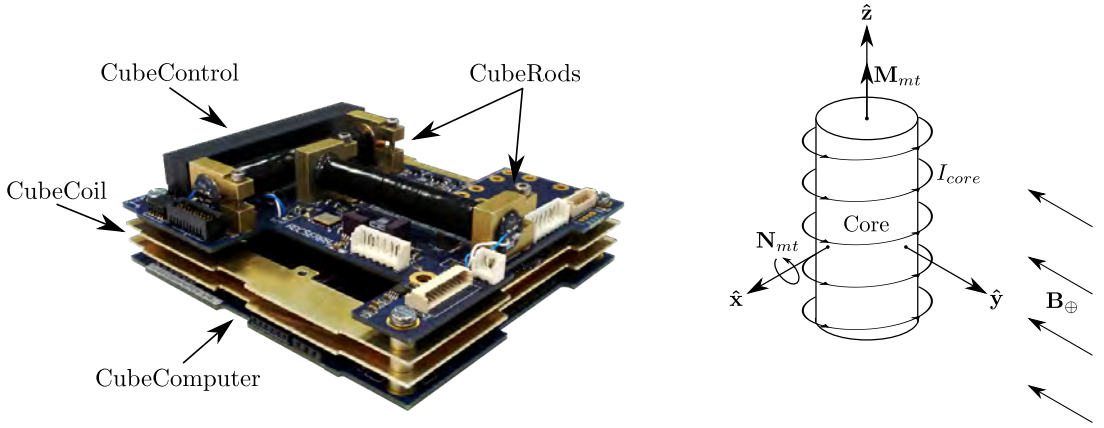

(a) CubeTorquers on the CubeControl Module [40]

(b) Magnetorquer Operation

Figure 3.6: CubeTorquers and Magnetic Control

The performance parameters for the CubeTorquers are taken from the product specifications sheet [41] and summarised in table 3.2. The CRs come in three sizes, small (S), medium (M) and large (L). All CR sizes have a linearity of 2.5%, where all CubeTorquers permit a maximum continuous current of 150 mA operating between −20 °C and 70 °C.

Table 3.2: Magnetorquer Summary

Property	**CR (S)**	**CR (M)**	**CR (L)**	**CO**
Mass (g)	28	36	72	46
Resistance at 25 °C (Ω)	31	65	66	83
Nominal Magnetic Moment at 25 °C ($\mathrm{A\,m^2}$)	±0.24	±0.66	±1.9	±0.13
Magnetic Gain ($\mathrm{A\,m^2\,A^{-1}}$)	2.8	8.2	25	2.1

3.5 CubeSense

Initially developed in 2011 [14], the CubeSense (CS) module consists of either one or two identical CMOS based cameras, shown in fig. 3.8. Each camera is fitted with a fisheye lens to provide an FOV of over 180°, where the cameras can be configured as either a fine sun sensor (FSS) or as a nadir sensor. Fig. 3.8a, shows a CS V2 with both an FSS and nadir sensor fitted to the module, where fig. 3.8b shows the latest CS V3 – a more compact CS which can be configured as either a stand-alone FSS or nadir sensor.

The CS V3 is a relatively new addition to the CubeSpace component suite and does not yet (at the time of writing) have flight heritage – unlike the CS V2. The main differences between the two are that the CS V3 uses around 33% less power on average and provides sensor updates at twice the frequency of the CS V2 [42]. Both primary differences can be attributed to the fact that the CS V3 only has one camera where, other than this, its electronics and software algorithms are in fact very similar. Shown in fig. 3.7, the CS V2 is intended to be integrated into the CubeADCS stack inbetween the CO and CL – as opposed

to the CS V3 which is connected to the top CubeConnect interface board via a harness as a peripheral component (seen in fig. 3.1).

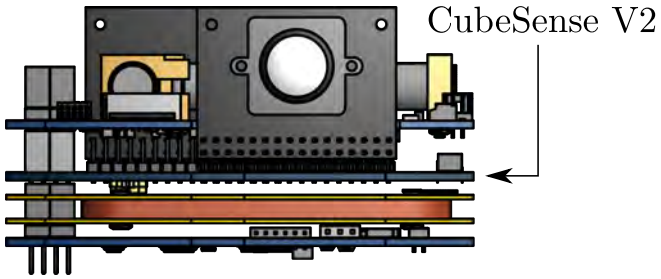

Figure 3.7: CubeSense V2 as Part of the CubeADCS Stack [43]

The CS is a visible light spectrum image-based sensor which performs sophisticated image processing techniques inside the module, outputting virtual angles relative to the camera boresight, allowing the OBC to calculate a Sun or Earth vector through some mathematical transformations (elaborated on in sec. 6.5). The sun detecting camera differs only to the nadir camera hardware, in that it has a neutral density filter (NDF), which ensures that the Sun is the only object visible in the image. The remainder of this section will discuss the workings of the CS and expand on its key features and drawbacks.

(a) CubeSense V2 with FSS and Nadir Sensor

(b) CubeSense V3 Configured as an FSS or Nadir Sensor

Figure 3.8: CubeSense Modules [42]

3.5.1 CubeSense Image Processing Methodology

The image processing portion performed by the CubeSense for both sun and nadir detection is executed by the following sequence [14]:

1. applying a desirable light detection threshold to the image,
2. running an edge detection algorithm,
3. correcting the image for distortion from the fitted fisheye lens,
4. applying centroiding algorithms, which determine the approximate centre of the celestial object, outputting the resulting virtual angles relative to the camera boresight.

In the case of the CS FSS, steps 3 and 4 above are switched around.

3.5.1.1 Image Thresholding

An image threshold is applied for both the sun and nadir cameras. Fig. 3.9 illustrates the concept behind thresholding an image, where a pre-defined threshold value is set to isolate the Sun or the Earth (Earth- or Sun-value), from the background in an image (space-value). The CubeADCS has preset exposure and thresholding values for both sun and nadir cameras which are best fitted to most satellite missions. The

user can also set their own thresholding value depending on the level of light sensitivity required. Only pixels with a higher pixel energy than that, set by the threshold, are subsequently considered by the edge detection algorithm.

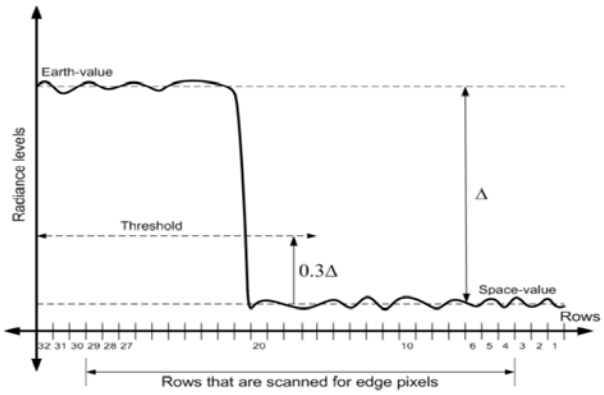

Figure 3.9: A Fixed Camera Threshold [14]

3.5.1.2 Edge Detection

A threshold will only identify pixels with a higher luminance than the background pixels. The edge pixels of an object will need to be identified to accurately determine the centroid of the relevant object. Efficient search algorithms are applied for both types of camera's in order to reduce image processing time [14]. In order to do so, a coordinate frame is defined for the image sensor and can be seen in fig. 3.10, where the grid represents pixel locations on the image sensor [14]. Pixel rows are positioned along the grid y-axis and pixel columns are distributed along the grid x-axis.

To locate the centroid of the Earth, a sequential "grid-search" method [14] is performed, which starts in the top left corner of the grid and samples equally spaced pixels in the grid (vertically and horizontally) to find qualifying edge pixels that are within the predefined threshold limit. The search algorithm samples the grid at a predefined rate set by a sampling factor, K. Both the horizontal and vertical searches can be described by the algorithm [14]:

$$\text{Edge search} = \sum_{i=0}^{\frac{N}{K}-1} \sum_{j=0}^{\frac{M}{K}-1} \text{pixel}(i \cdot K,\ j \cdot K) \tag{3.4}$$

N and M represent the total number of pixel columns and rows in the image respectively and $(i \cdot K,\ j \cdot K)$ is the pixel coordinate of the possible edge pixel. Candidates for edge pixels are those whose pixel intensity values lie between a background pixel and an object pixel. I.e. if the current pixel in the search is found to be above the threshold and the previous pixel was not (or vice versa), then the region between these pixels is likely to host an edge pixel. Subsequently, a smaller search is performed between the two aforementioned pixels and the actual edge pixel is identified. At least six edge pixels are required to perform a successful nadir detection [14].

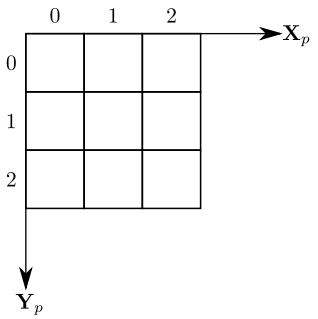

Figure 3.10: Image Pixel Coordinate Frame

Edge detection for the sun camera is somewhat simpler than the nadir. This process is much quicker than the nadir sensor, as the sun takes up a much smaller portion of the image sensor [14]. The sun camera edge detection algorithm takes advantage of the parallel processing power of an FPGA [14]. Its edge searching algorithm identifies the first pixel which is above the predefined threshold value whilst saving the image row by row to memory – starting at pixel (0, 0) [14]. Once this pixel is identified, a sun pixel enclosing area is found using a smaller version of the nadir "grid-search" method, which is subsequently fed back to the MCU for centroiding.

3.5.1.3 Distortion Correction

Edge pixels which are identified by both previously mentioned search algorithms are distorted by the wide-angle FOV, convex fisheye lens. The image distortion is a barrel type radial distortion, meaning that objects in the image that are close to the camera's edge of its FOV appear to get "squashed", where objects near the image centre are the least distorted.

Fig. 3.11 is adapted from [44] and shows an orthographic projection model using a projection sphere, which is used to describe the radial distortion. An incident light ray which passes through centre point, C, at angle θ, would form an image on the image plane at point p if there was no fisheye lens at C. The radial, undistorted distance from the centre of the image plane to point p is denoted as r_u. If there is a fisheye lens at C, which causes a refraction of the incident ray, then a virtual image at p' is created on the projection sphere, which, when orthogonally projected onto the image plane results in the distorted radial distance, r_d, from the image plane centre [44].

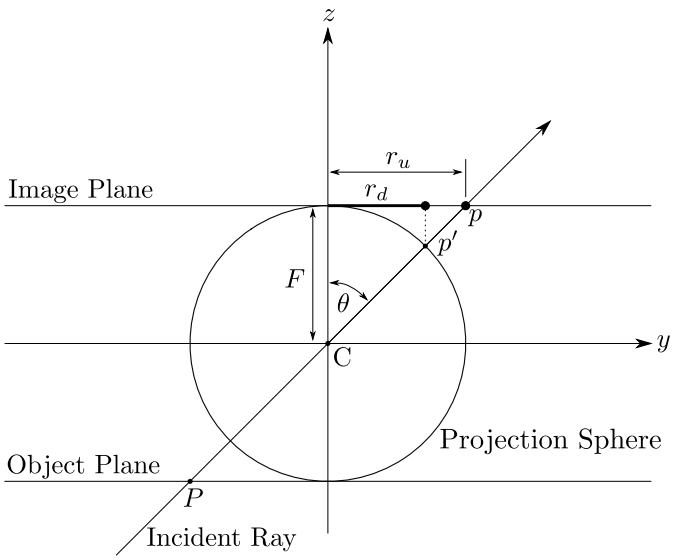

Figure 3.11: Orthographic Projection Model [44]

A rational function-based calibration model is used to relate the measured distorted radius to the expected undistorted radius. This is achieved by mounting a camera on a rotation stage and capturing raw datapoints at known reference angles along at least two orthogonal axes on the image plane. The distorted radius, r_d, can be calculated from the measured distorted pixel coordinates at (x_d, y_d) using

$$r_d = \sqrt{(x_d - x_c)^2 + (y_d - y_c)^2}, \tag{3.5}$$

where (x_c, y_c) is the location of the lens boresight on the image plane. The radial distortion is corrected by using an inverse form of a Polynomial Fish-Eye Transform (PFET)

$$r_d = a_0 + a_1 r_u + a_2 r_u^2 + a_n r_u^n = \sum_{i=0}^{n} a_i r_u^i, \tag{3.6}$$

proposed by Basu and Licardie [45].

3.5.1.4 Centroid Calculation for the Nadir Sensor

In the case of the nadir camera, each edge pixel identified as part of an Earth-like object, is passed through the camera specific lens distortion calibration model and corrected. The next step is to fit a circle to these undistorted edge pixels using the least squares circle fit method (discussed in greater detail by Loubser [14]), and finally outputting the undistorted Earth centroid at the circle centre.

3.5.1.5 Centroid Calculation for the FSS

Centroiding for a sun camera is first performed before any distortion correction takes place. The identified sun pixel enclosing area discussed at the end of sec. 3.5.1.2 is further processed, where the Sun's centroid is calculated through a weighted averaging method – otherwise known as a centre of gravity method. Each identified sun pixel coordinate is weighted by the respective light intensity value at the corresponding pixel coordinate, such that [14]

$$\text{Sun}_x = \frac{\sum_{i=0}^{N}\sum_{j=0}^{M}\text{pixel}(x_{ds}(i),\ y_{ds}(j))\cdot x_{ds}(i)}{\sum_{i=0}^{N}\sum_{j=0}^{M}\text{pixel}(x_{ds}(i),\ y_{ds}(j))} \tag{3.7}$$

and,

$$\text{Sun}_y = \frac{\sum_{i=0}^{N}\sum_{j=0}^{M}\text{pixel}(x_{ds}(i),\ y_{ds}(j))\cdot y_{ds}(j)}{\sum_{i=0}^{N}\sum_{j=0}^{M}\text{pixel}(x_{ds}(i),\ y_{ds}(j))}. \tag{3.8}$$

Variables x_{ds} and y_{ds} in eq. (3.7) and eq. (3.8) are arrays which store the sun pixel x and y coordinates respectively, N and M are the sun pixel enclosing area dimensions and pixel($x_{ds}(i)$, $y_{ds}(i)$) is the light intensity value at each corresponding pixel coordinate. Once the centroiding is complete, the calculated value is fed into the distortion correction model and the undistorted Sun centroid is returned.

3.5.2 CubeSense Key Performance Parameters

Errors in CubeSense measurements are largely caused by the errors in the centroid location of the relevant celestial object, which can be mainly attributed to image sensor resolution and noise, incorrect threshold and exposure settings, imperfect distortion correction, and the celestial object being partially out of the camera's FOV. The stated key performance parameters for the CubeSense (FSS and nadir sensor) are taken from the CubeSense ICD [46] and are stated to have:

- a sample rate of 1 Hz when both sensors are being used,
- a 1σ accuracy of less than 0.2° for the nadir sensor when the full Earth is in its FOV,
- a 1σ accuracy of less than 0.2° for the FSS over its entire FOV,
- a nadir horizontal and vertical FOV of 130° (160° diagonal) and
- a 170° horizontal and vertical FOV (200° diagonal) for the FSS.

The CS provides the CubeADCS with fine estimates of the Earth and Sun vectors over a large FOV. Limitations exist, where the CS is only able to provide these estimates in sun-lit portions of a satellite's orbit. Additionally, any bright objects which enter the cameras' FOVs can cause inaccurate or possibly no detections. Fortunately, the user can define a masking region to ignore certain pixel areas on the image sensor, however, this is only useful in cases where the location of bright objects is known and constant in the cameras' FOVs.

3.6 CubeStar

Developed in 2013 by Erlank [47], the CubeStar (CT) is a highly accurate miniaturised star tracker based on the ARM Cortex-M3 architecture [48], specifically designed to be implemented on CubeSats. The CT is shown in fig. 3.12, which shows its compact three layer stack and protruding lens assembly. Star trackers are the most accurate sensors at determining a satellite's attitude, where their high accuracy is traded for their relatively high power consumption and cost of purchase. High IPA is impossible without

a star tracker, making it a vital component in EO CubeSat missions and for analysis in this thesis.

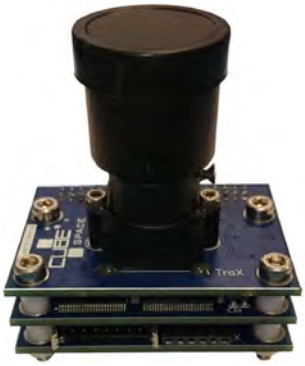

Figure 3.12: The CubeStar Module [48]

The remainder of this section will describe, in relatively brief detail, the underlying processes which allow the CT to perform its high accuracy attitude estimation. The section will end with a list of some key performance parameters pertaining to the CT, as well as CT limitations.

3.6.1 CubeStar Detection

The CT operates by first imaging a portion of stars in its FOV. Next, the on-board processor employs a star detection algorithm [47] consisting of:

1. image plane searching,
2. region growing,
3. centroiding and,
4. distortion correction,

which must be used to distinguish stars from the background noise [47].

3.6.1.1 Image Plane Searching

Stars captured by a perfectly in-focus lens assembly will only excite single pixels throughout the image plane. Erank [47] identifies two main underlying drawbacks which would result from using such perfectly focussed optics. Firstly, the accuracy of the star tracker would be limited to the resolution of the image sensor, and secondly, a single dead pixel will be incredibly hard to distinguish from an actual star – resulting in false positives. For this reason, the CT utilises slightly defocussed optics when capturing images. This results in the star light being spread over a slightly larger region (3×3 pixels in the CT's case), which easily distinguishes dead pixels from actual stars, and most importantly: allows for the centroiding algorithm to calculate the centroid of each star to within a sub-pixel accuracy.

After an image is captured, the image plane search operates similarly to that of the CS grid-search method (explained in sec. 3.5.1), including thresholding the image to distinguish stars from background noise sources. Pixels selected during the grid-search are each compared to the set threshold value to determine regions of interest containing possible stars. The spreading of each stars' light over multiple pixels has the added benefit of increasing the speed of the grid-search algorithm. The grid-search only looks at every third pixel column and row from the top left pixel, to the bottom right pixel in the image plane [47], as opposed to individually searching all 1024×512 pixels. Once a pixel is detected over the applied threshold, a region growing algorithm is initiated to group all the pixels belonging to the possible detected star [47]. Once a result is returned by the region growing algorithm, the grid-search resumes.

3.6.1.2 Region Growing

The region growing algorithm is best illustrated in fig. 3.13 as presented by Erlank [47]. The region growing algorithm is a recursive algorithm which begins by designating the detected pixel, identified by the image plane search, as the initial seed and growing the number of pixels around it classified as part of a star. A determined seed's value is first zeroed, to avoid it being detected again and the four adjacent pixels surrounding the seed are compared to the threshold value. Neighbouring pixels identified to be above the detection threshold are classified as new seeds, where the region growing algorithm is called recursively with each newly identified seed, until there are no more seeds to grow.

All identified seeds make up the grouped set of pixels which possibly belong to a star. Too many pixels indicate large, bright objects which have entered the camera's FOV, where too few pixels suggest that a dead pixel has been discovered or that the identified star is too dim for accurate centroiding and detection to take place [47]. In both of these cases, the grouped set of pixels must be discarded. If numerous discards are determined then the image plane search is halted [47]. Centroiding can be performed on the group of pixels which pass the aforementioned checks.

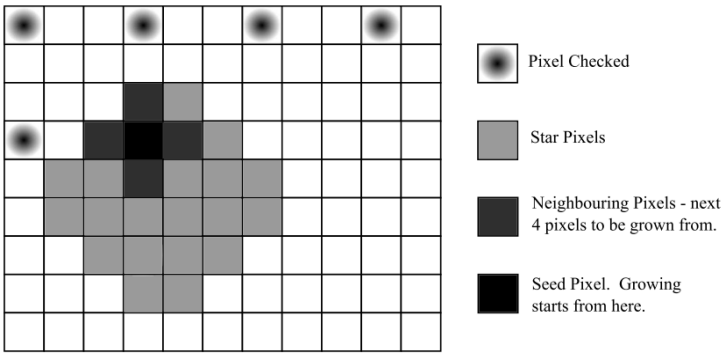

Figure 3.13: CubeStar Region Growing Algorithm [47]

3.6.1.3 Centroiding

The centroiding algorithm is what largely determines the accuracy of the CT, where the incorporated algorithm is said to be accurate to within 0.2 pixels [47]. Once the region growing algorithm is complete, the qualifying grouped pixels belonging to each detected star are then run through the same centre of gravity centroiding algorithm used by the CS for the sun camera, described by eqs. (3.7) and (3.8), to locate the x and y pixel centroid coordinates of the identified star. The main difference between the CT centroiding method and the CS method, is that the CT centroiding algorithm only utilises a 5×5 grid around the brightest pixel in the qualifying group of pixels [47].

3.6.1.4 Distortion Correction

Image distortion correction is done in order to correctly match stars in the image to stars in a known star catalogue. The distortion correction used is different to that of the CS, where the correction model compensates for both radial and tangential distortions [47]. The CT lens distortion is corrected through a simplified version of Brown's distortion model [47],[49], as the smaller lens FOV does not undergo as much distortion as the CS wide-angle lens. The undistorted pixel coordinates can be calculated using [47]:

$$x_u = x(1 + K_1 r_d^2 + K_2 r_d^4) + P_2(r_d^2 + 2x^2) + 2P_1 xy \tag{3.9}$$

and,

$$y_u = y(1 + K_1 r_d^2 + K_2 r_d^4) + P_1(r_d^2 + 2y^2) + 2P_2 xy, \tag{3.10}$$

where

$$x = \frac{x_d - x_c}{f_{pix}} \qquad y = \frac{y_d - y_c}{f_{pix}}. \tag{3.11}$$

The variables in eqs. (3.9) to (3.11) are described in table 3.3. Erlank [47] calculates the distortion coefficients for the lens by utilising MATLAB®'s Camera Calibration Toolbox [47] and a set of calibration checker board images. The focal length is determined by imaging a portion of stars in a known constellation and measuring the distance between these stars. The distance is then compared to the actual known distance between the stars, and the focal length is found. Finally, [47] finds the boresight pixel location on the image plane by imaging the exact same lens lined up with the CT lens assembly, and centroiding the resulting circle produced.

Table 3.3: CubeStar Distortion Variables

Variable(s)	Description
x_u, y_u	Undistorted star centroid pixel coordinates
x_d, y_d	Distorted star centroid pixel coordinates
x_c, y_c	Lens boresight pixel coordinates
f_{pix}	Lens focal length
K_n	n^{th} radial distortion coefficient
P_n	n^{th} tangential distortion coefficient
r_d	Distorted pixel radius from boresight shown by eq. (3.5)

Once the star detection portion is complete and the undistorted locations of each star are calculated in 2D image plane coordinates, the on-board processor then transforms the star centroid coordinates to 3D CT body unit vector centroid coordinates, which is further expanded on in chapter 6 during the CT simulation sensor modelling.

3.6.2 CubeStar Matching

Once the star detection is complete, a star matching algorithm is employed to match the detected stars in the image plane to stars in the Hipparcos star catalogue referenced by the CT. The CT must be able to take a centroided star's calculated boresight-referenced unit vector and either, match this vector to a corresponding inertial star unit vector, or reject the centroid as a false detection [47]. Erlank conducts a comparison of various possible matching algorithms in his thesis, where his main considerations were determined by the limitations of the CT processor speed and internal flash memory allocation [47]. The chosen matching algorithm was fairly novel at the time, known as the Geometric Voting Algorithm (GVA) – first published in 2008 by Kolomenkin et. al. [50].

The GVA's relatively low memory requirements, speed and robustness to false detections, made it a good choice for the CT to employ. Erlank presents a more in-depth explantation in his thesis [47] into the methodology and mathematics behind the algorithm. Only a brief summary of the algorithm will be discussed in this subsection to align with the scope of this thesis.

The GVA uses star-pairs and a subsequent voting mechanism to achieve it's matching. Erlank divides the algorithm into five key steps. First the angular distances of separation between all star-pairs in the image are calculated. Next, similar star-pair angular separation distances are looked for in the catalogue. Star-pairs in the catalogue which have separations that closely match the measured distances, each give votes to the two corresponding imaged stars under investigation, by allocating star catalogue IDs to each star. Following this, an initial matching is conducted which assigns each star its likely identity based on the number of votes it received. This matching is then verified by conducting a secondary round of voting, where a final verified list of confirmed star matches is ultimately generated.

The CT was initially developed to perform star matching in what is known as a lost-in-space mode [51]. Star trackers are said to be in such a mode, when they do not have any prior knowledge of their attitude when attempting to match stars. The main drawback to the lost-in-space mode, is that it takes up a lot

of computational time. The CT has since had its algorithms improved thanks to research conducted by Gabriël Roux in 2019 [51], where the researcher contributed to the development of a second star tracker, tracking mode. The tracking mode implemented is intended to drastically reduce the time and power consumption needed for the CT to successfully match stars in space, by using prior knowledge of the systems state [51]. The technique takes advantage of this prior knowledge and uses it to predict the expected and refined locations on the image plane in which to search and attempt to match the next set of stars. According to CubeSpace [52], both the lost-in-space and tracking modes are currently utilised by the CT.

3.6.3 CubeStar Attitude Determination

The primary objective of the CT, is to provide the CubeADCS with an accurate estimation of the CT's attitude with respect to an inertial frame of reference. This is the final step conducted by the CT, where it uses the matched star sensor body and inertial vectors to output its attitude in quaternion vector form.

The chosen algorithm used by the CT is the QUEST attitude determination algorithm, as it is able to use all the matched star vectors and provide a statistical solution to determining the CT's attitude [47]. Its wide usage in the spacecraft industry, robustness and efficiency also aided in its selection for the CT to implement. A full derivation of the QUEST algorithm is presented by Shuster and Oh in [53].

The QUEST algorithm requires at least three stars that have been successfully matched. Initial estimates presented by Erlank, on the potential best-case accuracy indicated a maximum simulated cross-boresight and about-boresight RMS error of 0.004° and 0.02° respectively [47]. The CT can additionally employ a tracking algorithm, which assists by providing an alternative to star matching. The condition which allows for this, is when previously identified stars in that frame can be found in the next frame. The CT tracking algorithm uses its prediction of where the previously identified stars should emerge in the next frame, and only looks in that exact region for the same star. This assists in the speed in which the CubeStar can determine its attitude, as well as improving its robustness and sky coverage [47].

3.6.4 CubeStar Specifications

CubeSpace have made several improvements on both the CT's hardware and software algorithms since its inception in 2013 by Erlank. CubeSpace reports the following specifications on the CT [48]:

- 3σ star locating accuracies within 0.01° about the camera cross axes and 0.03° about the camera boresight,
- a maximum FOV of $58° \times 47°$ (x and y-axis respectively),
- a sensitivity range < 3.8 star magnitude,
- a star catalogue of 410 stars and that
- the CT should be able to match three or more stars 99.71% of the time.

A large drawback related to the CT is that if the Sun, Earth or Moon is in the FOV, then it is highly likely that no stars will be matched, which will lead to a lower accuracy of attitude determination of the CubeADCS. Additionally, in order to obtain accurate results, the satellite needs to have a slow slew rate when imaging (the stars), to avoid image smearing. Primary sources of error lie in the CTs image sensor noise, errors from imperfect lens distortion calibration, inaccurate focal length calculation and boresight image plane coordinates, and algorithms possibly taking too long to return a solution.

In the unlikely event that the CT is unable to make detections in the eclipse portion of a satellites orbit, then the only sensor available for measurements will be the MM, which will limit the CubeADCS's stability. Fortunately, EO missions with visible light optical payloads (as is considered in this thesis), will conduct imaging during the sun-lit portion of the orbit. Care must be taken, however, not to let stray light rays enter the CT's FOV which would cause invalid or null CT attitude estimation outputs.

3.7 CubeWheels

As the name suggests, the CubeWheel (CW) is a reaction wheel suited to control CubeSats. Reaction wheels provide a satellite with the ability to exchange its momentum internally. This is different to other actuators, such as magnetorquers and thrusters which exchange momentum externally, between the satellite body and the Earth or between the satellite body and the ejected propulsion mass respectively.

3.7.1 Reaction Wheel Operation

All reaction wheels comprise a spinning disk with a relatively large mass moment of inertia, connected to an electric DC (usually brushless) motor. This motor is then controlled by an MCU which commands the drive electronics to employ various control schemes to track commanded torque or wheel speed references. A rotating CW creates a gyroscopic stiffness about its centre axis (shown in fig. 3.14) as it conserves its angular momentum. This gyroscopic stiffness is known as a control torque, which can be used to reduce the influence of various external environmental disturbance torques, such as aerodynamic or magnetic disturbances.

Additionally, using an orthogonal set of three reaction wheels holds the satellite stable and controllable about all three of its body axes. The internal momentum exchange cannot change the total satellite angular momentum, but it can redistribute this momentum, which allows for the satellite's attitude to be controlled. This change in attitude can be achieved at a very precise level with reaction wheels, making them critical components for any high accuracy IPA EO missions.

Several reaction wheel limitations exist, two of which are that they cannot produce external torques, and are constrained by their maximum rotation rates. This maximum rotation rate determines a reaction wheel's maximum momentum storage as the two are directly related to each other through:

$$\mathbf{h}_{wheel} = J_{wheel}\boldsymbol{\omega}_{wheel}, \tag{3.12}$$

where $\mathbf{h}_{wheel}$, J_{wheel} and $\boldsymbol{\omega}_{wheel}$ are the angular momentum vector, mass moment of inertia and rotation rate vector (in $\mathrm{rad\,s^{-1}}$) of the reaction wheel respectively.

Figure 3.14: CubeWheel Angular Momentum Vector [54]

Additionally, the constant absorbing of external disturbance torques gradually causes the wheel's momentum to accumulate. This build-up eventually causes the wheel to saturate, as it approaches its maximum momentum storage capabilities. This means that reaction wheels require momentum dumping through thrusters or through the on-board magnetorques to externally transfer the accumulated momentum in the wheel. If this is not done, then any additional external disturbance torques will cause the satellite to become unstable. It is also not recommended to operate a reaction wheel near 0 RPM to reduce the dominant frictional torques at low speeds. This can be achieved by biasing the reaction

wheels, however, this will have an impact on power consumption as well as quicker angular momentum build-up.

Inaccuracies in following suitable reference commands can be attributed to the CWs speed encoder resolution being too large, control signal noise, thermal variations, wheel imbalances and frictional torques acting on the wheels. The last of which, is prominent at low rotational speeds, where this could be mitigated by biasing the CW's – as discussed in sec. 2.4. Each wheel is balanced during manufacturing to avoid unwanted vibrations and inaccuracies. However, design considerations should still be taken to not mount wheels onto the same mounting platform as an imaging payload or the CT. This will assist to avoid image smearing due to imaging payload vibrations, and inaccurate star tracker measurements [55].

3.7.2 CubeWheel Specifications

CubeSpace now manufactures four different CubeWheel (CW) sizes, namely: small, small plus, medium and large sizes. For the purposes of this thesis, only the small, medium and large wheels were investigated to suit three separate CubeSat sizes (discussed in chapter 7). The specifications found in the CW ICD [55] for the three selected CW sizes are summarised in table 3.4.

Table 3.4: Reaction Wheel Summary

Property	**Units**	**Small**	**Medium**	**Large**
Max Speed	RPM	8000	6000	6000
Speed Resolution	RPM	0.50	0.50	0.50
Sample Rate	Hz	1.00	1.00	1.00
Worst-Case Control Error (3σ)	RPM	5.00	2.00	2.00
Max Angular Momentum	mN m s	1.77	10.82	30.61
Max Torque	mN m	0.23	1.00	2.30
MoI	kg mm^2	2.11	17.23	48.71
Static Imbalance	g mm	< 0.03	< 0.04	< 0.06
Dynamic Imbalance	g mm^2	< 0.50	< 1.40	< 5.00

3.7.3 Y-Momentum Wheel

In the case where a CubeADCS is selected to only be a Y-momentum configuration, then only one CW is required. If the Y-momentum wheel is a small wheel, then it is typically mounted on the CL PCB (as can be seen in fig. 3.2a), and is controlled by the CL MCU and drive electronics. In all other cases, the Y-momentum bundle uses a CW with its own drive electronics and MCU (a single reaction wheel). The Y-momentum wheel can only be activated when the satellite is in a stable Y-Thompson tumbling state [29]. It works in collaboration with the CubeTorquers in the Y-momentum control stage where it stops the satellite from spinning to achieve a stable nominal position of zero roll, pitch and yaw. Thereafter, only the pitch reference angle can be controlled in the Y-momentum control mode.

3.8 Summary

The CubeADCS sensors and actuators have all been discussed. Key performance parameters for each subcomponent have been laid out, with possible sources of errors identified. This chapter has laid the framework for proper CubeADCS sensor and actuator simulation modelling to be conducted in chapter 6. An initial analysis has revealed that the CubeADCS IPA can only be as accurate as the most accurate sensor – the CT. Its accuracy limits the CubeADCS to a best case IPA of 0.01° about its cross-boresight axes. To ensure a stable CubeSat attitude throughout the entire orbit period, design considerations must be made when mounting the CT onto the satellite, to avoid any stray light from entering its FOV.

Additionally, sensor characterisation and calibration must be performed on the ground before launch, to optimise their performances – especially in the case of the MEMS gyros, which are particularly sensitive

to thermal variations. Finally, the initial key performance parameters of the CWs, indicate that they should be able to track speed references to within 0.15% at speeds greater than 2000 RPM and that the wheels will cause very little vibrational disturbances on the satellite body. To avoid large tracking errors at low wheel speeds, the CWs can be biased in orbit. The implications of this are analysed in chapter 7.

Before sensor modelling and simulation testing can take place, an accurate simulation environment must be defined, and as a prerequisite, the mathematical theory and dynamics which govern this environment are discussed.

Chapter 4

Satellite Orbit and ADCS Concepts

4.1 Overview

An accurate simulation environment that is reflective of the true space environment and satellite dynamics, can only be defined once the underlying theory and mathematics behind the operation of an ADCS is understood. This chapter discusses the necessary fundamental ADCS concepts that are both needed and used throughout this thesis.

4.2 Coordinate Frames

In order to describe a satellite's relative position in space and time with respect to celestial objects and the Earth, various appropriate coordinate frames are defined. A rectangular coordinate frame (CF) can be described with three unit vectors which form a basis to create three orthogonal axes. A vector existing in such a space can be expressed as a linear combination of the base unit vectors.

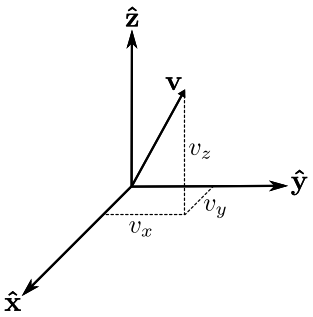

Figure 4.1: Example Coordinate Frame

For example, the vector $\mathbf{v}$, shown in fig. 4.1 can be expressed in terms of its orthogonal basis unit vectors as $\mathbf{v} = v_x\hat{\mathbf{x}} + v_y\hat{\mathbf{y}} + v_z\hat{\mathbf{z}}$. The location of the origin (or centre) of the three orthogonal unit vectors is also important to define, where the origin is usually at the centre of the Earth (nadir) or at the CoM of a satellite when working with relevant ADCS coordinate frames.

4.2.1 Earth-Centred Coordinate Frames

There are two important Earth-centred CFs to consider when describing a satellite's position in space and time, namely: the Earth-Centred Inertial (ECI) frame and the Earth-Centred Earth-Fixed (ECEF) frame. Fig. 4.2 is adapted from [56] and illustrates both the ECI and ECEF frames and their relation to each other.

As the name suggests, the ECI frame is an inertial frame of reference and does not rotate with the Earth. The ECI frame is a celestial coordinate system that is based on the Earth's orbit around the sun. This

orbit creates a track along the Earth's celestial sphere (illustrated in fig. 4.2) which is defined as the ecliptic, and is inclined at approximately 23.5° to the equatorial plane (obliquity of the ecliptic, ϵ). The point where the sun crosses the equatorial plane ascending from the southern to the northern hemisphere is known as the vernal equinox. The vector pointing from the vernal equinox towards the Sun and the first point of Aries (Υ) defines the x-axis in the ECI frame.

Angles α_P and δ_P are referred to as the right ascension and declination of an objects' position in the ECI frame respectively. They are celestial coordinates and are defined relative to Υ and the Earth's equatorial plane respectively. Finally, the z-axis in the ECI frame points in the direction of the north celestial pole along the Earth's axis of rotation and the y-axis simply completes the orthogonal set. Angles measured from, and along the ecliptic are known as ecliptic latitudes and longitudes – where longitude in this case is measured from Υ.

The ECEF frame x and y axes are both fixed to the Earth and thus rotate with it. The x-axis is defined to point in the direction of the node of intersection between the Greenwich Meridian and the equatorial plane. The z-axis is shared with the ECI frame z-axis and points towards the celestial north pole, where once again the ECEF frame y-axis completes the orthogonal set. Coordinates in the ECEF frame are defined in terms of a terrestrial geocentric latitude and longitude marked by angles ϕ_P and λ_P respectively in fig. 4.2.

The position vector in ECEF coordinates of an object on the surface of a spherical Earth can be obtained from a given geocentric latitude and longitude with

$$\mathbf{r}_{ECEF} = \begin{bmatrix} R_\oplus \cos\phi_{gc} \cos\lambda \\ R_\oplus \cos\phi_{gc} \sin\lambda \\ R_\oplus \sin\phi_{gc} \end{bmatrix}, \tag{4.1}$$

where $R_\oplus \cong 6378.14\,\text{km}$, denotes the Earth's equatorial radius. Eq. (4.1) gives an example of a position vector to a location on a spherical Earth's surface. However, a vector to a satellite in ECEF coordinates can equally be determined if the radial distance to the satellite and its geocentric latitude and longitude are known.

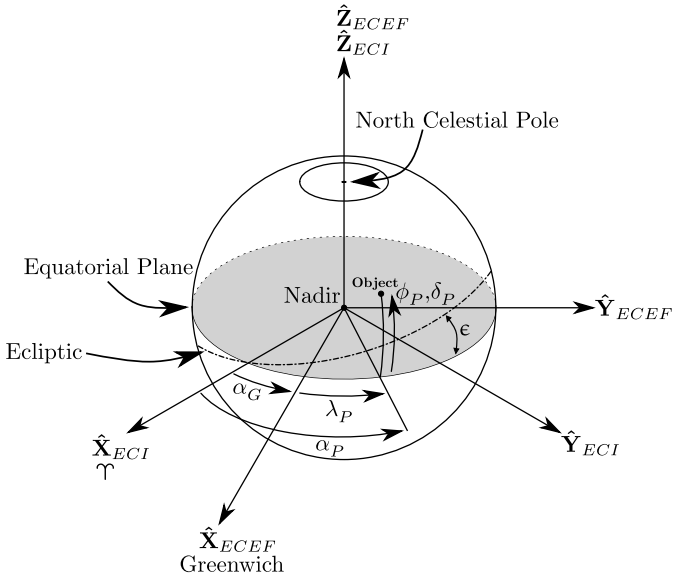

Figure 4.2: ECI and ECEF Coordinate Frames

In reality, the Earth is not a perfect spheroid, but rather an ellipsoid with an eccentricity of $e_\oplus \approx 0.0818$. Consequently, most Earth navigation and orbit propagation software such as *Google Earth* and *Orbitron*, give locations on Earth with reference to this ellipsoidal Earth in geodetic coordinates. This is important to take into account for satellites performing Earth target tracking manoeuvres. Seen in fig. 4.3, the geodetic latitude (ϕ_{gd}) of an object is the angle measured between the equator and the normal to the

surface of the oblate Earth at the point of interest, where the geocentric latitude (ϕ_{gc}) is the angle measured from Earth's centre to the same point.

The vector to a site on the ellipsoidal Earth in ECEF coordinates can thus, be more accurately calculated by replacing $R_\oplus$ in eq. (4.1) with the true radius (R_{site}) to an object on Earth's surface by [56]

$$R_{site} = R_\oplus \sqrt{1 - e_\oplus^2 \sin^2 \phi_{rd}} \tag{4.2}$$

if the geocentric latitude and longitude is known, where ϕ_{rd} is the reduced latitude, and is calculated as [56]

$$\phi_{rd} = \arcsin\left(\frac{\sin \phi_{gc}}{\sqrt{1 - e_\oplus^2 \cos^2 \phi_{gc}}}\right). \tag{4.3}$$

It must be noted that the radius R_{site} is the distance from Earth's centre to the mean sea level, and that for locations above or below this level, the relative site altitude can simply offset this radius.

A particular site's geocentric latitude can be obtained from a geodetic latitude by [56]

$$\phi_{gc} = \arctan\left[\left(1 - e_\oplus^2\right) \tan \phi_{gd}\right], \tag{4.4}$$

where conversely, the geodetic latitude can be calculated from the geocentric latitude through [56]

$$\phi_{gd} = \arctan\left[\frac{\tan \phi_{gc}}{\left(1 - e_\oplus^2\right)}\right] \tag{4.5}$$

It must be noted that eqs. (4.4) and (4.5) are only applicable for locations on Earth's surface [56]. Longitudinal coordinates are identical for both geodetic and geocentric coordinate systems, due to the oblate sphere being "flattened" from the poles towards the equator.

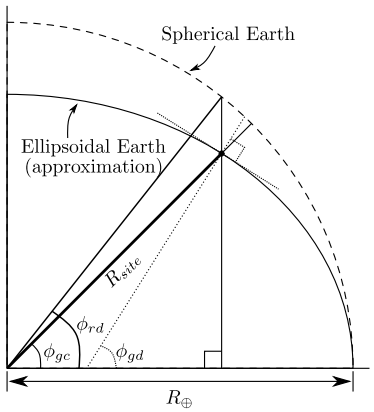

Figure 4.3: Geodetic and geocentric latitude

With a position vector in ECEF coordinates defined, a position vector in ECI coordinates can be determined with the following transformation

$$\mathbf{r}_{ECI} = \mathbf{A}_{ECEF}^{ECI} \mathbf{r}_{ECEF}, \tag{4.6}$$

where the transformation matrix $\mathbf{A}_{ECEF}^{ECI}$ is calculated as

$$\mathbf{A}_{ECEF}^{ECI} = \begin{bmatrix} \cos \alpha_G & -\sin \alpha_G & 0 \\ \sin \alpha_G & \cos \alpha_G & 0 \\ 0 & 0 & 1 \end{bmatrix}. \tag{4.7}$$

Seen in fig. 4.2, the angular distance α_G (measured from Υ to the Greenwich Meridian) is known as the Greenwich Sidereal Time (GST) and is calculated as [56]

$$\alpha_G = \omega_\oplus UT1 + \alpha_{G0}, \tag{4.8}$$

where $\omega_\oplus$ ($\cong 7.2921 \times 10^{-5}\,\mathrm{rad\,s^{-1}}$) is the Earth's mean angular rotation rate in radians per second, α_{G0} is the Greenwich Mean Sidereal Time (GSMT) at midnight on the day of interest and UT1 is the total time elapsed in solar seconds since midnight on the same day. Provided by [56], α_{G0} can be calculated using the J2000 epoch in radians as

$$\begin{aligned}\alpha_{G0} = 1.753\,368\,560 \;+\; 628.331\,970\,688 T_{UT1} \;+\; 6.7707 \times 10^{-6} T_{UT1}^2 \\ - 4.5 \times 10^{-10} T_{UT1}^3,\end{aligned} \tag{4.9}$$

where T_{UT1} is the number of Julian centuries elapsed since the J2000 epoch [56] and is calculated using eq. (4.10) [56] with JD_0 being the Julian Date (JD) at midnight on the day of interest.

$$T_{UT1} = \frac{\mathrm{JD}_0 + 2\,451\,545}{36\,525} \tag{4.10}$$

A satellite's geocentric and geodetic latitudes and longitudes (SSP) can additionally be determined from its ECI position vector. The longitude of a satellite, λ_{sat}, can be determined from

$$\lambda_{sat} = \alpha_{sat} - \alpha_G, \tag{4.11}$$

where α_{sat} is the right ascension of a satellite, shown by α_P in fig. 4.2. This angle can be calculated from the satellite ECI position vector x and y components, r_x^{ECI} and r_y^{ECI} respectively using the trigonometric relation

$$\alpha_{sat} = \mathrm{atan2}\left(r_x^{ECI},\; r_y^{ECI}\right). \tag{4.12}$$

The geocentric latitude, ϕ_{gc}, can be determined using all three vector components through

$$\phi_{gc} = \arctan\left(\frac{r_z^{ECI}}{\sqrt{\left(r_x^{ECI}\right)^2 + \left(r_y^{ECI}\right)^2}}\right). \tag{4.13}$$

As earlier alluded to, the calculation of the geodetic latitude and subsequently, the true altitude of a satellite involves a slightly more complex solution than the simple use of eq. (4.5). The algorithm is adapted from Vallado [56] and involves iteratively solving for ϕ_{gd} by using the initial guess of $\phi_{gd} \approx \phi_{gc}$. The algorithm is shown below in alg. 4.1, where the inputs to the algorithm are the satellite's geocentric latitude and position vector components in ECI coordinates, listed as ϕ_{gc}, r_x, r_y, and r_z respectively.

Algorithm 4.1: Obtain Satellite Geodetic Latitude and Altitude [56]

Data: ϕ_{gc}, r_x, r_y, r_z, $R_\oplus$, $e_\oplus$

Result: ϕ_{gd}, h_{sat}

$\phi_{gd} \leftarrow \phi_{gc}$

do

$\phi_{gd(old)} \leftarrow \phi_{gd}$

$C_\oplus \leftarrow \frac{R_\oplus}{\sqrt{1 - e_\oplus^2 \sin^2 \phi_{gd(old)}}}$

$\phi_{gd} \leftarrow \frac{r_z + C_\oplus e_\oplus^2 \sin \phi_{gd(old)}}{\sqrt{r_x^2 + r_y^2}}$

while $|\phi_{gd} - \phi_{gd(old)}| < Tolerance$

$h_{sat} \leftarrow \frac{\sqrt{r_x^2 + r_y^2}}{\cos \phi_{gd}} - C_\oplus$

4.2.2 Satellite-Centred Coordinate Frames

Next, it is necessary to define three important satellite-centred CFs, namely: the orbit-referenced coordinate (ORC) frame, the inertial-referenced coordinate (IRC) frame and finally, the satellite body coordinate (SBC) frame.

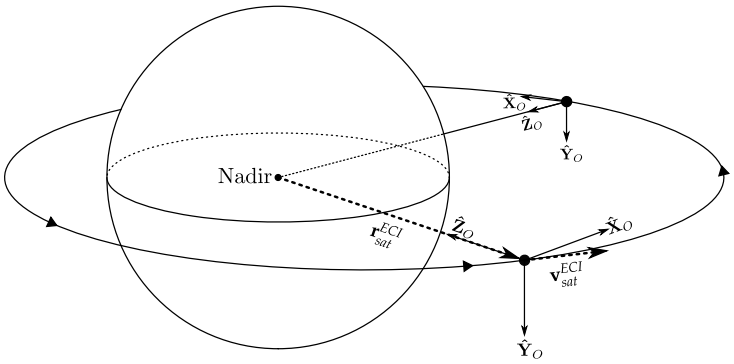

Figure 4.4: ORC frame

Seen in fig. 4.4, the ORC frame is fixed to the satellite's orbit position and rotates with the orbital motion, where the origin of the ORC frame is at the satellite's CoM. The $\hat{\mathbf{Z}}_O$ axis is defined to point towards the centre of the Earth (nadir) at all times, the $\hat{\mathbf{Y}}_O$ axis points in the orbit anti-normal direction and the $\hat{\mathbf{X}}_O$ axis completes the orthogonal set.

Fig. 4.4 illustrates how to transform vectors from the ECI frame to the ORC frame, with knowledge of the ECI referenced position and velocity vectors, $\mathbf{r}_{sat}^{ECI}$ and $\mathbf{v}_{sat}^{ECI}$ respectively. The transformation matrix $\mathbf{A}_{ECI}^{O}$, can be determined in terms of the normalised versions of these vectors and the definition of the ORC frame. The $\hat{\mathbf{Z}}_O$ axis is simply the vector pointing in the opposite direction to $\hat{\mathbf{r}}_{sat}^{ECI}$. The velocity unit vector, $\hat{\mathbf{v}}_{sat}^{ECI}$, is in the same plane as $\hat{\mathbf{Z}}_O$, where taking the cross product of the two forms $\hat{\mathbf{Y}}_O$. Finally, as earlier mentioned, the axis $\hat{\mathbf{X}}_O$ completes the orthogonal set of ORC axes and is the cross product of $\hat{\mathbf{Y}}_O$ and $\hat{\mathbf{Z}}_O$, which determines the transformation matrix as [57]

$$\mathbf{A}_{ECI}^{O} = \begin{bmatrix} (\hat{\mathbf{r}}_{sat}^{ECI} \times (\hat{\mathbf{v}}_{sat}^{ECI} \times \hat{\mathbf{r}}_{sat}^{ECI}))^T \\ (\hat{\mathbf{v}}_{sat}^{ECI} \times \hat{\mathbf{r}}_{sat}^{ECI})^T \\ -\hat{\mathbf{r}}_{sat}^{ECI} \end{bmatrix}, \tag{4.14}$$

where a vector $\mathbf{w}_{ECI}$ in ECI coordinates is transformed to the ORC frame by

$$\mathbf{w}_O = \mathbf{A}_{ECI}^{O} \mathbf{w}_{ECI}. \tag{4.15}$$

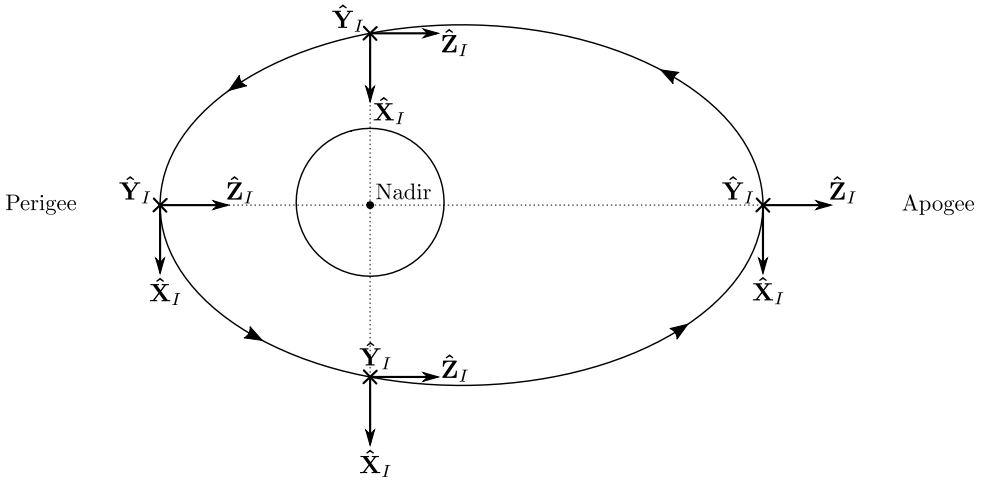

Figure 4.5: IRC frame

The IRC frame is mainly used as a reference frame for satellite dynamic equations of motion. Seen in fig. 4.5, the IRC frame is defined to have its axes pointing in the same direction as that of the respective axes in the ORC frame when the satellite is at its perigee. However, it does not rotate with the satellite's orbital motion and is nearly fixed in inertial space.

From this perspective, the ORC frame is observed to be rotating about the $\hat{\mathbf{Y}}_I$ axis at a rate opposite to that of the time varying satellite orbit rotation rate, $\omega_o(t)$, about the Earth.

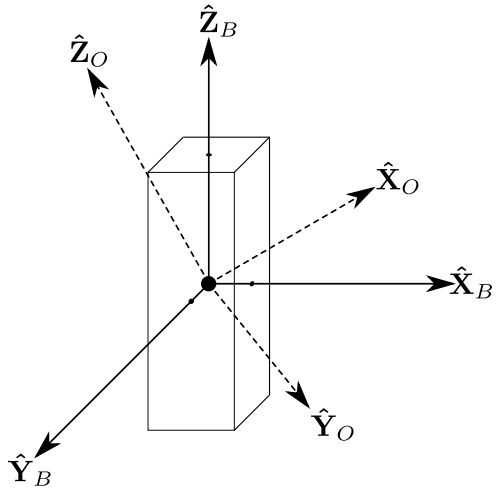

Figure 4.6: SBC frame within the ORC frame

Finally, the SBC frame is defined to be fixed the satellite body with its origin at the satellite's CoM. The SBC axes are custom defined to suit various mission requirements and provides a reference frame for ADCS sensor measurements and actuator outputs. The chosen SBC axes orientation is to usually coincide with the ORC frame when the satellite is in its nominal flight orientation. Fig. 4.6 shows an arbitrary orientation of the SBC frame within the ORC frame where transformations between the two frames are discussed in sec. 4.4 on attitude dynamics.

4.3 Orbital Mechanics

In order to place the satellite into the various aforementioned CFs and to accurately predict its position in space, the properties of its particular orbit must be understood.

4.3.1 Classic Orbital Elements

There are six fundamental properties, which are commonly referred to as the classical orbital elements. Two of the elements can be seen in fig. 4.7. They describe the shape and size of the satellite's orbit ellipse and are respectively known as the semi-major axis, a, and the eccentricity of the orbit, e. Element a, describes the distance between the centre of the ellipse and either of its vertices, or half the distance of the ellipse's major axis. Eccentricity, e represents how flat or circular the orbit is and can be described by

$$e = \frac{c}{a} = \sqrt{1 - \frac{b^2}{a^2}}, \tag{4.16}$$

where c is the distance between the centres of the orbit ellipse and Earth, and b is the semi-minor axis (half of the ellipse minor axis).

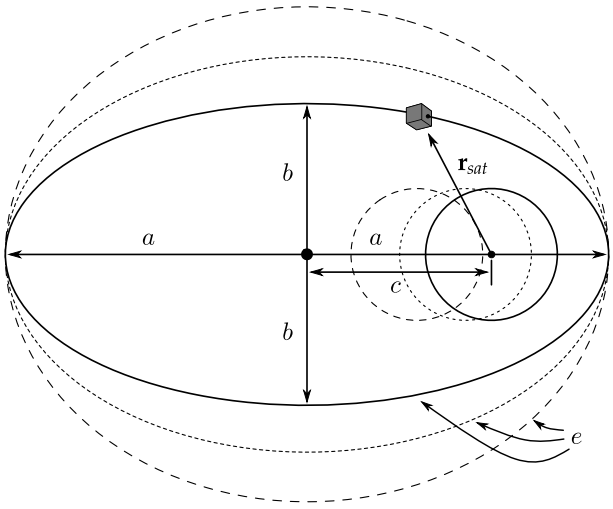

Figure 4.7: Shaping Orbital Elements

The next four classical elements are all angular elements, which are used to characterise the orientation of the orbit ellipse in space, and the satellite's position along its orbit trajectory. All four of these elements are illustrated in fig. 4.8 which has been adapted from [58], and are defined with reference to the ECI frame, discussed in sec. 4.2.1. Element i, describes the inclination of the orbit and is the angle between the orbital plane and the equatorial plane measured at the right of the ascending node, which is the point where the satellite crosses the equatorial plane moving in a northerly direction [59].

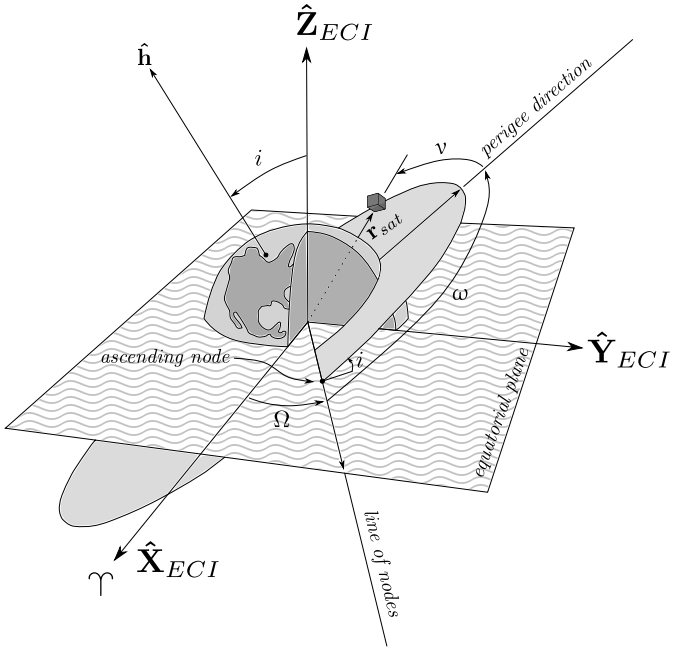

Figure 4.8: Angular Orbital Elements

The next element, the right ascension of the ascending node (RAAN), is described by symbol, Ω, and is the angle between ♈ and the ascending node. The RAAN determines how the satellite orbital plane is orientated with respect to the sun as the Earth moves along its orbit [59]. The argument of perigee, ω, is the element which describes the position of the orbit perigee (the closest point to Earth) with respect to the ascending node. It can otherwise be thought of as the orientation of an orbit within its own plane [59]. The sixth and final classical element to define, is known as the true anomaly represented by ν in fig. 4.8. It is measured relative to the perigee direction and is the only one of the six elements which is used to describe the position of a satellite within its orbit as opposed to the shape, size and orientation of that orbit.

The radial distance between nadir and a satellite in orbit, $r_{sat} = |\mathbf{r}_{sat}|$, can be calculated by solving for the two-body vector equation of motion

$$m_{sat}\ddot{\mathbf{r}}_{sat} + m_{sat}\frac{\mu}{r_{sat}^3}\mathbf{r}_{sat} = 0, \tag{4.17}$$

which yields [59]

$$r_{sat} = \frac{a(1-e^2)}{1+e\cos\nu}, \tag{4.18}$$

where m_{sat} is the mass of the satellite and $\mu \approxeq 398\,601\,\mathrm{km}^3\,\mathrm{s}^{-2}$ is the Earth's gravitational constant. It is clear in the case of circular orbits ($e = 0$), that $r_{sat} = a$. It follows that eq. (4.18) is only useful for calculating the angular distance between the satellite and nadir if the orbit is elliptical and the true anomaly is known. Owing to the fact that the large majority of orbits are never perfectly circular, it is important to calculate the true anomaly. Two additional conceptual anomaly angles are defined to assist with this calculation, denoted by E and M, they are the eccentric and mean anomalies respectively.

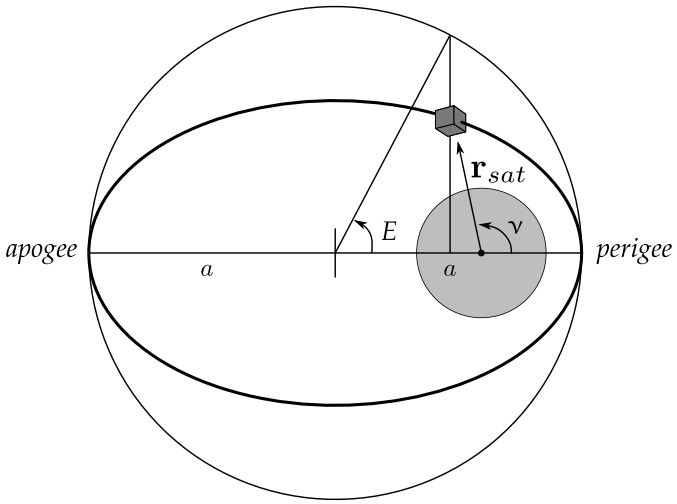

Figure 4.9: Eccentric and True Anomalies

Fig. 4.9 is adapted from [59], and geometrically illustrates the eccentric anomaly of a satellite in its orbit. The average angular velocity of a satellite in any orbit is defined as its mean motion, n, calculated as

$$n = \frac{2\pi}{\tau}, \tag{4.19}$$

where τ is the orbit period of the satellite in question, calculated by

$$\tau = 2\pi\sqrt{\frac{a^3}{\mu}}, \tag{4.20}$$

for both elliptical and circular orbits. The mean anomaly is the angular correspondent of time and is the resultant integral of the mean motion n, described by

$$M = M_0 + n(t - t_0), \tag{4.21}$$

where M_0 is the mean motion of a satellite at time t_0. It follows from eq. (4.21), that it is not possible to show the mean anomaly geometrically in fig. 4.9. The mean anomaly can additionally be defined in terms of the eccentric anomaly, E, with [59]

$$M = E - e\sin E, \tag{4.22}$$

where E can be represented in terms of the true anomaly, ν through [59]

$$\cos E = \frac{e + \cos \nu}{1 + e \cos \nu}. \tag{4.23}$$

Finally, through the use of some elaborate series expansions and manipulations of eqs. (4.22) and (4.23), the true anomaly can be approximated as [59]

$$\nu \approx M + 2e \sin M + 1.25e^2 \sin 2M, \tag{4.24}$$

for small values of e.

The North American Aerospace Defence Command (NORAD) generates and maintains a dataset of two-line elements (TLE) for every single Earth orbiting satellite which has been launched to date. Each TLE file consists of two lines of 69 characters which includes relevant information about the satellite, such as its NORAD ID, classification and the epoch at time of TLE generation. The information also includes a satellite's classical orbit elements, in addition to its drag and ballistic coefficients at time of generation. These TLE's are important sets of data which allow mission designers to monitor and track their satellites, which may not be equipped with a GPS in orbit. The data is additionally important to ADCSs to assist with knowledge of the satellite vector in ECI coordinates to accurately control the satellite and perform desired tracking manoeuvres. The data is fed into simplified perturbation models (SPM) which propagate a satellite along its orbit trajectory to some accuracy. The SPM used to propagate satellites investigated in this thesis is the SGP4 model, which is discussed in greater detail in sec. 5.2.1.

4.3.2 Derived Elements and Sun-Synchronous Orbits

There are several additional orbital elements which are derived from the classic orbital elements – of which only a few will be discussed, to align with the scope of this thesis. The orbital period τ, has already been defined in eq. (4.20). The next element to define, is the velocity of a satellite as it tracks along its trajectory. For elliptical orbits the velocity of a satellite can be calculated with [59]

$$v_{sat} = \sqrt{\mu \left(\frac{2}{r_{sat}} - \frac{1}{a} \right)}, \tag{4.25}$$

where it follows that for circular orbits ($r_{sat} = a$) [59]

$$v_{sat} = \sqrt{\frac{\mu}{a}}. \tag{4.26}$$

Owing to the law of conservation of angular momentum, a satellite in orbit will remain in that orbit unless it is acted upon by any external forces which consequently alter its angular momentum. There are a number of orbit perturbations caused by several external space environment forces acting on a satellite, such as gravitational and aerodynamic forces. These perturbations manifest as a drift or fluctuation of the classical elements discussed in sec. 4.3.1. Most applicable to this thesis is a drift in a satellite's RAAN, known as nodal drift.

The nodal drift phenomenon is directly related to the oblateness of the Earth. This can be seen in fig. 4.10, where the oblateness of the Earth causes the satellite to experience a more significant gravitational pull from the Earth as it nears the equatorial bulge. When the satellite is heading from the southern to the northern hemisphere, it experiences a pull "upwards" towards the equator until it enters the northern hemisphere and begins to experience a force "downwards" towards the equator [59]. This induces a perturbing torque, $\hat{\mathbf{N}}_p$, where the satellites orbital angular momentum vector, $\hat{\mathbf{h}}$, will proceed to track towards this torque vector and result in a coning motion about the north pole. As a consequence of this motin, the RAAN changes ever so slightly by an amount of $\Delta\Omega$ with each crossing of the equator (south to north or vice versa).

In a single day the amount of nodal drift which can occur can be expressed by

$$\Delta\Omega \cong -1.5 n J_2 \left(\frac{R_\oplus}{a} \right)^2 \frac{\cos i}{\left(1 - e^2\right)^2}, \tag{4.27}$$

where $J_2 = 0.001\,082\,635\,9$ is the second zonal harmonic geopotential coefficient and the principal term which approximates for the bulge at the equator [60].

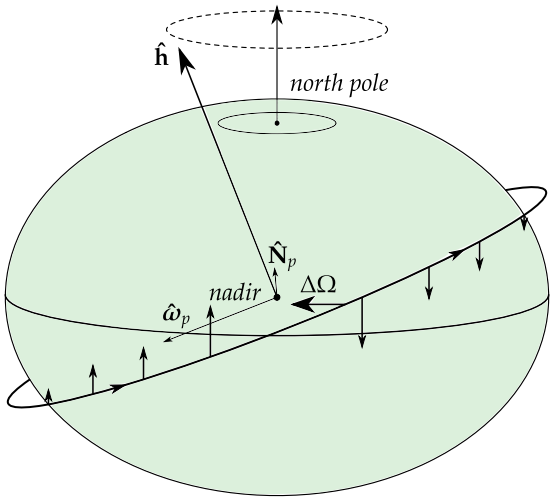

Figure 4.10: Nodal Drift Observed from Ascending Node Side

Eq. (4.27) shows that this drift can be quite significant for highly circular, low orbiting and gently inclined orbits. The equation also shows, that prograde orbits (same rotation direction as Earth) where $i < 90°$, the nodal precession is in the opposite direction to the Earths rotation, for polar orbits ($i = 90°$) no precession occurs, and for retrograde orbits ($i > 90°$) the nodal precession proceeds in the same direction as Earths rotation.

The direction of rotation about Earth's own axis is the same as that of the Earth around the Sun. In a single day the Earth rotates $\frac{360°}{365} = 0.9856°$ per day. Mission designers take advantage of this fact and engineer their satellites into retrograde orbits at inclinations determined by their desired orbit altitudes as they maintain a close to constant nodal precession equal to that of the Earth's rotation around the Sun each day. This ensures that the sun angle, β, remains nearly fixed to the orbit plane throughout the entire year. This angle can be translated into an approximate local time when the satellite is crossing the equator as it refers to the time for a particular region at the sub-satellite point at the time of crossing. For example, a midnight-noon orbit will have a constant sun angle of 0°, and a 6am – 6 pm orbit will have a sun angle of 90° throughout the year. The latter of the two orbits will result in the satellite going into almost no eclipses and thus a maximum amount of solar energy is available for the satellite to use. Satellite's equipped with imager payloads are often placed into SSO's, as the lighting conditions on Earth will be mostly the same throughout each orbit at the same ECI sub-satellite point.

4.3.3 Angular Relationship Between Earth and a Satellite

Adapted from [60], fig. 4.11 defines the angular relationships (for a spheroid Earth) between a satellite, nadir, and a target on Earth. From the perspective of a satellite, the Earth appears as a disk with a radius which changes with its altitude. This angular radius of the Earth disk, $\rho_\oplus$, is calculated with

$$\rho = \arcsin\left(\frac{R_\oplus}{R_\oplus + h_{sat}}\right), \tag{4.28}$$

where $R_\oplus \cong 6378.14\,\text{km}$ and is the equatorial radius of the Earth, and h_{sat} as the altitude of the satellite above the sub-satellite point (SSP). The Earth central angle, λ is measured at nadir from the SSP to the satellite's target. The maximum Earth central angle, λ_0, is simply calculated with

$$\lambda_0 = \arccos(\sin\rho). \tag{4.29}$$

If λ is known then one can calculate the nadir angle, η, measured at the satellite from the SSP to the satellite's target, where

$$\eta = \text{atan2}(\sin\rho\sin\lambda, 1 - \sin\rho\cos\lambda). \tag{4.30}$$

Otherwise, if η is known, then one can calculate the elevation angle, ε, measured from the target's local horizon to the satellite with

$$\varepsilon = \arccos\left(\frac{\sin\eta}{\sin\rho}\right) \tag{4.31}$$

and alternatively if ε is known then

$$\eta = \arcsin\left(\cos\varepsilon\sin\rho\right). \tag{4.32}$$

The final angle can be determined with the relationship

$$\eta + \lambda + \varepsilon = 90°, \tag{4.33}$$

where the distance from the satellite to the target, D_{sat}, can then be calculated using

$$D_{sat} = R_{\oplus} \cdot \left(\frac{\sin\lambda}{\sin\eta}\right) \tag{4.34}$$

and the distance from the satellite to the true horizon ,D_0 , can be calculated with

$$D_0 = \frac{R_{\oplus}}{\tan\rho} = \sqrt{(R_{\oplus} + h_{sat})^2 + R_{\oplus}}. \tag{4.35}$$

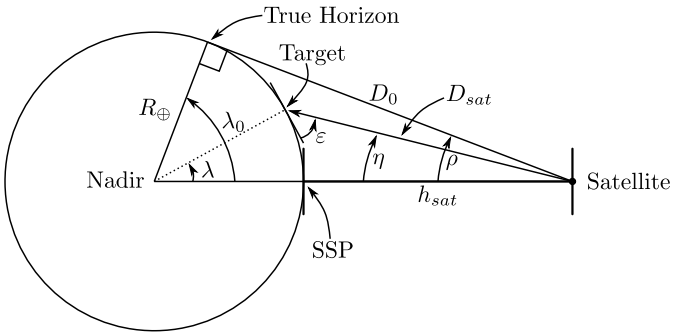

Figure 4.11: Earth and Satellite Angular Relationship

4.4 ADCS Theory

Secs. 4.2 and 4.3 address the position of a satellite within the broader space environment. The next important theory to discuss is with regard to describing the orientation of a satellite within these respective frames and the subsequent control of this orientation. More specifically, the relationship between the SBC and ORC frames is of primary interest in this section.

4.4.1 Euler Angles

The attitude of a satellite can be described in terms of angular rotations relative to a nominal orientation such as the ORC frame. These angular rotations are known as Euler angles and are referred to as a roll (ϕ), pitch (θ) and yaw (ψ) about the respective x, y and z axes of the SBC frame. These individual Euler angles can be used to create transformation matrices, where a roll rotation about $\hat{\mathbf{X}}_B$ is described by the transformation matrix

$$\mathbf{A}_{\phi} = \begin{bmatrix} 1 & 0 & 0 \\ 0 & \cos\phi & \sin\phi \\ 0 & -\sin\phi & \cos\phi \end{bmatrix}, \tag{4.36}$$

for pitch rotations about $\hat{\mathbf{Y}}_B$

$$\mathbf{A}_\theta = \begin{bmatrix} \cos\theta & 0 & -\sin\theta \\ 0 & 1 & 0 \\ \sin\theta & 0 & \cos\theta \end{bmatrix}, \tag{4.37}$$

and finally for yaw rotations about $\hat{\mathbf{Z}}_B$

$$\mathbf{A}_\psi = \begin{bmatrix} \cos\psi & \sin\psi & 0 \\ -\sin\psi & \cos\psi & 0 \\ 0 & 0 & 1 \end{bmatrix}. \tag{4.38}$$

4.4.2 The Direction Cosine Matrix

The Direction Cosine Matrix (DCM) (also known as a rotation matrix) describes the orientation of a particular orthogonal rotated CF with relation to another fixed orthogonal CF with the same origin [61]. Each element in the DCM is the cosine of the unsigned angle between the fixed axes and the associated rotated axes such that the DCM can be described as [62]:

$$\mathbf{A} = \begin{bmatrix} \cos(\theta_{x',x}) & \cos(\theta_{x',y}) & \cos(\theta_{x',z}) \\ \cos(\theta_{y',x}) & \cos(\theta_{y',y}) & \cos(\theta_{y',z}) \\ \cos(\theta_{z',x}) & \cos(\theta_{z',y}) & \cos(\theta_{z',z}) \end{bmatrix}, \tag{4.39}$$

where, for example, $\theta_{x',z}$ is the unsigned angle between the rotated CF's x-axis and the fixed CF's z-axis. Euler angles can be used to describe a satellite's DCM which can be calculated by combining a particular sequence of Euler rotations to define the SBC frame's orientation with respect to the ORC frame (fixed frame in this case). Fig. 4.12 illustrates a Euler-312 rotation sequence or a yaw, roll and pitch rotation about the satellites respective z, x and y body axes respectively. The order of rotation is significant which can be observed both mathematically and graphically (as seen in the aforementioned figure). For instance, a Euler-312 rotation would obtain the DCM

$$\begin{aligned} \mathbf{A}_{312} &= \mathbf{A}_\theta \mathbf{A}_\phi \mathbf{A}_\psi \\ &= \begin{bmatrix} \mathrm{C}_\theta\mathrm{C}_\psi - \mathrm{S}_\theta\mathrm{S}_\phi\mathrm{S}_\psi & \mathrm{C}_\theta\mathrm{S}_\psi + \mathrm{S}_\theta\mathrm{S}_\phi\mathrm{C}_\psi & -\mathrm{S}_\theta\mathrm{C}_\phi \\ -\mathrm{C}_\phi\mathrm{S}_\psi & -\mathrm{C}_\phi\mathrm{C}_\psi & \mathrm{S}_\phi \\ \mathrm{S}_\theta\mathrm{C}_\psi + \mathrm{C}_\theta\mathrm{S}_\phi\mathrm{S}_\psi & \mathrm{S}_\theta\mathrm{S}_\psi - \mathrm{C}_\theta\mathrm{S}_\phi\mathrm{C}_\psi & \mathrm{C}_\theta\mathrm{S}_\phi \end{bmatrix}, \end{aligned} \tag{4.40}$$

where the same rotations performed in a different order such as a Euler-213 rotation (as used in this project) would obtain the DCM

$$\begin{aligned} \mathbf{A}_{213} &= \mathbf{A}_\psi \mathbf{A}_\phi \mathbf{A}_\theta \\ &= \begin{bmatrix} \mathrm{C}_\psi\mathrm{C}_\theta + \mathrm{S}_\psi\mathrm{S}_\phi\mathrm{S}_\theta & \mathrm{S}_\psi\mathrm{C}_\phi & -\mathrm{C}_\psi\mathrm{S}_\theta + \mathrm{S}_\psi\mathrm{S}_\phi\mathrm{C}_\theta \\ -\mathrm{S}_\psi\mathrm{C}_\theta + \mathrm{C}_\psi\mathrm{S}_\phi\mathrm{S}_\theta & \mathrm{C}_\psi\mathrm{C}_\phi & \mathrm{S}_\psi\mathrm{S}_\theta + \mathrm{C}_\psi\mathrm{S}_\phi\mathrm{C}_\theta \\ \mathrm{C}_\phi\mathrm{S}_\theta & -\mathrm{S}_\phi & \mathrm{C}_\phi\mathrm{C}_\theta \end{bmatrix}, \end{aligned} \tag{4.41}$$

with the letters S and C representing the sine and cosine functions respectively.

The Euler angles can be extracted from the DCM $\mathbf{A}_{213}$ as

$$\phi = -\sin(a_{32}), \tag{4.42}$$

$$\theta = \operatorname{atan2}(a_{31}, a_{33}), \tag{4.43}$$

$$\text{and} \quad \psi = \operatorname{atan2}(a_{12}, a_{22}). \tag{4.44}$$

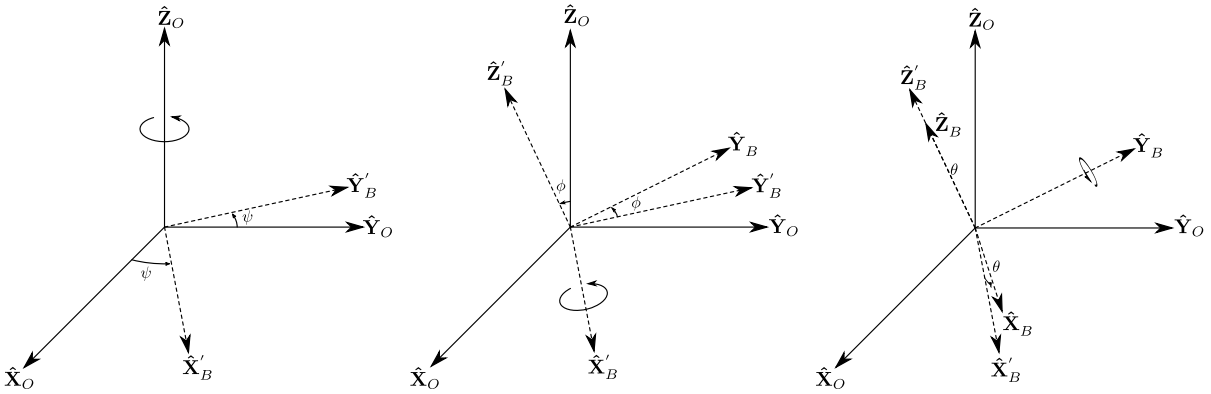

(a) Yaw Rotation **(b)** Roll Rotation **(c)** Pitch Rotation

Figure 4.12: A successive Euler-312 rotation sequence

Euler angles are useful, as they provide a clear human interpretation to describe the attitude of a satellite and they do not require any redundant parameters to be calculated. However, limitations exist where certain rotation angles and rotation orders could produce singularities and thus, no solution. They also require the use of trigonometric functions, rotation order is important where no beneficial product rule exists, and they do not provide a convenient method for numerical integration.

The DCM on the other hand: produces no singularities, it does not require the use of trigonometric functions and a convenient product rule exists for successive rotations. The main disadvantage with the DCM is that it requires the calculation of six redundant parameters.

4.4.3 Quaternions

A third method exists that is widely used in the field of ADCS to determine and propagate the attitude of a satellite, which uses a mathematical tool known as quaternions. Quaternions are a four-parameter representation of attitude consisting of both a scalar part and a vector part. Euler states that "any two independent orthonormal coordinate frames may be related by a single rotation about some axis" [63], where this axis remains unchanged throughout the motion. It follows that the SBC frame can be related to the ORC frame by a single rotation angle (Φ) about a single shared axis known as the Euler or Eigen axis. This rotation can be mathematically defined by the attitude quaternion

$$\mathbf{q} = \begin{bmatrix} q_1 \\ q_2 \\ q_3 \\ q_4 \end{bmatrix} = \begin{bmatrix} e_1 \sin\frac{\Phi}{2} \\ e_2 \sin\frac{\Phi}{2} \\ e_3 \sin\frac{\Phi}{2} \\ \cos\frac{\Phi}{2} \end{bmatrix}, \tag{4.45}$$

where (e_1, e_2, e_3) represent the components of the unit vector $\hat{\mathbf{e}}$, which is shared by both frames, and which lies along the Euler axis.

The four components of the quaternion vector are not independent and are in fact constrained by the property that,

$$q_1^2 + q_2^2 + q_3^2 + q_4^2 = 1 \tag{4.46}$$

The DCM used to transform a vector from the ORC frame to the SBC frame can be represented in terms of the components the quaternion unit vector by

$$\mathbf{A}_O^B = \begin{bmatrix} q_1^2 - q_2^2 - q_3^2 + q_4^2 & 2(q_1q_2 + q_3q_4) & 2(q_1q_3 - q_2q_4) \\ 2(q_1q_2 - q_3q_4) & -q_1^2 + q_2^2 - q_3^2 + q_4^2 & 2(q_2q_3 + q_1q_4) \\ 2(q_1q_3 + q_2q_4) & 2(q_2q_3 - q_1q_4) & -q_1^2 - q_2^2 + q_3^2 + q_4^2 \end{bmatrix}. \tag{4.47}$$

Conversely, the elements of a quaternion vector can be calculated from the satellite DCM with

$$q_4 = \frac{1}{2}\sqrt{a_{11} + a_{22} + a_{33}}, \tag{4.48}$$

$$q_1 = \frac{1}{4q_4}(a_{23} - a_{32}), \tag{4.49}$$

$$q_2 = \frac{1}{4q_4}(a_{31} - a_{13}), \tag{4.50}$$

$$\text{and} \quad q_3 = \frac{1}{4q_4}(a_{12} - a_{21}). \tag{4.51}$$

The error in a satellite's attitude quaternion vector, $\mathbf{q}_e$, is defined as the difference between a commanded attitude quaternion, $\mathbf{q}_c$, and the measured or estimated current attitude quaternion $\mathbf{q}$ [64]. The error quaternion is calculated from the quaternion difference between the two as

$$\begin{bmatrix} q_{e1} \\ q_{e2} \\ q_{e3} \\ q_{e4} \end{bmatrix} = \begin{bmatrix} q_{4c} & q_{3c} & -q_{2c} & -q_{1c} \\ -q_{3c} & q_{4c} & q_{1c} & -q_{2c} \\ q_{2c} & -q_{1c} & q_{4c} & -q_{3c} \\ q_{1c} & q_{2c} & q_{3c} & q_{4c} \end{bmatrix} \begin{bmatrix} q_1 \\ q_2 \\ q_3 \\ q_4 \end{bmatrix}, \tag{4.52}$$

where q_{ie}, q_{ic} and q_i make up the components of the error, commanded and current quaternion vectors respectively.

The main advantages to using quaternions are that: they will always provide a solution to a three-dimensional rotation of a rigid-body within a reference frame (i.e. no singularities), the use of quaternions does not require any trigonometric functions, and they offer a convenient solution to propagate a satellite's attitude by numerical integration. The only distinct disadvantage is that they do not offer an obvious human interpretation.

4.4.4 Small Angle Approximation

A useful approximation which is used by ADCS engineers is the small angle approximation. This allows one to locally linearise non-linear functions such as sinusoids. This is especially useful when using estimation algorithms such as the Extended Kalman Filter (EKF) that are used to estimate non-linear systems which can be well approximated through local linearisations. For a very small angle (γ) which is close to zero, this approximation implies that

$$\sin\gamma \approx \gamma, \tag{4.53}$$

and that

$$\cos\gamma \approx 1. \tag{4.54}$$

4.4.5 Calculating Angular Errors

Various ADCS sensors ultimately provide the system with a measurement vector which indicate the relative positions of a celestial objects or the direction of the surrounding magnetic field. As attitude describes a satellite's angular orientation about its respective axes, a good indication of how these measurements may effect the accuracy of attitude estimations, is to measure the angular distance between the measured unit vector in the SBC frame and the actual expected unit vector in the same frame. This can be achieved by modifying the definition of the dot product through

$$\begin{aligned} \hat{\mathbf{w}}_B \bullet \hat{\mathbf{v}}_B &= |\hat{\mathbf{w}}_B| \cdot |\hat{\mathbf{v}}_B| \cos(\xi) \\ \therefore \xi &= \arccos(\hat{\mathbf{w}}_B \bullet \hat{\mathbf{v}}_B), \end{aligned} \tag{4.55}$$

where $\hat{\mathbf{w_B}}$ and $\hat{\mathbf{v_B}}$ represent the expected and measured unit vectors in the SBC frame respectively.

It is important to note that both vectors are normalised (unit vectors) and are in the same reference frame.

4.4.6 Attitude Kinematics & Dynamics

A satellite's angular body rates can be measured relative to the IRC frame or relative to the ORC frame. Angular motion as measured by gyroscopes fixed to a satellite's body are determined relative to the IRC frame and are combination of both the satellite's angular body rates within the ORC frame and the satellite's orbit angular rate about the Earth with

$$\begin{aligned} \boldsymbol{\omega}_B^I &= \boldsymbol{\omega}_B^O + \boldsymbol{\omega}_O^I \\ \therefore\ \boldsymbol{\omega}_B^O &= \boldsymbol{\omega}_B^I - \boldsymbol{\omega}_O^I, \end{aligned} \tag{4.56}$$

where

$$\boldsymbol{\omega}_B^I = \omega_{ix}\hat{\mathbf{X}}_B + \omega_{iy}\hat{\mathbf{Y}}_B + \omega_{iz}\hat{\mathbf{Z}}_B \tag{4.57}$$

is the inertially-referenced body rate vector,

$$\boldsymbol{\omega}_B^O = \omega_{ox}\hat{\mathbf{X}}_B + \omega_{oy}\hat{\mathbf{Y}}_B + \omega_{oz}\hat{\mathbf{Z}}_B \tag{4.58}$$

is the orbit-referenced body rate vector and,

$$\boldsymbol{\omega}_O^I = \omega_{ix}\hat{\mathbf{X}}_O + \omega_{iy}\hat{\mathbf{Y}}_O + \omega_{iz}\hat{\mathbf{Z}}_O \tag{4.59}$$

is the inertially-referenced orbit rate vector.

The vector $\boldsymbol{\omega}_O^I$ can be transformed by the DCM, $\mathbf{A}_O^B$ to obtain the subsequent angular body rates relative to the ORC frame. As discussed in sec. 4.2.2, fig. 4.5 shows that the ORC frame can be observed as rotating at a rate of $-\omega_o(t)$ within the IRC frame which means that $\boldsymbol{\omega}_B^O$ in eq. (4.56) can in fact be expressed as

$$\boldsymbol{\omega}_B^O = \boldsymbol{\omega}_B^I - \mathbf{A}_O^B \begin{bmatrix} 0 \\ -\omega_o(t) \\ 0 \end{bmatrix}. \tag{4.60}$$

Kinematics is the study of an objects motion which is independent of considering the forces which caused that motion. The kinematic equations of motion can be expressed in terms of: Euler angle kinematics, DCM kinematics and quaternion kinematics. To avoid trigonometric singularities in 3-axis control systems, the quaternion control model is used.

The body rates of a satellite can be converted to quaternion rates through

$$\dot{\mathbf{q}} = \frac{1}{2}\boldsymbol{\Omega}\mathbf{q}, \tag{4.61}$$

where

$$\boldsymbol{\Omega} = \begin{bmatrix} 0 & \omega_{oz} & -\omega_{oy} & \omega_{ox} \\ -\omega_{oz} & 0 & \omega_{ox} & \omega_{oy} \\ \omega_{oy} & -\omega_{ox} & 0 & \omega_{oz} \\ -\omega_{ox} & -\omega_{oy} & -\omega_{oz} & 0 \end{bmatrix}. \tag{4.62}$$

The new quaternion attitude can then be propagated by numerically integrating these rates with

$$\mathbf{q} = \int \dot{\mathbf{q}} dt\ . \tag{4.63}$$

Once propagated, it is important to normalise the calculated quaternion so that

$$\mathbf{q}_{norm} = \frac{\mathbf{q}}{\|\mathbf{q}\|}. \tag{4.64}$$

Contrary to the definition of attitude kinematics; the attitude dynamics of a satellite are concerned with the forces that bring about attitude motion of a satellite body in an inertial frame – where Newton's laws apply. The attitude motion is represented by the angular rates of the body axes relative to the IRC frame and the rotational forces causing that motion are represented by torque vectors in the SBC frame. The Euler dynamic equation of motion describes that the change in a satellite's angular momentum must be equal to the sum of all torques (both internal and external) acting on the satellite. This equation can be expressed as [64]

$$\dot{\mathbf{H}} = \mathbf{N}_{ext} + \mathbf{N}_{gyro} - \mathbf{N}_{wheel}, \tag{4.65}$$

where

$$\dot{\mathbf{H}} = \mathbf{J}\dot{\boldsymbol{\omega}}_B^I, \tag{4.66}$$

$$\mathbf{N}_{gyro} = -\boldsymbol{\omega}_B^I \times (\mathbf{J}\boldsymbol{\omega}_B^I + \mathbf{h}), \tag{4.67}$$

$$\mathbf{N}_{wheel} = \dot{\mathbf{h}}, \tag{4.68}$$

and

$$\mathbf{N}_{ext} = \mathbf{N}_m + \mathbf{N}_d. \tag{4.69}$$

In eqs. (4.66) and (4.67) $\mathbf{J}$ is the moment of inertia matrix of the satellite and $\mathbf{h}$ is the angular momentum vector of the reaction wheels, where $\mathbf{N}_{gyro}$ is the satellite's gyroscopic coupling torque. Shown in eq. (4.69), $\mathbf{N}_{ext}$ is the sum of the external torques acting on the satellite body – with $\mathbf{N}_m$ and $\mathbf{N}_d$ being the satellite's magnetic control and environmental disturbance torques respectively.

4.4.7 Quaternion Feedback Controller Gains

During reaction wheel control manoeuvres, it is sufficient to assume that the large reaction wheel control torques will be orders of magnitude greater than the external disturbance torques acting on the satellite. This reduces eq. (4.65) to

$$\mathbf{J}\dot{\boldsymbol{\omega}}_B^I = \mathbf{N}_{gyro} - \mathbf{N}_{wheel}, \tag{4.70}$$

where the PD type quaternion feedback control law [64]

$$\mathbf{N}_{wheel} = K_p\mathbf{J}\mathbf{q}_{vec} + K_d\mathbf{J}\boldsymbol{\omega}_{err} - \boldsymbol{\omega}_B^{IRC} \times (\mathbf{J}\boldsymbol{\omega}_{SBC}^{IRC} + \mathbf{h}) \tag{4.71}$$

acts to control the ORC referenced body rates and error quaternion to zero, where it additionally compensates for the gyroscopic coupling torque.

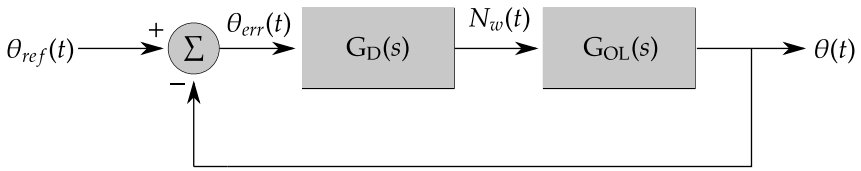

Figure 4.13: Basic Pitch Control Loop

In eq. (4.71), the term $\mathbf{q}_{vec}$ represents the vector portion of the quaternion error, $\mathbf{q}_e$ and $\boldsymbol{\omega}_{err}$ is the ORC angular rate error. Fig. 4.13 illustrates the basic feedback loop for an uncoupled single axis pitch manoeuvre with a PD type controller. If $\mathbf{q}_{vec} = [0 \quad \sin\frac{\theta}{2} \quad 0]^T$ and one assumes that the inertially

referenced x and z body rates are ≈ 0, and $\omega_{yo} \cong \omega_{yi}$, then after substituting eq. (4.71) into eq. (4.70), it follows that

$$J_{yy}\ddot{\theta} = -K_p J_{yy} \sin\frac{\theta}{2} - K_d J_{yy}\dot{\theta},$$

or

$$J_{yy}\ddot{\theta} + K_d J_{yy}\dot{\theta} + K_p J_{yy} \sin\frac{\theta}{2} = 0.$$

If it is further assumed that there will be small pitch error angles then the small angle approximation in eq. (4.53) is valid, and

$$J_{yy}\ddot{\theta} + J_{yy}K_d\dot{\theta} + J_{yy}K_p\frac{\theta}{2} = 0 \tag{4.72}$$

is obtained. The controller and open loop transfer functions in fig. 4.13 can be represented as

$$\mathrm{G_D}(s) = K'_p + K'_d s, \tag{4.73}$$

and

$$\mathrm{G_{OL}}(s) = \frac{1}{J_{yy}s^2} \tag{4.74}$$

respectively, which determines the closed loop transfer function, $\mathrm{G_{CL}}$, to be

$$\mathrm{G_{CL}}(s) = \frac{K'_p + K'_d s}{s^2 + \frac{1}{J_{yy}}K'_d s + \frac{1}{J_{yy}}K'_p}, \tag{4.75}$$

where gains K'_p and K'_d can be related to the quaternion controller feedback gains with

$$K'_p = \frac{J_{yy}}{2}K_p, \tag{4.76}$$

and

$$K'_p = J_{yy}K_d. \tag{4.77}$$

The Laplace transform of eq. (4.72) obtains the same second order closed loop pole equation as in eq. (4.75), which can be used to relate the desired damping and natural frequency terms of a typical second order system to the satellite pitch control response. It follows that the quaternion controller feedback gains can thus be calculated with

$$\begin{aligned} \frac{K'_d}{J_{yy}} &= 2\zeta\omega_n \\ \therefore\ K_d &= 2\zeta\omega_n, \end{aligned} \tag{4.78}$$

and

$$\begin{aligned} \frac{K'_p}{J_{yy}} &= \omega_n^2 \\ \therefore\ K_p &= 2\omega_n^2, \end{aligned} \tag{4.79}$$

where the tailoring of the desired natural frequency and damping response approximately produces the resulting quaternion feedback controller gains.

4.4.8 Target Tracking

Satellites perform target tracking manoeuvres for several purposes such as: pointing at ground stations (GS) during satellite overpasses for communications, continuous monitoring of various Earth locations, or for EO imaging of desired targets [65].

In order to track a desired location on Earth's surface, the target in question must necessarily be in range of the satellite. This can be determined using eqs. (4.34) and (4.35), where target tracking is only possible when $D_{sat} < D_0$. Distance D_{sat} can be calculated with knowledge of the geocentric coordinates of a target and the propagated SSP, using the Earth central angle from satellite to target, λ, as calculated from the law of cosines for sides where

$$\begin{aligned}\cos\lambda &= \cos\phi'_S\cos\phi'_T + \sin\phi'_S\sin\phi'_T\cos\Delta\lambda_{S/T}\\ &= \sin\phi_S\sin\phi_T + \cos\phi_S\cos\phi_T\cos\Delta\lambda_{S/T}.\end{aligned} \tag{4.80}$$

The angular relationships in eq. (4.80) are illustrated in fig. 4.14, where

$$\phi'_S = 90° - \phi_S \qquad \phi'_T = 90° - \phi_T \tag{4.81}$$

and

$$\Delta\lambda_{S/T} = |\lambda_S - \lambda_T|. \tag{4.82}$$

The heading or azimuth angle, as measured from north to the great circle passing through the SSP and target coordinates, can be calculated with

$$\cos\theta_{Az} = \frac{\sin\phi_T - \cos\lambda\sin\phi_S}{\sin\lambda\cos\phi_S}. \tag{4.83}$$

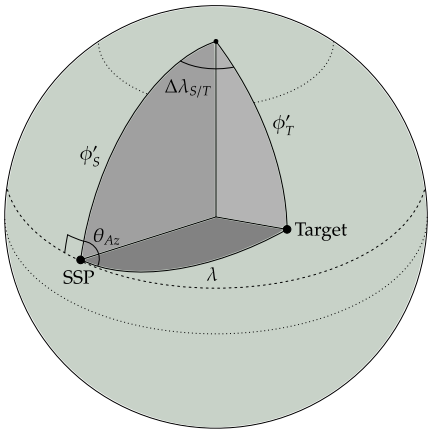

Figure 4.14: Satellite to Target Earth Geometry

Once it is determined that the target is indeed in range of the satellite, a desired vector from the satellite towards the target must be calculated to determine the error quaternion which allows the controller to point the satellite towards the target. The ECEF target vector, $\mathbf{r}_T^{ECEF}$, can be calculated with eq. (4.1), where $R_\oplus$ is instead replaced with R_{site} in eq. (4.2) as determined from the Earth's geodetic coordinates.

The target vector is then transformed to ECI coordinates using eq. (4.6), where

$$\mathbf{r}_T^{ECI} = \mathbf{A}_{ECEF}^{ECI}\mathbf{r}_T^{ECEF}.$$

The vector pointing from the satellite to the target in ORC coordinates, $\mathbf{r}_{S/T}^{ORC}$, uses eq. (4.15) and the propagated satellite vector, $\mathbf{r}_{sat}^{ECI}$, with

$$\mathbf{r}_{S/T}^{ORC} = \mathbf{A}_{ECI}^{ORC}\left(\mathbf{r}_{T}^{ECI} - \mathbf{r}_{sat}^{ECI}\right). \tag{4.84}$$

If it is assumed that an imaging payload will point along the satellite z body axis, then the commanded unit vector to be fed to the quaternion feedback controller can be calculated with [66]

$$\hat{\mathbf{r}}_c = \frac{\hat{\mathbf{z}}_{SBC} \times \hat{\mathbf{r}}_{S/T}^{ORC}}{|\hat{\mathbf{z}}_{SBC} \times \hat{\mathbf{r}}_{S/T}^{ORC}|}, \tag{4.85}$$

where $\hat{\mathbf{z}}_{SBC}$ and $\hat{\mathbf{r}}_{S/T}^{ORC}$ are the normalised SBC imager and ORC satellite to target vectors respectively. The commanded quaternion is finally determined by [66]

$$\mathbf{q}_c = \begin{bmatrix} \hat{\mathbf{r}}_c \sin\frac{\Phi}{2} \\ \cos\frac{\Phi}{2} \end{bmatrix}, \tag{4.86}$$

where angle Φ can be determined from the vector dot product in eq. (4.55). Finally, the commanded angular ORC referenced body rates during tracking can be calculated with [66]

$$\boldsymbol{\omega}_c^{ORC} = \hat{\mathbf{r}}_c \times \dot{\hat{\mathbf{r}}}_c, \tag{4.87}$$

where the time derivative of $\hat{\mathbf{r}}_c$ ($\dot{\hat{\mathbf{r}}}_c$) can be approximated as [66]

$$(\dot{\hat{\mathbf{r}}}_c)_n \approx \frac{1}{T_{ws}}\big((\hat{\mathbf{r}}_c)_n - (\hat{\mathbf{r}}_c)_{n-1}\big), \tag{4.88}$$

where T_{ws} is the sample period of the CWs, allowing for the the angular rate error to ultimately be calculated as

$$\boldsymbol{\omega}_{err} = \boldsymbol{\omega}_{SBC}^{ORC} - \boldsymbol{\omega}_c^{ORC}. \tag{4.89}$$

4.5 Summary

Satellite orbital dynamics and control theory are discussed and expanded on in this chapter. The concepts and tools elaborated on in the chapter are used throughout the remainder of this thesis to assist with understanding the laws which govern the simulation environment and satellite dynamics. The final two topics discussed in this chapter will additionally aid in understanding the control and error dynamics of a satellite performing tracking manoeuvres. Before the accuracy and stability of such manoeuvres can be expanded on, it is necessary to define a simulation environment describing both the satellite external space environment and the various limiting factors which affect its IPA and attitude stability.

Chapter 5

CubeSat Simulation Environment

5.1 Overview

A realistic simulation environment is required in order to investigate the expected IPA of a satellite in LEO, equipped with a CubeADCS. To test the various simulation environment models, this chapter assumes a basic set of physical and orbital parameters for a CubeSat in LEO, where the CubeSat is defined to be:

- 3U in size,
- to have mass moments of inertia elements, $[I_{xx}\ I_{yy}\ I_{zz}] = [0.0361\ 0.0365\ 0.0075]\ \mathrm{kg\,m^2}$,
- to have body mounted solar panels,
- to be at an orbit altitude of $\pm\ 500\,\mathrm{km}$,
- to be in an SSO with a sun angle of approximately 30°,
- to have its SBC axes aligned with the ORC axes in its nominal orientation,
- is 3-axis stable whilst constantly pointing nadir, and
- to have it's -Y panel facing towards the Sun at all times (not sun tracking).

First, the external space environmental models are discussed, after which, the resultant external disturbance torques affecting the CubeSat's dynamics are modelled. Finally, the satellite dynamics and kinematics with no control are modelled.

5.2 Low Earth Orbit Space Environment

This section describes the external space environment that a satellite in a LEO would experience. This includes the modelling of its orbit trajectory around the Earth, the relative position of the Sun, and the surrounding external geomagnetic field.

5.2.1 Orbit Propagation with SGP4

Several SPMs exist which aim to predict and propagate a satellite's position and velocity in its orbit. The first SPM was developed in 1966 by Hilton and Kuhlman, and is known as the SGP model [67]. The SGP model was intended to be used for low orbiting satellites with orbit period of less than 225 min [67].

The second model, SGP4, made several improvements to the SGP model was initially developed by Cranford and Lane in 1969 and 1970, where an improved version was published in a US Air Force document known as "Space Track Report No. 2" [68]. In 1980, Hoots and Roerich published the orbit propagation documentation and algorithms written in FORTRAN IV computer code in "Space Track Report No. 3" (STR#3), which was the first report to be released to the public [67]. TLE sets are generated by NORAD using the SGP4 model, where the orbital periodic variations are removed, and the mean values are published [67]. Hoots and Roerich subsequently stress the importance of using the same

model to reconstruct the periodic variations that were previously removed [67].

In 2006, Vallado et. al. released a revised version of STR#3, accompanied by computer code written in the C++ programming language. The revision aimed to mitigate various rare cases of inaccuracies in the model whist remaining compatible with the NORAD generated TLE sets. The simulated model used in this thesis is based on the revised SGP4 model and is implemented in C code to be run as an S-Function in MATLAB®'s Simulink® software. The CubeADCS additionally relies on an SGP4 propagator and so it is fitting that the same model is used. The original and revised models additionally make use of the World Geodetic System 72 (WGS72) constant terms, which is considered throughout the investigations that follow.

The simulated SGP4 model takes in a unique TLE data set assigned to a particular CubeSat, as well as the elapsed time (Δt) since the initial TLE generation unix time (t_0) in seconds. The model subsequently propagates the satellite in its orbit, outputting the satellite's instantaneous RAAN, inclination, orbit radius from nadir (R_{sat}), the satellite position ($\mathbf{r}_{sat}^{ECI}$) and velocity ($\mathbf{v}_{sat}^{ECI}$) vectors in ECI coordinates, the mean (M) and true anomalies (ν) and, the orbit angular rate ($\omega_o(t)$). With $\mathbf{r}_{sat}^{ECI}$ known, the elapsed and current time, Δt and t respectively, is used to calculate the satellite geocentric and geodetic latitudes and longitude from eqs. (4.8) to (4.13) together with the iterative algorithm in alg. 4.1. Additionally, the satellite velocity and position vectors are used to generate the transformation matrix in eq. (4.14) to transform vectors to and from the ORC frame.

A TLE set was obtained to suit the physical specifications stipulated in sec. 5.1 where the RAAN was adjusted to suit the sun angle criteria. The TLE can be found in appendix A where the date of TLE generation by NORAD is set to be around the Northern Hemisphere Spring solstice in 2019 (20 March 2019), when the ECI x-axis is pointing directly towards the Sun which additionally lies on the equatorial plane. The set of TLE parameters is used throughout the remainder of this chapter to model the remaining simulation environmental properties.

The TLE was used to propagate the CubeSat using the simulated SGP4 model over one orbit period. The results of the simulated model can be seen in figs. 5.1 to 5.3 which plots the satellite position vector, velocity vector, and orbit angular rate respectively. Fig. 5.3 shows a nearly constant angular rate, which indicates a near circular orbit.

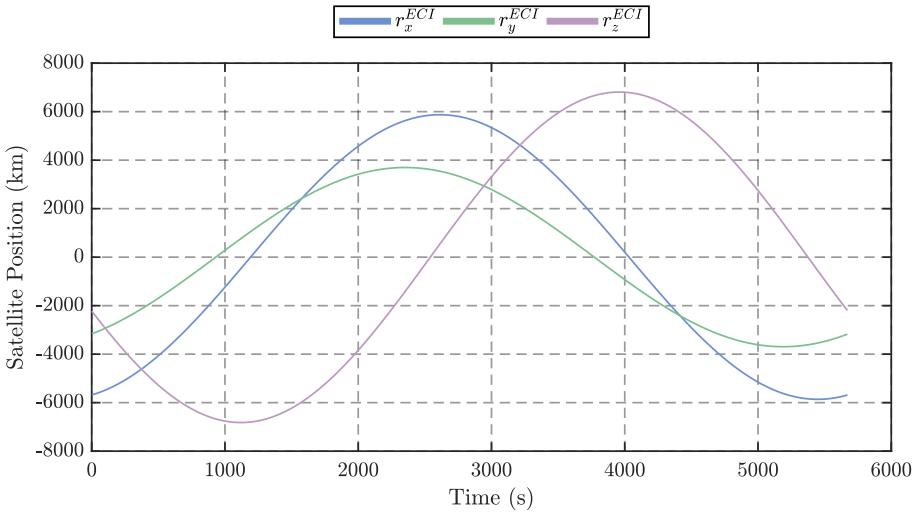

Figure 5.1: Simulated CubeSat Position Vector in ECI Coordinates

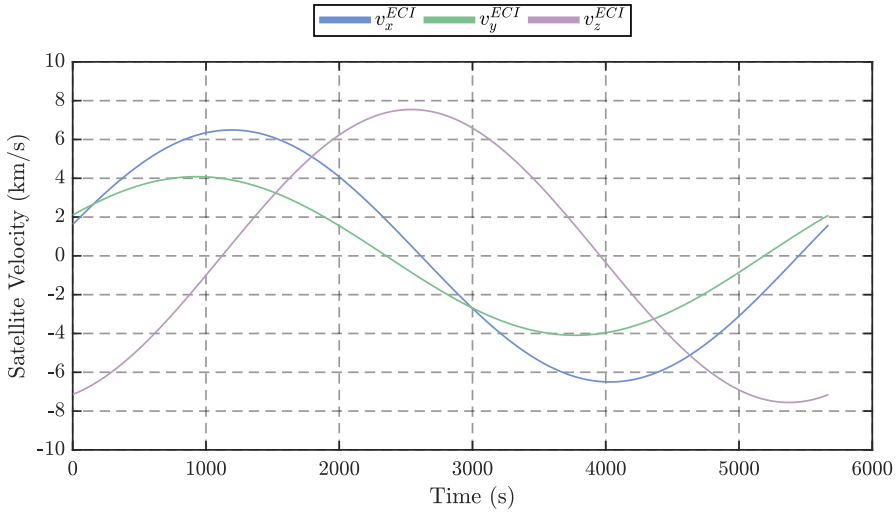

Figure 5.2: Simulated CubeSat Velocity Vector in ECI Coordinates

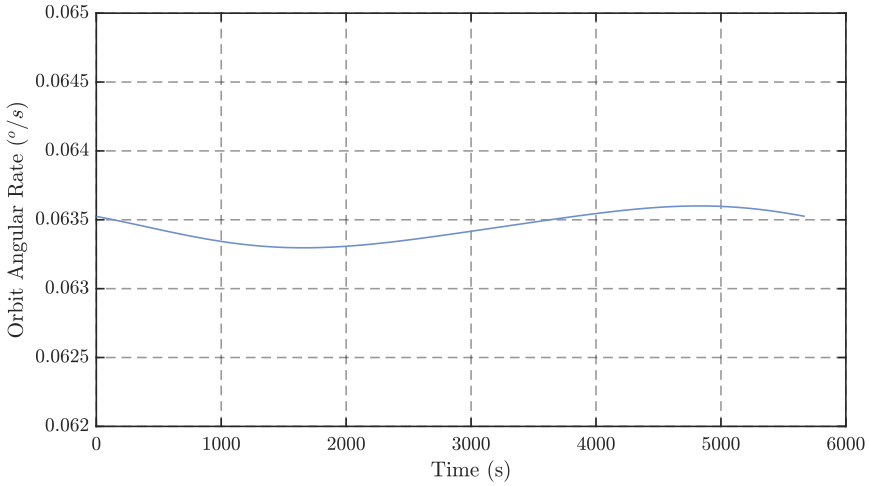

Figure 5.3: Simulated CubeSat Orbit Angular Rate

5.2.1.1 SGP4 Accuracy

Several CubeSat ADCS's, including the CubeADCS, rely on SGP4 models to propagate their orbits and to determine its positional knowledge in space. Whilst the model is a good approximation of a satellite's orbit trajectory, environmental disturbances such as aerodynamic drag, can cause the SGP4 model to become significantly inaccurate over several days. This error, or SGP4 drift, is more significant at lower orbit altitudes where the Earth's atmosphere is denser.

A simulation was conducted to measure the typical SGP4 drift for three similarly orientated, 3U CubeSats with similar masses, in three different orbits. To measure the drift, a dataset of 21 TLE's for each satellite spaced approximately one day apart, was first obtained over the same time period (1 January 2019 to 21 January 2019). Next, each satellite was initialised to a reference centre TLE and propagated approximately 10 days ahead and 10 days behind the starting ephemeris at time intervals matching the dates in each CubeSat's TLE dataset. The error was finally obtained, by initialising the SGP4 model at each TLE in the dataset per CubeSat, and calculating the RMS error between the initialised position vectors and the previously calculated propagated position vectors.

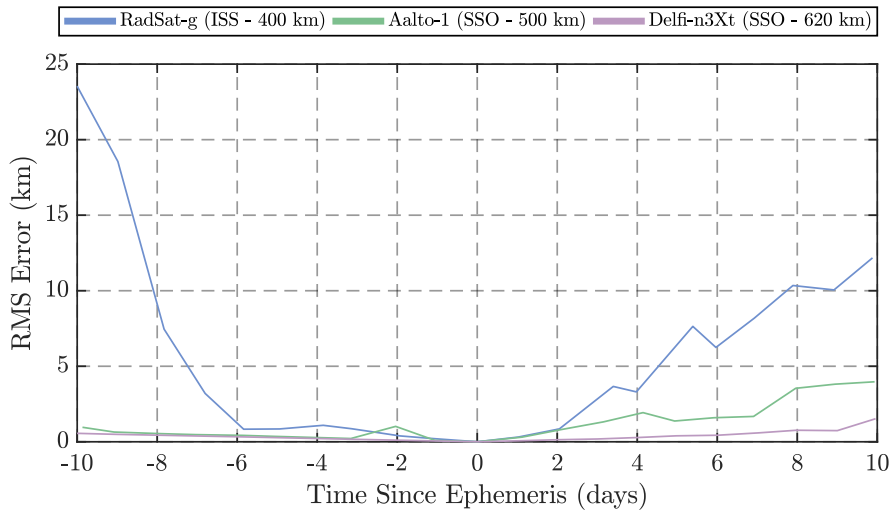

Figure 5.4: SGP4 Drift of 3U CubeSats

Fig. 5.4 shows the SGP4 drift results of the three 3U CubeSats. The CubeSats chosen were RadSat-g, Aaalto-1 and Delfi-n3Xt, which were in a 400 km ISS orbit, a 500 km SSO, and a 620 km SSO respectively. The results show a large SGP4 drift for CubeSats in a low orbit such as for RadSat-g. Over a period of 10 days, the positional knowledge error could translate to a IPA error greater than 3° at such a low altitude – which would be unacceptable for satellites with high IPA requirements. The drift is less significant for Aalto-1 and Delfi-n3Xt which are both in higher orbits, but it can be seen that in just a few more days, that the error would eventually also become unacceptable. Additionally, the investigation shown in fig. 5.4 makes the assumption that the centre reference TLE produces accurate positional knowledge, where Rossouw shows in his research in 2015 that the RMS error can already be as much at 1 km when the NORAD TLE positional data is compared to GPS positional data [69].

To mitigate the drift error, CubeSat mission designers send TLE updates to the respective satellites which reinitialise the on-board SGP4 orbit propagators. These updates need to be sent to CubeSats regularly for satellites at lower orbit altitudes – such as RadSat-g. For CubeSats in slightly higher LEOs (such as for the simulated satellite used throughout this chapter), the update frequency does not need to be that high, unless the mission requires a good IPA. For the purposes of this investigation, it is assumed that the TLE's of the various simulated CubeSat's are updated at regular intervals, in order to reflect the accuracy of the CubeADCS independent of positional knowledge errors.

5.2.1.2 SGP4 Corrections with the Integration of a GPS

As an alternative to regularly updating a CubeSat's SGP4 propagator with a new TLE set, CubeSats can be fitted with a GPS which allow its system to obtain accurate positional knowledge in near real-time. This unfortunately comes with the drawback of a high power consumption which is typically not suitable for CubeSat power budgets. Rossouw proposes two solutions to this problem which aims to conserve power by only activating the on-board GPS at less than a 15% duty cycle [69].

The first solution involves the use of an adaptive SGP4 (aSGP4) analytical method. The method is simply a slight adaptation of the industry proven SGP4 propagator which uses GPS measurements to adjust the orbital parameters in the TLE, and was found to produce a simulated RMS and maximum 3D positional knowledge error of 200 m and 1 km respectively – operating at a duty cycle of 12.5% [70]. The numerical integration method incorporates an EKF with a Runge-Kutta integrator to estimate the satellite's position and velocity. The latter method produced significantly lower RMS and maximum positional knowledge errors of 60 m and 300 m respectively – operating at a duty cycle of 10.7% [70].

Although the numerical integration method produced better results than the aSGP4 method, Rossouw points out the substantial flight heritage of the SGP4 propagator versus the use of an entirely new system

[70]. The use of a simple adaptation of the TLEs presents a lower risk. Additionally, the aSGP4 method can propagate to any time in one step, where the EKF method needs to propagate in a stepwise fashion to a point 30 s in the future [70]. Although the CubeADCS does not come standard with a GPS, nor does CubeSpace manufacture one – an interface does exist on the CubeControl PCB which allows for the integration of a GPS.

5.2.2 Sun Position Model

The Sun's positional model is important to define for several reasons in this simulation. The first of which, is that it provides both the CSS and the FSS with positional knowledge of where a satellite is with respect to the Sun, and to assist the EKF attitude estimation algorithms implemented by the CubeADCS. Part of the relative positional knowledge will also indicate when the Sun enters the CubeStar's FOV, effecting its performance.

The Sun also influences the solar panel magnetic disturbance torques acting on the satellite body and so it is important to model the intensity of the solar flux, as well as when the resultant torques are being applied (i.e. when the satellite is in the sunlit portion of its orbit). Solar radiation pressure contributes to external disturbance torques acting on satellite's in space, however, this force is negligible for CubeSats, especially in comparison to the resultant magnetic torques generated. As such solar radiation pressure disturbance torques are ignored in sec. 5.3.

The following method and equations for determining the vector from the centre of the Earth to the centre of the Sun (Sun vector) in the ECI frame, $\mathbf{r}_{\odot}$, is acquired from Meeus [71]. The author states that the method yields a Sun positional knowledge accuracy of within 0.01°; which is sufficient for this project, especially since the expected accuracy of a sensor such as the CubeSense FSS is within 0.2°.

First, the number of Julian centuries from the J2000 epoch to the current epoch (ephemeris), T_{UT1}, is calculated using eq. (4.10). The geometric mean ecliptic longitude (with reference to the mean equinox), $\lambda_{M_{\odot}}$, of the sun is then calculated with

$$\lambda_{M_{\odot}} = 280.466\,45^{\circ} \; + \; 36\,000.769\,83 T_{UT1} \; + \; 0.000\,303\,2 T_{UT1}^2. \tag{5.1}$$

Next, the mean anomaly, $M_{\odot}$, for the Sun is calculated as

$$\begin{aligned} M_{\odot} = {} & 357.529\,10^{\circ} \; + \; 35\,999.050\,30 T_{UT1} \; - \; 0.000\,155\,9 T_{UT1}^2 \\ & - 0.000\,000\,48 T_{UT1}^3, \end{aligned} \tag{5.2}$$

which allows the Sun's equation of the centre, $C_{\odot}$, to be calculated as

$$\begin{aligned} C_{\odot} = {} & \left(1.914\,600^{\circ} \; - \; 0.004\,817 T_{UT1} \; - \; 0.000\,014 T_{UT1}^2\right) \sin M_{\odot} \\ & + \; (0.019\,993^{\circ} \; - \; 0.000\,101 T_{UT1}) \sin 2M_{\odot} \\ & + \; 0.000\,290 \sin 3M_{\odot}. \end{aligned} \tag{5.3}$$

Following this, the eccentricity of the Earth's orbit around the sun, $e_{\oplus_{\odot}}$, is calculated with

$$e_{\oplus_{\odot}} = 0.016\,708\,617 \; - \; 0.000\,042\,037 T_{UT1} \; + \; 0.000\,000\,123\,6 T_{UT1}^2. \tag{5.4}$$

The Sun's true geometric ecliptic longitude, $\lambda_{T_{\odot}}$, is defined as

$$\lambda_{T_{\odot}} = \lambda_{M_{\odot}} + C_{\odot}, \tag{5.5}$$

and its true anomaly, $\nu_{\odot}$, is defined as

$$\nu_{\odot} = M_{\odot} + C_{\odot}. \tag{5.6}$$

The final apparent ecliptic longitude, $\lambda_{A_\odot}$, of the sun (as referenced from the true equinox) is calculated as

$$\lambda_{A_\odot} = \lambda_{T_\odot} \; - \; 0.005\,69^\circ \; - \; 0.004\,78 \sin \Omega, \tag{5.7}$$

where

$$\Omega = 125.04^\circ \; - \; 1934.136 T_{UT1}. \tag{5.8}$$

Next in the process of calculating the sun vector, the radius, $R_{\odot(AU)}$ (measured in AU), is the radius from the centre of the Earth to the sun and is calculated with

$$R_{\odot(AU)} = \frac{1.000\,001\,018\left(1 - e_{\oplus_\odot}^2\right)}{1 + e_{\oplus_\odot} \cos \nu_\odot}. \tag{5.9}$$

The radius, $R_{\odot(AU)}$, is then converted to kilometres with

$$R_\odot = 1.495\,978\,70 \times 10^8 \cdot R_{\odot(AU)}, \tag{5.10}$$

and the obliquity of the Sun's ecliptic to the equatorial plane is calculated as:

$$\begin{aligned} \epsilon_\odot = {} & 23.439\,291\,11^\circ \; - \; 0.013\,004\,167 T_{UT1} \\ & - 1.638\,89 \times 10^{-7} T_{UT1}^2 \; + \; 5.036\,11 \times 10^{-7} T_{UT1}^3 \\ & + 0.002\,56 \cos \Omega. \end{aligned} \tag{5.11}$$

Finally, the sun vector in the ECI frame, $\mathbf{r}_\odot$, is calculated with:

$$\mathbf{r}_\odot = \begin{bmatrix} r_{\odot x} \\ r_{\odot y} \\ r_{\odot z} \end{bmatrix} = \begin{bmatrix} R_\odot \cos \lambda_{A_\odot} \\ R_\odot \sin \lambda_{A_\odot} \cos \epsilon_\odot \\ R_\odot \sin \lambda_{A_\odot} \sin \epsilon_\odot \end{bmatrix} \tag{5.12}$$

Fig. 5.5 illustrates the relationship between the satellite's Sun vector, $\mathbf{S}_{ECI}$, and the Earth's Sun vector, $\mathbf{r}_\odot$, in the ECI frame where

$$\mathbf{S}_{ECI} = \mathbf{r}_\odot - \mathbf{r}_{sat}. \tag{5.13}$$

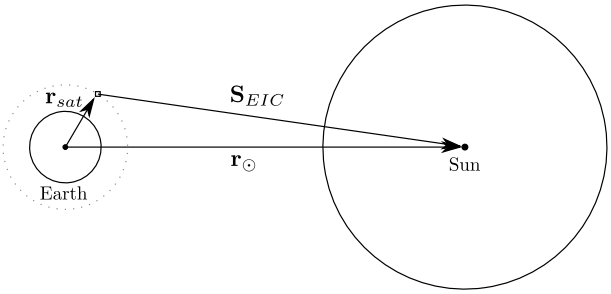

Figure 5.5: Sun Vector in ECI

Once the satellite's Sun vector is calculated in the ECI frame, the vector is normalised and transformed to the ORC frame using eq. (4.15), and then to the SBC frame with the calculated satellite DCM.

The Sun angle to the satellites orbit-plane, β_{sat}, is calculated with

$$\beta_{sat} = \arcsin\left[\cos \delta_\odot \sin i_{sat} \sin\left(\Omega_{sat} - \alpha_\odot\right) + \sin \delta_\odot \cos i_{sat}\right], \tag{5.14}$$

where $\alpha_\odot$ is the right-ascension of the sun and is calculated as

$$\alpha_\odot = \operatorname{atan2}\left(\cos \epsilon_\odot \sin \lambda_{A_\odot}, \cos \lambda_{A_\odot}\right), \tag{5.15}$$

and $\delta_\odot$ is the declination of the Sun can be calculated with

$$\delta_\odot = \sin \epsilon_\odot \sin \lambda_{A_\odot}. \tag{5.16}$$

5.2.2.1 Determining Eclipse

In order to determine when the satellite is in eclipse, the Earth angle, $\eta_{\oplus\odot}$, between the Sun's point (SP) on Earth and the SSP is first calculated by using the spherical geometry cosine law illustrated in fig. 5.6, where

$$\begin{aligned}\eta_{\oplus\odot} &= \arccos\big[\cos(90° - \phi_{sat})\cos(90° - \phi_\odot) \\ &\quad + \sin(90° - \phi_{sat})\sin(90° - \phi_\odot)\cos\Delta\lambda_{\oplus\odot}\big] \\ &= \arccos\big[\sin\phi_{sat}\sin\phi_\odot + \cos\phi_{sat}\cos\phi_\odot\cos\Delta\lambda_{\oplus\odot}\big].\end{aligned} \tag{5.17}$$

The angles ϕ_{sat} and $\phi_\odot$ in eq. (5.17) are the satellite and Sun's geocentric latitudes respectively, where $\Delta\lambda_{\oplus\odot} = \lambda_{sat} - \lambda_\odot$ is the difference between the satellite's longitude, λ_{sat}, and the Sun's longitude, $\lambda_\odot$.

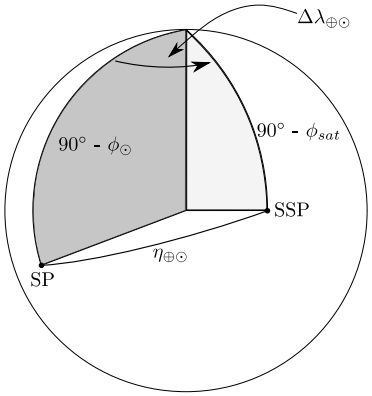

Figure 5.6: Satellite-Sun Earth Angle

Fig. 5.7 shows how to determine if the satellite is in eclipse or not. The angle at which the Sun's rays strike the Earth is approximated to 90° do to the immense distance that the Sun is away from the Earth. With this in mind, the satellite is defined to be in eclipse if $|\eta_{\oplus\odot}| > 90° + \arccos\left(\frac{R_\oplus}{R_{sat}}\right)$.

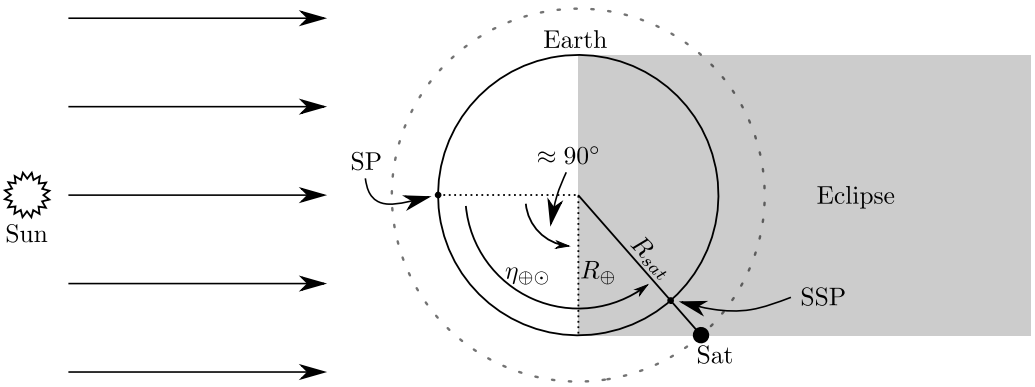

Figure 5.7: Satellite Eclipse

Fig. 5.8 shows the Sun vector model as measured in the ORC frame of five orbit periods which includes the applied eclipse periods. The y vector component remains constant throughout the orbits which is expected for an SSO, where the arcsine of the component corresponds nicely to the desired sun angle of 30°. The eclipse period is additionally short and is expected to remain roughly the same throughout an

entire Earth year as is additionally typical of an SSO. The simulated model Sun vector in the SBC frame is always calculated with the eclipse applied to it.

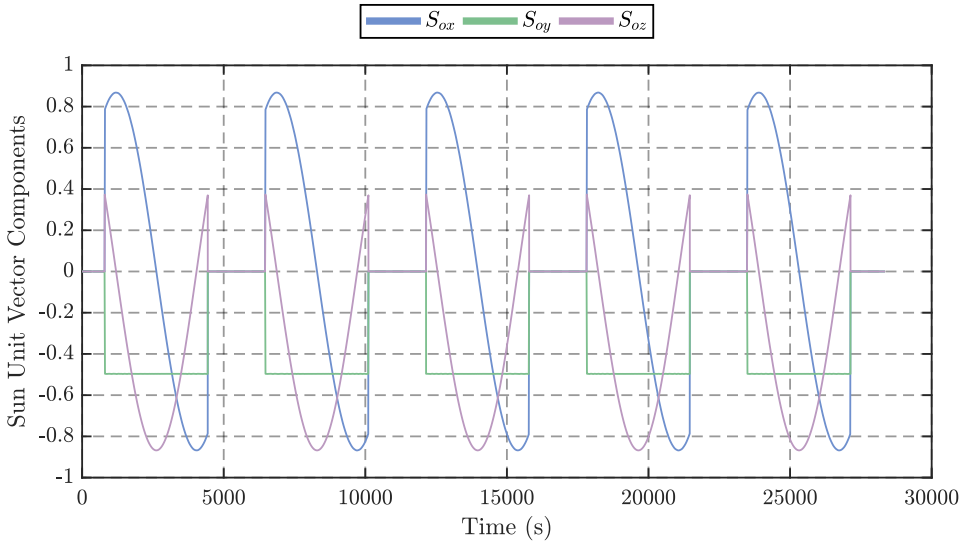

Figure 5.8: Simulated Sun Model Unit Vector Components in the ORC Frame

5.2.3 The Geomagnetic Field Model

The final model discussed is the geomagnetic field model. The Earth's magnetic field is important to model as it has a significant impact on satellite's in orbit – especially those in LEO. Satellites' residual and induced solar panel magnetic dipoles interact with the Earth's magnetic field and influence its dynamics in the form of disturbance torques. A satellite can also take advantage of the magnetic field by taking measuremnts of the surrounding magnetic field vector to provide a coarse estimate of its orientation in space and, to subsequently control its orientation by periodically activating its on-board magnetorquers.

A satellite's attitude, through geomagnetic field observations, is determined by comparing magnetometer measurements to a geomagnetic field model. Earth's magnetic field is often thought of as a simple "bar magnet" or dipole model for ease of visualisation. However, this is not a true representation of the geomagnetic field, where a more accurate and sophisticated model is required for ADCS operations. The dominant model adopted by scientists and engineers alike is the International Geomagnetic Reference Field (IGRF) model, which is maintained and released by the International Association of Geomagnetism and Aeronomy (IAGA).

The IAGA releases a new IGRF model approximately every five years, as the Earth's magnetic field varies slowly over time. The model provides a "snapshot" of numerical Gaussian coefficients since the year 1900 up until the year of release in five-year intervals. Each release additionally includes a secular variation predictive average coefficient [72] which allows the user to predict the expected behaviour of the geomagnetic field over the next corresponding five-year period predating the next updated release.

The Earth's magnetic field strength in ECI coordinates, $\mathbf{B}_{ECI}(r, \phi'_{gc}, \lambda, t)$, is described by

$$\mathbf{B}_{ECI} = \mathbf{A}^{ECI}_{ECEF} \nabla V, \tag{5.18}$$

where $V(r, \phi'_{gc}, \lambda, t)$ is the scalar potential function which is expressed as a finite series containing the aforementioned Gaussian coefficients [72] such that [72]

$$V(r, \phi'_{gc}, \lambda, t) = a \sum_{n=1}^{N} \sum_{m=0}^{n} \left(\frac{a}{r}\right)^{n+1} [g_n^m(t) \cos m\lambda + h_n^m(t) \sin m\lambda] \cdot P_n^m(\cos \phi'_{gc}). \tag{5.19}$$

Variables r, ϕ'_{gc}, λ, t and $a = 6371.2\,\text{km}$ in eq. (5.19) represent the radial distance of a satellite observing the geomagnetic field from Earth's centre, the satellites's geocentric co-latitude (90° - ϕ_{gc}), the satellite's longitude, the year to which the IGRF coefficients are propagated to and, the magnetic spherical radius respectively. The Gaussian coefficients are shown by $g_n^m(t)$ and $h_n^m(t)$ respectively, where P_n^m describes the Legendre functions of degree n and order m [72].

In order to propagate the IGRF Gaussian coefficients to the predicted coefficients for a particular year in the interval between the release year and the valid five-year period after that, simple linear extrapolation is used, such that [72]

$$g_n^m(t) = g_n^m(T_0) + \dot{g}_n^m(T_0)(t - T_0), \tag{5.20}$$

where T_0 is the IGRF model release year and $\dot{g}_n^m(T_0)$ is the aforementioned secular variation predictive average coefficient. The extrapolation is described in exactly the same way when calculating $h_n^m(t)$. The model used to simulate the magnetic field in this thesis is the 12^{th} generation IGRF model which was released in December 2014 and is valid between 2015-2020, where only the 10^{th} order coefficients are used. Fig. 5.9 shows the geomagnetic field strength for the simulated CubeSat in its SSO as experienced in the ORC frame, where the field components are obtained from ECI coordinates using the $\mathbf{A}_{ECI}^{O}$ transformation matrix in eq. (4.14). The results of the geomagnetic field model correspond nicely to the expected outcomes as the CubeSat is in a near polar orbit and thus has a small y component throughout its orbit.

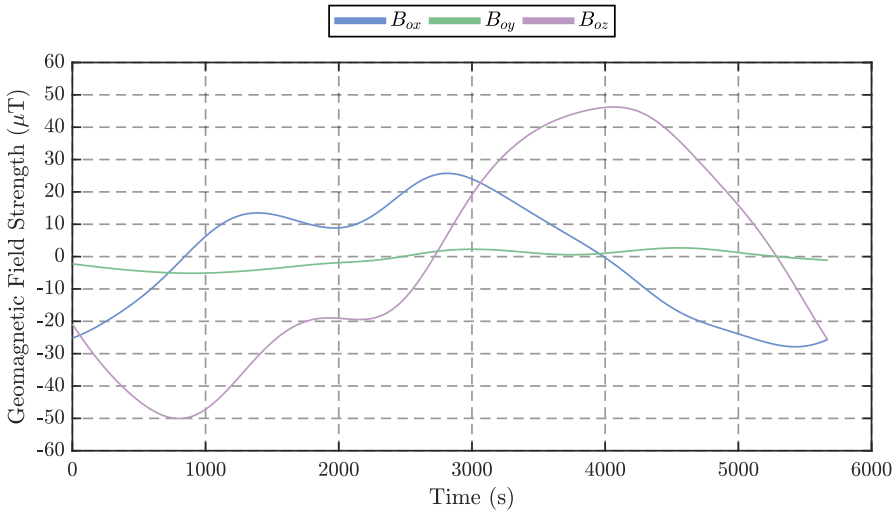

Figure 5.9: Geomagnetic Field Components in ORC Frame

5.3 Environmental Disturbance Torques

Satellite environmental disturbance torques are caused by external forces acting on the CubeSat which subsequently influence its attitude. Three external forces which have the greatest impact on a CubeSat's attitude in LEO are considered in this thesis.

Three main environmental disturbance torques are described by $\mathbf{N}_{\text{D}}$ (shown in eq. (5.21)), and can be expanded as

$$\mathbf{N}_D = \mathbf{N}_{gg} + \mathbf{N}_{ad} + \mathbf{N}_{msp}, \tag{5.21}$$

with $\mathbf{N}_{\text{gg}}$ being the gravity gradient torque acting on a CubeSat, $\mathbf{N}_{ad}$ being the aerodynamic torque acting on a CubeSat - which is substantial for CubeSats in LEO, and the final term, $\mathbf{N}_{msp}$ is the magnetic disturbance torques induced by a CubeSat's solar panels when it is in the sunlit part of its orbit.

5.3.1 Gravity Gradient Torque

Gravity gradient torque can be best visualised with a dumb-bell analogy as shown in fig. 5.10, where the balance between the centrifugal force towards zenith, and the gravitational force towards nadir acts to passively stabilise the satellite along its long body axis. In other words, the auxiliary mass of the satellite that is further away from Earth will feel the greatest centrifugal force, and likewise, the auxiliary mass that is closest to the Earth will feel the greatest gravitational force [59].

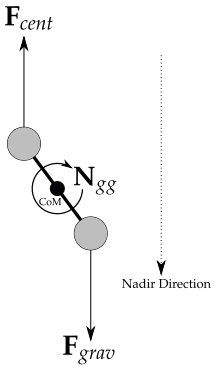

Figure 5.10: Gravity Gradient Torque

As a result, a torque is induced about the satellite's centre of mass (CoM), which is described by [66]

$$\mathbf{N}_{gg} = 3\omega_0^2 \left(\mathbf{z}_O^B \times \mathbf{J}\mathbf{z}_O^B\right), \tag{5.22}$$

where $\mathbf{z}_O^B$ is the ORC referenced vector pointing along towards the ORC z-axis transformed to the SBC frame as [66]

$$\mathbf{z}_O^B = \mathbf{A}_B^O \begin{bmatrix} 0 \\ 0 \\ 1 \end{bmatrix}. \tag{5.23}$$

Eqs. (5.22) and (5.23) can be combined to solve for the vector components of $\mathbf{N}_{gg}$ as [66]

$$\mathbf{N}_{gg} = 3\omega_0^2 \cdot \begin{bmatrix} (J_{zz} - J_{yy})\, A_{23} A_{33} \\ (J_{xx} - J_{zz})\, A_{13} A_{33} \\ (J_{yy} - J_{xx})\, A_{13} A_{23} \end{bmatrix}. \tag{5.24}$$

ADCS estimators take advantage of the gravity gradient disturbance torque as it can be modelled accurately, which separates this kind of external disturbance from others which are somewhat less predictable and thus more challenging to precisely model.

5.3.2 Aerodynamic Torque

The atmospheric density surrounding satellites in LEO, is substantial enough to induce atmospheric drag, and subsequently – atmospheric disturbance torques [60]. Such disturbance torques, occur when a satellite's centre of pressure (CoP) is misaligned with its centre of mass (CoM) [60]. Variations in atmospheric velocities cause deviations in pressures acting on the numerous surfaces of a satellite. The CoP is determined as the average location of these pressure deviations [73].

The atmospheric drag is determined by the satellite's orbit velocity and the angular rotation of the Earth, as the outer atmosphere rotates with it [74]. The resultant relative atmospheric velocity vector, $\mathbf{v}_a^{ECI}$, in ECI coordinates is calculated as

$$\mathbf{v}_a^{ECI} = \begin{bmatrix} 0 \\ 0 \\ \omega_\oplus \end{bmatrix} \times \mathbf{r}_{sat}^{ECI} - \mathbf{v}_{sat}^{ECI}, \tag{5.25}$$

where the velocity vector, $\mathbf{v}_a^O$, in the ORC frame is also obtained using the $\mathbf{A}_{ECI}^O$ transformation matrix in eq. (4.14). In order to determine the relative atmospheric velocity vector inducing drag on the surfaces of the satellite, the DCM is applied to $\mathbf{v}_a^O$ to produce the vector in the SBC frame, $\mathbf{v}_a^B$.

The aerodynamic disturbance model, is adapted from Steyn and Lappas [74] where the external disturbance torques acting on each facet of the satellite body are summed. The total aerodynamic disturbance torque vector is thus calculated as [66]

$$\mathbf{N}_{ad} = \sum_{i=1}^{n} \rho ||\mathbf{v}_a^B||^2 A_i H(\cos\alpha_i) \cos\alpha_i \Big\{ \sigma_t \left(\mathbf{r}_{pi} \times \hat{\mathbf{v}}_a^B\right) + \left[\sigma_n S + (2 - \sigma_n - \sigma_t)\cos\alpha_i\right] \left(\mathbf{r}_{pi} \times \hat{\mathbf{n}}_i\right) \Big\}, \quad (5.26)$$

where ρ is the atmospheric density at a particular altitude in LEO, $\hat{\mathbf{v}}_a^B$ is the unit relative velocity vector in SBC, α_i is the incidence angle of the relative velocity vector on facet i, A_i is the projected surface area of facet i, $\mathbf{r}_{pi}$ is facet i's CoM to CoP vector, and $\hat{\mathbf{n}}_i$ is the normal unit vector of facet i – where $\cos\alpha_i$ is the dot product between $\hat{\mathbf{v}}_a^B$ and $\hat{\mathbf{n}}_i$. $H(...)$ represents the Heaviside function where

$$\begin{aligned} H(x) &= 0 \quad \text{if } x < 0 \text{ and} \\ H(x) &= 1 \quad \text{if } x \geq 0. \end{aligned} \quad (5.27)$$

Variables S, σ_n and σ_t represent the ratio of molecular exit velocity, v_b, to atmospheric velocity, the normal accommodation coefficient, and the tangential accommodation coefficient respectively. For this study it is assumed that $\sigma_n \cong \sigma_t \cong 0.998$ and that $S \cong 0$, which reduces eq. (5.26) to

$$\mathbf{N}_{ad} \cong \sum_{i=1}^{n} \rho ||\mathbf{v}_a^B||^2 A_i H(\cos\alpha_i) \cos\alpha_i \cdot 0.998 \cdot \left(\mathbf{r}_{pi} \times \hat{\mathbf{v}}_a^B\right). \quad (5.28)$$

The atmospheric density, ρ, is dependent on a satellite's altitude and approximately decreases exponentially [60]. To calculate the atmospheric density of a satellite at a particular altitude, the formula [60]

$$\rho \approx \rho_0 e^{\frac{-\Delta h}{h_0}} \quad (5.29)$$

is used, where ρ_0 is the known atmospheric density at a particular altitude relating to the atmospheric scale height, h_0 at that same altitude, and Δh is the difference in altitude of the satellite and the altitude producing ρ_0. Known atmospheric densities and scale heights at altitudes between 400 km and 700 km are used in this simulated model and are adapted from [60], where the solar maximum values are used to create a "worst-case" scenario.

5.3.3 Solar Panel Induced Magnetic Torques

CubeSat's in orbit utilise solar panels as their primary source of energy to power their subsystem components (including the ADCS). In addition to supplying the subsystem components with energy during the sunlit portion of the orbit, the solar array is responsible for recharging the on-board battery system which powers the subcomponents during orbital eclipse periods.

When a solar panel is active, it produces internal current loops which subsequently induce magnetic moments, which interact with the Earth's magnetic field to create unwanted magnetic torque disturbances. These current loops, worsened by current carrying harnesses within the spacecraft, have been found to be the dominant source of undesirable disturbance torques experienced by CubeSats in LEO [75], which make it challenging for on-board ADCSs to control such small moments of inertia.

The source of these disturbances can be minimised if solar panel design engineers pursue good design practices which aim to mitigate these current loops [75], however, several surveys suggest that the majority of CubeSat COTS solar panels are not in fact designed with this in mind [9], [76]. As a result, CubeSat

design engineers are prompted to follow their own magnetic cleanliness programmes to lower the resultant residual magnetic disturbances to an acceptable level [75].

As described by eq. (3.3) and illustrated in fig. 3.6b, a magnetic torque is induced as a result of the interaction between the Earth's magnetic field, $\mathbf{B}_{\oplus}$, and the generated magnetic moment. The disturbance torque generated as a result of the current loops in a solar array, functions in exactly the same way as a magnetorquer rod, except in that the torque is an uncontrolled and undesirable one. The model for the solar panel induced magnetic disturbance torque, $\mathbf{N}_{msp}$, is described in this study by

$$\mathbf{N}_{msp} = \mathbf{M}_{sp} \times \mathbf{B}_{\oplus}, \tag{5.30}$$

where $\mathbf{M}_{sp}$ is the magnetic moment vector generated by the external solar panels on the various facets of the CubeSat body, which is calculated as

$$\mathbf{M}_{sp} = M_{sp_{3U}} \cdot \begin{bmatrix} n_{\mathrm{X}\pm} \cdot S_{bx} \\ n_{\mathrm{Y}\pm} \cdot S_{by} \\ n_{\mathrm{Z}\pm} \cdot S_{bz} \end{bmatrix}, \tag{5.31}$$

where $M_{sp_{3U}}$ is the maximum magnetic dipole moment generated by a 3U solar panel array and, S_{bx}, S_{by}, and S_{bz} are the unit Sun vector components in SBC. Variables $n_{\mathrm{X}\pm}$, $n_{\mathrm{Y}\pm}$, $n_{\mathrm{Z}\pm}$ is the number of 3U solar panel arrays on the satellite body x, y and z-axes respectively, which differs depending on whether the solar panel is on the negative or positive side of the respective SBC axes. The maximum solar panel dipole moment is assumed to be time-invariant, as highly accurate dynamic dipole modelling is out of the scope this study. The goal is to merely introduce the magnetic torque as a disturbance to a simulated CubeSat, and to observe the CubeADCS's ability to reject it. $M_{sp_{3U}}$ is assumed to be at a worst case of $1\,\mathrm{mA\,m^2}$ for the simulations conducted in chapter 7.

5.4 Satellite Kinematics and Dynamics

The final simulation model implemented is concerned with the CubeSat dynamics and kinematics, as it orbits within the space environment. The model implements the Euler dynamic equation of motion described by eq. (4.65) in sec. 4.4.6. The equation of motion is incorporated into a Simulink® block which starts with an assumed initial satellite inertial angular rate vector, $\boldsymbol{\omega}^I_{B_0}$, to solve for the inertial angular acceleration vector, $\dot{\boldsymbol{\omega}}^I_B$.

Each update to the simulated CubeSat's dynamics is performed at a simulated frequency of 10 Hz where the previous time-step output result of $\dot{\boldsymbol{\omega}}^I_B$ is integrated with a continuous-time 4^{th} order Runga-Kutta solver Simulink® block, to obtain the new value of $\boldsymbol{\omega}^I_B$ which is once again fed into the dynamic satellite model.

The model takes in five additional inputs which include: the external disturbance torque vector $\mathbf{N}_D$ (modelled in sec. 5.2) the inertia matrix, $\mathbf{J}$, of the CubeSat, as well as the CubeTorquer controlled magnetic torque outputs, and the resultant CubeWheel torque and angular momentum vectors generated, $\mathbf{N}_m$ and $\mathbf{h}_{wheel}$ respectively – both of which are discussed in chapter 7.

Finally, the satellite kinematic model uses eqs. (4.60) and (4.62) to calculate the CubeSat's quaternion rate vector, $\dot{\mathbf{q}}$, starting at an initial assumed attitude state quaternion vector, $\mathbf{q}_0$. The updated quaternion vector $\mathbf{q}$ is then also propagated with a continuous-time 4^{th} order Runga-Kutta solver Simulink® block. Fig. 5.11 shows the dynamic and kinematic response of the simulated satellite described in the beginning of this chapter from this model. The attitude is represented in terms of its respective Euler angles, which are obtained from quaternion calculated DCM matrix in eq. (4.47) and from eqs. (4.42) to (4.44). The initial conditions of the CubeSat are set to be $\mathbf{q}_0 = [0\ 0\ 0\ 1]^T$ and $\boldsymbol{\omega}^I_{B_0} = [0.5\ 0.5\ 0.5]^T\ ^\circ\,\mathrm{s}^{-1}$, with no attitude control implemented whatsoever.

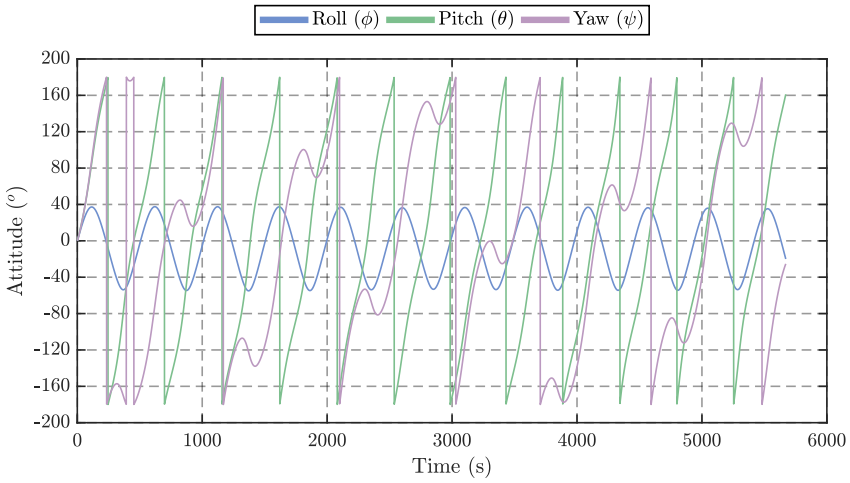

(a) Euler Angles

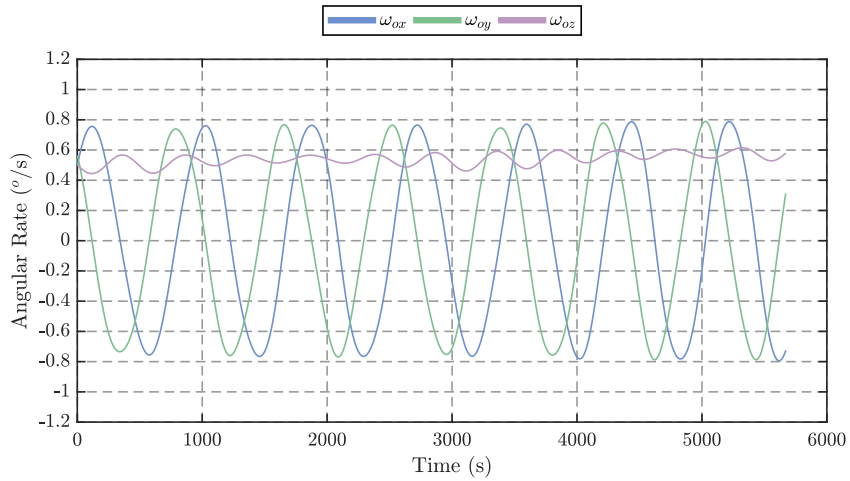

(b) ORC Referenced Body Rates

Figure 5.11: Simulated CubeSat Dynamic and Kinematic Models

5.5 Summary

This chapter has established the CubeSat Simulation Environment which will be used to determine the IPA and stability of the CubeADCS aboard a CubeSat in a LEO.

First, the space environment was discussed which introduced three of the most important models responsible for replicating the LEO. The SGP4 model was the selected orbit propagator, based on its use by CubeSpace and its heritage in industry. The accuracy of the propagator was briefly investigated, where an augmented SGP4 propagator using intermittent GPS measurements was investigated in its ability to provide an ADCS with more accurate positional knowledge estimates. The Sun model was next discussed, which enables relative positional CubeSat-to-Sun vectors to be calculated. The final space environment model implemented was the 10^{th} order IGRF model which produces an accurate simulated geomagnetic environment and subsequent magnetic field vectors.

The resultant disturbance torques, dependent on the space environment were next discussed. Three primary sources of external disturbance torques were identified to have the largest impact on a CubeSat in LEO, namely: the gravity gradient, aerodynamic, and solar panel induced magnetic moment torques. The latter was determined to have the largest potential impact on a CubeSat with low mass moments of inertia – the effect of which is analysed in chapter 7.

Finally, the satellite dynamic and kinematic model was implemented, which simulates the laws of physics governing a satellite in orbit and its natural responses to external and internal disturbance torques. All models have been implemented through both S-Function and other Simulink® blocks which all utilise the 4^{th} order Runga-Kutta solver.

The well-defined CubeSat simulation environment is used in chapters 6 and 7 to test and model the various CubeADCS sensors and actuators, and to finally investigate the performance of its IPA and stability.

Chapter 6

CubeADCS Hardware Investigation and Modelling

6.1 Overview

In order to obtain simulation results which realistically reflect the CubeADCS' performance, an analysis is done which assesses the performances of each sensor and actuator on the integrated CubeADCS. This chapter focuses on the real noise and error characteristics of each sensor and actuator, which forms a basis to create accurate simulation models shown in each subsequent section. The satellite used to build and test these models has the same parameters as defined in chapter 4.

During the model investigation, the simulated CubeSat was set to complete two orbits, where only one particular sensor or actuator was investigated at a time. All other components were set to an ideal model in order to isolate the sensor or actuator under investigation. There were also no disturbance torques acting on the satellite during the investigation and a gyro EKF was used to estimate the satellite's attitude to create a very stable CubeSat body.

Most sensor models in the simulation were set up to take the standard deviation of a sensor's error (σ_e) as a parameter input into a Gaussian random number generator. The noise is then typically passed through a digital low pass filter with the discrete transfer function:

$$H(z) = \frac{(1-\alpha)z}{z-\alpha}, \tag{6.1}$$

where the correlation coefficient, α, is adjusted accordingly to change the level of correlation in the noise and thus allow through less, or more, high frequency errors. The σ_e parameters were chosen accordingly to suit the typical errors for each particular component in the CubeADCS.

6.2 Magnetometer

This section first discusses an analysis of the magnetometer sensors implemented on the CubeADCS, and from this, the model is described with similar error characteristics. All magnetometer parameters used for the calculations in this section, are referenced from sec. 3.4.2.

6.2.1 Magnetometer Analysis

The 3-axis magnetometer produces a voltage output for each axis which is proportional to the magnetic field it is measuring, allowing a magnetic field vector to be calculated. The HMC105X range of sensors have a high bandwidth (BW) >5 MHz, however, the respective voltage outputs for each axis are passed to a differential low-pass op-amp filter (with a gain $G = 235$) which lowers the bandwidth to approximately 132 Hz. The low bandwidth considerably reduces the amount of $\frac{1}{f}$ (flicker noise) and broadband noise in the magnetometer measurements. A theoretical calculation for the expected RMS broadband noise can be calculated using:

$$\begin{aligned} E_{n_{BB}} &= e_n \cdot \sqrt{\text{BW} \cdot K_n} \\ &= 5 \times 10^{-9} \cdot \sqrt{132 \cdot 1.57} \\ &= 72.15\,\text{nV}, \end{aligned} \tag{6.2}$$

where K_n represents the brick wall correction factor which includes the "skirt" of the low pass filter. The expected RMS flicker noise on the other hand is calculated from the $\frac{1}{f}$ lower and upper cut-off frequencies and can be calculated as:

$$\begin{aligned} E_{n_{flicker}} &= e_{n_{1Hz}} \cdot \sqrt{\ln\left(\frac{f_H}{f_L}\right)} \\ &= 50 \times 10^{-9} \cdot \sqrt{\ln\left(\frac{10}{0.1}\right)} \\ &= 107.3\,\text{nV}. \end{aligned} \tag{6.3}$$

The combination of the RMS flicker and broadband noise is calculated as:

$$\begin{aligned} E_{n_{total}} &= \sqrt{{E_{n_{BB}}}^2 + {E_{n_{flicker}}}^2} \\ &= 129.3\,\text{nV}. \end{aligned} \tag{6.4}$$

The magnetometer supply voltage is 3.3 V, which places its worst-case measurement sensitivity at $33\,\mu\text{V}\,\mu\text{T}^{-1}$. The subsequent theoretical sensor 1σ B-field noise, B_n is thus calculated to be 3.91 nT if one does not take the op-amps noise contributions into consideration.

6.2.1.1 In-Orbit Magnetometer Data

Calibrated, in-orbit B-field measurement errors relative to the modelled IGRF magnetic field, from the nSight-1 satellite (developed and operated by SCS Space), provided by CubeSpace [52] is shown in fig. 6.1. The satellite is equipped with a CubeADCS to handle its attitude requirements, where it uses its 3-axis magnetometer output as a reference for the EKF.

The results indicate that the measured in-orbit SBC B-field has a 1σ magnitude error of 482.9 nT and a peak-to-peak magnitude error of 2.85 µT. The higher frequency periodic variations in the figure are due to the fact that the satellite was in a Y-Thompson spin of around $-3\,^\circ\,\text{s}^{-1}$ during the time of measurement. It is therefore likely, that the measured B-field error is largely attributed to internal satellite current loops (magnetic moments) varying with the spin angle, from the observed results. However, the total error is a combination of the errors caused by the aforementioned varying magnetic moments, errors in the IGRF magnetic field model, stochastic magnetometer errors, and imperfect orthogonality calibration in the sensitivity matrix.

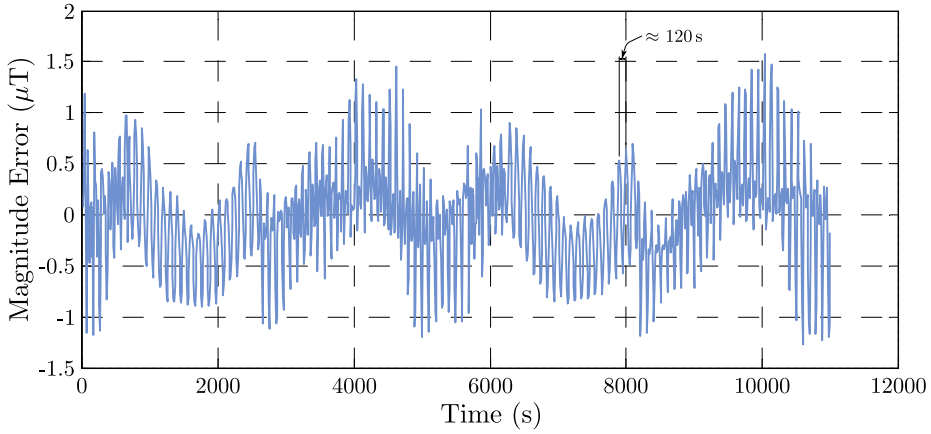

Figure 6.1: B-field Magnitude Error After Calibration [77]

Fig. 6.1 provides a good indication of what to expect with regard to the B-field magnitude error. However,

in order to get the difference between the measured and modelled unit vectors, as used by the EKF, one must use the magnetic unit vector angular error as seen in fig. 6.2, where the 1σ unit vector angular error is 0.9084°.

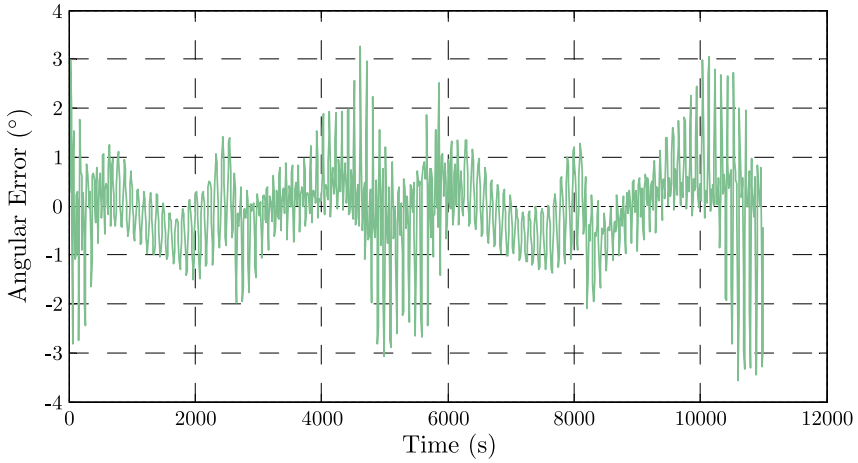

Figure 6.2: B-field Angular Vector Error After Calibration [77]

The results from the in-orbit data suggest that the measured SBC magnetic field errors can be largely attributed to the external magnetic moment disturbances, where the stochastic sensor measurement noise does not contribute to any significant errors in comparison.

6.2.2 Magnetometer Model

The model for the magnetometer measurements for the simulated CubeADCS utilises the true simulated IGRF geomagnetic field model to obtain the magnetic field vector in SBC (as described in sec. 5.2.3), where the on-board B-field vector measurements can be seen in fig. 6.3 with a superimposed noise.

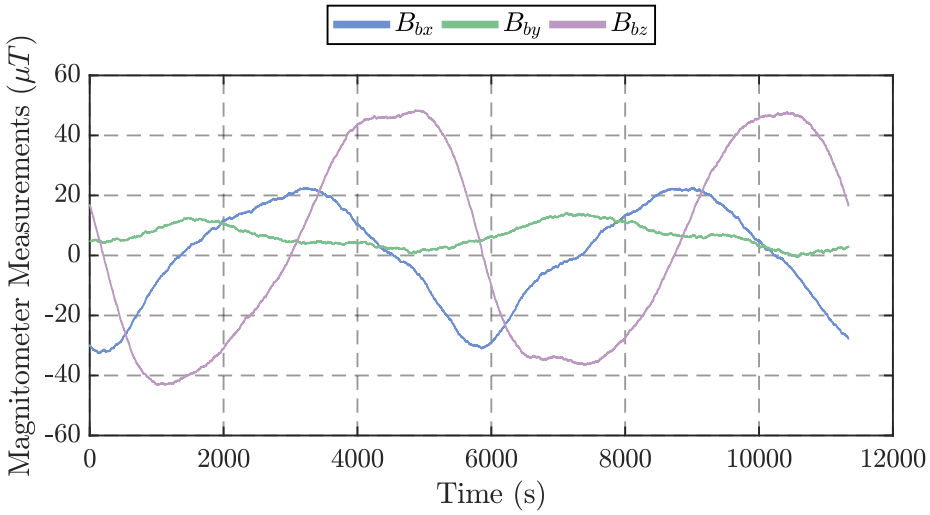

Figure 6.3: Modelled Magnetometer Measurements

Gaussian noise is passed through the low pass filter in eq. (6.1), which is then added to the magnetic field vector components as measured sensor outputs in the SBC frame and fed back to the simulation for the EKF to use. A correlation coefficient, $\alpha = 0.01$, was selected to obtain the slow, highly correlated error seen in fig. 6.4. A $\sigma_e = 9.5\,\mu\text{T}$ was then selected to obtain a similar 1σ error in the angular vector error seen in fig. 6.5. A test was conducted over ten orbits, where the resultant 1σ magnitude error was calculated to be 366.5 nT.

The angular error in the magnetometer unit vector measurement, as used by the EKF, was calculated

with eq. (4.55). Although, the magnitude of an angular error between two vectors is always positive, fig. 6.5 shows negative angles when the magnitude error is negative – in the same fashion as fig. 6.2. The results from the same test show that the modelled magnetometer measurements have a 1σ angular error of 0.9269° on average – closely matching the measured calibrated magnetometer angular error.

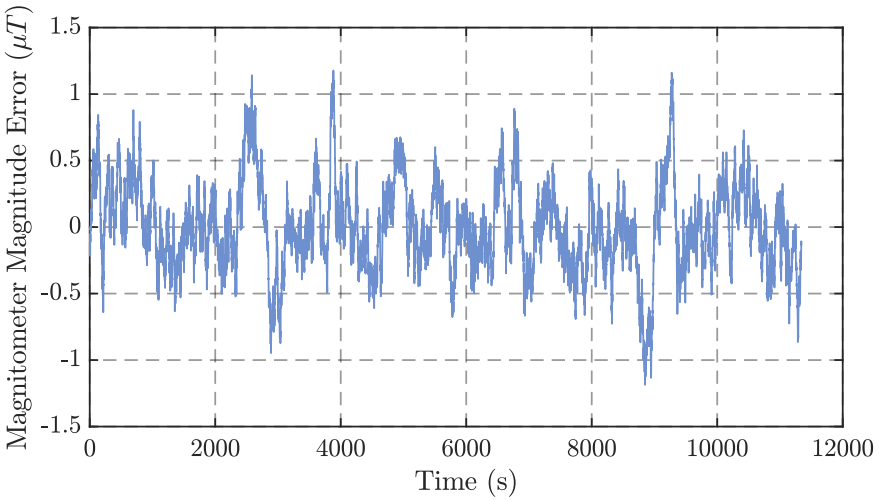

Figure 6.4: Modelled Magnetometer B-Field Magnitude Error

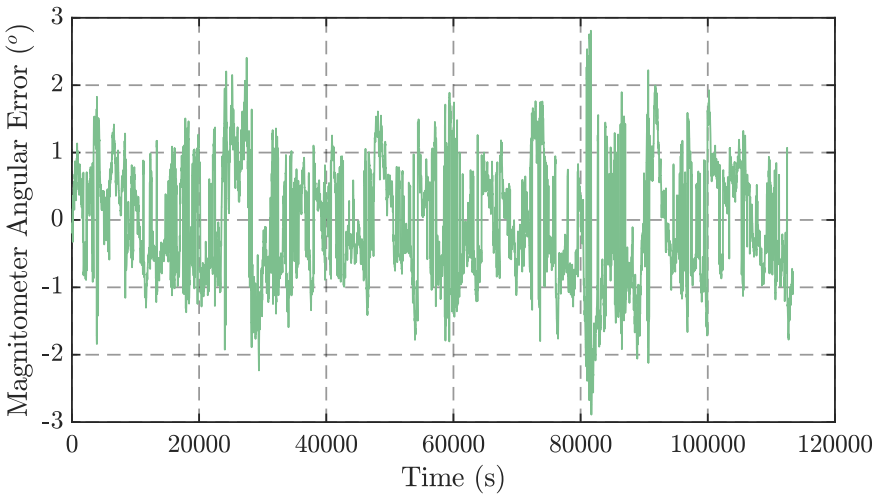

Figure 6.5: Modelled B-field Vector Angular Error

6.3 The CSS

An analysis of the CSS is discussed in this section, in order to determine its error characteristics. Following this, the model is described to accurately follow the CSS inaccuracies.

6.3.1 CSS Analysis

By measuring the amount of short circuit current passing through a photodiode, one can measure the intensity of the light deflected. The amount of short circuit current passing through a photodiode is ideally proportional to the light incidence angle, θ_i by the cosine rule, where

$$I(\theta_i) = I_{sc}\cos(\theta_i), \tag{6.5}$$

where I_{sc} is the maximum short circuit current which can pass through the diode at $\theta_i = 0°$ and where θ_i is typically measured from the surface normal. The specifications indicated in sec. 3.4.3, show that at an average solar irradiance of 136 mW cm^{-2}, the expected maximum short circuit current is 926 µA. In reality, the output short circuit current does not follow an ideal cosine curve due to reflection errors off

of the cell or from added light intensities from Earth albedo. However, for the intended application of the CSS, a cosine approximation is sufficient for calculating the light incidence angle on a cell.

A previous study was done [78] to investigate the resultant CSS Sun vector angular error to a light source at different azimuth and elevation angles (θ_{az} and θ_{el} respectively) relative to a satellite. The setup (illustrated in fig. 6.6) shows a cube (CubeSat model) fitted with three cells on each axis of rotation and positioned on a two-stage rotation platform in a dark room,with a light source activated directly in front of it.

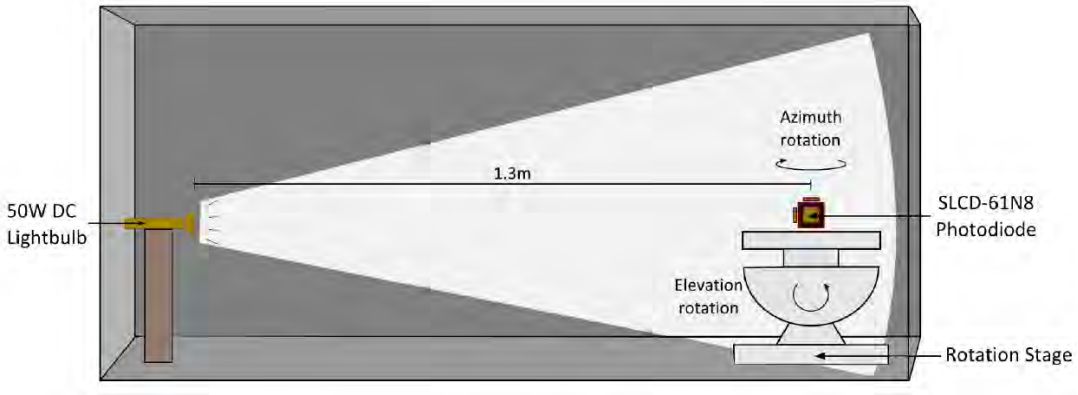

Figure 6.6: CSS Experimental Setup [78]

Three separate tests on each cube axis (face) were conducted which kept one axis fixed, whilst rotating the cube about the remaining two axes. The voltage of each cell's short circuit current sense resistor was sampled by an MCUs ADC, to measure the corresponding light intensities.

As opposed to eq. (6.5), the researcher defined the incidence angle to be measured from the tangential line to the surface where a fitted sinus wave is used in eq. (6.6) [78] to determine the incidence angle on each cube axis from an ADC voltage measurement ($f_{AD}(\theta_i)$).

$$\theta_i = \frac{\arcsin\left(\frac{f_{AD}(\theta_i)-K_4}{K_1}\right) - K_3}{K_4} \tag{6.6}$$

The error between the fitted sinus wave and the actual ADC output is shown in figs. 6.7a and 6.7b. Eq. (3.2) was then used calculate the error in the Sun vector angle.

The results indicate, that the CSS is not especially accurate in determining the Sun vector, particularly at extreme light incidence angles relative to the cube's normal axes. Errors in the test are likely due to reflection errors, the use of a light source with a wider beam than that of the Sun as well as mounting and calibration inaccuracies. With the proper placement of the sensors, the azimuth and elevation error magnitudes should be identical, which will result in Sun vector angular errors of less than 5°.

6.3.2 CSS Model

The coarse Sun sensor is modelled by using the calculated Sun position vector in the SBC frame (described in sec. 5.2.2). In the model, θ_{az} and θ_{el} are calculated from the true Sun vector $\hat{\mathbf{S}}_b$ (illustrated in fig. 3.5) where

$$\theta_{az} = \text{atan2}\left(S_{by}, S_{bx}\right) \tag{6.7}$$

$$\text{and } \theta_{el} = \text{atan2}\left(S_{bz}, \sqrt{S_{bx}^2 + S_{by}^2}\right). \tag{6.8}$$

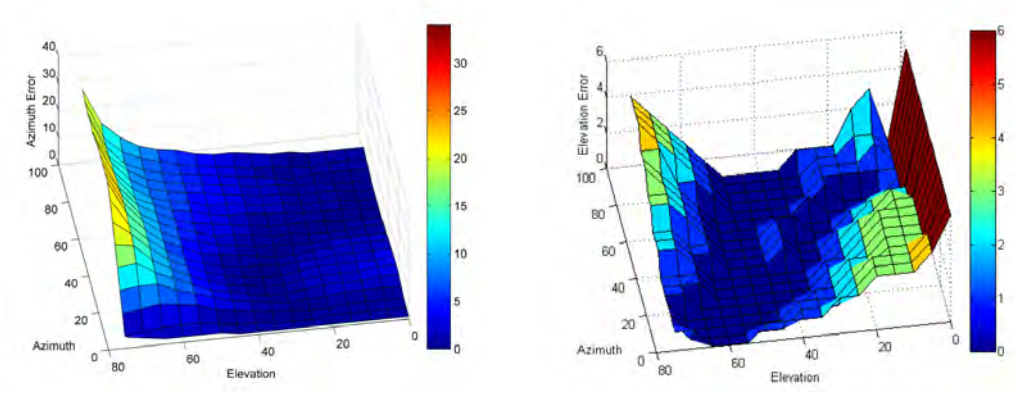

(a) Azimuth Error **(b)** Elevation Error

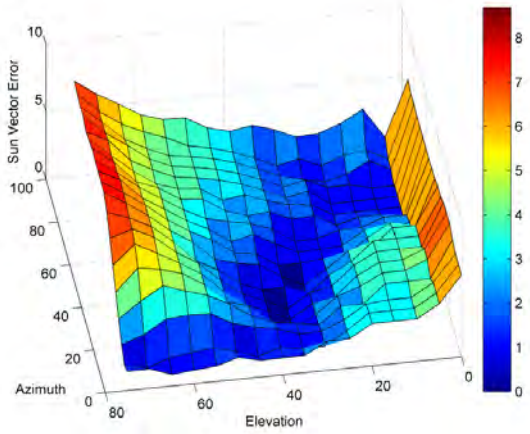

(c) Sun Vector Angular Error

Figure 6.7: CSS Errors [78]

The placement of the CSS sensors is assumed to be accurate, where errors in elevation are expected to be the same as that of the azimuth. Gaussian noise is similarly passed through low pass filter in eq. (6.1) with a correlation coefficient, $\alpha = 0.05$, and added to the true azimuth and elevation angles (the results of which can be seen in fig. 6.8) which are then fed back into the simulation to be used by the EKF.

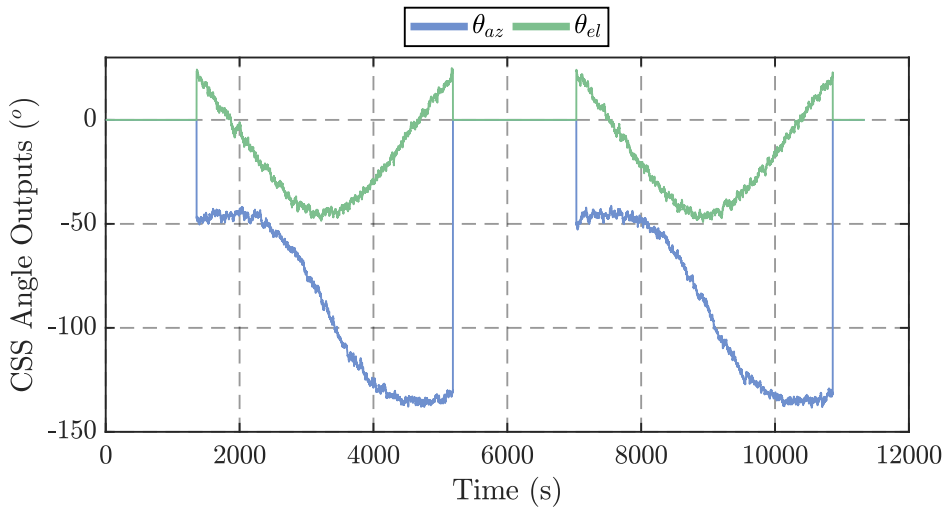

Figure 6.8: CSS Measured Azimuth and Elevation Model

Multiple tests were conducted to find a suitable value of σ_e for the noise to be passed through the low pass filter in eq. (6.1). Eq. (3.2) was used to calculate the measured Sun vector from the noisy CSS

azimuth and elevation output angles. It was then compared with the true Sun vector in the SBC frame to determine its angular Sun vector error with eq. (4.55). Five consecutive tests were run for different noise values where a value of $\sigma_e = 10°$ was chosen as it produced a 3σ angular Sun vector error of 4.628° on average.

The resultant error of the azimuth and elevation output angles is shown in fig. 6.9, where the results from the same five tests obtained an average azimuth and elevation 3σ error of 3.235° and 3.336° respectively.

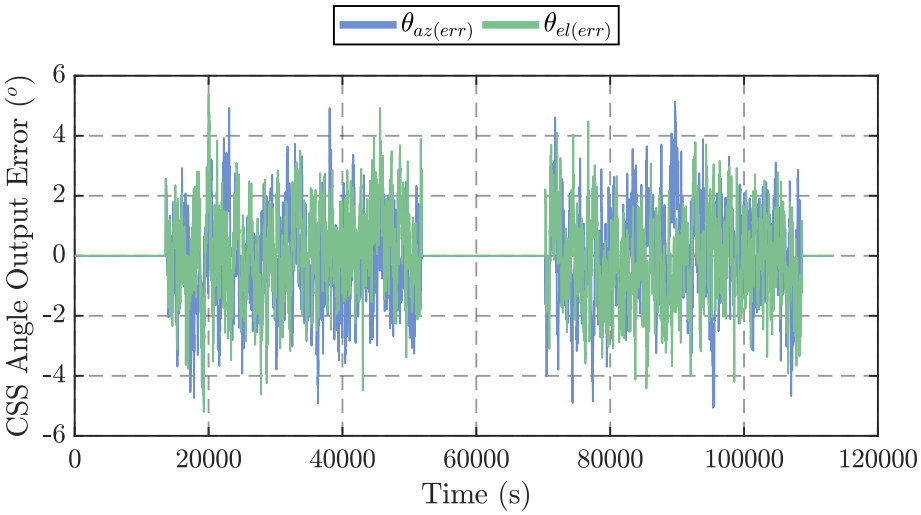

Figure 6.9: Modelled CSS Azimuth and Elevation Errors

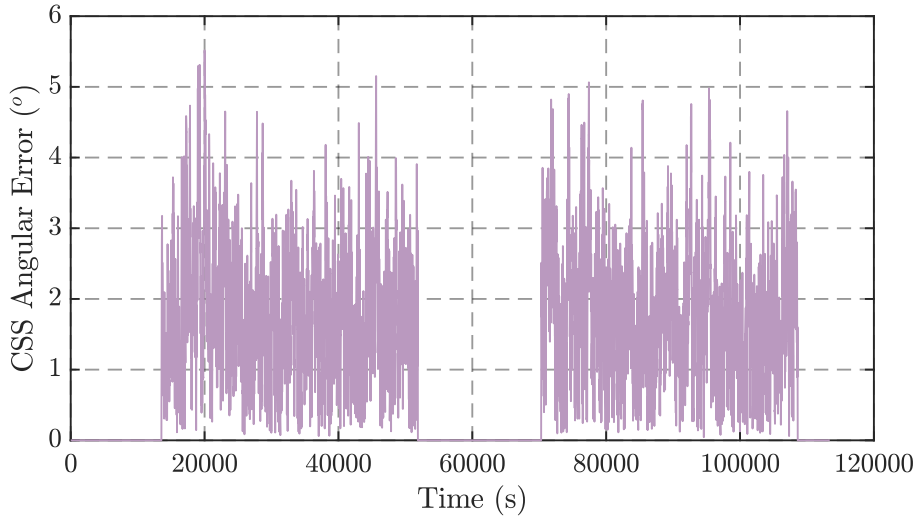

Figure 6.10: Modelled CSS Sun Vector Angular Error

Large errors in the CSS output are why it is typically used by the CubeADCS to make attitude estimates directly after launch, when the FSS is facing away from the Sun, or when the satellite's pointing requirements do not need to be precise.

6.4 MEMS Gyro

Three CRM100 gyros were experimented on in order to measure the variability between separate individual sensors of the same model which also represent well the three separate sensor axes. An analysis is completed on the sensors to determine their error characteristics, where the MEMS gyro model is then defined to closely mimic the true CubeADCS MEMS gyro characteristics.

6.4.1 MEMS Gyro Analysis

This section analyses the most significant error characteristics effecting the CRM100 MEMS gyros, where these errors are be broken up into stochastic and deterministic errors. The gyros have both an analogue and digital output mode which can be utilised (not at the same time). CubeSpace uses the digital SPI interface, which allows one to optimise the oversampling of the gyro's on-board ADC [37] and to also implement digital filtering with the CC.

To suit the same gyro interfacing method as CubeSpace and as suggested in the CRM100 datasheet [37], an identical PCB was designed (see appendix B) which mounted three separate CRM100 gyros with digital SPI output pins to interface with an MCU. The bandwidth capacitor was set to 560 pF to allow for the aforementioned ADC oversampling.

According to CubeSpace [52], the CC takes an average of 400 samples per axis in a window of 200 ms and then outputs the averaged inertially referenced satellite body rate vector components at a frequency of 1 Hz. Obtaining 400 samples per 200 ms is equivalent to sampling the gyros at a frequency where $f_s = 2\,\text{kHz}$, which is the frequency used to sample the gyros for the remainder of this analysis.

6.4.1.1 MEMS Stochastic Errors

The stochastic errors of a gyro are most accurately observed when they are held motionless and at a constant temperature in order to minimise thermal bias variations and obtain accurate results. With this in mind, the PCB mounting the gyros was kept stationary in a sealed container at a relatively constant ambient temperature of $\approx 26\,°\text{C}$, whilst measurements were taken from each gyro. Five separate 45 minute datasets were captured for each gyro in order to observe the variation between separate gyros, where fig. 6.11 shows the stationary output of a single such dataset for each gyro. These datasets were then used to perform a statistical analysis on the respective output rates.

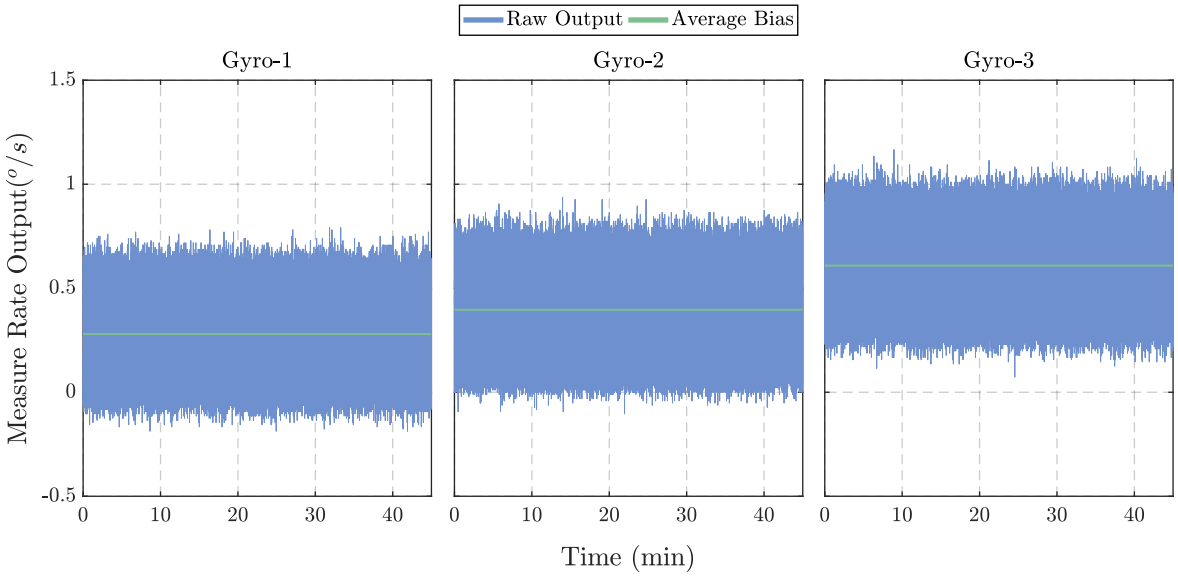

Figure 6.11: MEMS Gyro Stationary Output

6.4.1.1.1 Allan Variance Method

A gyro EKF uses the satellites angular body rates to propagate its attitude via numerical integration, which makes it important to analyse how a particular gyro's angular rate changes and, thus, how its resultant apparent orientation changes. The rate noise density of a gyro describes the expected noise of a gyro with respect to the sensor's bandwidth, however, it is often more intuitive to observe the statistical properties of a gyro's rate output with respect to time.

To accomplish this, the Allan variance (AVAR) of a gyro is determined which allows one to statistically

analyse the characteristics of underlying random processes producing noise in gyros, accelerometers and other oscillatory sensors [79]. The IEEE suggests estimating a gyro's AVAR by using the overlapping AVAR method [79]. This is estimated by first obtaining a set of N gyro angular rate outputs, $\omega(n)$. The AVAR of a gyro is then defined in terms of discrete output angles (corresponding to each rate sample) which are calculated by numerically integrating $\omega(n)$ with

$$\theta(k) = \sum_{n=1}^{k} \omega(n) \cdot \tau_0, \tag{6.9}$$

where $\theta(k)$ represents the discrete output angles and τ_0 represents the sample period of the gyro. Fig. 6.12 shows the result of such an integration over the first five minutes of the dataset for gyro-1 in fig. 6.11 (with the average bias over the whole 45 minutes removed). This shows how the stochastic processes are able to cause large errors in attitude determination, without any EKF bias estimation.

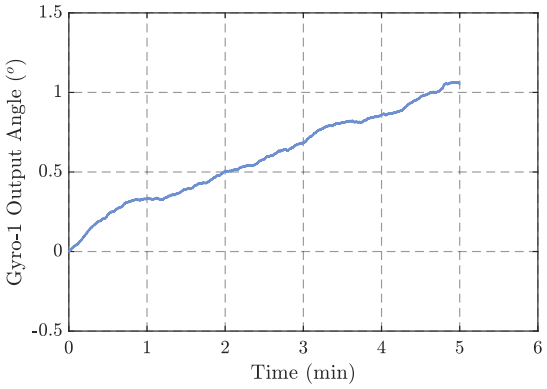

Figure 6.12: Output Gyro-1 Orientation Drift

Following the integration of each dataset, the output angles are divided into finite averaging time clusters of length $\tau = m\tau_0$, where $m < \frac{(N-1)}{2}$ and $m \in \mathbb{Z}$ chosen arbitrarily. This is illustrated in fig. 6.13 which gives an example for one of the possible averaging time clusters for $m = 2$ portraying the overlapping samples.

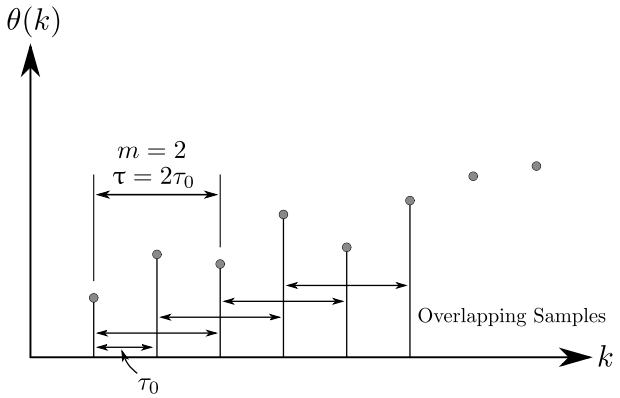

Figure 6.13: Overlapping Allan Variance Method

In order to make optimal use of each dataset, the values of m were chosen to be logarithmically spaced, where approximately 400 unique values were selected to obtain a satisfactory resolution. Next, the Allan variance, $\sigma^2(\tau)$, was calculated for each time cluster with [80]

$$\sigma^2(\tau) = \frac{1}{2\tau^2(N-2m)} \sum_{k=1}^{N-2m} \left[\theta(k+2m) - 2\theta(k+m) + \theta(k)\right]^2. \tag{6.10}$$

The final step is to characterise the noise of each gyroscope by calculating the Allan deviation (ADEV), $\sigma(\tau)$, for each time cluster with $\sigma(\tau) = \sqrt{\sigma^2(\tau)}$. The characterization was determined by plotting the

resultant ADEV's on a log-log scaled graph, where up to seven different noise terms can be extracted, namely: angle random walk (ARW), rate random walk (RRW), quantization noise (QN), rate ramp (RR), sinusoidal noise, correlated noise and the bias instability (BI).

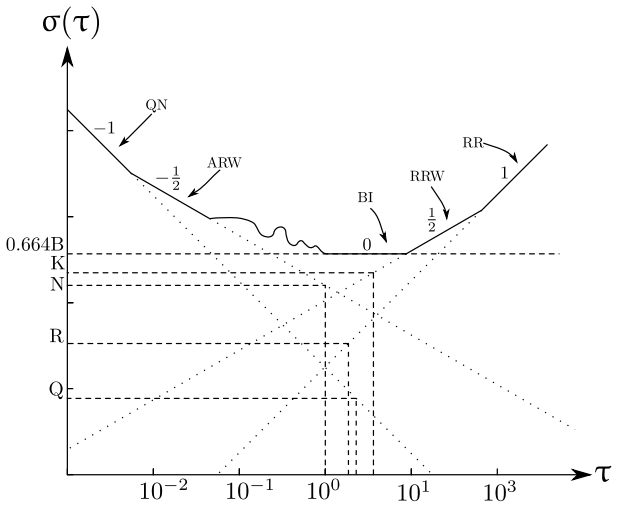

Figure 6.14: Allan Deviation Example Plot

These noise terms can all be identified in fig. 6.14, where five of the terms are determined from different regions of τ where the various random processes are associated with different ADEV slope gradients on the log-log plot. For modern MEMS sensors, only two of the random processes are considered as principle error terms [81], namely: the ARW and the BI.

The ARW is a high frequency noise term characterised by a white noise spectrum on the gyro [81], with smaller correlation times than the sample period. The gyro ARW is represented by the coefficient, N (with units $^\circ\,\mathrm{h}^{-0.5}$), and is associated with the gyro noise deviation by [82]

$$\sigma_N(\tau) = \frac{N}{\sqrt{\tau}}, \tag{6.11}$$

where N is extracted from the Allan deviation plot by fitting a tangent line of slope $-\frac{1}{2}$ in the log-log scale to the ADEV curve near the smaller time clusters and reading the value from this line at $\tau = 1\,\mathrm{s}$. Simply put, an ARW value of $0.2^\circ\,\mathrm{h}^{-0.5}$ means that the standard deviation of the orientation error after 1 h, is expected to be 0.2° [83].

The BI is a more correlated random process observed as a lower frequency deviation in a gyro's bias, caused by electronics susceptible to random flickering [82]. The BI is represented by the coefficient, B (with units $^\circ\,\mathrm{h}^{-1}$), associated with the gyro noise deviation by [82]

$$\sigma_B(\tau) = \sqrt{\frac{2\ln 2}{\pi}}B \cong 0.664B, \tag{6.12}$$

where B is extracted from the Allan deviation plot by fitting a tangent line of slope 0 in the log-log scale to the ADEV curve and reading the value of $\sigma(\tau)$ along this tangent line (at the lowest point on the ADEV curve) and dividing it by 0.664. Over time, the BI of a gyro creates a random walk in the gyro bias which is constrained within some range [83].

The ADEV plots for the three respective sensors over the five separate datasets can be seen in fig. 6.15, where the average ADEV plot for each sensor can be seen in fig. 6.16. The average ADEV plots for each sensor were calculated by taking the RMS the respective AVAR's.

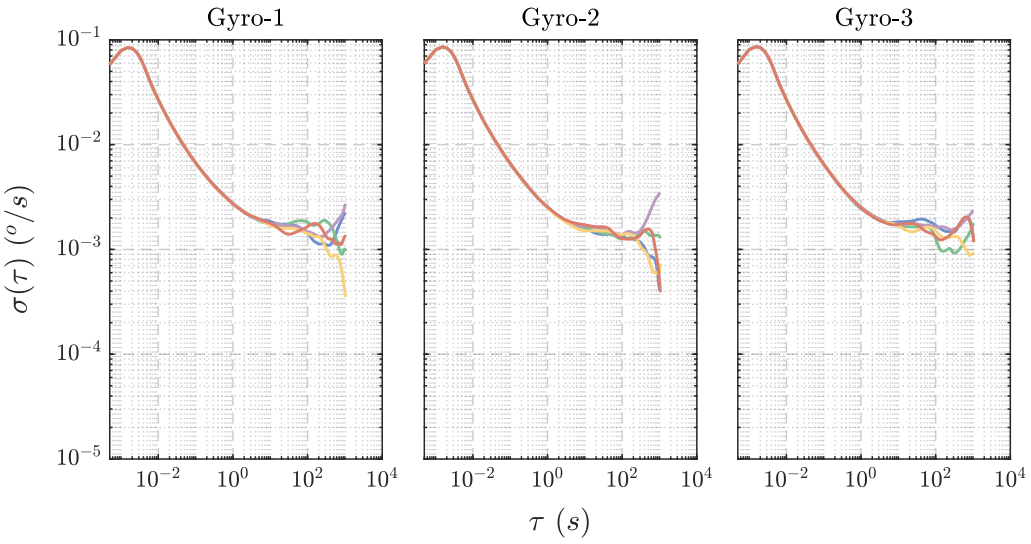

Figure 6.15: Allan Deviation of MEMS Gyros

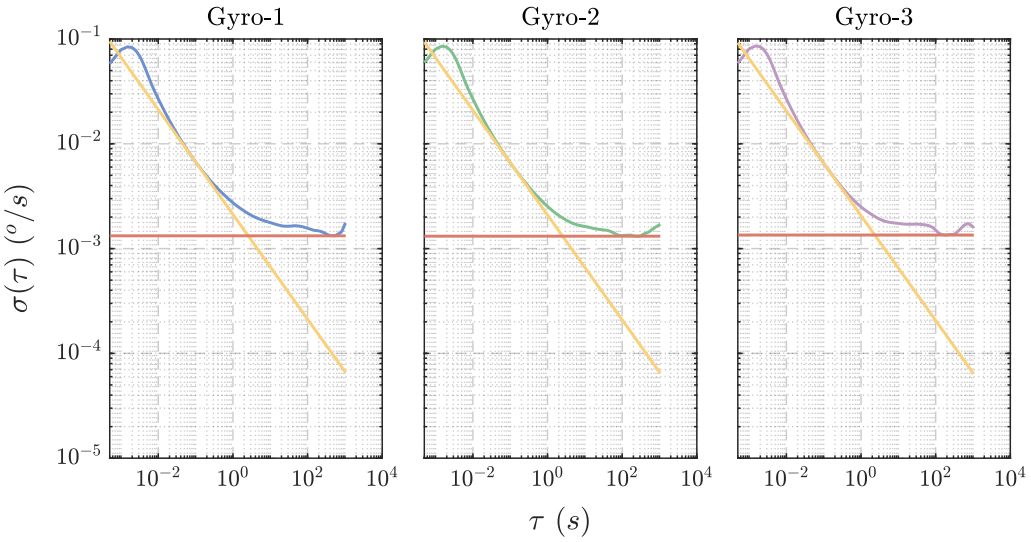

Figure 6.16: Average Allan Deviation of MEMS Gyros

Table 6.1 summarises the results of the statistical analysis, where it can be observed that all three of the gyros performed similarly and all outperformed the given datasheet specifications – most noticeably with regard to the BI of the gyros. However, in a presentation given by the manufacturer in 2013 [84], they stated that the expected BI of the CRM100 gyro's is $7.2\,^\circ\,\mathrm{h}^{-1}$ and that the ARW is closer to $0.18\,^\circ\,\mathrm{h}^{-0.5}$. This shows that the datasheet has provided the worst-case performance for the gyros, where the measured BI more closely matches the value from the presentation rather than that from the datasheet.

Table 6.1: MEMS Gyro Raw Output Statistical Analysis Summary

Property	Units	Datasheet	Gyro-1	Gyro-2	Gyro-3
ARW	$^\circ\,\mathrm{h}^{-0.5}$	0.28	0.1272	0.1254	0.1236
BI	$^\circ\,\mathrm{h}^{-1}$	24	7.1784	7.1208	7.3044

6.4.1.2 MEMS Digital Filtering

Applying a digital filter to a gyro's rate output reduces the impact of the added white noise to the signal and thus the ARW. To align with the sampling method used by CubeSpace, a moving average FIR low-pass filter was implemented to obtain the filtered gyro output, $y(n)$, from the unfiltered gyro input, $x(n)$, where

$$y(n) = \sum_{k=0}^{399} 0.0025 \cdot x(n-k). \tag{6.13}$$

The results of the applied filter on one of the gyro-3 datasets can be seen in fig. 6.17. Fig. 6.17a shows the significant decrease in the white noise component on the gyro, where fig. 6.17b confirms this as the ARW can no longer be determined in the ADEV plot. It is clear that the most dominant stochastic process is now the BI, which cannot be removed with a low-pass filter.

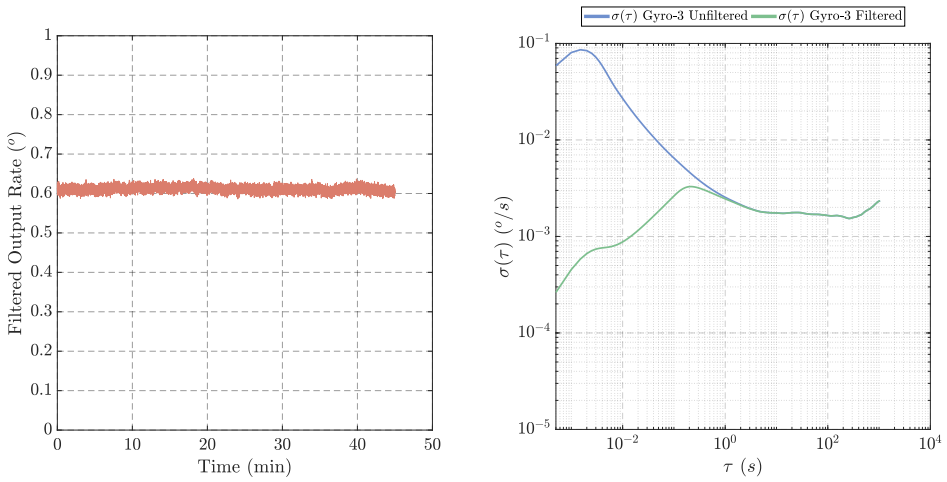

(a) Gyro-3 Filtered Output **(b)** ADEV Gyro-3 Filtered Output

Figure 6.17: Gyro-3 Digital Filter Implementation

To observe each gyro's BI and its associated upper and lower limits, the unfiltered datasets for each gyro were passed through a second order Butterworth filter with a cut-off frequency of 20 mHz.

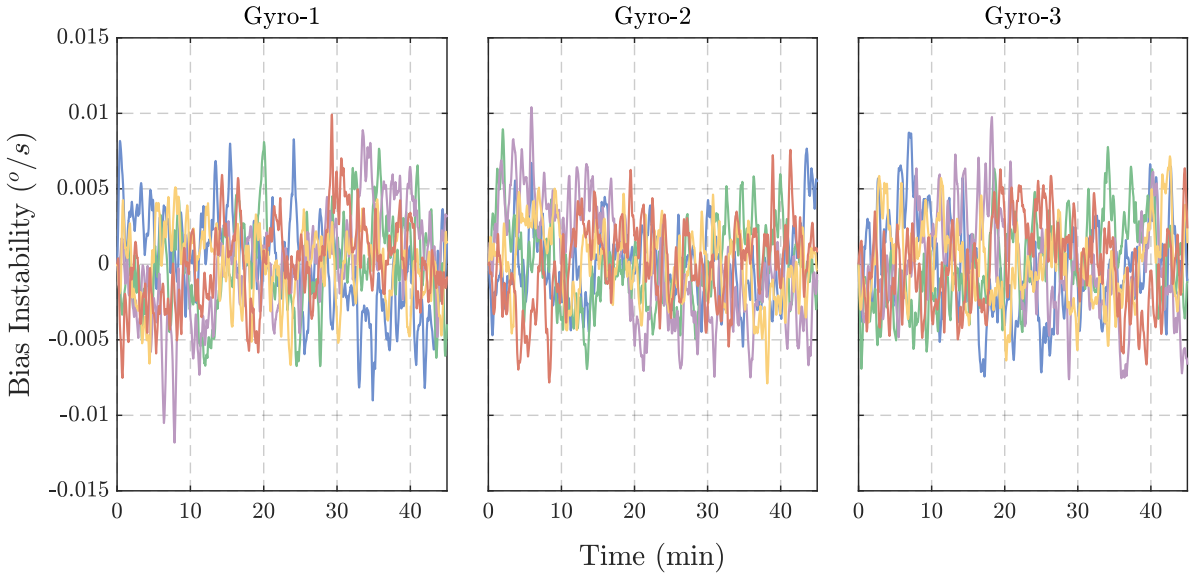

Figure 6.18: Average Allan Deviation of MEMS Gyros

The BI was removed from each gyro measurement in order to analyse the remaining higher frequency components on the filtered output in order to model the sensors correctly. The results of the filtered gyro properties are summarised in table 6.2, where the RMS for each gyro's bias instability is given over the five different datasets.

Table 6.2: MEMS Gyro Filtered Stochastic Properties Summary

Property	Units	Gyro-1	Gyro-2	Gyro-3
High Frequency (1σ error)	$^\circ\,h^{-1}$	21.042	19.858	19.897
RMS Bias	$^\circ\,h^{-1}$	10.555	10.073	10.436

6.4.1.3 MEMS Deterministic Errors

The deterministic errors of a gyro sensor are those which can be analysed and compensated for to a certain level of accuracy. This section mainly addresses the effects of temperature changes on a gyro's measured output as they cause the most significant errors on this output.

The effects of scale factor non-linearities are difficult to compensate for, however, this is not of a large concern as the effects are considerably small at slow angular rates. Additionally, the misalignment errors of the sensors were assumed to be compensated for to a satisfactory accuracy and were thus neglected in this analysis.

The average over 400 samples was taken in a 200 ms window (for both rate and temperature measurements) for each gyro by the MCU where the resultant output was then polled every second during this analysis. This was done to match the CubeContol module's sampling of the gyros.

6.4.1.3.1 In-Orbit MEMS Gyro Data

Before the results of the temperature variation on three gyro sensors is shown, an initial examination of the MEMS CRM100 gyro placed on the nSight-1 CubeSat body y-axis is presented. nSight-1s magnetic Y-spin controller used the MEMS gyro measurement to determine the Y-body spin rate when the satellite was in its Y-Thompson spin mode, after which the MEMS gyro output was only used for data analysis.

The gyro's rate and temperature data was captured every 120 s in the analysed WOD (Whole Orbit Data) file. The resolution of the internal temperature sensor output in the WOD file is only 1 °C, however, this was still enough to determine the effects of the MEMS temperature on the rate output. Fig. 6.19 shows the measured gyro angular rate output and its corresponding temperature at the time of measurement for over 270 orbits, during which the satellite was 3-axis stable in Y-momentum control mode (average Y-body rate must be close to zero). A second order polynomial line-of-best-fit (LOBF) was fitted to the data to show the correlation between the sensors bias and internal temperature.

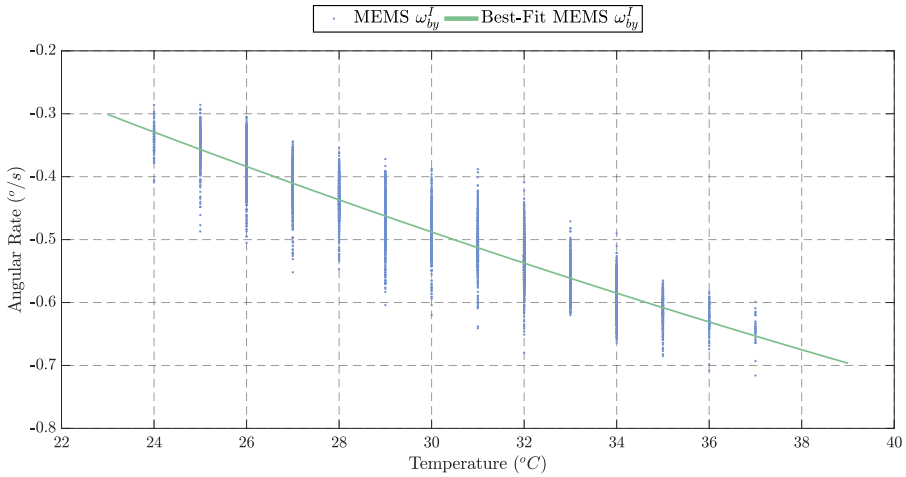

Figure 6.19: nSight-1 MEMS Gyro Angular Rate vs. MEMS Temperature

Fig. 6.20 shows the magnetometer EKF estimated ω_{by}^I, the measured gyro ω_{by}^I and gyro internal temperature data over just under 24 hours. Additionally, the figure shows the measured gyro ω_{by}^I with an instantaneous temperature bias compensation performed using the polynomial LOBF in fig. 6.19.

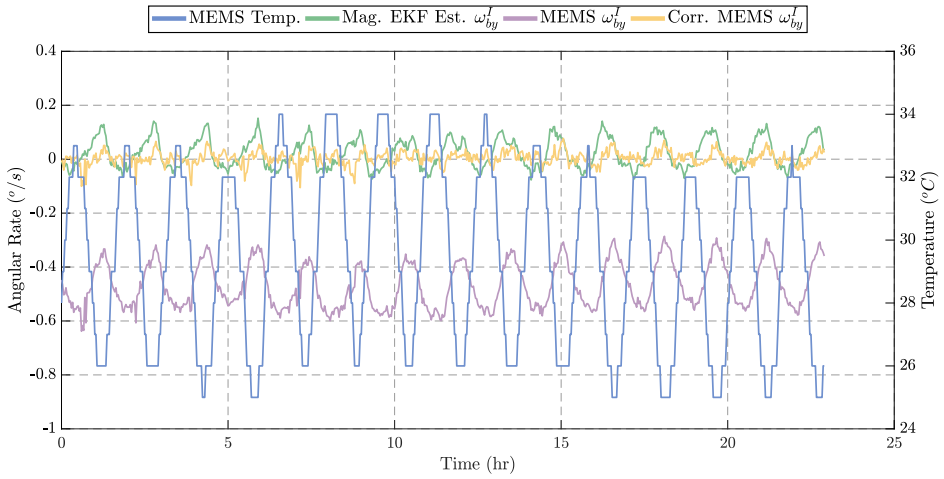

Figure 6.20: nSight-1 Angular Rate and Temperature Data

The satellite is striving to be y-axis stable, with $\omega^I_{by} \approx 0\,^\circ\mathrm{s}^{-1}$. The y-axis rate is now likely to be better represented by the compensated gyro output as it is expectedly more accurate than the EKF estimation as the EKF only uses the magnetometer to perform attitude and rate estimations. Both aforementioned figures show a strong relationship between a MEMS gyro's bias and temperature.

6.4.1.3.2 Thermal Bias Variation

The common downfall of MEMS sensors is their sensitivity to changes in temperature – especially with regards to the effects on its bias. Currently, CubeSpace does not perform any temperature compensation on the gyros, which makes the effect important to analyse.

The gyro manufacturers highly recommend using the internal temperature sensor on the gyros to perform temperature compensation in order to avoid system level thermal gradients from an external temperature sensor [37]. It must be noted that the temperature output for each gyro can only be obtained in the digital output mode.

The soak method [35] is a common technique used to measure the effects of temperature change on a gyro's bias, in two parts. The first part involves heating a gyro at regular intervals, allowing the temperature of the gyro to settle for a period of time and measuring the average bias at each temperature settling point. The second part is conducted in exactly the same way, although the gyro is instead cooled at regular intervals.

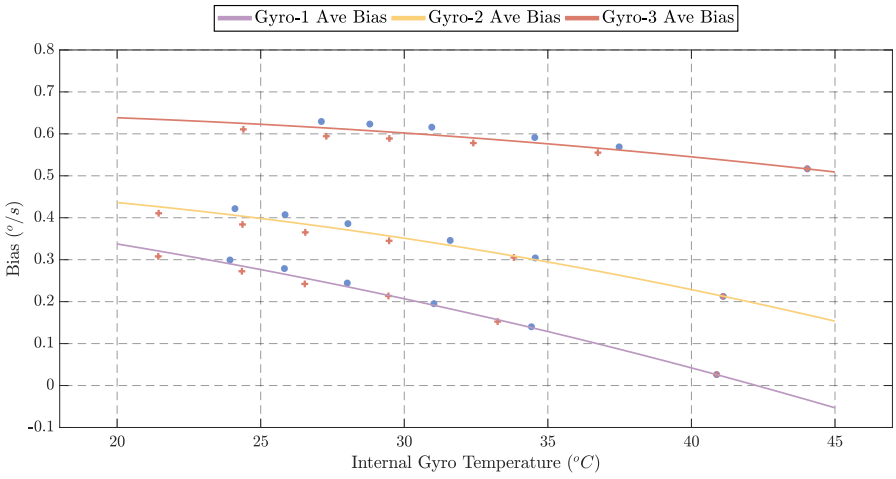

Figure 6.21: Gyro Bias vs. Internal Temperature

A piece of aluminium was mounted to the sensors with a layer of thermal paste between them to increase heat transfer, where a heat gun was set to warm and cool the sensors to different settling temperatures in

order to replicate the soak method as closely as possible. It is noted that the settling temperatures during the heating and cooling processes were not controlled to precise values, where the heat gun was simply used to heat up or cool down the sensors within a desired temperature range. The temperature range over the gyros was chosen to be similar to the temperature range seen over the nSight-1 CubeSat.

Fig. 6.21 shows the relationship between the three tested gyros and their respective internal temperatures. Each gyro is affected by thermal variations differently, where gyro-1 shows the greatest variation over temperature and gyro-3 the least. Three different second order polynomial LOBFs were chosen to model the change in each gyro's bias as a function of temperature which fits the average change in bias over heating and cooling processes.

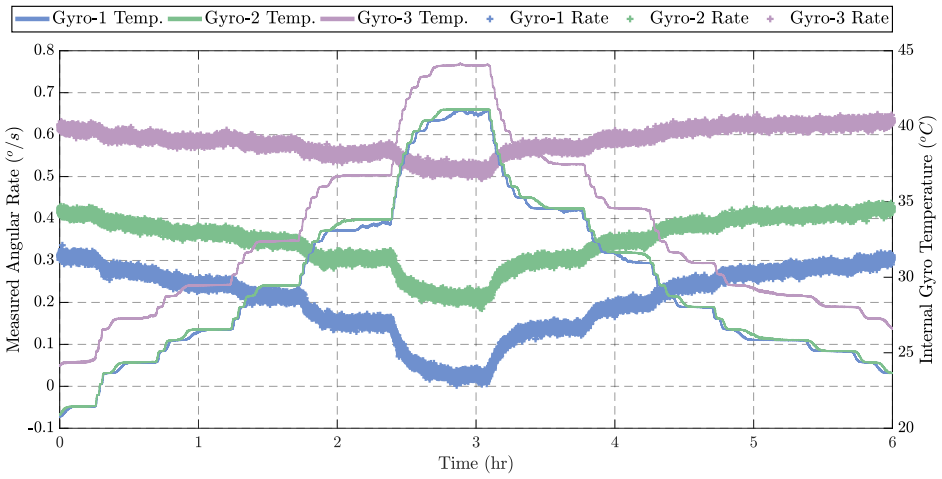

(a) Uncompensated Gyro Rate with Varying Temperature

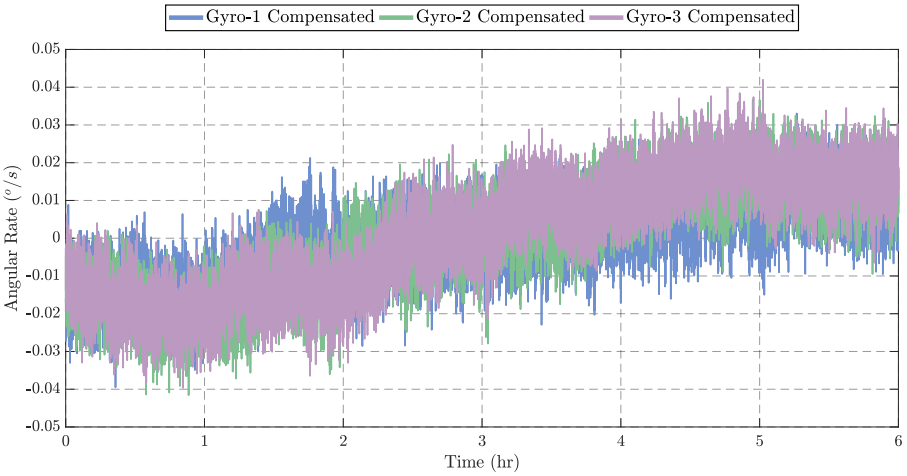

(b) Compensated Gyro Rate with Varying Temperature

Figure 6.22: Gyro Temperature Analysis

Fig. 6.22a presents the results of the temperature varying test conducted over time. It is apparent that each internal temperature sensor has an offset from the true chip temperature. This temperature varies linearly with time, however, where the offset is of little significance when using the temperature measurement to model a gyro's bias. Although gyro-1 showed the greatest bias variation over temperature, it also showed the lowest hysteretic variation as it closely followed the same modelled path through both heating and cooling processes.

Fig. 6.22b concludes the thermal bias experiment where each gyro was compensated against temperature to remove the respective biases, regardless of internal temperature. The results show that thermal bias removal is possible, with gyro- 1 to 3 each indicating an RMS error of $0.0108\,^{\circ}\,\mathrm{s}^{-1}$, $0.0146\,^{\circ}\,\mathrm{s}^{-1}$ and

$0.0153\,^\circ\,s^{-1}$ respectively over the full tested temperature range.

6.4.1.3.3 Prior Literature

A previous study was conducted on an earlier model of the CRM100 gyros by students in the United States Army Research Laboratory (ARL) [85]. The study examined the stochastic and deterministic errors of the sensors over temperature variation which covered the full operating temperature range ($-40\,^\circ$C to $85\,^\circ$C). The researchers used a much more accurate setup which utilised an integrated rate table and temperature chamber developed by Acutronic USA, Inc.

The study conducted an analysis on the sensors in the analogue mode and thus used an external temperature sensor during the analysis. Being an older model, the gyros were also quoted to have a significantly worse expected BI and ARW of $24\,^\circ\,h^{-1}$ and $0.28\,^\circ\,h^{-0.5}$ respectively. The results from the report are summarised for the performance of one of the gyros tested in table 6.3. For more information on the results, the reader is requested to refer to the authors' report [85].

Table 6.3: ARL Tested Results for One Gyro [85]

Property	**Units**	**$-40\,^\circ$C**	**$-15\,^\circ$C**	**$10\,^\circ$C**	**$35\,^\circ$C**	**$60\,^\circ$C**	**$80\,^\circ$C**
ARW	$^\circ\,h^{-0.5}$	0.186	0.188	0.179	0.181	0.179	0.187
BI	$^\circ\,h^{-1}$	12.88	11.75	11.14	9.79	9.64	10.09
Measured Bias	$^\circ\,s^{-1}$	0.83	0.58	0.17	−0.33	−0.17	0.5
SF (from nominal)	%	−0.54	−0.50	−0.47	−0.52	−0.58	−0.75

It must be noted that the researchers mistakenly omitted to divide the measured bias instabilities by the value of 0.664 and so the values in table 6.3 differ from those in the actual report. The results show, nonetheless, that both the stochastic and deterministic outputs for a given gyro are expected to vary with temperature.

The largest error is dominated by the variation in a gyro's bias, where in comparison, the SF variation will have a significantly lower influence on the measured rate output (especially at low angular rates). In conclusion, a small temperature variation (such as that measured by the rate sensor on nSight-1) will only have a significant impact on the bias of the sensor, where changes in the scale factor, BI and ARW will be comparatively insignificant over the same small temperature range.

6.4.2 MEMS Gyro Model

Having completed the analysis of the MEMS gyros, this section discusses the model for the three different gyros that are be implemented in the simulation in chapter 7 on each CubeSat axis. Only the most significant errors were chosen to be modelled unlike in eq. (3.1), namely: the noise of the gyros and the variation in the gyro's bias with temperature where the measured gyro vector is calculated with

$$\boldsymbol{\omega}^{\boldsymbol{I}}_{\boldsymbol{B}_{(meas)}} = \boldsymbol{\omega}^{\boldsymbol{I}}_{\boldsymbol{B}_{(true)}} + \boldsymbol{\omega}_{\boldsymbol{bias}} + \boldsymbol{\omega}_{\boldsymbol{noise}}. \tag{6.14}$$

6.4.2.1 Stochastic Model

The stochastic model was chosen to only consist of a high frequency component and a low frequency correlated BI, from which, the stochastic error vector was modelled with

$$\boldsymbol{\omega}_{\boldsymbol{noise}} = \boldsymbol{\omega}_{\boldsymbol{HF}} + \boldsymbol{\omega}_{\boldsymbol{BI}}. \tag{6.15}$$

The resultant full stochastic model is shown in fig. 6.23, where the high frequency component is modelled as Gaussian white noise with a standard deviation $\sigma_{HF} = 0.005\,85\,^\circ\,s^{-1}$. Also in the figure, the BI is modelled as a highly correlated signal with uniformly distributed noise having a maximum value of $0.018\,^\circ\,s^{-1}$ being passed through eq. (6.1) with correlation coefficient, $\alpha = 0.02$.

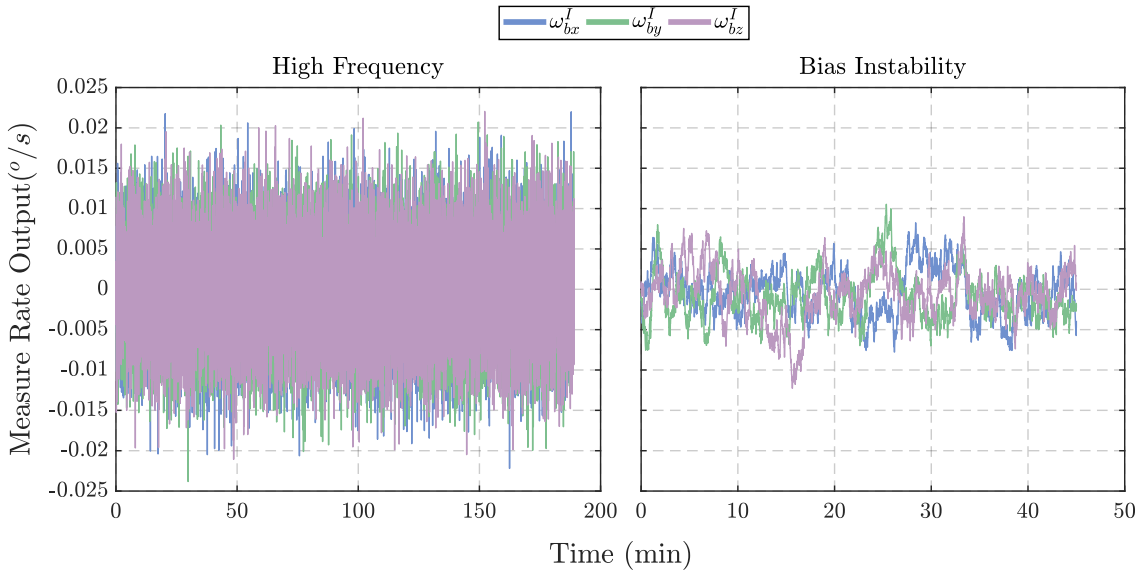

Figure 6.23: Gyro Stochastic Error Models

The resultant high frequency components show errors extremely close to the chosen standard deviation as expected, where the BI has a worst case RMS error of $11.88\,^\circ\,\mathrm{h}^{-1}$ tested over ten orbits.

6.4.2.2 Thermal Bias Drift Model

In order to model the effects of temperature variation on the simulated gyros' biases, it was necessary to model the internal temperature variations for a typical CubeSat in LEO. Fig. 6.24 plots a portion of the internal temperature variation measured on nSight-1 for the on-board gyro, where the grey portions on the plot represent when the CubeSat was in eclipse.

Examining the full dataset of over 270 orbits, reveals that the measured maximum and minimum internal gyro temperatures were 39 °C and 24 °C respectively. The temperature is shown to vary approximately sinusoidally with an amplitude of 4 °C and a lag after the change in each eclipse state. The mean of the eclipse varying temperature is also observed to change approximately sinusoidally with a period of ≈ 200 h and an amplitude of 3.5 °C. The resulting temperature model is shown in fig. 6.25, which is shown to vary per orbit as well as every 200 h covering the whole temperature range.

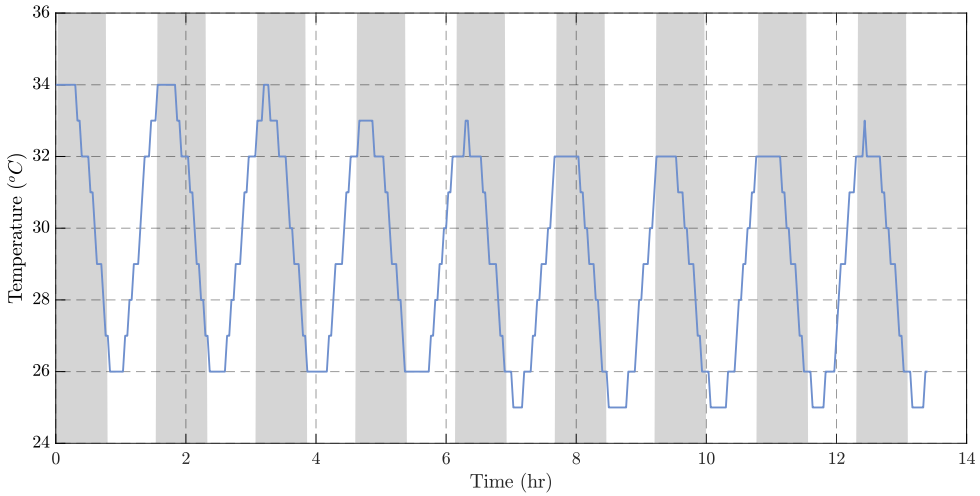

Figure 6.24: nSight-1 Temperature Variation with Eclipse

Each gyro's change in bias over temperature is chosen to be modelled with the second order polynomial

LOBFs seen in fig. 6.21, where the vector, $\boldsymbol{\omega_B}$, representing the gyros' biases is defined as

$$\begin{aligned}\boldsymbol{\omega_{bias}} = \begin{bmatrix}\omega_{bias_x}\\ \omega_{bias_y}\\ \omega_{bias_z}\end{bmatrix} &= \begin{bmatrix}a_1 & b_1 & c_1\\ a_2 & b_2 & c_2\\ a_3 & b_3 & c_3\end{bmatrix}\begin{bmatrix}T^2_{gyro}(t)\\ T_{gyro}(t)\\ 1\end{bmatrix}\\ &= \begin{bmatrix}-1.705\times10^{-4} & -4.538\times10^{-3} & c_1\\ -1.867\times10^{-4} & 8.253\times10^{-4} & c_2\\ -1.029\times10^{-4} & 1.512\times10^{-3} & c_3\end{bmatrix}\begin{bmatrix}T^2_{gyro}(t)\\ T_{gyro}(t)\\ 1\end{bmatrix}.\end{aligned} \tag{6.16}$$

The coefficients $\{c_1, c_2, c_3\}$, are calculated at the beginning of each simulation, in-order to zero the bias of each gyro to whatever the starting temperature is for a particular orbit, with

$$\begin{bmatrix}c_1\\ c_2\\ c_3\end{bmatrix} = -\begin{bmatrix}a_1\cdot T^2_{gyro}(0) + b_1\cdot T_{gyro}(0)\\ a_2\cdot T^2_{gyro}(0) + b_2\cdot T_{gyro}(0)\\ a_3\cdot T^2_{gyro}(0) + b_3\cdot T_{gyro}(0)\end{bmatrix}. \tag{6.17}$$

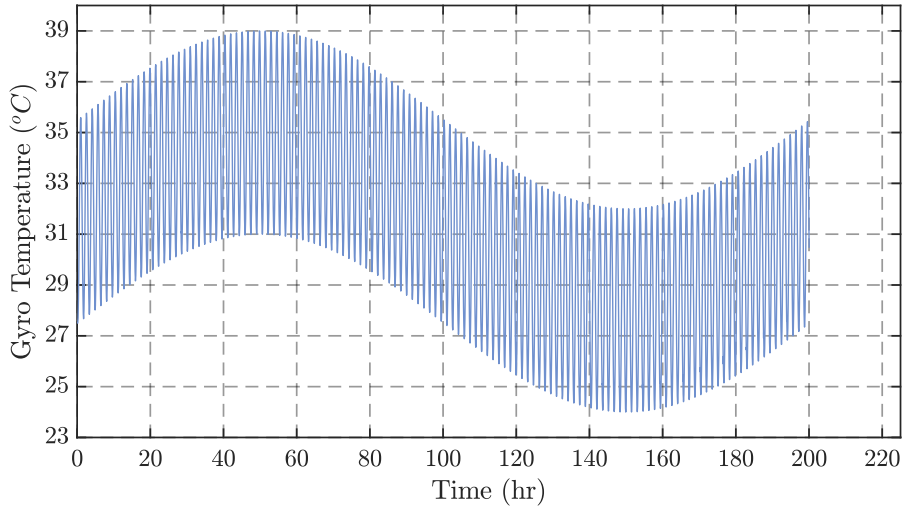

Figure 6.25: Long Term Simulation Temperature Model

The resultant bias drift with temperature model is shown in fig. 6.26 over two successive orbits.

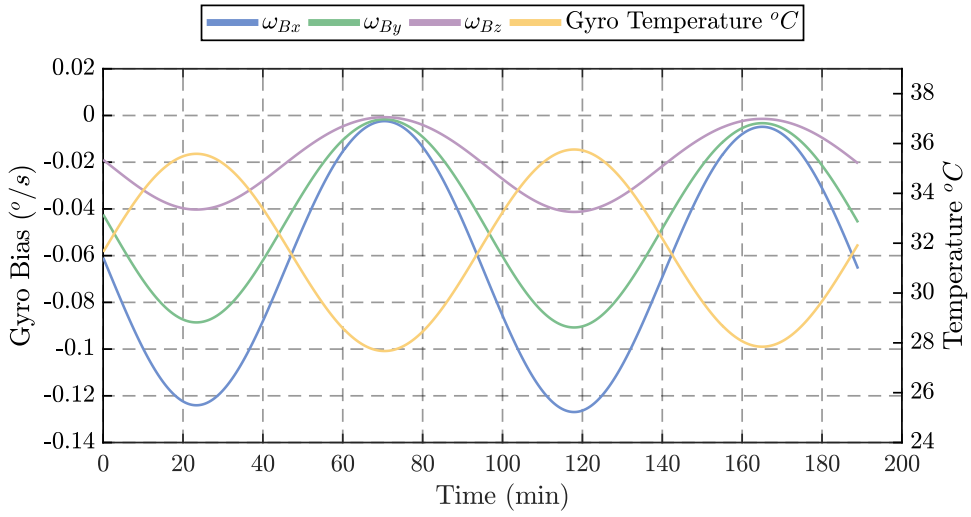

Figure 6.26: Simulation Temperature Model

6.4.2.3 Complete Model

The final step was to combine all of the different gyro errors to form a full gyro measurement model in the simulation, where these errors were added to the true angular rotation rates calculated in the satellite dynamics block of the simulation as described in sec. 5.4.

Fig. 6.27 plots the typical gyro vector component measurements aboard the simulated 3-axis stable CubeSat using a full state EKF without a gyro in order to measure the true angular rate output. The angular rotation rates for both the x and the z satellite body axes should be measuring $\approx 0\,^{\circ}\mathrm{s}^{-1}$, where the body y-axis should be measuring a rotational rate of $\approx 0.063\,^{\circ}\mathrm{s}^{-1}$ (the orbit rotation rate) in the IRC frame.

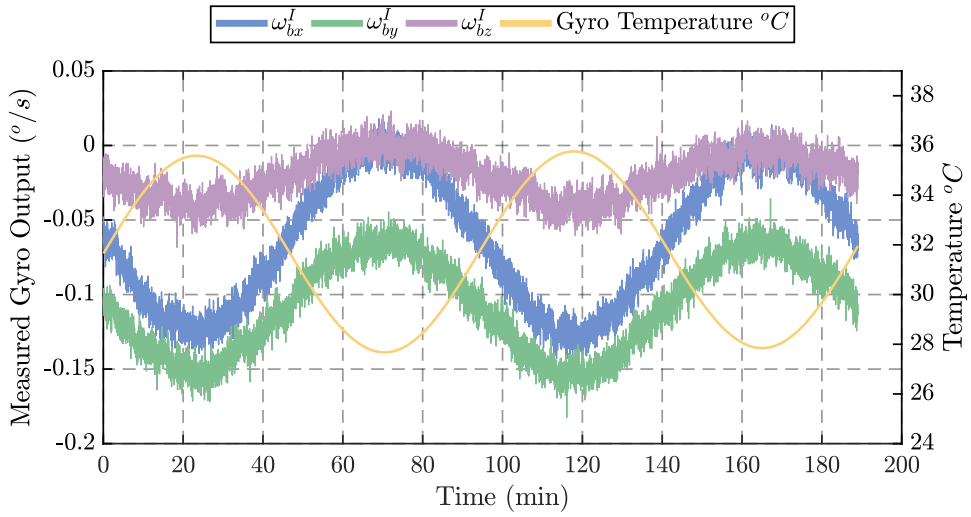

Figure 6.27: Simulation Temperature Model

6.5 CubeSense

The theory behind the operation of the CS has been discussed in sec. 3.5. This section analyses the error characteristics of the CS as well as the modelling of the CS components. First, the FSS on the CS is investigated and modelled, which is then followed by the analysis and modelling of the nadir sensor.

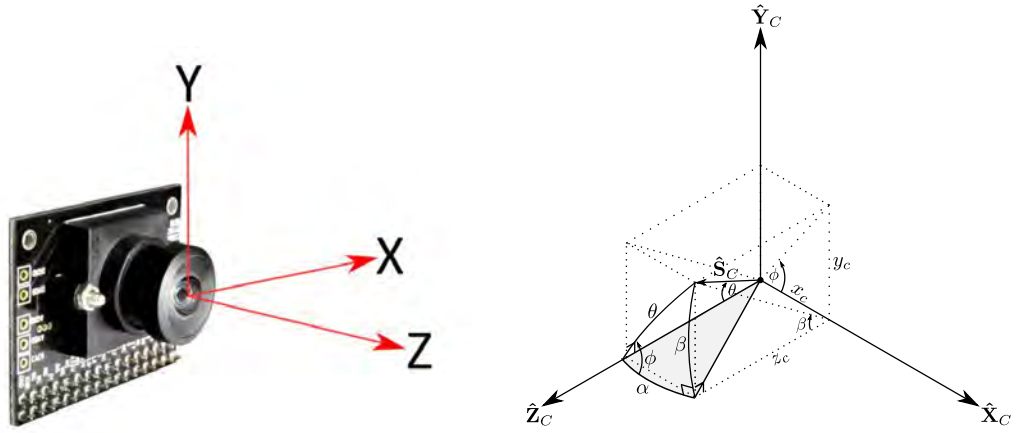

(a) CubeSense Camera Axes [86]

(b) CubeSense Camera Angles

Figure 6.28: CubeSense Camera Axes and Angle Visualisation

After the centroid is located for either the Sun or the Earth, the CS generates two centroid x and y angles, α and β (in centi-degrees), which can then be used to calculate the relevant Sun and Earth vectors with respect to the camera boresight (BS). The camera's coordinate frame is shown in fig. 6.28a, where the

camera z-axis, $\hat{\mathbf{Z}}_C$, is defined to be along the camera BS, the y-axis, $\hat{\mathbf{Y}}_C$, is defined to be pointed upwards, away from connector of the camera, and the x-axis, $\hat{\mathbf{X}}_C$ completes the orthogonal set.

Fig. 6.28b illustrates how the respective rectangular coordinates are determined, where the angle θ, is calculated as

$$\theta = \sqrt{\left(\frac{\alpha}{100}\right)^2 + \left(\frac{\beta}{100}\right)^2} \tag{6.18}$$

and is measured from the $\hat{\mathbf{Z}}_C$ axis to the celestial body position vector. The angle ϕ is calculated as

$$\phi = \text{atan2}(\beta, \alpha) \tag{6.19}$$

and is the angle between the camera xz-plane and the plane passing through the $\hat{\mathbf{Z}}_c$ axis and the celestial body position vector. Once angles θ and ϕ are calculated, then the celestial body position vector, $\mathbf{v}_c$, in the camera frame rectangular coordinates, is calculated as

$$\mathbf{v}_c = \begin{bmatrix} v_{cx} \\ v_{cy} \\ v_{cz} \end{bmatrix} = \begin{bmatrix} \sin\theta\cos\phi \\ \sin\theta\sin\phi \\ \cos\theta \end{bmatrix} \tag{6.20}$$

6.5.1 CubeSense FOV and Detection Range

The fisheye lens provides a theoretical FOV close to 200° for both the FSS and nadir cameras. Pixels which fall out of a 180° FOV are ignored to prevent irregularities from reflections on the satellite's side-panels. Furthermore, the outer perimeter of the lens is cut off at the edges of the image plane, reducing the FOV to 170° at these edges. Lastly, the nadir sensor will begin to produce significantly inaccurate measurements as the Earth moves further away from the BS.

Table 6.4: Maximum and Minimum DRs

Property	**FSS**	**Nadir**
DR_{max}	180°	160°
DR_{min}	170°	130°

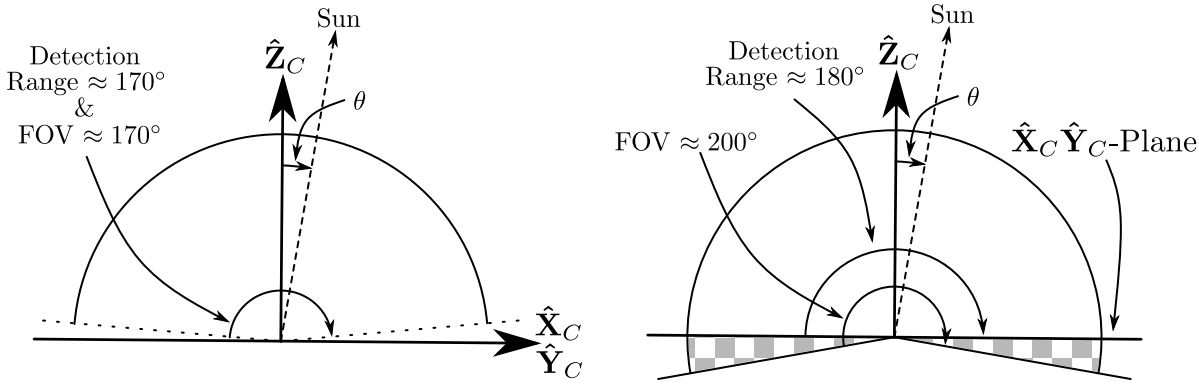

(a) FSS Hor. and Ver. FOV/DR

(b) FSS Diagonal FOV/DR

Figure 6.29: FSS FOVs and DRs

A detection range (DR) is defined which describes a new FOV for each sensor which will produce valid position vector measurements for a particular celestial body. Figs. 6.29 and 6.30 illustrate the detection ranges at the horizonal and vertical edges as well as along the diagonal for both the FSS and nadir sensor. Table 6.4 shows the maximum and minimum DRs for the FSS and nadir sensor respectively. If it

is determined that an SBC referenced Sun or nadir vector is outside of the respective sensor's DR then the vector is ignored and marked as a null detection.

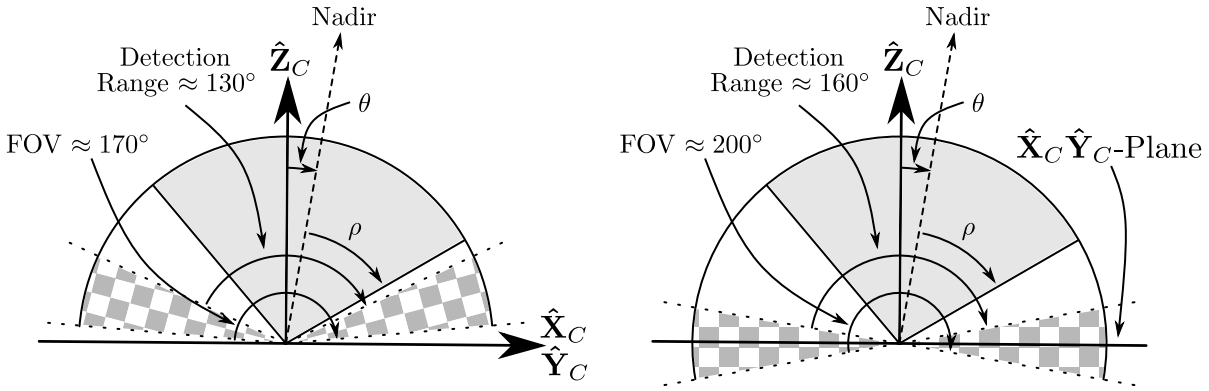

(a) Nadir Sensor Hor. and Ver. FOV/DR

(b) Nadir Sensor Diagonal FOV/DR

Figure 6.30: Nadir Sensor FOVs and DRs

The simulation modelling of the DR is done slightly differently for each sensor. For the FSS, most of the image sensor's 1024×1024 pixels are utilised within the DR as Sun detections with acceptable accuracy can occur near or even on the image sensor edges. To model how the DR changes for the Sun sensor, it is firstly assumed that after distortion correction of the lens that the linear relationship

$$\mathrm{DR}_{FSS}(\phi) = \frac{R_{max}(\phi)}{R_{FOV_{BS}}} \cdot \mathrm{FOV}_{BS} \tag{6.21}$$

exists, where $\mathrm{DR}_{FSS}(\phi)$ is the maximum possible DR for an object along line described at ϕ, $R_{max}(\phi)$ is the maxium possible pixel radius to an object on the image plane, $\mathrm{FOV}_{BS} = 200°$ is the maximum boresight FOV and, $R_{FOV_{BS}}$ is the pixel radius at the maximum boresight FOV. It is known from table 6.4 that at the edges of the image sensor ($R_{max}(0°) = 512$ pixels), where it can be deduced using eq. (6.21) that $R_{FOV_{BS}} = 602.35$ pixels, and furthermore that $R_{max}(\phi) = 542.12$ pixels, at $\mathrm{DR}_{FSS}(\phi) = 180°$.

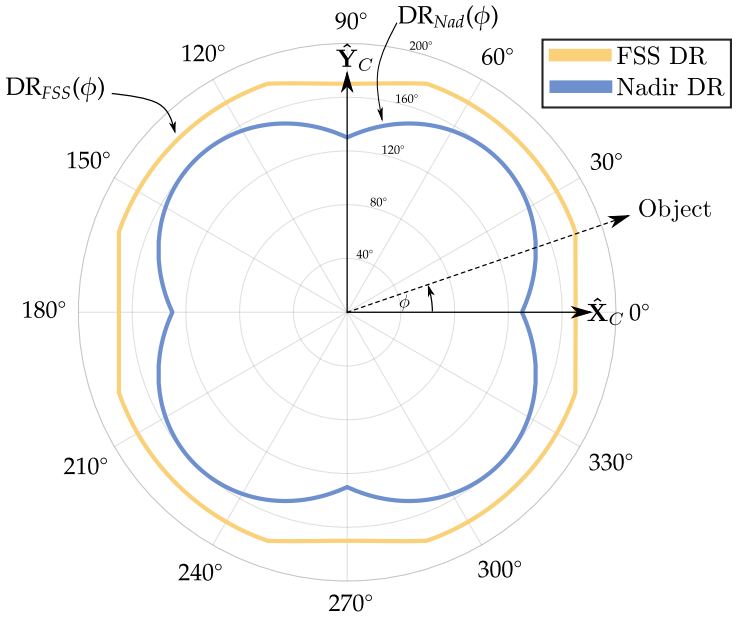

Figure 6.31: CubeSense DR

As the Sun centroid begins to move off of the image sensor at the positive x side of the image sensor (i.e X_{pix} is increasing past 512 pixels) the maximum possible radius in this position can be calculated as

$$R_{max}(\phi) = \sqrt{512^2 + Y_{pix}^2}, \tag{6.22}$$

where the maximum radius is calculated similary for all edges of the image sensor as it is a square sensor, the difference being that Y_{pix} is the value that is fixed for the top and bottom edges. The algorithm for calculating the maximum detection range and whether a Sun vector is within that range is described by alg. 6.1, where a Sun vector is not accepted if the DR_{flag} is false.

Detections for the nadir sensor begin to become unacceptably inaccurate at points before the image sensor edges and even before the FSS DR limit. For this reason, the DR for the nadir sensor is defined differently using

$$\mathrm{DR}(\phi) = (\mathrm{DR}_{\max} - \mathrm{DR}_{\min}) \cdot |\sin(2\phi)| + \mathrm{DR}_{\min}, \tag{6.23}$$

where $\mathrm{DR}_{\max}$ and $\mathrm{DR}_{\min}$ represent the maximum and minimum DRs for the nadir sensor (see table 6.4). Angle ϕ, is determined from known celestial body position coordinates in camera axes by

$$\phi = \mathrm{atan2}(v_{cy}, v_{cx}), \tag{6.24}$$

If the nadir vector is determined to be outside of the DR then the vector is ignored. Eq. (6.23) and alg. 6.1 are visualised in polar form in fig. 6.31 as ϕ changes.

Algorithm 6.1: FSS Detection Range

Data: S_{cx}, S_{cy}, S_{cz}

Result: DR_{flag}, DR_{max}

$\mathrm{DR}_{flag} \leftarrow$ True
$\phi \leftarrow \mathrm{atan2}(S_{cy}, S_{cx})$
$R_{max}(\phi) \leftarrow 542.12$
if $S_{cz} < 0$ **then**
  $\mathrm{DR}_{flag} \leftarrow$ False
else
  $X_{pix} \leftarrow S_{cx} \cdot R_{max}(\phi)$
  $Y_{pix} \leftarrow S_{cy} \cdot R_{max}(\phi)$
  $XY_{lim} \leftarrow \sqrt{R_{max}^2(\phi) - 512^2}$
  if $|X_{pix}| < XY_{lim}$ **then**
    $R_{max}(\phi) \leftarrow \sqrt{512^2 + Y_{pix}^2}$
    if $|Y_{pix}| > 512$ **then**
      $\mathrm{DR}_{flag} \leftarrow$ False
    end
  else if $|Y_{pix}| < XY_{lim}$ **then**
    $R_{max}(\phi) \leftarrow \sqrt{X_{pix}^2 + 512^2}$
    if $|X_{pix}| > 512$ **then**
      $\mathrm{DR}_{flag} \leftarrow$ False
    end
end
$\mathrm{DR}_{max} \leftarrow \frac{R_{max}(\phi)}{602.35} \cdot 200°$

6.5.2 Fine Sun Sensor Analysis

In order to test the error of the FSS, the sensor was placed on the roof of a tall building on a sunny day with the setup shown in fig. 6.32. The FSS was left to locate the Sun over a period of approximately 4.5 hours, sampling at a rate of 1 Hz, as the Sun moved across the sky.

After the test was complete, the α and β angles were extracted from the data log and the Sun position vector, $\mathbf{S}_C$, was calculated using eqs. (6.18) to (6.20). The results of the test are seen in fig. 6.33, which plots the individual vector components with respect to time during the investigation.

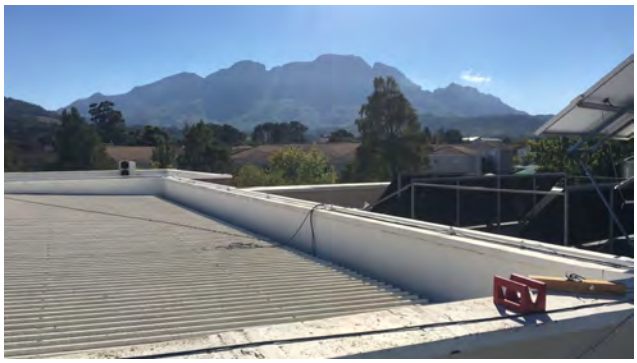

(a) CubeSense FSS Placement

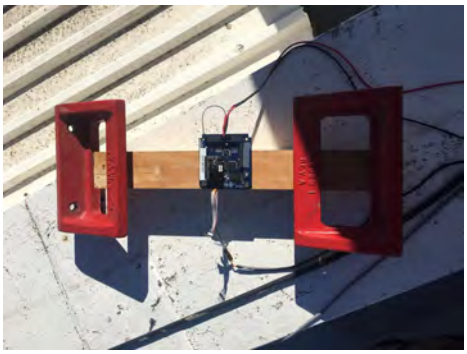

(b) CubeSense FSS Setup

Figure 6.32: CubeSense FSS Roof Setup

To find the error in the vector component measurements, a fourth order polynomial LOBF was determined for each of the vector component outputs as a function of time, in order to find a mean path as measured by the FSS for the position of the Sun. The error is therefore a deviation from the mean path which is assumed to be the true location of the Sun during this investigation.

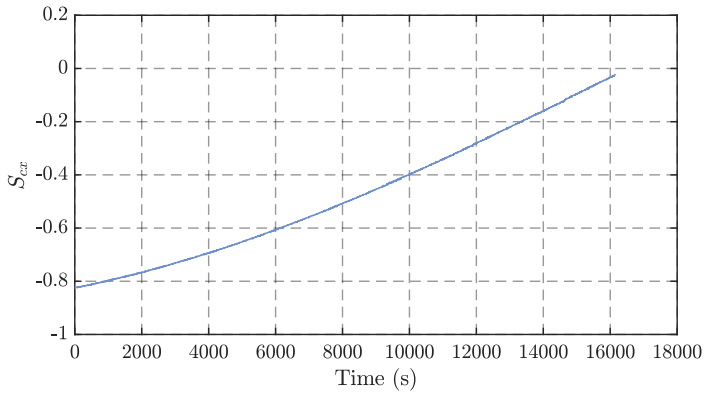

(a) Vector Component S_{cx}

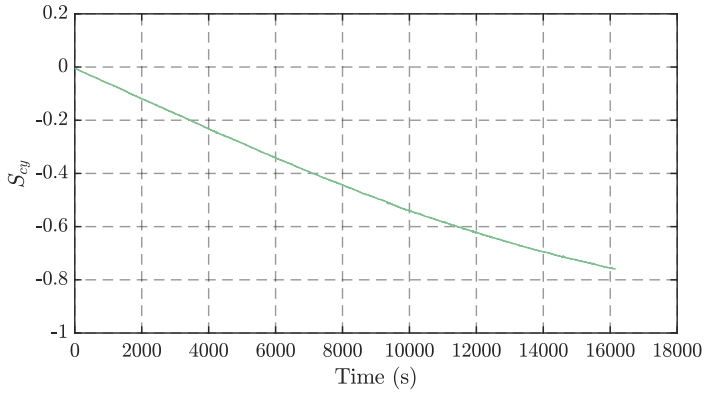

(b) Vector Component S_{cy}

Figure 6.33: FSS Camera Sun Vector Components

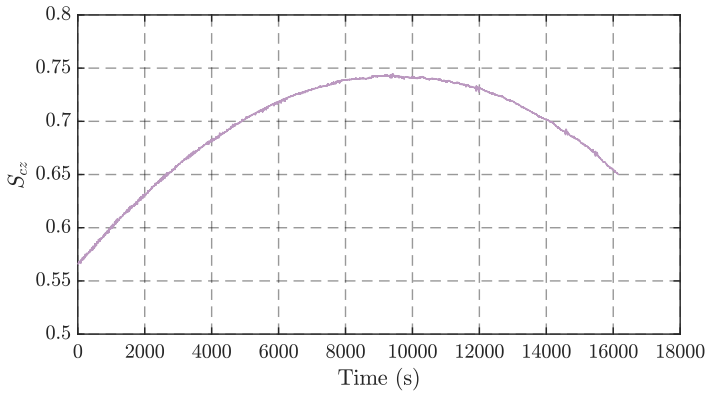

(c) Vector Component S_{cz}

Figure 6.33: FSS Camera Sun Vector Components

Fig. 6.34a shows the deviation from the mean for each of the Sun vector components where the 3σ errors for each component were calculated as 2.455×10^{-3}, 2.351×10^{-3} and 2.232×10^{-3} respectively. Eq. (4.55) was once again used to calculate the expected angular vector error from the mean Sun vector – the results of which can be seen in fig. 6.34b. The random spikes in the errors in both figures particularly after the 8000 s mark, could be attributed to small clouds passing over the Sun during the investigation. Even with this as the case however, 99.59 % of the angular errors still remained much lower than the stated 1σ error of 0.2° where this particular test obtained a 3σ accuracy of 0.233° which reflects the random measurement noise error, not the lens distortion corrected angular error.

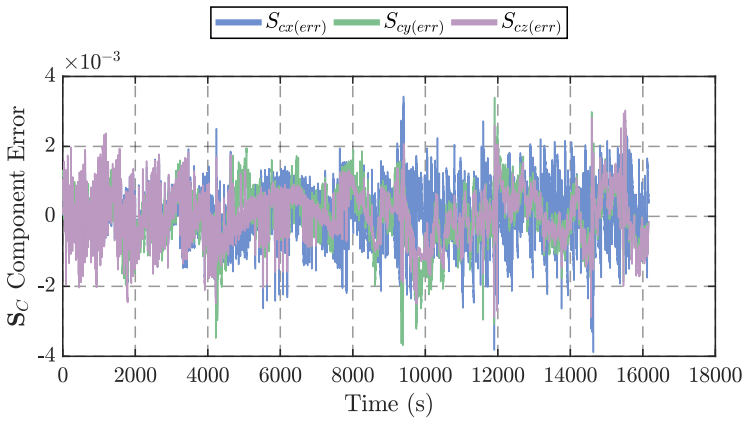

(a) FSS $\mathbf{S}_C$ Component Error

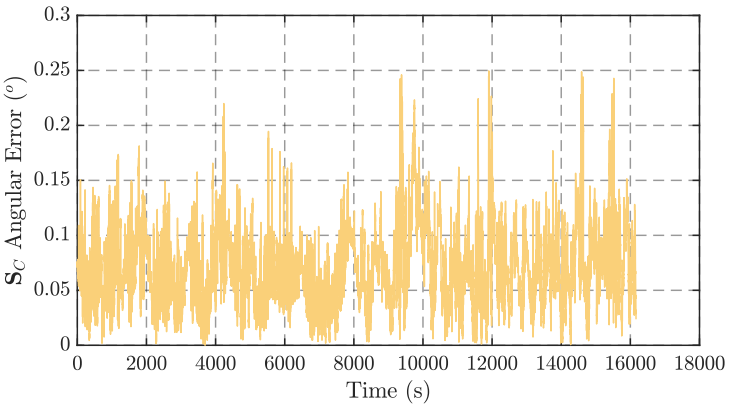

(b) FSS $\mathbf{S}_C$ Angular Error

Figure 6.34: FSS Error

Upon the conclusion of the FSS analysis, where the findings show that FSS's reported accuracy is likely to actually be better than stated, as the test conducted for this research was completed on Earth's surface – where atmospheric and cloud conditions played a role in accurately measuring the error in the FSS. With satellite's in space, the error is likely to be lower, where weather conditions and atmospheric diffraction will not be a factor influencing the accuracy of the FSS.

6.5.3 Fine Sun Sensor Model

The FSS was modelled similarly to that of the CSS, where a correlated Gaussian noise was instead added to each of the Sun vector components in the SBC frame. The FSS model only includes the random noise errors and not its absolute angular errors. The FSS was chosen to be placed with the camera BS to be pointing towards the -Y facet of the satellite, where the FSS camera axes are transformed to the satellite body axes by

$$\mathbf{S}_B = \begin{bmatrix} 1 & 0 & 0 \\ 0 & 0 & -1 \\ 0 & 1 & 0 \end{bmatrix} \mathbf{S}_C. \tag{6.25}$$

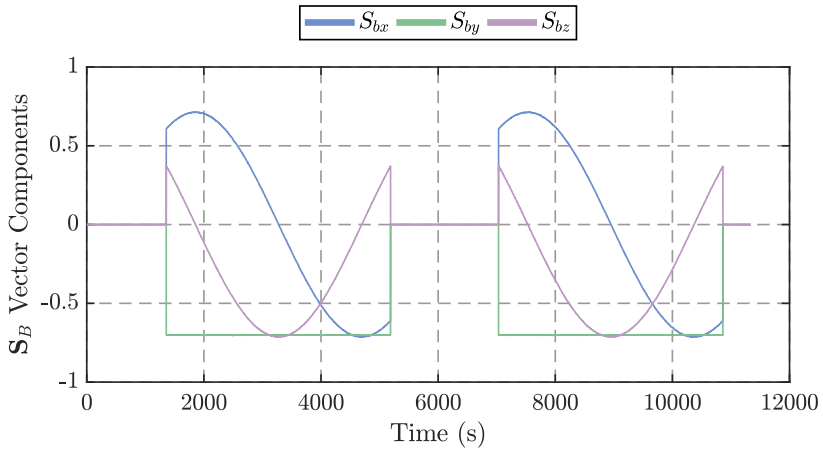

Figure 6.35: Modelled FSS $\hat{\mathbf{S}}_B$ Components

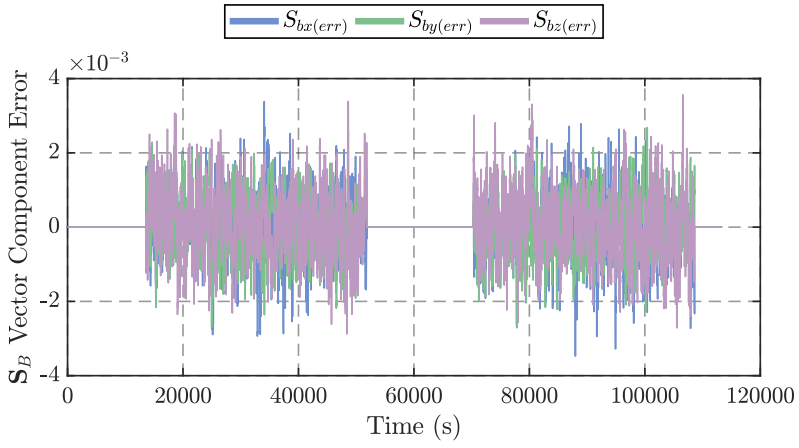

(a) Modelled FSS $\hat{\mathbf{S}}_B$ Component Error

Figure 6.36: Modelled FSS Error

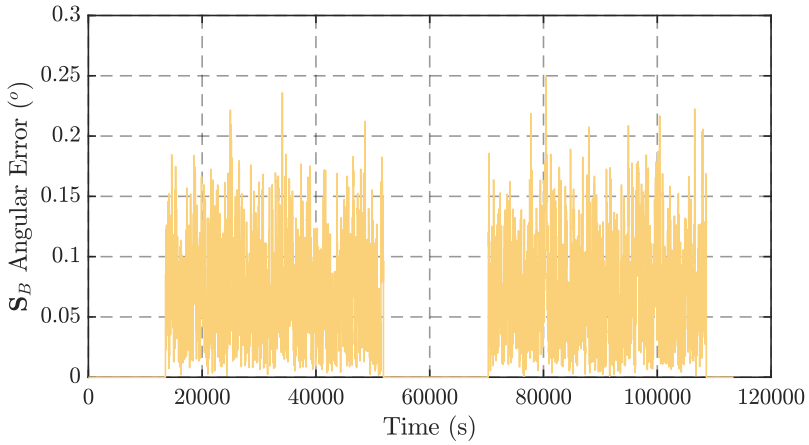

(b) Modelled FSS $\mathbf{S}_B$ Angular Error

Figure 6.36: Modelled FSS Error

The Gaussian noise is correlated through the same low-pass filter as in eq. (6.1) with $\alpha = 0.1$ in order to allow higher frequency components to pass. Multiple tests were conducted to find the best suited noise output for the FSS, where a value of $\sigma_e = 4.5 \times 10^{-3}$ obtained to most realistic error output. The resultant Sun vector component errors can be seen in fig. 6.36a and the measured Sun vector in SBC is shown in fig. 6.35, where the FSS model is set to give no measurements if the satellite is in the eclipse portion of its orbit or if the Sun is out of the DR as explained in sec. 6.5.1.

The 3σ errors were calculated over ten orbits. The $\hat{\mathbf{X}}_B$ and $\hat{\mathbf{Z}}_B$ Sun vector errors were similar at 2.1216×10^{-3} and 2.1412×10^{-3} respectively, where, the 3σ error on the BS axis was the smallest in the simulation at 1.7582×10^{-3}. This is because the Sun vector components are normalised after noise is added and the $\hat{\mathbf{Y}}_B$ component remained relatively large and constant during the simulation. The resultant angular error can be seen in fig. 6.36b, where the 3σ error was calculated to be 0.2013° on average – closely matching the expected error for the FSS.

6.5.4 Nadir Sensor Analysis

Fig. 6.37 shows the setup of the nadir camera that was used to investigate its performance. The setup was based in a darkroom at the CubeSpace head-office, where an illuminated ball was used to represent the Earth as detected by the nadir camera.

In order to maintain accuracy, CubeSpace has set the nadir camera (in software) to only calculate nadir measurements for a minimum Earth disk radius $\rho_\oplus = 37.5°$, which equates to a maximum satellite altitude of approximately 4100 km [52]. The ball in the test setup has a radius, $R_{ball} = 30$ cm. By modifying eq. (4.28) and treating the ball as the Earth and the camera as a satellite, the angular radius of the ball relative to the camera, ρ_{ball}, could be calculated with

$$\rho_{ball} = \arcsin\left(\frac{R_{ball}}{R_{ball} + d_{ball}}\right). \tag{6.26}$$

Similarly, the distance d_{ball} could be calculated with

$$d_{ball} = \frac{R_{ball} \cdot (1 - \sin\rho_{ball})}{\sin\rho_{ball}}, \tag{6.27}$$

where the theoretical maximum distance for the camera to be placed from the ball is calculated to be 19.28 cm before the camera will report an error.

To make sure that the camera was well within range of the ball, it was placed at a distance $d_{ball} = 5.5$ cm (not the same as in the figure). Additionally, fewer errors are to be expected if the camera is placed

in close proximity to the ball as more edges are likely to be detected for the circle fitting algorithm to utilise.

Next, the camera was fixed to a rotation stage set to change its azimuth angle relative to the ball's centre along the xz-plane in the camera frame to observe the increase in error as the ball moves towards the edge of the nadir DR. Additional care was taken to ensure that the camera BS was aligned with the axis of rotation to minimise external errors in the measurements.

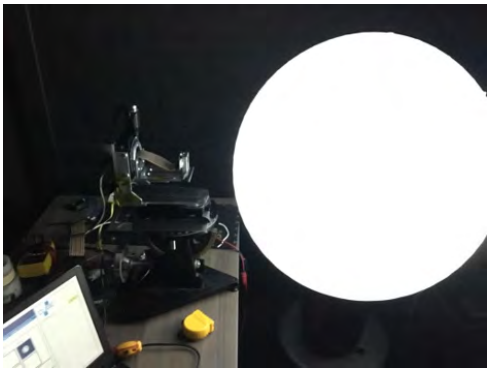

Figure 6.37: Nadir Camera Test Setup

During the experiment, the camera's azimuth was changed from $-10°$ to $50°$ in increments of $1°$. Five consecutive measurements were then captured at each angle increment to observe the deviation of error. Fig. 6.38 shows the actual distorted images captured by the nadir camera at the two outer limits of the tested angles and at the camera BS. Fig. 6.39 shows a contrast equalised version of each image which allows one to see previously hidden objects in the background; but more importantly, it shows the edge of the camera lens on the image plane.

It is typically difficult to perfectly align the BS with the centre of an image plane, which is clearly seen in fig. 6.39b. This, in turn, skews the horizontal DR and limits the maximum camera rotation angle for positive azimuth angles, resulting in a detection error occurring sooner than expected as the ball moves towards the right-hand side of the image.

Each measured nadir vector component was obtained using eqs. (6.18) to (6.20) where a true reference vector was also calculated to determine the error of each component with α_{ref} being set to the negative camera rotation angle and $\beta_{ref} = 0°$. Fig. 6.41 shows the errors in each vector component from its respective reference vector component, as well as the angular errors between the measured vector and the true reference vector.

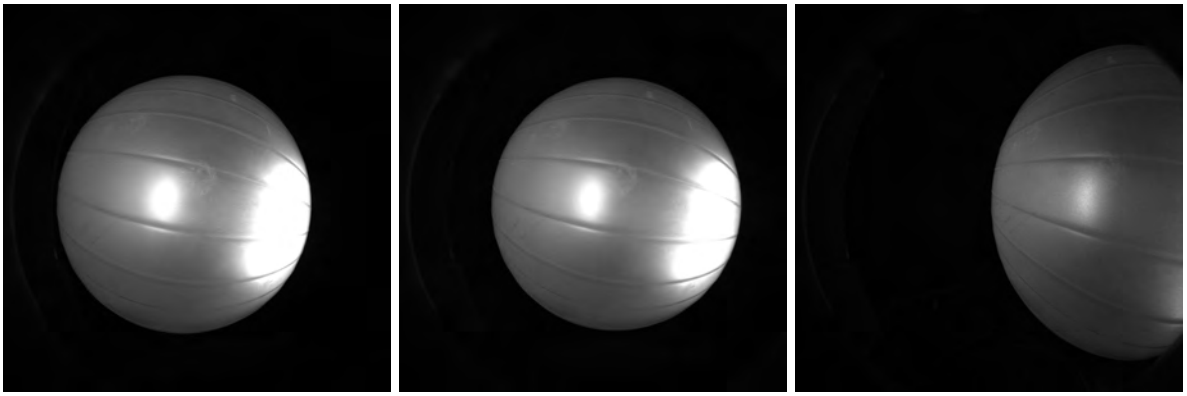

(a) $-10°$ **(b)** $0°$ **(c)** $50°$

Figure 6.38: Nadir Camera Images

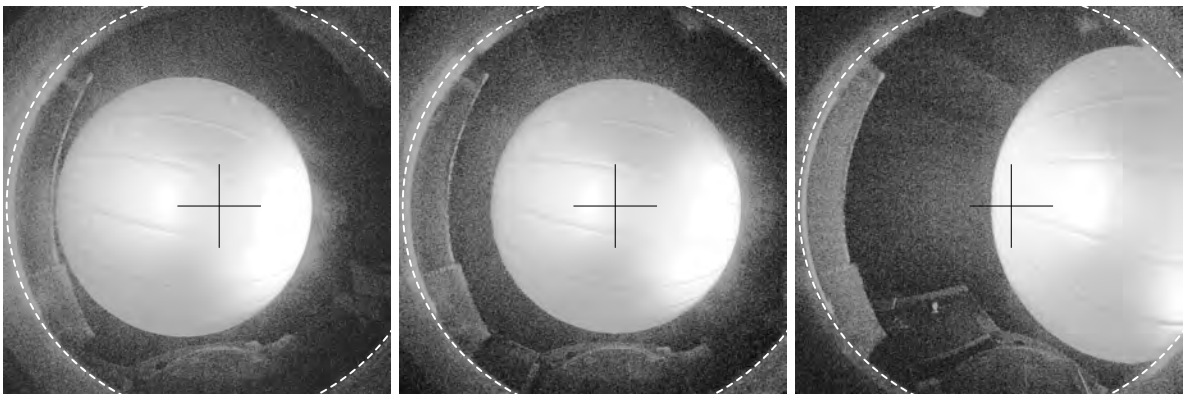

(a) −10° **(b)** 0° **(c)** 50°

Figure 6.39: Nadir BS on Image Plane

The camera was expected to obtain an error when the camera azimuth angle was at 65° (the edge of the DR). However, due to the misalignment of the BS, the camera instead started producing errors for azimuth angles greater than 50°. This was also worsened by the errors in the distortion correction model increasing as the ball moved further away from the BS. Additionally, less light from the ball reached the camera at extreme angles which caused fewer pixels to pass through the detection threshold.

Fig. 6.40 shows angular errors found during error testing for the nadir camera during the original design and experimentation of the CS [14]. These previous results bare a close similarity to results obtained in this experiment seen in fig. 6.41b which used a very similar setup and Earth disk to this analysis. Angular errors are shown, in both cases, to increase as the BS moves further away from the ball, where both errors remain below 1° before the camera azimuth angles reaches 40°.

Fig. 6.41c plots the angular errors found whilst the full ball is still in the camera's DR. The 3σ angular error in this region is calculated to be 0.1904° which is well within the stated expected accuracy. This error then increases to 0.9283° for camera azimuth angles less than 40°, where after this range, the errors become unacceptable.

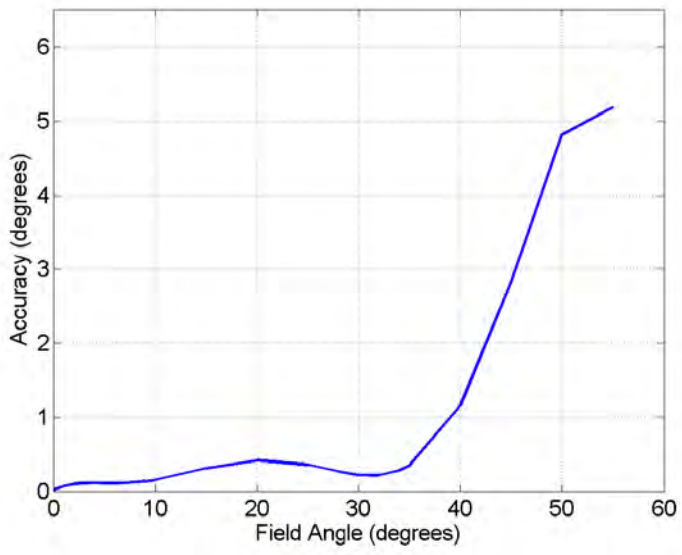

Figure 6.40: Original Nadir Camera Accuracy Results [14]

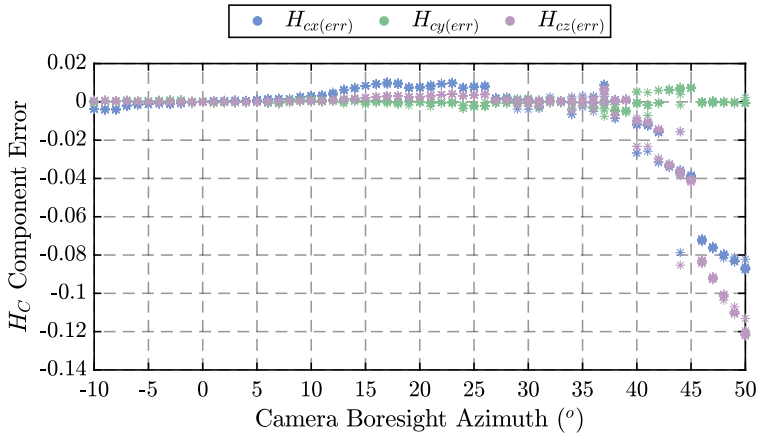

(a) Vector Component Error

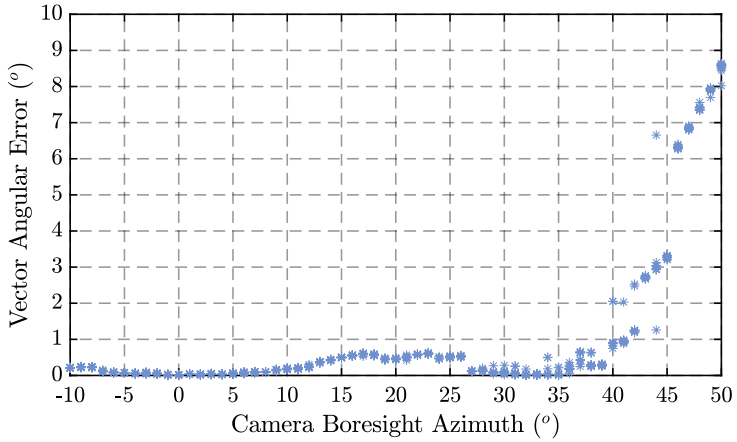

(b) Angular Error

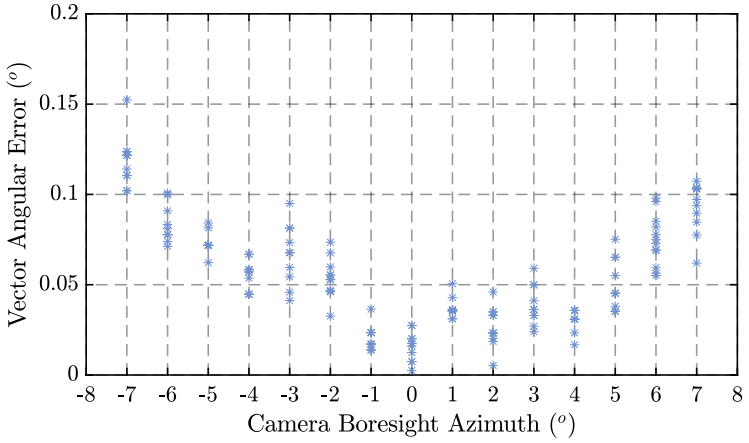

(c) Angular Error – Full Ball in DR

Figure 6.41: Nadir Sensor Errors

6.5.5 Nadir Sensor Model

Using the results from the nadir sensor analysis, a nadir camera model is defined. The nadir camera is intuitively placed on the +Z facet of the satellite, which aligns the satellite body axes to the nadir camera axes. By definition of the ORC frame, the nadir vector in ORC is defined as

$$\hat{\mathbf{H}}_O = \begin{bmatrix} H_{ox} \\ H_{oy} \\ H_{oz} \end{bmatrix} = \begin{bmatrix} 0 \\ 0 \\ 1 \end{bmatrix}, \tag{6.28}$$

where the true nadir vector in the SBC frame is simply the 3rd column of the satellite DCM. The nadir camera can only detect an illuminated Earth and so the model is designed to produce no measurements if the simulated satellite is in the eclipse portion of its orbit.

Furthermore, the DR is continuously calculated in the simulation using eqs. (6.23) and (6.24) where no nadir sensor measurements could be produced if the nadir vector was out of the camera's DR. Gaussian noise was correlated through eq. (6.1) with a correlation coefficient $\alpha = 0.01$ and was once again added to each nadir vector component. The errors were then set to increase as soon as a portion of the Earth begins to leave the DR.

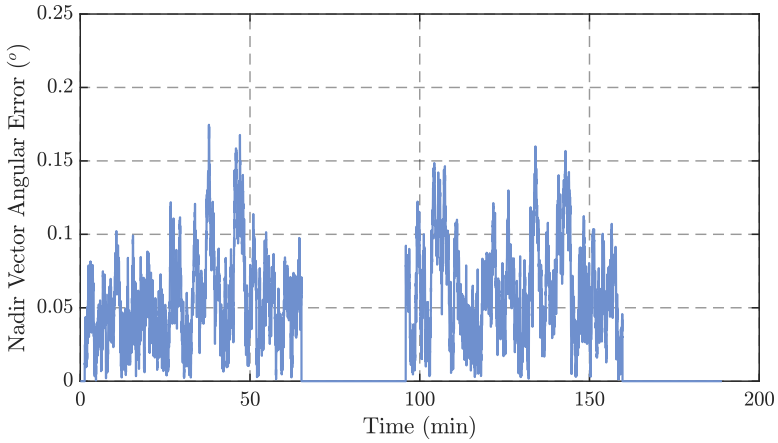

Figure 6.42: Modelled Nadir Sensor Angular Errors – Full Earth in DR

Fig. 6.42 plots the angular error measured when the full Earth is still in the camera's DR, where fig. 6.43 plots the measured nadir vector angular error for a satellite performing a slowly increasing and decreasing pitch manoeuvre. The errors are seen to increase as the Earth moves further out of the nadir DR. A test conducted over ten orbits revealed a 3σ error of 0.2124° when the full Earth is in the DR, where five tests run over two orbits performing the same pitching manoeuvre as in fig. 6.43 produced an average 3σ error of 0.9124° – closely matching the measured results.

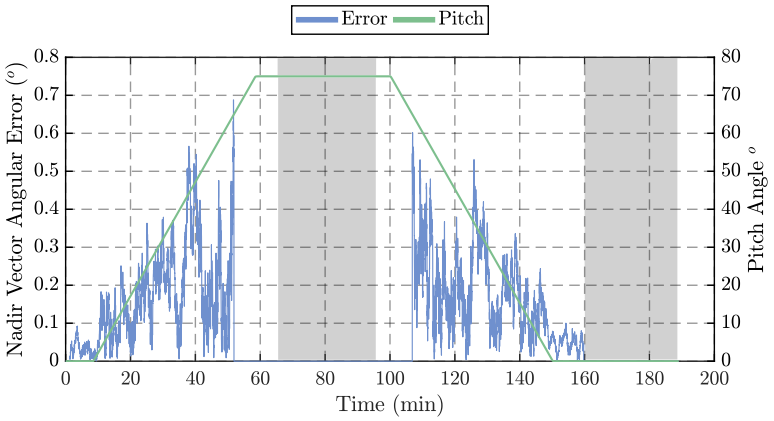

Figure 6.43: Modelled Nadir Sensor Angular Errors – Satellite Pitching

6.6 CubeStar

This section discusses the analysis and modelling for the CT (the final sensor discussed), and addresses the main theory behind the operation of the CT presented in sec. 3.6. Fig. 6.44 shows the two-dimensional pixel coordinate frame for the image sensor on the CT, where the top right-hand corner represents the sensors $(0, 0)$ pixel coordinate. Increases in x-axis pixels represent an increase in image sensor pixel columns (of which there are 1280), where increases along the image sensor y-axis represent changes in

pixel rows (of which there are 1038). The subsequent image produced, when viewed, will be mirrored about the image sensor x-axis due to the pixels being stored from left to right and top to bottom [48].

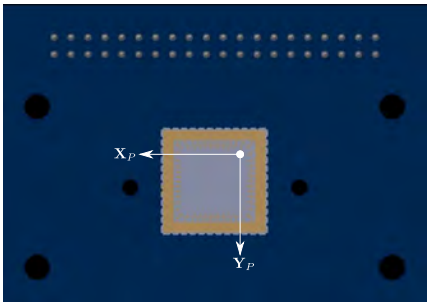

Figure 6.44: CubeStar Image Sensor Coordinate Frame [52]

The CT's body coordinate system is shown in fig. 6.45, where the orthogonal set of the camera body axes are defined relative to the lens's principal point shown in the centre of the lens. The location of the origin in fig. 6.45 is different to that in fig. 6.44, where it has been moved to the principal point of the image plane [48]. The unit body vectors pointing to identified stars is generated in the defined body axes.

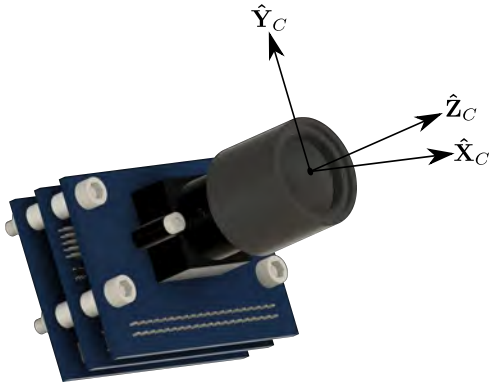

Figure 6.45: CubeStar Camera Body Coordinate Frame [52]

6.6.1 CubeStar Field of View

Shown in fig. 6.47, the CT lens and image sensor provide the camera a horizontal FOV of 58° and a vertical FOV of 47°. This is limited to both a vertical and horizontal FOV of 42° by a defined "valid image region" [48] used for valid star detection, represented as a square block on the image sensor shown in fig. 6.46. The square block thus defines a diagonal FOV of approximately 60°.

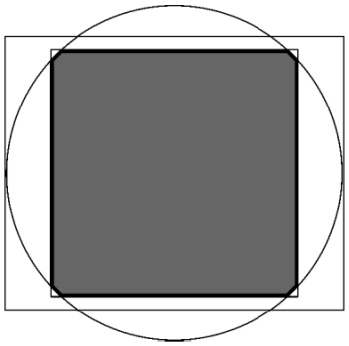

Figure 6.46: CubeStar Valid Image Region [48]

If the Sun, illuminated Moon or Earth are in or near the camera's FOV, then the CT is likely to produce an invalid detection due to its long exposure time causing the image sensor to take in a lot of external

light. If the satellite is in the eclipse portion of its orbit and the Moon is either not visible or illuminated, then the Earth would be the source of most errors if the CT is pointing nadir as the Earth will block the light from stars behind it. Care should be taken to position the CT in a location on the satellite which would minimise such errors.

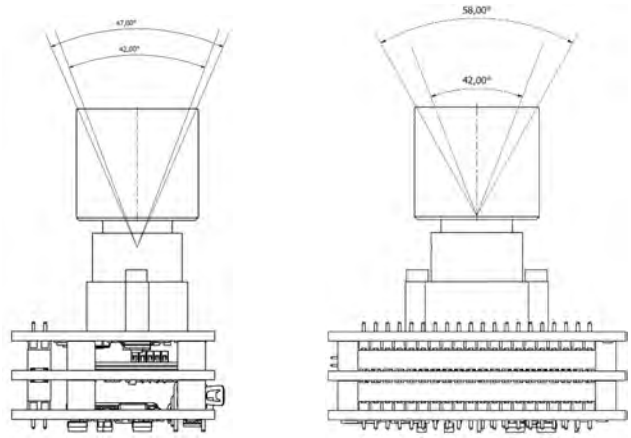

(a) CubeStar FOV – Side View

(b) CubeStar FOV – Front View

Figure 6.47: CubeStar FOVs [48]

6.6.2 CubeStar Star Catalogue

The identified stars are matched to a reduced set of 410 stars in the Hipparcos star catalogue from which an inertial vector to the star is generated with reference to the International Celestial Reference System (ICRS) having an epoch of J1991.25 [48] and its axes "fixed" in space. The ICRS frame differs in origin to the ECI frame in that its origin is at the barycentre of the solar system, however, the ICRS coordinates are considered to be approximately the same as ECI coordinates.

At the beginning of each year, the positions of the stars are updated by having their epochs set to 12h (TT) on 1 January. The inertial and corresponding body referenced star vectors form a star vector pair which is then used to estimate the CT's attitude [48] using a QUEST algorithm. The CT outputs both its attitude in quaternion form together with its RA and declination celestial coordinates in degrees.

It is stated that with the combination of the FOV and star catalogue, the CT will be able to observe a maximum and minimum of 38 and 2 stars respectively and that it should be able to match three or more stars 99.71 % of the time. Additionally, the CT has been tested and proven to perform correctly under a maximum slew rate of $0.3\,^{\circ}\,s^{-1}$ when the CT is in its lost-in-space mode, and up to $1\,^{\circ}\,s^{-1}$ when in its tracking mode [52]. Angular rates any higher than the rated maximums in each mode will cause the stars to be "smeared" across the image due to the long integration time of the camera – leading to poor or null star detection and matching results.

6.6.3 CubeStar Analysis

A dataset obtained from an experiment conducted by CubeSpace [52] was used to analyse the accuracy of the CT. In preparation for the test, before any imaging took place, the CT was placed at rest on the Earth's surface with the camera BS facing the clear night-sky. Over a period of about 26 min, the CT took images of the stars approximately every 3 s and calculated a corresponding quaternion attitude vector as the Earth rotated. The accuracy test is one which measures the CT's ability to estimate its attitude.

The results show that the CT was able to estimate its attitude 504 times out of a total 511 measurements (matched 3 or more stars 98.63% of the time) and that the processor matched a total of 4138 out of a possible 5256 detected stars. The measurement errors that did occur could also likely be due to

atmospheric disturbances during the test as it was conducted on Earth and not in space where the accuracy is expected to be improved.

In orbit, a satellite's DCM would relate its SBC frame to the ORC frame. If the attitude quaternion is known, then the DCM, $\mathbf{A}_O^B$, can be calculated with eq. (4.47). The DCM calculated for a CT placed on Earth's surface relates its body frame to the ECI frame and is thus represented by $\mathbf{A}_{ECI}^B$. Both the calculated star vector, $\mathbf{v}_B$ and the corresponding ideal star vector from the catalogue, $\mathbf{w}_{ECI}$ can be obtained from the output test data. The vectors are first normalised, then $\mathbf{v}_B$ is transformed to the ECI coordinate frame using:

$$\mathbf{v}_{ECI} = {\mathbf{A}_{ECI}^B}^{-1}\mathbf{v}_B. \tag{6.29}$$

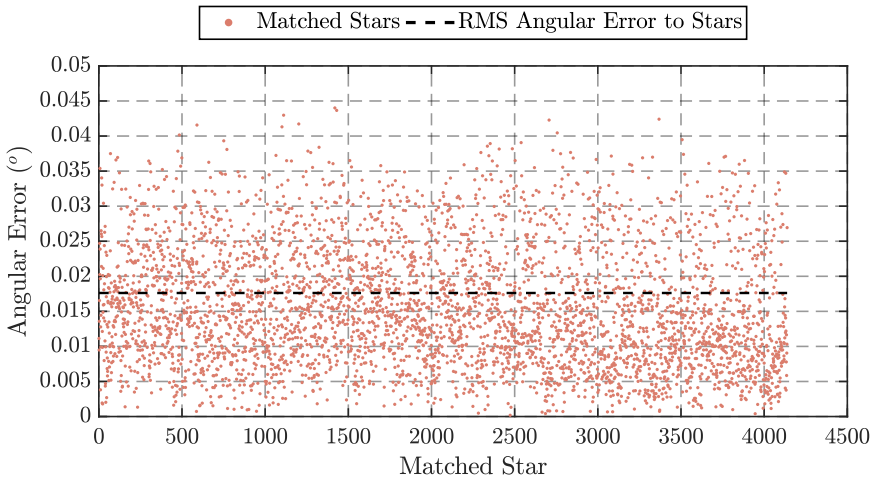

Figure 6.48: Calculated Star Vector Error

Eq. (4.55) is used to calculate the angular error, between the vector pair $\mathbf{v}_{ECI}$ and $\mathbf{w}_{ECI}$. The results from calculated error angle for each vector pair relating to a matched star and the CT's attitude can be seen in fig. 6.48, the RMS of which was found to be 0.0176° represented in the figure by the black dashed line. The results indicated that 64.14 % of the errors were below the RMS error. The errors shown in fig. 6.48 calculate the angular error between a matched star and its reference star, and is not a measure of how accurately the CT can determine its true attitude.

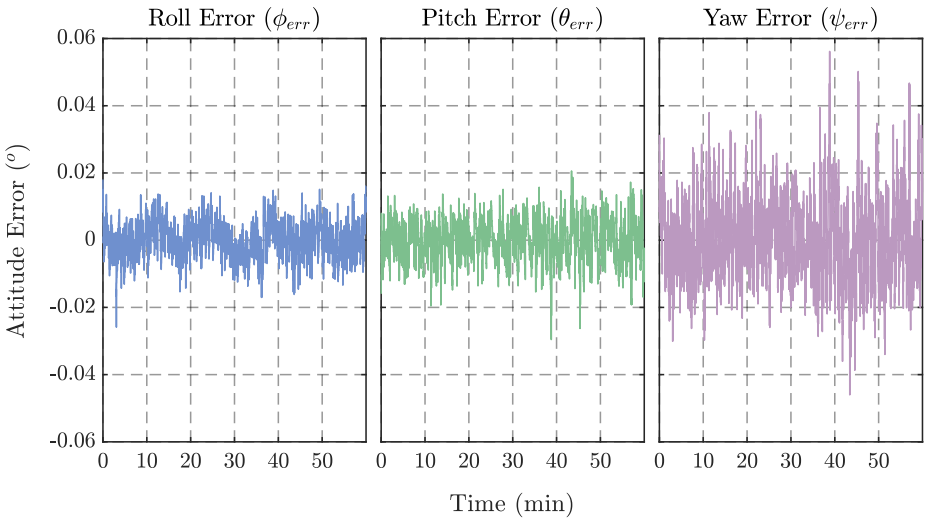

Figure 6.49: CubeStar Attitude Deviation from Mean

A separate dataset provided by CubeSpace [52] logged the calculated attitude quaternion for a CT in a

similar setup at 1 Hz over a period of 1 h as the Earth rotated with it. Once again, eq. (4.47) was used to calculate the DCM between the CT body frame and the ECI frame which was further used to calculate the respective Euler angles at each instant. The resultant roll, pitch and yaw angles obtained were then fitted individually with their own respective LOBFs from which their deviations from the mean Euler angle was calculated.

The resultant errors can be seen in fig. 6.49, where the RMS roll, pitch and yaw errors were calculated to be 0.005 29°, 0.005 95° and 0.011 71° respectively. Notably, 94.22 % and 91.36 % of the respective roll and pitch (cross-axis) errors remained below 0.01° in magnitude, where 98.61 % of the yaw (BS roll) errors remained below 0.03° in magnitude. Factors contributing to the magnitude of these errors could once again possibly be attributed to atmospheric disturbances or stray light in the environment. The accuracy is expected to be improved when in the CT is tested in space.

6.6.4 CubeStar Model

Fig. 6.50 illustrates the conversion of a star's projected 2-dimensional centroid coordinates in the image plane (not pixel coordinates) to 3-dimensional camera coordinates. Coordinates for a star centroid on the 2-dimensional image plane can be represented as (x_i, y_i) in mm, where (x_{i0}, y_{i0}) represent the coordinates for where the camera BS passes through the centre of the image plane. The distance coordinates from the camera boresight centre point to the star centroid on the image plane is given as $(\Delta x_i, \Delta y_i) = (x_i - x_{i0}, y_i - y_{i0})$.

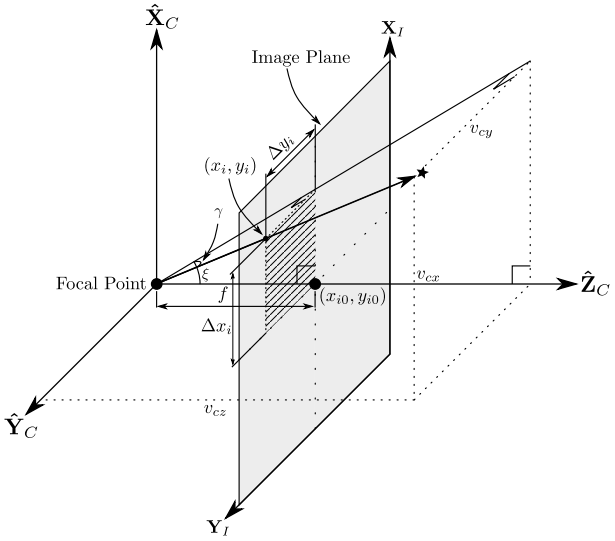

Figure 6.50: CubeStar Projection

In the simulation, three different star distance coordinates were given and were unchanged relative to the image plane frame in order to represent the CT being able to match at least three different stars. These coordinates were then used together with the focal length, f, to calculate the camera body three-dimensional unit vector coordinates, (v_{cx}, v_{cy}, v_{cz}). First the angle ξ was calculated with

$$\xi = \arctan\left(\frac{\Delta x_i}{f}\right), \tag{6.30}$$

where the angle γ was next calculated with

$$\gamma = \arctan\left(\frac{\Delta y_i \cdot \cos\xi}{f}\right). \tag{6.31}$$

Finally, the star unit vector body coordinates were calculated using

$$\hat{\mathbf{v}}_C = \begin{bmatrix} v_{cx} \\ v_{cy} \\ v_{cz} \end{bmatrix} = \begin{bmatrix} \sin\xi \cdot \cos\gamma \\ \sin\gamma \\ \cos\xi \cdot \cos\gamma \end{bmatrix} \tag{6.32}$$

Both reference star vectors and a measurement star vectors were calculated in the simulation. The measurement vector components had a Gaussian distributed noise added to the image plane distance coordinates to represent errors in centroid calculation after the reference vector is initially calculated with the noise-free coordinates. It was decided to orient the CT at 45° between the -Z_B and +Y_B axes, and so, both the reference and measurement star vectors were transformed to the SBC frame by rotating about the CT's $\hat{\mathbf{X}}_C$-axis with

$$\hat{\mathbf{v}}_B = \begin{bmatrix} v_{bx} \\ v_{by} \\ v_{bz} \end{bmatrix} = \begin{bmatrix} 1 & 0 & 0 \\ 0 & -\cos(45°) & \sin(45°) \\ 0 & -\sin(45°) & -\cos(45°) \end{bmatrix} \begin{bmatrix} v_{cx} \\ v_{cy} \\ v_{cz} \end{bmatrix}. \tag{6.33}$$

The final step was to observe if the measurements are valid in the surrounding space environment. First, the CT BS vector was converted from the SBC frame to the ORC frame using the DCM. The angles between the BS and the Sun and the Earth were then calculated in order to see if the stars were actually visible and that the measurements were valid. If the satellite is in eclipse, then the angle between the BS and nadir must be larger than the sum of the Earth disk radius and half of the camera's FOV (set at a worst case of 30°). If the satellite is not in eclipse, then the angle between the Sun and the BS must be greater than half the FOV chosen as 39°. Additionally, the angle between nadir and the BS was chosen to be 10° larger than the Earth disk radius to account for Earth albedo from the local horizon.

Next, the simulation implemented the worst-case lost-in-space mode angular rate requirements, which ensured that no detections would be made at inertially referenced body angular rates higher than $0.3\,°\,s^{-1}$. The effect of this, combined with the effect of stray light entering the CT's FOV was tested by commanding the simulated CubeSat into a target tracking mode and attempting to track a location on Earth as it passed overhead. The results of this can be seen in fig. 6.51c, where it is clear that the CT is not able to make valid detections at high pitching angles and slew rates. In reality, the CT will likely be in a tracking mode when performing target tracking manoeuvres, and will instead be able to make valid detentions at angular rates less than $1\,°\,s^{-1}$. This is accounted for in the simulations conducted in chapter 7.

Finally, a random number generator was run to generate numbers between 0 and 1, where if the number generated was greater than 0.9971 then the measurements were considered invalid. This represented the probability of the CT matching three or more stars 99.71 % of the time.

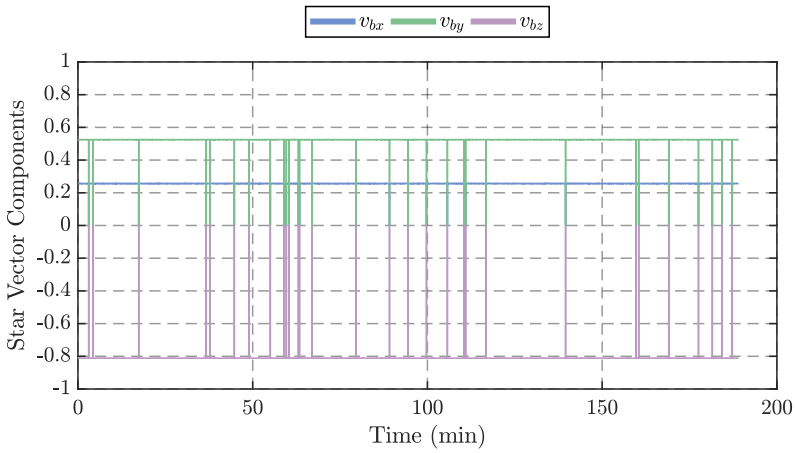

(a) Star Vector Components

Figure 6.51: CubeStar Star Tracking Components and Errors

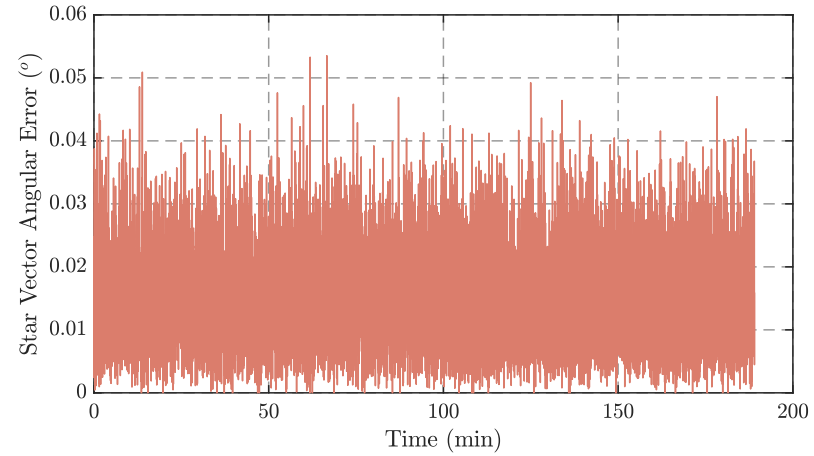

(b) Star Vector Angular Error

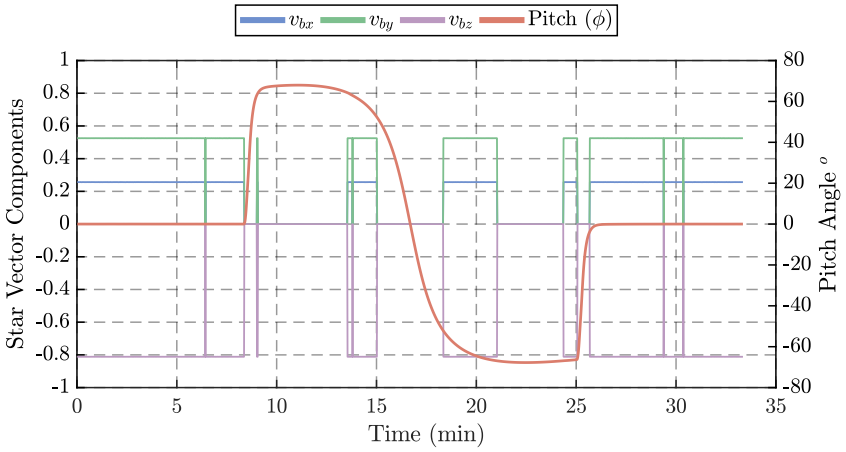

(c) Star Vector Components While Pitching

Figure 6.51: CubeStar Star Tracking Components and Errors

Fig. 6.51 shows the modelled CT vector components and errors for one of the matched stars in the simulation. Fig. 6.51a shows how there is no match for three of the stars for 0.29 % of the time, where fig. 6.51c shows how the change in pitch effects the CT measurement errors caused by a contribution of both the Earth albedo coming close to the CT baffle and the increase in the satellite's angular rates. Fig. 6.51b shows the angular errors between the measured star vector for one matched star and its reference star vector during the simulation where a 1σ error of 1.6 µm in the calculated x and y coordinates for the star centroid was found to produce a similar RMS angular error of 0.017° with 63.17 % of the errors being below this RMS value.

6.7 CubeWheels

The CWs are fundamental to achieving a high IPA in EO satellite missions. In addition to enabling a complete 3-axis control, the CWs absorb external environmental disturbances in space and assist to hold the satellite stable through its orbit. The CW comprises of a 2610 series brushless DC (BLDC) micromotor developed by Faulhaber [87] and a rotating flywheel which can be controlled to follow either a reference torque or a reference speed command.

The CW speed can be measured by two separate independent sensors, namely: a primary magnetic encoder with a resolution of 0.5 RPM and secondary Hall sensor with a resolution of 10 RPM for redundancy. The primary encoder has an adjustable update rate from 1 Hz to 10 Hz where the secondary sensor has a maximum update rate of 1 Hz. The control algorithm can use either speed measurements

for feedback, however, the primary sensor is the default.

Table 6.5 is adapted from [55] and shows the typical sizes of CWs which should typically be used on a CubeSat with a specific size.

Table 6.5: Typical CubeWheel to CubeSat Size Matching

	CubeSat Size						
CubeWheel Size	**2U**	**3U**	**4U**	**6U**	**8U**	**12U**	**Larger**
Small and Small+	X	X	X	-	-	-	-
Medium	-	-	X	X	X	-	-
Large	-	-	-	-	X	X	X

6.7.1 CubeWheel Analysis

An analysis was conducted on a medium-sized CW to measure its performance in relation to its ability to track a broad spectrum of different reference speeds. It is of particular interest to observe how accurately the CW is able to track slower reference speeds as the wheels will be primarily operating at slower rates during the majority of a satellite's orbit.

Table 6.6: Stated CubeWheel 3σ Error

	CubeWheel Size			
Reference Speed (RPM)	**Small**	**Small+**	**Medium**	**Large**
50	±5	±5	±2	±2
500	±2.5	±2.5	±1.5	±1
2000	±3	±3	±1	±1
6000	±3	±3	±0.5	±2

The CWs are controlled by a custom logic PID controller, the performance of which is worsened when controlling a CW at lower speeds. The data in table 6.6 is adapted from [55] and is the stated speed control 3σ error margins for each of the four CW sizes. Fig. 6.52 plots the measured errors at each commanded speed reference on a log scale, where 27 different data points between (and including) 0.5 RPM to 6000 RPM were collected to gain a good idea of the kind of errors that can be expected at each reference.

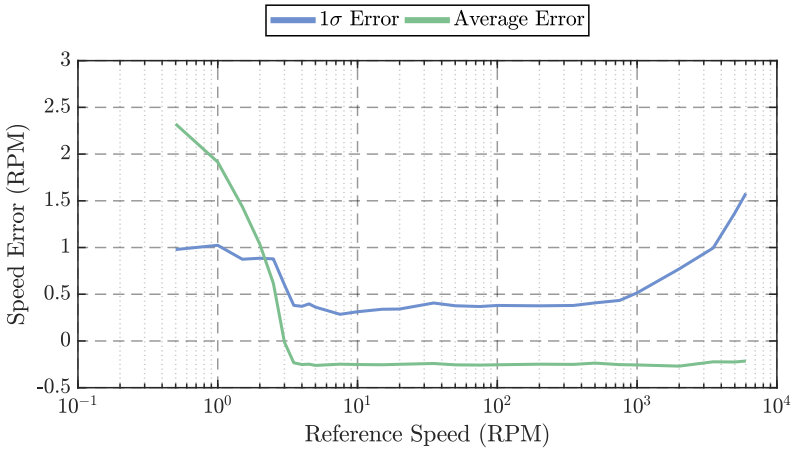

Figure 6.52: CubeWheel Medium Reference Speed Tracking Errors

For reference speeds lower than 3 RPM, the CW controller struggles to maintain a constant speed. The measured output is found to vary considerably, and to have an average speed which is always greater than the actual reference. Once the reference speeds increase past 3 RPM, the errors reduce rapidly with an average 1σ error below 0.5 RPM which only begins to increase again after 1000 RPM. Additionally,

the average speed outputs are consistently measured to be 0.25 RPM below the reference – all the way up to 6000 RPM. Discrepancies between the stated expected errors and the measured errors (especially at 6000 RPM) may be attributed to testing a wheel which is not brand new and which has been experimented on multiple times in various laboratories.

The last step in the analysis was to measure the expected torque outputs of the medium CW in order to determine a suitable torque saturation point to consider in the simulated model. Two different derivations of torque were calculated in this analysis where the first was to measure the motor torque, N_{motor}, from the measured motor current, I_m, by

$$N_{motor} = k_m \cdot I_m, \tag{6.34}$$

where k_m is the motor torque constant for the motor driving the wheel obtained from [87]. The second torque derivation was to determine the wheel torque, N_{wheel}, by calculating the discrete derivative of the measured angular momentum of the CW, h_{wheel}, with

$$N_{wheel} = \frac{\Delta h_{wheel}}{\Delta t_{wheel}}, \tag{6.35}$$

where

$$h_{wheel} = J_{wheel} \cdot \omega_{wheel}, \tag{6.36}$$

with J_{wheel} and ω_{wheel} being the medium CW's moment of inertia (obtained from sec. 3.7) and angular speed of rotation in $\mathrm{rad\,s^{-1}}$ respectively.

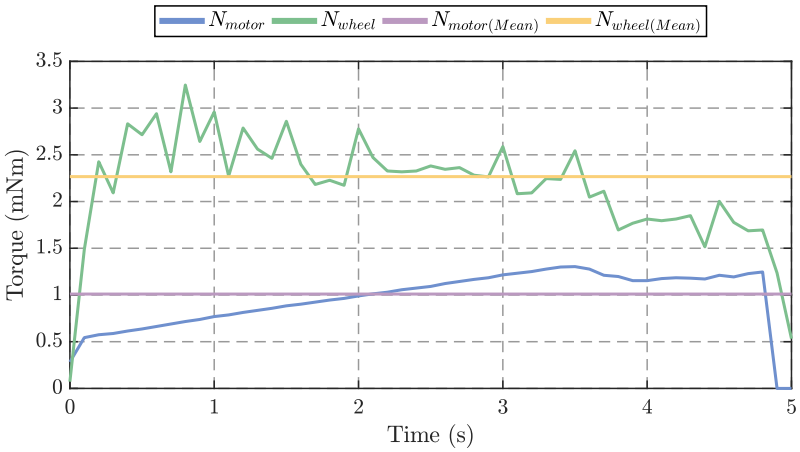

Figure 6.53: CubeWheel Medium Maximum Torques

To measure the maximum possible torque output, a constant torque PWM reference with a 100 % duty-cycle was commanded to the CW until the wheel speed reached its maximum rotation rate of 6000 RPM – the results of which are shown in fig. 6.53. The measured change in the CW's angular momentum is shown to be considerably higher than the measured motor torque where the average maximum wheel and motor torques over full commanded torque period were calculated as 2.267 mN m and 1.01 mN m respectively, where the latter more closely resembles the stated maximum CW medium torque. Eq. (6.34) assumes the motor current measurement is calibrated correctly, which could explain the difference seen between motor torque and wheel torque.

6.7.2 CubeWheel Model

The CW open-loop step response for a BLDC motor plant is typically a first-order response and is thus chosen to be modelled with the continuous transfer function

$$G(s) = \frac{\tau_m}{(s + \frac{1}{\tau_m})}, \tag{6.37}$$

where $\tau_m = 69\,\text{ms}$, is the BLDC motor's mechanical time constant acquired from [87].

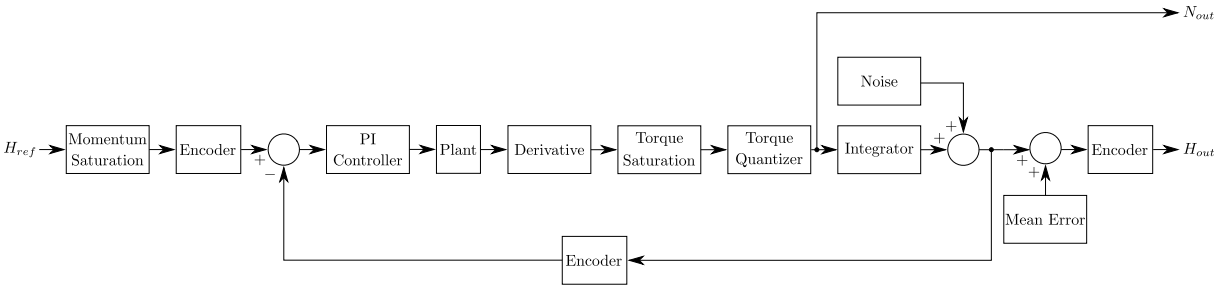

Figure 6.54: CubeWheel Model Control Loop

Fig. 6.54 illustrates the modelled CW control loop where the plant is discretised and transformed to the Z-domain using the minimum CW sample time of 0.1 s. It was decided to control the plant using a discrete-time PI (Proportional and Integrator) controller as this proved to be the closest match to the tested medium CW response. To acquire the expected torque output for the CW, the derivative of the angular momentum from the plant output was obtained and further passed through a saturation block which limits the maximum possible torque that can be delivered as well as through a quantizer which represents the minimum control torque increments which can be commanded by the CW controller.

The resultant torque was then integrated, where a measurement noise was further added to the output signal and fed back to complete the control loop. Additionally, the input angular momentum reference was fed through a saturation block to represent the CW maximum rotation speed limit, where the output angular momentum had a mean error added to it in order to match the CW average errors seen in fig. 6.52. Finally, the encoder blocks represent the rotation speed magnetic encoder which has a resolution of 0.5 RPM.

The angular momentum and torque saturation limits as well as the encoder and quantizer parameters were calculated with the CW parameters in table 6.6 and were adjusted based on the CW size required for a specific CubeSat size in the simulation. Fig. 6.55 plots the resultant modelled error for a medium CW at different commanded rotation speeds and is shown to closely match the results in fig. 6.52.

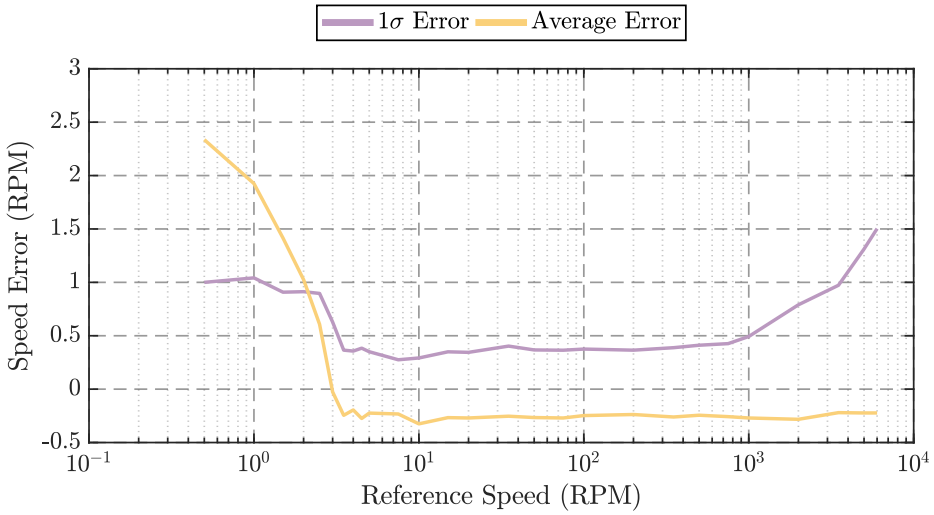

Figure 6.55: CubeWheel Model Errors

The modelled mean and 1σ errors were referenced against the measured reference rotation speed from two spline-fitted lookup tables based on the results from fig. 6.52. The errors were modelled to be correlated

low frequency noise proportional to the referenced lookup table value at wheel speeds lower than 8 RPM – as was observed from the actual CW output. At higher wheel speeds, the errors were modelled as Gaussian noise with a standard deviation equal to that from the referenced lookup table value.

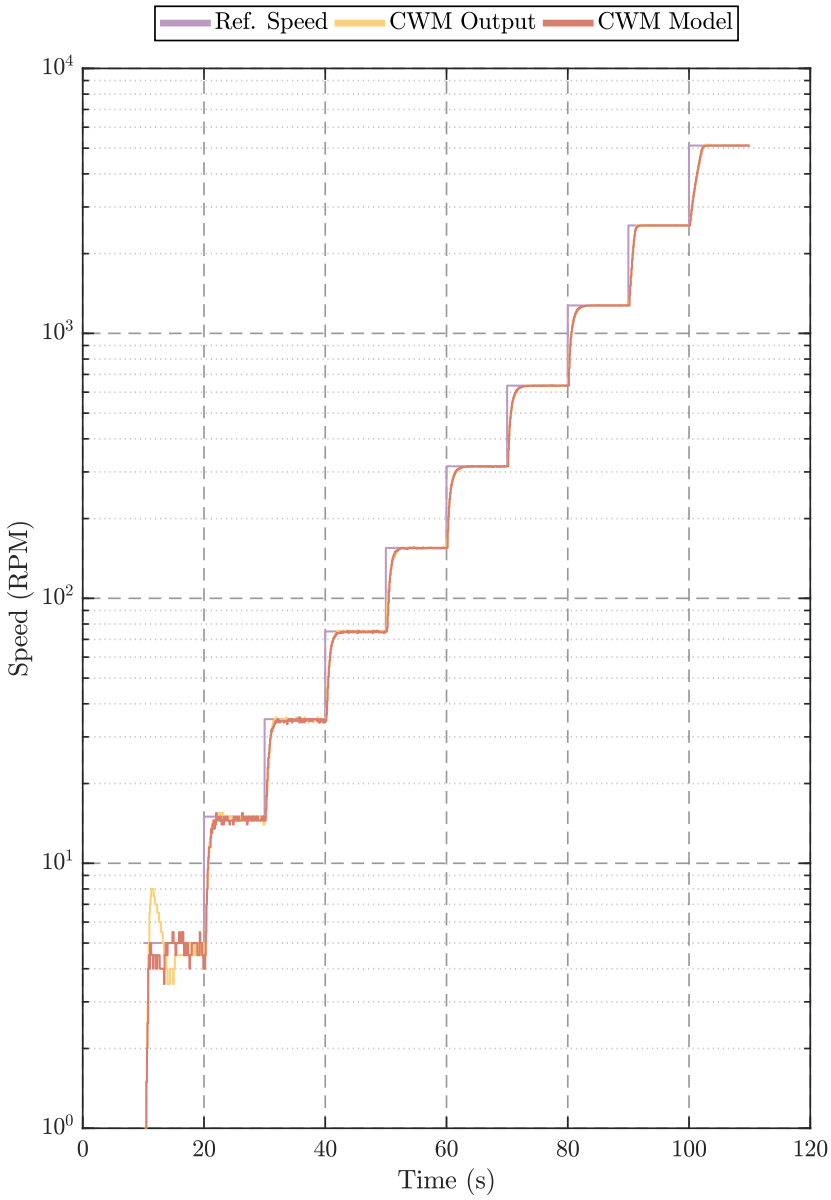

Figure 6.56: CubeWheel Model Step Responses

Whilst testing the medium CW, it was observed that the closed-loop step responses were different for alternating increments in speed references. To match this response as closely as possible, the PI controller was modelled with varying PI gains for different increments in speed references ($\Delta\omega$). An experiment was conducted which doubled the change in the speed reference ($\Delta\omega$) every 10 s starting at 5 RPM and ending at 2560 RPM in order to find the best PI gains to match the real CW's response.

Table 6.7: Modelled CubeWheel PI Controller Gains

	$\Delta\omega$ (RPM)		
Gain	**≤ 100**	**≤ 1100**	**> 1100**
P	0.05	0.2	0.5
I	1.3	1.4	3.0

The resulting PI gains chosen can be seen in table 6.7, where $\Delta\omega$ is given in RPM. Fig. 6.56 shows the final results implementing the chosen PI controller gains, where the model was found to closely resemble

the real CW exhibiting approximately equal 2% settling times for each step increment.

The final implementation of the CW model was tested in the main project simulation over ten orbits. The satellite sensors were set to have no noise, however, the external disturbances were set to be active. As described in the beginning of this chapter, the simulated CubeSat is 3U and thus uses small CWs on all three of its body axes – where the wheel parameters were adjusted accordingly. In this particular experiment, the momentum dumping controller was chosen to be permanently off.

The results of the CWs tracking the simulated angular momentum references is shown in fig. 6.57 (converted to an equivalent small CW speed), where the speed is shown to increase as time progresses due to angular momentum build-up.

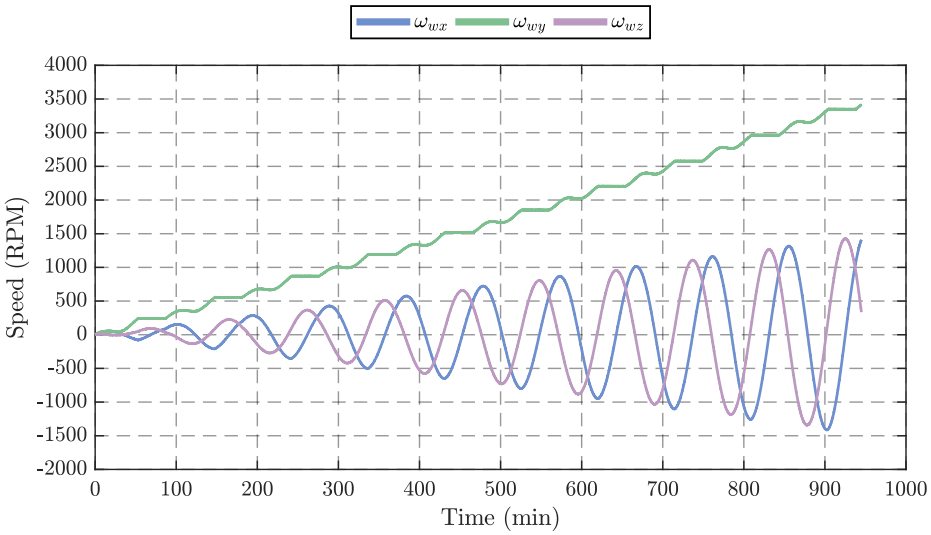

Figure 6.57: CubeWheel Model In-Orbit Simulation

The wheel dynamics models proved to accurately track the desired reference angular momentum. Fig. 6.58 shows the error between the modelled CW's tracking response and the reference wheel speed at the time, where the errors are shown to increase as the associated wheel speeds increase. It is noted that for all three wheels, the wheel speed error begins to increase substantially at approximately the 400 minute mark, where the maximum magnitudes of all three wheel speeds' are greater than 500 RPM after this point.

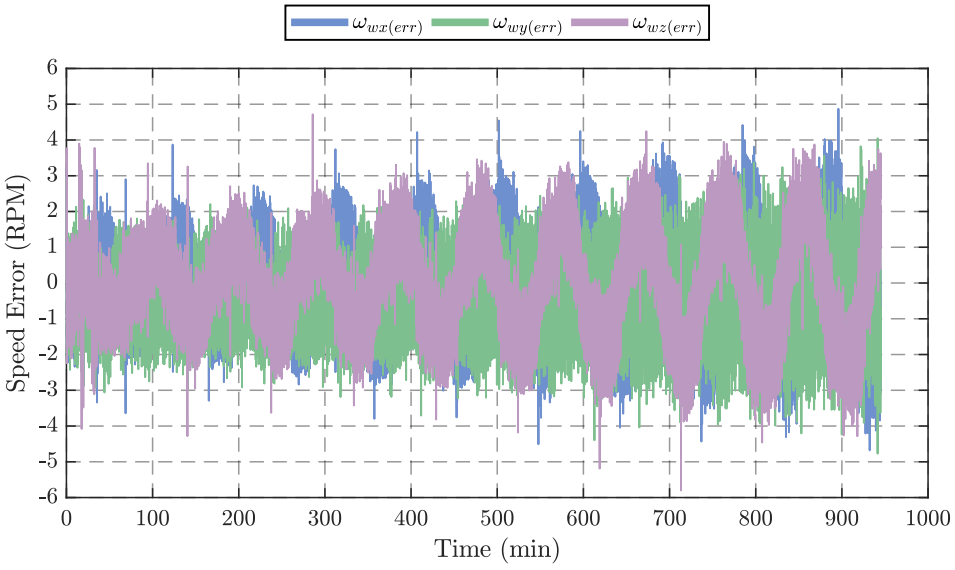

Figure 6.58: CubeWheel Model In-Orbit Simulation Errors

The x, y and z wheels each have an RMS error of 1.339 RPM, 0.987 RPM and 1.312 RPM respectively. The x and z wheels show similar errors as they are following similar sinusoidal angular momentum patterns, where the y wheel is increasing in speed almost linearly with time. Although the y wheel is spinning much faster than the x and z wheels, the larger errors exhibited by the latter two wheels can be more closely attributed to the wheel controllers lagging behind the reference speeds as they track the nearly sinusoidal references.

6.8 CubeTorquers

The CubeTorquers aboard a 3-axis stable CubeADCS do not contribute towards a high IPA. They are instead intended to be used to perform angular momentum dumping as reaction wheels have a limited angular momentum storage capacity and consume more power when operating at higher rates. The benefits to using magnetorquers are that they are low in cost, they have no mechanical parts which wear out, and they do not consume large amounts of power.

Each CubeRod size as well as the CubeCoil have their own respective maximum magnetic moment seen in table 3.2. By applying a PWM signal to pulse the required magnetorquer on and off for longer and shorter periods of time, the required magnetic moment can be generated which then interacts with Earth's magnetic field to generate magnetic torques which work to reduce the angular momentum build-up in the CWs.

For the remainder of this project, where IPA is of the utmost importance, it was decided to only activate the momentum dumping magnetic controller during the satellite's eclipse period in a stable nadir pointing attitude, when no target tracking imaging is occurs. Fig. 6.59 shows the CubeTorquers working to dump the CWs angular momentum during the satellite's eclipse period and its effect on the CW speed. Comparatively, fig. 6.57 shows the resultant wheel speeds where no momentum dumping is implemented.

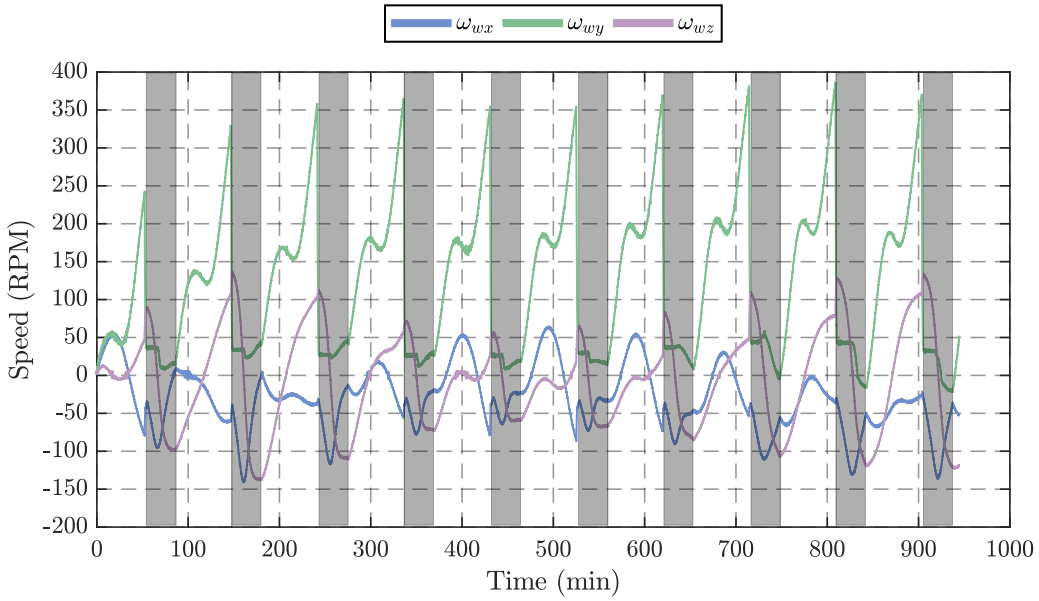

Figure 6.59: CubeTorquer Momentum Dumping

6.9 Summary

This chapter investigated the sensors and actuators implemented by the fully integrated CubeADCS with 3-axis stability. Additionally, the equivalent simulation models were designed to exhibit the expected errors in the measured outputs of each component. The error models were chosen to represent a worst-case scenario in order to show that the true IPA measured in chapter 7 is also the maximum IPA error

which could be expected for a CubeSat in LEO.

Primary focus was placed on the sensors and actuators contributing to a high IPA such as the CS, the MEMS gyros, the CT and the CWs. The magnetometer and CSS were modelled for, nonetheless, due to their outputs being used by the EKF – where their models show errors which closely match the measured outputs. The CubeTorquer errors were not designed for as its only main error is caused by remanence in each magnetorquer causing a magnetic torque disturbance which is so low that it is dwarfed by the aerodynamic and solar panel induced magnetic torque disturbances.

In-orbit data was found to be extremely valuable when determining a component's expected accuracy in space. This is seen in both secs. 6.2 and 6.4 which showed the magnetometer errors after calibration as well as the errors caused by temperature variations during a satellites orbit on both the magnetometer EKF estimates and the MEMS gyro rate outputs.

The MEMS gyro was found to exhibit the largest range of errors. The main improvement which could be made to reducing these errors would be to calibrate the gyros in a highly accurate temperature chamber with a rate table built in. This would drastically reduce the effects of temperature on the gyro outputs. Additionally, averaging a larger number of gyro samples per second would further minimise the high frequency error components measured. The modelled MEMS gyros are shown to closely mimic the characteristics measured from the true outputs, especially with regards to the effects of temperature on the bias.

The FSS and CT errors were found to resemble the stated accuracy closely, where the models implemented could replicate this. Additionally, accuracies in space are expected to be better than those measured on Earth. The nadir camera was one of the hardest components to analyse due to experimental setup limitations. The measured accuracies were still shown to match those stated for when the full Earth is in the DR. The model shows the increase in errors expected as the Earth moves further and further out of the camera's DR.

Finally, the CW's performance was shown to worsen at lower rotation rates under 3 RPM but to drastically improve when tracking high rotation speeds until friction begins to play a role in the errors after $\approx$ 4000 RPM. The model is very accurate and is able to closely match the 2 % settling times for different increases in speed references. The errors at each rate are also shown to closely resemble those measured in the CW analysis.

This concludes the hardware investigation and modelling portion of this research. With the components behaviours and errors closely resembling that of the CubeADCS components implemented, the further simulation investigations should, to a large degree, indicate the expected IPAs and stabilities for various EO CubeSats in LEOs.

Chapter 7

Simulation Investigations

7.1 Overview

In order to gain a broader understanding of the expected IPA of a CubeSat in LEO, multiple simulation investigations are conducted in this chapter in which several physical and orbital CubeSat parameters were considered. Different simulation scenarios are created by adjusting

1. the size of the CubeSat,
2. the number of solar panels on a CubeSat and their mounting configurations,
3. the nominal orientation of the CubeSat in its orbit,
4. the type of orbit (altitude and inclination),-
5. the type of estimator used to estimate the CubeSat's attitude and angular rates and,
6. the sensor placements on the CubeSat.

Altering these parameters influences the way in which the environmental disturbances will affect the CubeSat as well as the accuracy at which the CubeADCS can estimate and control its attitude. These investigations are conducted to determine the conditions in which the CubeADCS will perform best as well as to identify possible adaptions which could improve the CubeADCS's performance in the future. Additionally, two different satellite pointing methods will be tested, where the first will test the satellites' IPA whilst tracking a constant nadir reference, and the other will test the satellites' target tracking performance.

7.2 CubeSat Configurations and Orbit Considerations

A significant amount of permutations involving different parameter combinations can be explored to develop a multitude of different scenarios. As a result, the selection of these parameters is refined to investigate a modest, but diverse, set of different scenarios likely to be found in typical EO CubeSat missions in which a high IPA is required. The selection of these parameters is discussed in this section.

7.2.1 Size and Mass

By altering a CubeSat's dimensions and mass, one changes the its's MoI and thus, its dynamics, as well as its exposed surface areas which effect disturbance torques. Three separate CubeSat sizes are considered in the simulations that follow, namely: 3U, 6U and 12U. The sizes were selected to be double the previous size in order to gain a diverse understanding of how the CubeADCS performs as it controls different moments of inertias. Additionally, the CubeSat's each require different CubeWheel and CubeTorquer sizes to control the satellite's attitude, which imply different wheel speeds and different momentum dumping strategies and thus, different error dynamics.

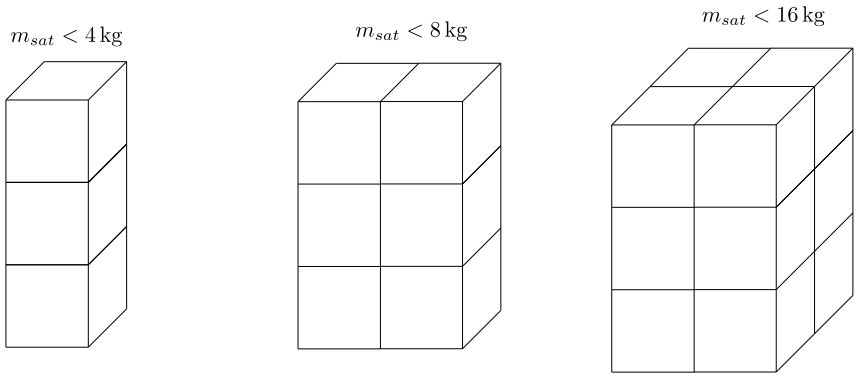

(a) 3U CubeSat **(b)** 6U CubeSat **(c)** 12U CubeSat

Figure 7.1: CubeSat Sizes

7.2.2 Solar Panel Configurations

As described in sec. 5.3.3, the number of solar panels a CubeSat greatly influences its magnetic disturbance torques. Additionally, deployed solar panels create greater aerodynamic disturbance torques and change the CubeSat's dynamics. There are two types of CubeSat solar panel configurations for the 3U and 6U CubeSat sizes: deployed and body-mounted solar panels, DSP and BMSP respectively. The 12U CubeSat size is considered to only have BMSPs.

Figs. C.1 to C.3 in appendix C, illustrate the typical solar panel configurations for each CubeSat type as well as their typical MoIs which are used in the simulations that follow. None of the CubeSat's have solar panels on their +Z and -Z facets, as the Zenith and anti-Zenith sides of the CubeSats are assumed to be used for communications and imager payload purposes respectively. The remaining facets are all covered in solar panels for the BMSP designs.

The DSP 3U and 6U CubeSat body types are chosen to have a pair of deployed 3U and 6U solar panels on either side of their -Y facets respectively, with body-mounted solar panels on the remaining facets – excluding the facets from which the solar panels are deployed.

7.2.3 Long-body Axis Configuration

Fig. 7.2 illustrates the two different CubeSat orientations chosen to be investigated in this chapter which suit typical conventions followed in most CubeSat missions. The two different orientations are defined such that, the long-body axis of the CubeSat is aligned with either the SBC z or x-axis. Implying that when the CubeSat is in its nominal ORC frame aligned orientation, that the long-body axis will either be nadir pointing or in the ram direction. This determines how the environmental disturbances will impact each CubeSat, where the long-body axis configuration also defines the axis with the lowest MoI needed to be controlled.

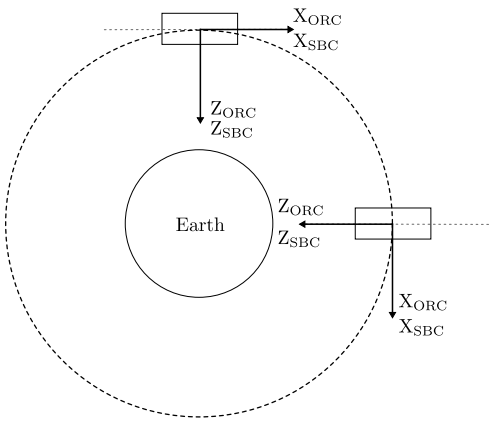

Figure 7.2: CubeSat Orientations for Simulations

7.2.4 Orbit Type and Parameters

The type of orbit a CubeSat is in additionally affects the way in which it interacts with its surrounding environment. Three separate LEO's are considered which align with common CubeSat missions existing at present. A large number of CubeSat's currently orbiting the Earth have been deployed from the ISS and so it is appropriate that one of the orbits to be investigated is the same as that of the ISS. Furthermore, to align with the project scope, two separate SSO's are investigated which exhibit different orbit altitudes and resulting inclinations.

As such, the orbits considered are ±400 km for the ISS orbits, a ±500 km SSO and another SSO with an altitude of ±650 km, where the remaining orbit parameters are summarised in table 7.1. All chosen satellite orbits have additionally been selected to have near perfect circular orbits (i.e. $e \approx 0$). The CubeSat TLE's are chosen to begin at approximately the same date to create equal solar positions for each satellite. The chosen date is set to be at the March equinox where the two SSO's were set to have a RAAN = 30°, in order to create a sun angle to the orbit plane of ≈ 30° – allowing for CubeStar to be placed in an orientation which is unobscured by the Sun.

Table 7.1: Simulation Investigation Orbit Parameters

No.	Type	TLE Epoch	i_{sat}	Ω_{sat}	e_{sat}	ω_{sat}	M_{sat}	n_{sat}
1	ISS	19 079.81	51.64°	75.02°	0.00054	149.95°	210.19°	15.59
2	SSO	19 079.89	97.50°	30.00°	0.00086	202.35°	157.73°	15.24
3	SSO	19 079.67	98.00°	30.00°	0.00081	254.35°	105.69°	14.72

7.2.5 Estimators and Star Tracker Orientation

The type of estimator used has a significant impact on the CubeADCS's ability to estimate and propagate a CubeSats's attitude and body angular rates. The simulated CubeSats all use a full EKF and a full gyro EKF, which both make use of the complete suite of sensors on the CubeADCS (including the CT). Both EKF algorithms have been provided to the author by CubeSpace [52], where the same algorithms adopted by the CubeADCS in its CubeACP software have been modified to suit the format of a MATLAB® S-function, compiled into an executable mex file to be implemented by this author for this investigation.

A high IPA is not possible without the use of a CT and so the only change in sensor placement which is implemented is the orientation at which the CT is mounted on each CubeSat. There are two chosen CT orientations under investigation: 1) the CT is placed with the boresight pointing 45° from the +X facet towards the -Z facet on the CubeSat, and 2) the ST is placed with its boresight pointing in the direction of the -Z facet on the CubeSat. The two different orientations will provide two different scenarios, where the first scenario will ensure that the CubeADCS will always have valid CT measurements and another scenario where the CubeADCS will not have ST measurements for the middle part of the sunlit portion of its orbit, due to the sun being within 30° of its boresight when nadir pointing.

7.3 Maximum Disturbance Torques

The maximum disturbance torques were determined for each simulated CubeSat based on body MoI, solar panel configuration, and orbit types. The maximum disturbance torques account for a worst case scenario when determining the maximum gravity gradient, aerodynamic, and solar panel induced magnetic disturbance torques – regardless of nominal orientation. For example, when calculating the maximum aerodynamic disturbance torques, the cross-sectional area is assumed to be as large as it can be, where in reality, this area will be much smaller.

The maximum gravity gradient torque can be approximated by

$$N_{gg(max)} = \frac{3\mu_{\oplus}}{2R_{sat}^3}|J_{zz} - J_{xx}|\sin 2\theta, \tag{7.1}$$

or

$$N_{gg(max)} = \frac{3\mu_{\oplus}}{2R_{sat}^3}|J_{zz} - J_{yy}|\sin 2\phi, \tag{7.2}$$

where a pitch or roll angle of 45° (whichever produces the larger outcome) would result in the highest possible torque value. The maximum solar panel induced magnetic moment torque can be approximated by

$$N_{sp(max)} = D_{max}B_{max}, \tag{7.3}$$

where B_{max} is the maximum magnitude of the surrounding magnetic field, and D_{max} is the maximum possible magnetic moment that can be produced by the CubeSat face with the largest solar panel array with the Sun pointing directly at the panels – assumed to be 1 mA m^2.

The maximum aerodynamic torque was determined differently, where each simulated CubeSat was instead commanded to assume an attitude that would induce the largest aerodynamic torque disturbances on it, where the maximum magnitude was found over one orbit. In each simulation, the CubeSat is assumed to have its CoM at 2 cm away from the centre of the SBC frame along the negative z-axis, where each CoP is at the geometric centre of each external BMSP or DSP array.

Tables 7.2 to 7.4 summarise the maximum possible disturbance torques which could be experienced by a CubeSat in each type of the three simulated orbits, with each possible size and solar panel configuration. In reality, when the simulated CubeSat's are in their nominal orientations, they will not come close to experiencing these magnitudes of disturbance torques. The summary is, however, a good indicator of the major contributing factors influencing the IPA of the CubeADCS, and outline which conditions will be the most significant for the CubeADCS to overcome.

It is clear from the data, that CubeSats in an ISS orbit will experience the greatest magnitudes of disturbance torques, with aerodynamic torques being the largest possible contributing factor for CubeSats with deployed solar panels. For both SSO's the effect of the aerodynamic torque quickly begins to diminish with rising altitude, where the maximum solar panel induced and gravity gradient torques remain relatively and consistently high. Although the gravity gradient torques appear to be a close contender to the solar panel induced torques, the nominal orientation of the CubeSat's will once again reduce these torques to nearly 0 N m, which leaves the latter as the dominant disturbance source for CubeSats in all three orbits.

Table 7.2: ISS Orbit – Maximum Possible Disturbance Torques

		3U		**6U**		**12U**
Disturbance Torque	**Unit**	**BMSP**	**DSP**	**BMSP**	**DSP**	**BMSP**
$N_{gg(max)}$	nN m	55.68	72.96	103.67	107.52	201.60
$N_{aero(max)}$	nN m	17.95	314.10	35.91	494.97	71.82
$N_{sp(max)}$	nN m	51.73	155.19	103.46	310.38	103.46

Table 7.3: Sun-Synchronous 500 km Orbit – Maximum Possible Disturbance Torques

		3U		**6U**		**12U**
Disturbance Torque	**Unit**	**BMSP**	**DSP**	**BMSP**	**DSP**	**BMSP**
$N_{gg(max)}$	nN m	53.28	69.82	99.22	102.90	192.93
$N_{aero(max)}$	nN m	9.50	183.96	21.03	316.67	42.07
$N_{sp(max)}$	nN m	50.35	151.1	100.7	302.1	100.7

Table 7.4: Sun-Synchronous 650 km Orbit – Maximum Possible Disturbance Torques

		3U		6U		12U
Disturbance Torque	**Unit**	**BMSP**	**DSP**	**BMSP**	**DSP**	**BMSP**
$N_{gg(max)}$	nN m	49.95	65.45	93.00	96.45	180.84
$N_{aero(max)}$	nN m	1.31	23.12	2.64	39.42	5.29
$N_{sp(max)}$	nN m	46.21	138.63	92.42	277.26	92.42

7.4 Initial Attitude Estimation and Control Analysis

The selection of quaternion feedback controller gains is done before the main simulation scenarios that follow are investigated. The feedback gains are calculated using the second order system approximation in sec. 4.4.7, where a damping coefficient $\zeta = 0.707$ is selected for optimal damping of a second order system. A system with too quick of a response (i.e. a short 2% settling time) can lead to instability, especially when controlling low MoI's such as those of CubeSats. The natural frequency, ω_n, of the approximately second order system described in sec. 4.4.7, can be calculated from the desired 2% settling time, $t_{2\%}$, using

$$\omega_n = \frac{4}{\zeta t_{2\%}}, \tag{7.4}$$

where a time of $t_{2\%} = 50\,\text{s}$ was found to produce the most optimal and desired response for all CubeSat types tested in the next section. Substituting in, the calculated $\omega_n = 0.113\,\text{rad}\,\text{s}^{-1}$ into eqs. (4.78) and (4.79) obtains proportional and derivative gains of $K_p = 0.0256$ and $K_d = 0.16$ respectively.

A simulation was conducted using the same 3U CubeSat parameters defined in sec. 5.1, where an attitude reference of RPY = [5° 10° 15°] was commanded to the quaternion feedback controller to test its effectiveness. The command was issued at $t = 500\,\text{s}$ and held there for a further 500 s before being commanded back to the zero reference. The results show that the controller is able to track the commanded references well, exhibiting roll, pitch and yaw root-mean-square errors (RMSE) of 22.87″, 50.84″, and 75.02″ respectively during the steady-state period.

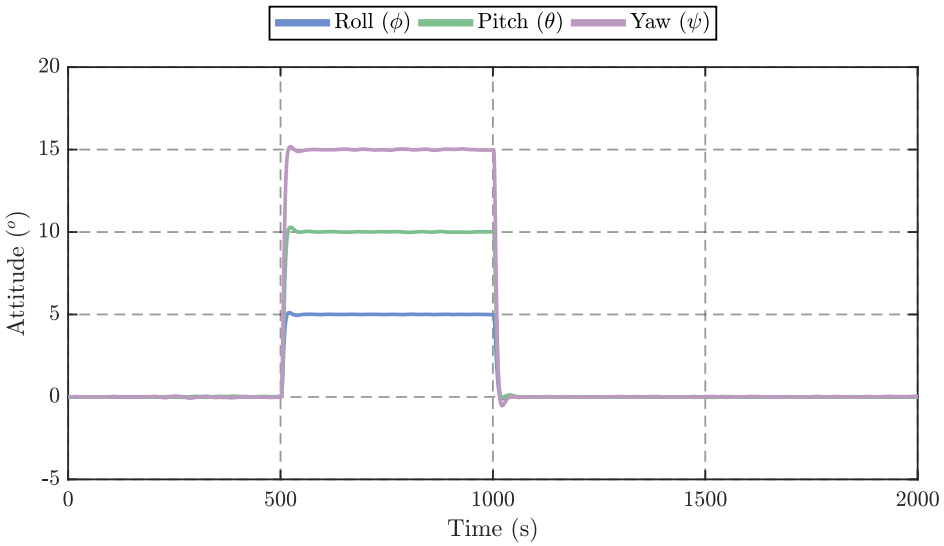

Figure 7.3: Quaternion Feedback Controller reference Tracking

The ADCS uses the full suite EKF in the simulation conducted in this section, which includes CT star tracker measurements. The resultant attitude estimation error can be seen in fig. 7.4, where te largest errors occur during the transient periods where the attitude is approaching its commanded references.

The estimation error for the roll, pitch, and yaw over the same steady-state period is 13.13″, 30.87″, and 43.19″ respectively.

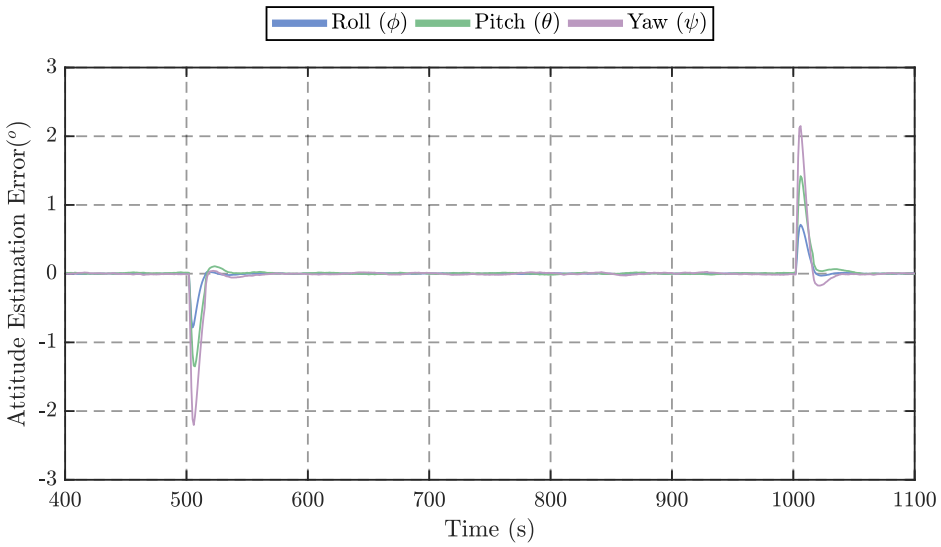

Figure 7.4: Attitude Estimation Error

For the simulations that follow, the imager pointing error (IPE) is defined using only the roll and pitch angles of each CubeSat such that

$$\text{IPE} = \sqrt{\phi_e^2 + \theta_e^2}, \tag{7.5}$$

where ϕ_e and θ_e represent the CubeSat attitude roll and pitch errors respectively. This means that the RMSE of the simulated CubeSat in this section is 55.74″. An error in a satellite's yaw, although not desirable, does not have a significant effect on the overall pointing accuracy, which is why it is not considered when determining the IPA of a CubeSat.

7.5 Simulated CubeADCS Performance – Nadir Tracking

This section conducts the first main set of simulations to determine the IPA of all combinations of CubeSat's defined to have the different properties described throughout sec. 7.2. The simulations will asses their ability to continuously track a commanded zero reference for all roll, pitch and yaw angles, otherwise described as a continuous nadir reference. The results are divided up between each orbit type described in sec. 7.2.4. Within each orbit type, the results of CubeSats with BMSPs are shown separately from those with DSPs, where the key, "{*Long-body Axis*}{*Size*}", distinguishes between the size of the CubeSat and the alignment of its long-body axis in the SBC frame. For example, the key "X3U" describes a 3U CubeSat with it's long-body axis lying along the SBC x-axis.

Furthermore, the attitude estimator configurations are categorised to be either a full EKF (FEKF) or a gyro EKF (GEKF), which both use the full suite of CubeADCS sensors and actuators (excluding the gyro's in the FEKF implementation). Each estimator is tested with the first CT orientation canted 45° where no sunlight enters its FOV, and in the second orientation with the CT pointing zenith, where sunlight enters the FOV for a portion of each orbit. The GEKF is further tested by measuring its performance when the on-board gyro's either do or do not have temperature compensation calibrated for. All errors are given in terms of an RMS value to include the effect of any mean pointing error, as opposed to a 1σ value which represents a deviation about a mean error.

First, the results pertaining to each orbit are shown in the subsections that follow, where the best and worst performing CubeSat scenarios will be briefly pointed out and discussed. An overview of the data is then presented at the end of this section, which elaborates on the results in greater detail.

7.5.1 ISS Orbit

The first orbit tested is the ISS orbit. The external disturbances at this altitude are expected to be considerably higher than those experienced by CubeSats in the selected SSOs, resulting in an expectedly poorer performance of the CubeADCS. Figs. 7.5 and 7.6 show the RMS IPE of the simulated CubeADCS for CubeSats with BMSPs and DSPs respectively, where the actual values of the calculated errors are shown in tables 7.5 and 7.6.

Table 7.5: RMS IPE Data of CubeSats with BMSPs in an ISS Orbit

Estimator Properties	X3U	Z3U	X6U	Z6U	X12U	Z12U
FEKF CT Canted	0.0648°	0.0364°	0.0175°	0.0144°	0.0102°	0.0100°
FEKF CT Zenith	2.078°	0.188°	0.371°	0.170°	0.0822°	0.0516°
Compensated GEKF CT Canted	0.0687°	0.0631°	0.0626°	0.0608°	0.0643°	0.0614°
Compensated GEKF CT Zenith	0.187°	0.149°	0.289°	0.196°	0.270°	0.150°
Uncompensated GEKF CT Canted	0.119°	0.120°	0.120°	0.125°	0.122°	0.129°

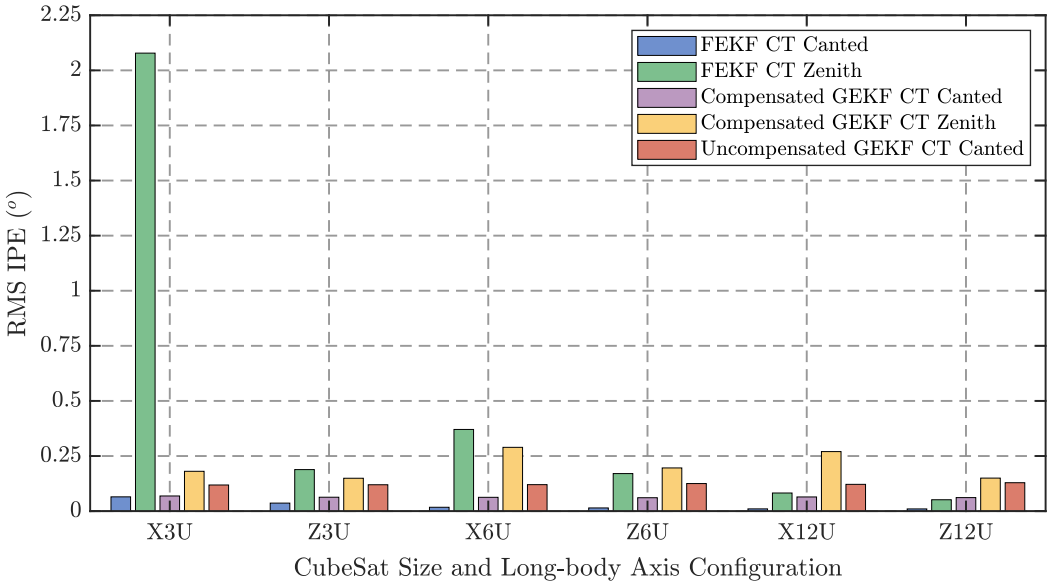

Figure 7.5: RMS IPE of CubeSats with BMSPs in an ISS Orbit

It can be seen from the data, that the worst performing CubeSat is the X3U CubeSat with BMSPs, utilising an FEKF with its CT pointing zenith, which exhibits an RMS IPE far greater than all the other simulated CubeSats. The X3U CubeSat with DSPs in the same scenario appears to perform slightly better, which is likely because of the increased MoI about the long-body axis being easier to control, despite the larger disturbance torques experienced. The best performing CubeSats are the X12U and the Z12U CubeSats, whose IPE is better represented in terms of arcseconds as having an RMS value of 36″. In general, the CubeSats with their long-body axis aligned with their SBC x-axis, show a larger IPE than their long-body z-axis aligned counterparts. This is likely due to it being harder to control the smaller MoIs about the CubeSats' roll axes. The effect of this for CubeSats in ISS orbits is then worsened by the more extreme external disturbance torques experienced at such a low altitude.

Table 7.6: RMS IPE Data of CubeSats with DSPs in an ISS Orbit

Estimator Properties	X3U	Z3U	X6U	Z6U
FEKF CT Canted	0.0712°	0.0413°	0.0213°	0.0197°
FEKF CT Zenith	1.542°	0.494°	0.739°	0.513°
Compensated GEKF CT Canted	0.0691°	0.0612°	0.0632°	0.0600°
Compensated GEKF CT Zenith	0.212°	0.174°	0.210°	0.150°
Uncompensated GEKF CT Canted	0.124°	0.123°	0.121°	0.125°

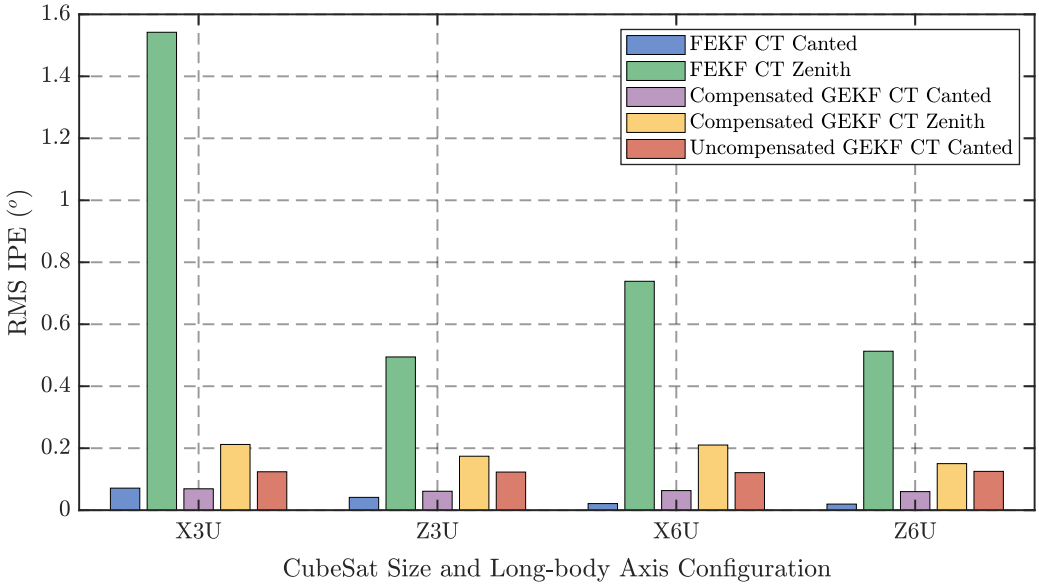

Figure 7.6: RMS IPE of CubeSats with DSPs in an ISS Orbit

7.5.2 SSO Orbit at 500 km

The next orbit tested is a 500 km SSO and is more aligned with the project scope. The external disturbances are expected to be weaker at this altitude than that of the ISS orbit, especially with regards to the aerodynamic disturbance torques experienced. The effect of the solar panel induced disturbance torque still remains relatively large and is the dominant disturbance in the simulations that follow. The measured IPEs are illustrated and tabulated in figs. 7.7 and 7.8 and tables 7.7 and 7.8 respectively.

Table 7.7: RMS IPE Data of CubeSats with BMSPs in an SSO 500 km Orbit

Estimator Properties	X3U	Z3U	X6U	Z6U	X12U	Z12U
FEKF CT Canted	0.0619°	0.0125°	0.0195°	0.0120°	0.0103°	0.009 56°
FEKF CT Zenith	1.051°	0.284°	0.192°	0.124°	0.0558°	0.0587°
Compensated GEKF CT Canted	0.0668°	0.0655°	0.0580°	0.0637°	0.0613°	0.0612°
Compensated GEKF CT Zenith	0.210°	0.253°	0.212°	0.270°	0.293°	0.247°
Uncompensated GEKF CT Canted	0.112°	0.123°	0.123°	0.126°	0.122°	0.123°

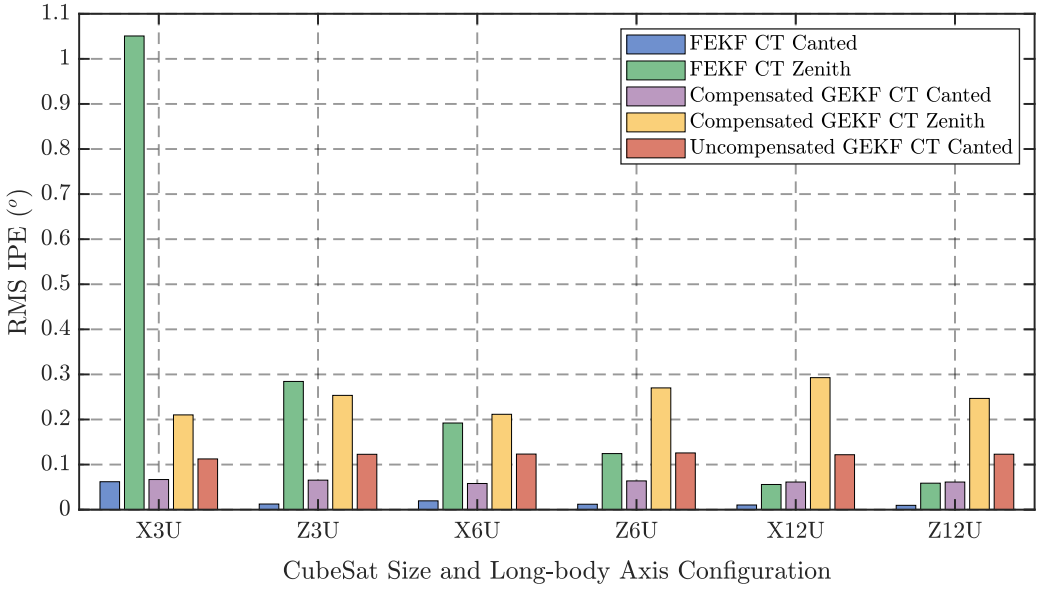

Figure 7.7: RMS IPE of CubeSats with BMSPs in an SSO 500 km Orbit

The Z12U CubeSat using an FEKF with continuous CT measurements remains the best performing

CubeSat with an RMS error of nearly 34″. As is expected, the X3U CubeSat with the zenith pointing CT and BMSPs performs the worst, but is still twice as good as the same CubeSat in an ISS orbit, due to the lower disturbance torques experienced. The performance of the Z3U CubeSat with DSPs using an FEKF with a zenith pointing CT is worse than expected, with an error that is actually greater than the same CubeSat in the ISS orbit – despite the smaller disturbance torques. After examining the data, however, it appears that the CubeADCS in the ISS orbit was able to receive CT measurements for a longer period during the sunlit portion of the orbit than the same CubeSat in this SSO. This explains why it would have a poorer performance, nearly equal to that of its X3U fitted with DSPs counterpart.

Table 7.8: RMS IPE Data of CubeSats with DSPs in an SSO 500 km Orbit

Estimator Properties	X3U	Z3U	X6U	Z6U
FEKF CT Canted	0.0418°	0.0236°	0.0209°	0.0181°
FEKF CT Zenith	0.786°	0.735°	0.280°	0.209°
Compensated GEKF CT Canted	0.0620°	0.0599°	0.0600°	0.0594°
Compensated GEKF CT Zenith	0.178°	0.253°	0.224°	0.192°
Uncompensated GEKF CT Canted	0.115°	0.122°	0.120°	0.120°

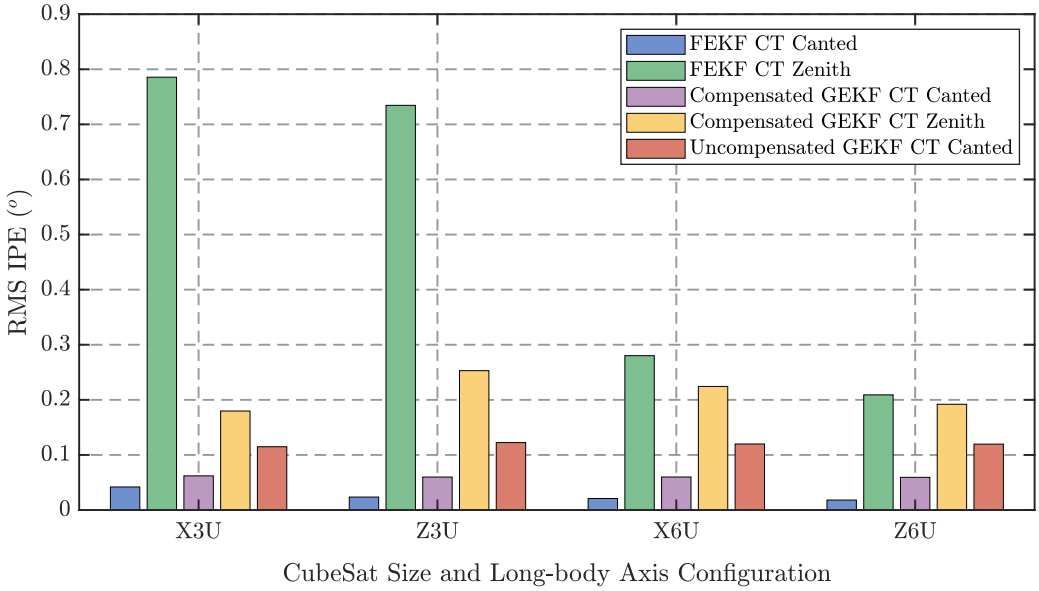

Figure 7.8: RMS IPE of CubeSats with DSPs in an SSO 500 km Orbit

7.5.3 SSO Orbit at 650 km

The final orbit tested is a 650 km SSO. The aerodynamic disturbance torques at this altitude as dwarfed by the solar panel induced magnetic disturbance torques. The performances of each CubeSat in their respective categories are expected to be the best performances seen in all three orbits. The measured IPEs are similarly illustrated and tabulated in figs. 7.9 and 7.10 and tables 7.9 and 7.10 respectively.

Table 7.9: RMS IPE Data of CubeSats with BMSPs in an SSO 650 km Orbit

Estimator Properties	X3U	Z3U	X6U	Z6U	X12U	Z12U
FEKF CT Canted	0.0595°	0.0128°	0.0180°	0.0121°	0.009 62°	0.008 88°
FEKF CT Zenith	0.956°	0.304°	0.185°	0.147°	0.0541°	0.0558°
Compensated GEKF CT Canted	0.0667°	0.0578°	0.0625°	0.0639°	0.0642°	0.0636°
Compensated GEKF CT Zenith	0.243°	0.199°	0.174°	0.251°	0.248°	0.347°
Uncompensated GEKF CT Canted	0.103°	0.119°	0.113°	0.116°	0.116°	0.118°

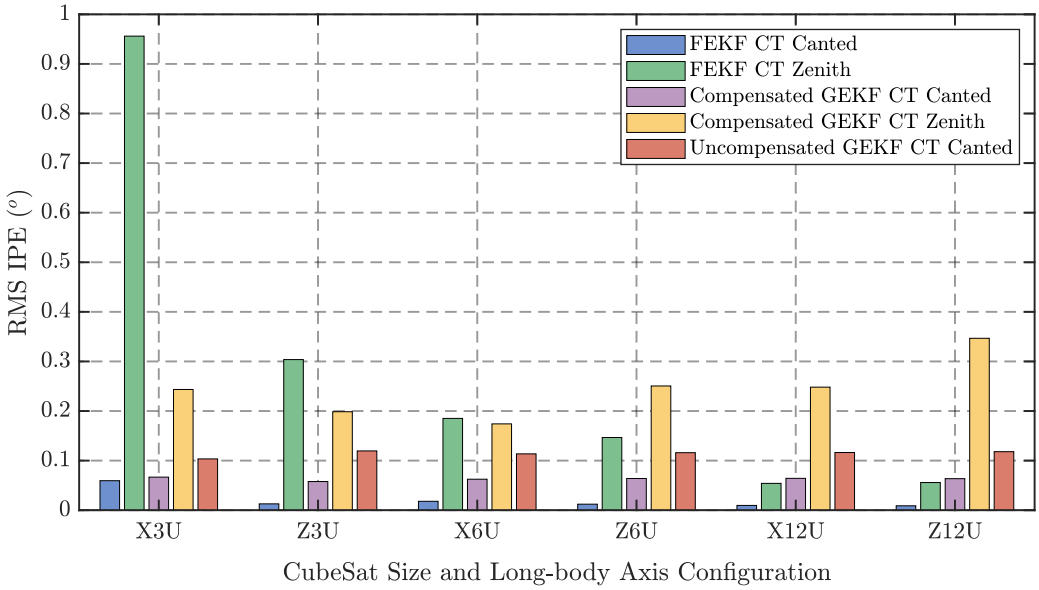

Figure 7.9: RMS IPE of CubeSats with BMSPs in an SSO 650 km Orbit

As expected, the Z12U CubeSat using an FEKF with continuous CT measurements outperforms all other CubeSats tested throughout these simulations. The CubeADCS was able to track a nadir reference with the Z12U satellite with an error of less than 32″. The same X3U CubeSat with a zenith pointing CT and BMSPs continues to show the worst performance, despite it having the lowest error in its own category throughout all three orbits. Its error is only slightly lower than the error seen in the 500 km SSO, which suggests that the main cause of the poor performance is a combination of solar panel induced magnetic disturbance torques acting on an axis with a tiny principle MoI.

Table 7.10: RMS IPE Data of CubeSats with DSPs in an SSO 650 km Orbit

Estimator Properties	**X3U**	**Z3U**	**X6U**	**Z6U**
FEKF CT Canted	0.0421°	0.0184°	0.0206°	0.0165°
FEKF CT Zenith	0.686°	0.365°	0.287°	0.226°
Compensated GEKF CT Canted	0.0693°	0.0582°	0.0563°	0.0689°
Compensated GEKF CT Zenith	0.249°	0.269°	0.223°	0.314°
Uncompensated GEKF CT Canted	0.111°	0.116°	0.114°	0.115°

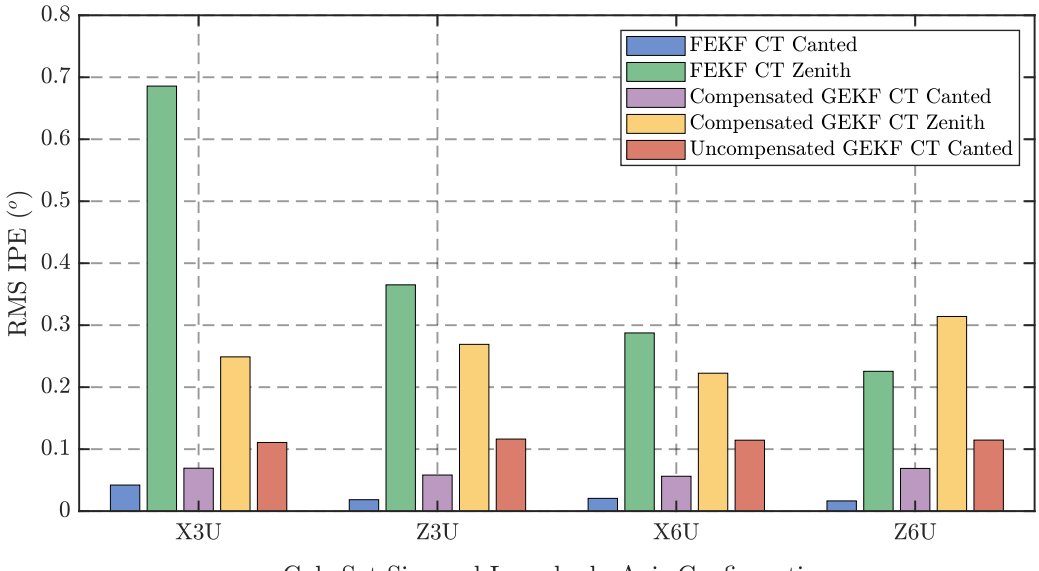

Figure 7.10: RMS IPE of CubeSats with BMSPs in an SSO 650 km Orbit

7.5.4 Overview of the CubeADCS's Nadir Tracking Performance

The first observation made, is that the IPA of a CubeSat in LEO generally improves as its altitude increases. Additionally, it is clear from the data represented that the FEKF performs most poorly when CT star tracker data is not available. In each key group, the performances of CubeSat's with their long-body axis aligned on the SBC z-axis is better than those with their long-body axis aligned on the SBC x-axis. This is attributed to the CubeADCS needing to control a much smaller MoI when attempting to control the CubeSats roll orientations. Each GEKF in its own category has the same consistent performance throughout each CubeSat size and long-body axis alignment, regardless of small MoIs or solar panel configuration. This is due to the fact that the CubeSat angular rates do not need to be estimated by the EKF as they are directly obtained from the gyros.

The main poor performing outliers for both types of solar panel configurations are for CubeSats utilising the FEKF with zenith pointing CTs. The absence of data from the star tracker makes it more difficult to reject the external disturbance torques. The effect is only worsened for CubeSats with the lowest MoIs, where it can be seen that for 12U CubeSats, that an absence of star tracker measurements has the lowest relative impact on its IPA due to its greater size. The CubeSats affected the most by the FEKF with a zenith pointing CT are the 3U CubeSats with their long-body axes aligned with their SBC x axes.

All Z3U CubeSats with DSPs actually perform better than the 3U CubeSats with BMSPs despite being more susceptible to external disturbance torques. This is likely due to the larger MoI along their long-body axes of CubeSats with DSPs, making it slightly easier to control despite larger disturbance torques. This is not the case with the remaining CubeSat categories, however, where the CubeSats with DSPs generally perform worse than their BMSP counterparts for CubeSats using an FEKF. As was discovered in sec. 7.5.2, the performance of the Z3U CubeSat with DSPs using an FEKF with a zenith pointing CT was worse in the 500 km SSO than the same CubeSat in an ISS orbit. This was found to be attributed to the CubeSat in the ISS orbit receiving more intermittent CT measurements than the former.

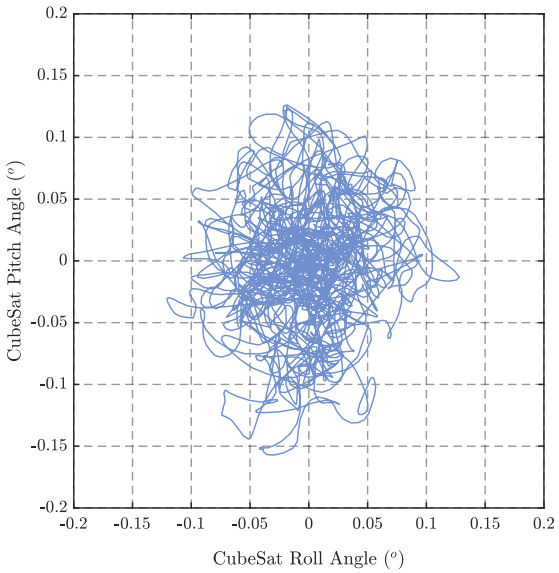

Figure 7.11: GEKF Canted CT Cross-Boresight Roll and Pitch Angles – Z12U CubeSat in 650 km SSO

The GEKFs in all categories are able to mostly reject the external disturbances felt. This can be seen throughout the data in all three orbits where the general performances of each of the three GEKF scenarios remain relatively consistent. The CubeSats using the temperature compensated version of the GEKF with a zenith pointing CT performed much better than the corresponding FEKF scenarios, and only three times worse than those with continuous CT measurements, showing that it can still reject the external disturbances fairly well. From the data, it is also apparent that the performance of the

temperature compensated GEKF is limited by the noise and random bias drift of the gyros, this is presented in fig. 7.11 which shows how the cross-boresight errors are mainly Gaussian in nature and evenly distributed, rather than as a result of external disturbance torques which present non-Gaussian IPEs, an example of which is shown in fig. 7.12.

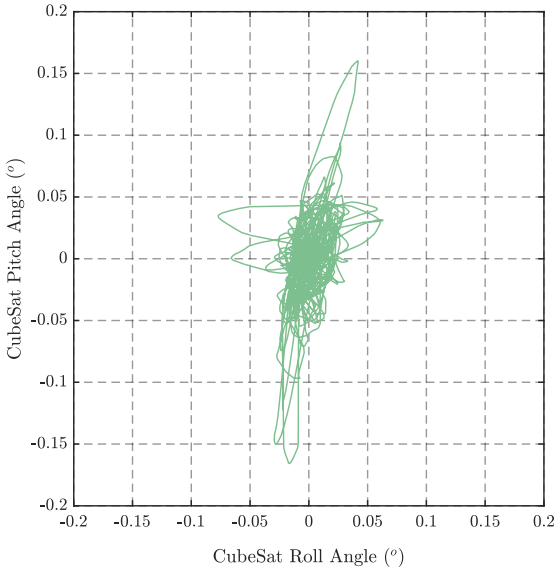

Figure 7.12: FEKF Canted CT Cross-boresight Roll and Pitch – Z3U CubeSat in ISS Orbit

The effect of not implementing gyro temperature bias compensation was tested and shown in the last category of each group. It can be seen that the EKF was not able to completely remove the various gyro biases, which resulted in approximately double the error of GEKFs with continous CT measurements. The CubeSats which utilised GEKFs with a zenith pointing CT and uncompensated gyros performed the worst and are actually omitted from all data representations. Without star tracker measurements, the GEKF is simply not able to adequately estimate each gyros bias to an acceptable degree, resulting in an IPE drift of more than 5° over the entire sunlit portion of each orbit, until it could be removed again when CT data once again became available.

7.6 Simulated CubeADCS Performance – Target Tracking

In order to test the target tracking capabilities of the CubeADCS, two CubeSats were selected from each orbit in sec. 7.5 to track a predetermined target that the CubeSat will be passing over in its orbit. The two selected CubeSats are the best performing Z12U CubeSat as well as the Z3U CubeSat, the latter of which more commonly aligns with the CubeSats typically selected by CubeSat mission designers in the industry. Two estimators are selected, namely: the FEKF and the temperature compensated GEKF, both having canted CTs.

The predetermined targets were selected by using the Orbitron satellite propagating software to propagate each respective CubeSat in its orbit using the corresponding TLEs defined in sec. 7.2.4. A location along the orbit track for each CubeSat was selected, which is provided as geodetic coordinates in Orbitron. The altitudes of the selected locations were obtained from Google Earth, where both the geodetic coordinates and altitudes above mean sea level are used to calculated the corresponding geocentric coordinates and altitude above or below the equatorial radius, $R_{\oplus}$, of each location using eqs. (4.2) and (4.4). The geocentric coordinates and relative altitudes are then fed into the simulation, which continuously calculates the ORC referenced vector to the location on Earth's surface. The CubeADCS is then placed into target tracking mode when the CubeSat is approaching the selected target where its controller attempts to track the desired reference by appropriately setting the required roll, pitch and yaw references. The timing and selection of locations in the simulation is set up such that the target

tracking occurs during the sunlit portion of each orbit.

To account for random variations from simulation to simulation, the average IPE for five of the same orbits per CubeSat was calculated over each imaging period. The proportional and derivative gains have also been adjusted to achieve a faster 2% settling time of 30 s with a damping coefficient of $\zeta = 1$. The results of the target tracking simulations are first presented and individually discussed, where the end of the section summarises the findings.

7.6.1 ISS Orbit

For the ISS orbit, the CubeSats were set to track a location at the Southern tip of South America with geodetic coordinates: $\phi_{gd} = -51.6794°$ and $\lambda = -73.6902°$, at a mean sea-level altitude of 400 m. Fig. 7.13 shows each CubeSat's Euler angles during the target tracking manoeuvre using the FEKF estimator, where figs. 7.14 and 7.15 show the corresponding IPEs for each CubeSat during the imaging period for both the GEKF and FEKF estimators. The IPEs at the precise time when the CubeSats passed over the desired target (2500 s in the simulation) is shown in table 7.11.

Table 7.11: CubeADCS Target Tracking IPE Per CubeSat in an ISS Orbit

	FEKF	**GEKF**
Z3U	155.52″	393.12″
Z12U	179.64″	638.64″

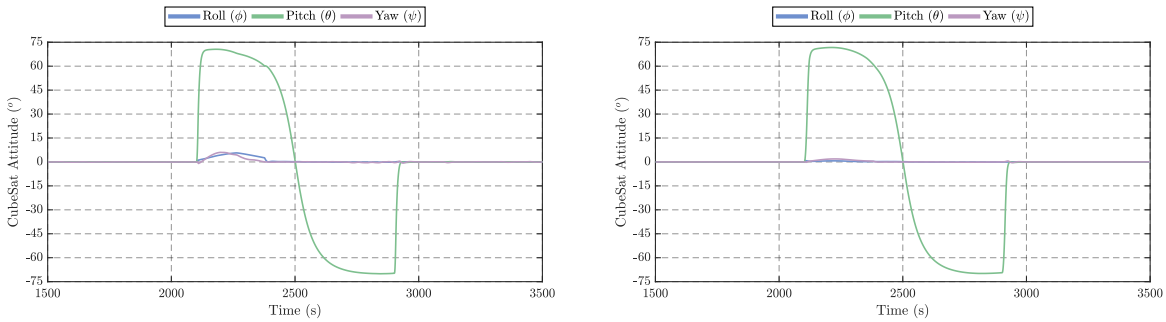

(a) Z3U CubeSat

(b) Z12U CubeSat

Figure 7.13: CubeADCS Target Tracking Manoeuvre for CubeSats in an ISS Orbit

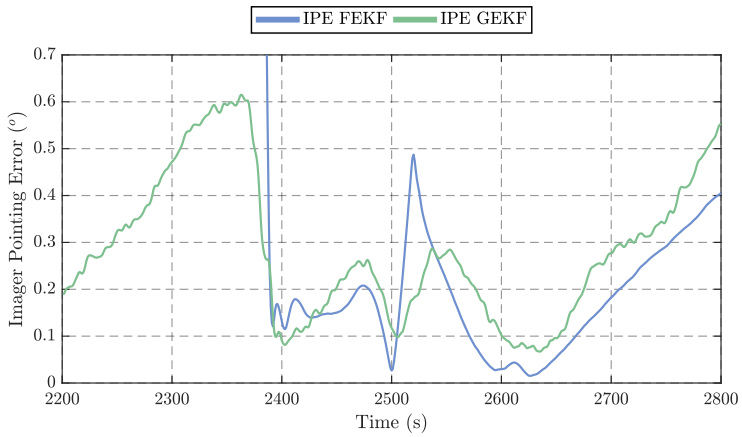

Figure 7.14: Imager Pointing Error During Target Tracking – 3U CubeSat in an ISS Orbit

As expected from the results in sec. 7.5, the FEKF is worse at rejecting external disturbances than the GEKF – especially in ISS orbits. This is not necessarily apparent from the results in table 7.11, but can easily be seen as the case in figs. 7.14 and 7.15, where the CubeSats using the GEKF have a lower average

IPE over the 600 s periods shown. Additionally, the CubeADCS did not receive CT measurements for the portions of the manoeuvre where the Earth albedo entered the CT's FOV at high pitching angles. This explains the sudden changes in IPE at around the 2400 s and 2600 s marks in the simulations. The CubeADCS additionally did not receive CT measurements for a small portion of the period near the time of imaging when the angular rate of the CubeSat's increased to slightly over $1\,^{\circ}\,s^{-1}$. On average, the 12U CubeSats perform better than the 3U CubeSats over the shown period, but better at the time of imaging for both estimators.

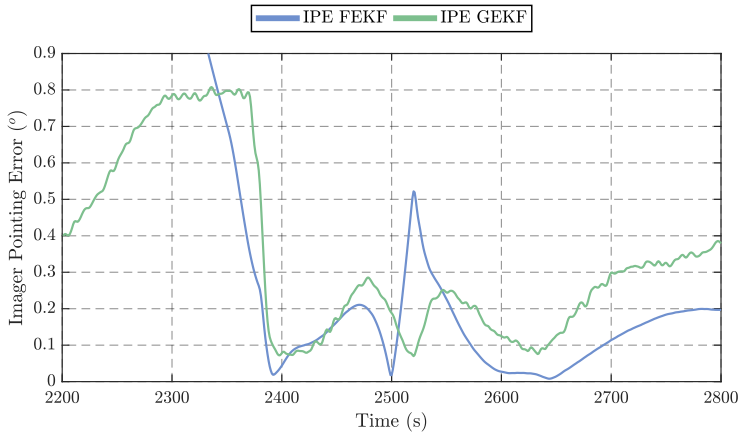

Figure 7.15: Imager Pointing Error During Target Tracking – 12U CubeSat in an ISS Orbit

7.6.2 SSO Orbit at 500 km

In the 500 km SSO, the CubeSats were set to track a Northern Canadian location with geodetic coordinates: $\phi_{gd} = 75.1336°$ and $\lambda = -90.1626°$, with a mean sea-level altitude of 312 m. Fig. 7.16 similarly shows each CubeSat's Euler angles during the target tracking manoeuvre, with each CubeSat using the FEKF estimator. Figs. 7.17 and 7.18 then show the corresponding IPEs over the imaging period, where table 7.12 tabulates the IPEs for each CubeSat and estimator at target passover time.

Table 7.12: CubeADCS Target Tracking IPE Per CubeSat in a 500 km SSO Orbit

	FEKF	**GEKF**
Z3U	42.12″	283.32″
Z12U	95.4″	218.52″

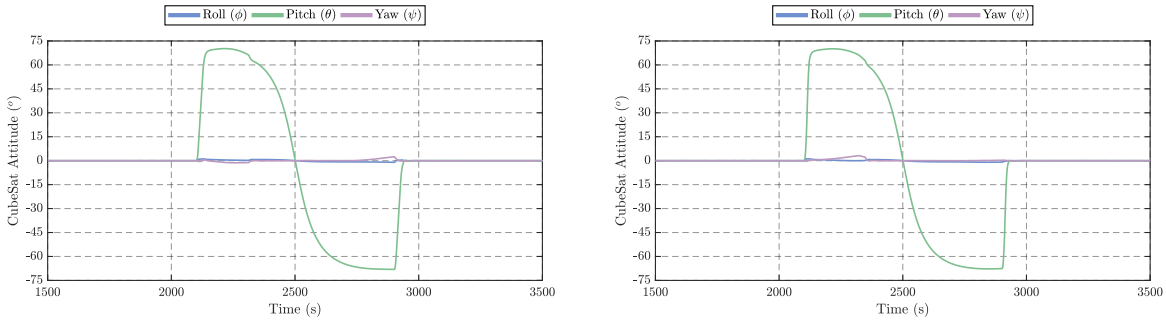

(a) Z3U CubeSat

(b) Z12U CubeSat

Figure 7.16: CubeADCS Target Tracking Manoeuvre for CubeSats in a 500 km SSO

The performance of the CubeADCS in this SSO is significantly better than in the ISS orbit, at both the time of imaging, and over the 600 s period shown. The CubeADCS once again did not receive CT measurements at high pitch angles due to Earth albedo entering its FOV, but the CT was able to obtain valid detections at the highest angular rates, as they did not exceed $1\,^{\circ}\,s^{-1}$ in magnitude at the 2500 s

mark. This is due to the increased altitude of the CubeSats, resulting in a lower required angular rate to track a target as it passes overhead. The performance of the FEKF is once again worse on average over the shown period than the GEKF, due to disturbance torques remaining fairly high. However, GEKF appears to have a more dampened response, despite the proportional and derivative gains of the controller being the same, which is why the IPE at the time of imaging is much higher than CubeSats using the FEKF. The 12U CubeSats actually show a slightly worse performance on average than the 3U CubeSats over the shown period, but this is suspected to only be due to the yaw angle positively increasing and letting in more Earth albedo for longer until the 2350 s mark shown in figs. 7.16b and 7.18. The 3U CubeSat IPE still remains better than the 12U IPE at the time of imaging.

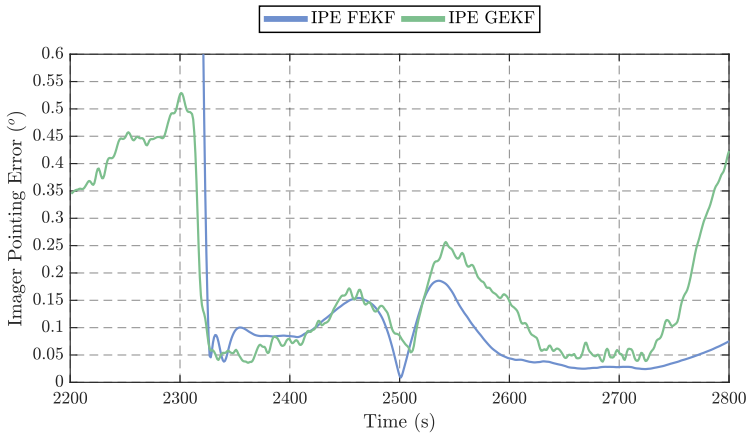

Figure 7.17: Imager Pointing Error During Target Tracking – 3U CubeSat in a 500 km SSO

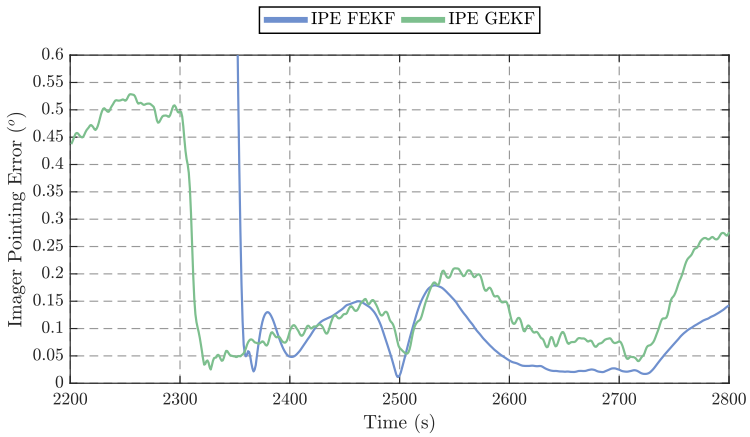

Figure 7.18: Imager Pointing Error During Target Tracking – 12U CubeSat in a 500 km SSO

7.6.3 SSO Orbit at 650 km

The final location selected for the 650 km SSO, is similar to that of the previous SSO with geodetic coordinates: $\phi_{gd} = 74.0552°$ and $\lambda = -93.6725°$, having a mean sea-level altitude of 75 m. Once again, the fist plot shown in fig. 7.19 shows each CubeSat's Euler angles during the target tracking manoeuvre using the FEKF estimator. Figs. 7.20 and 7.21 then displays the IPE plots for each estimator, where table 7.13 presents the IPEs for each CubeSat and estimator at the exact time of target passover.

Table 7.13: CubeADCS Target Tracking IPE Per CubeSat in a 650 km SSO Orbit

	FEKF	**GEKF**
Z3U	30.6″	238.68″
Z12U	56.16″	237.24″

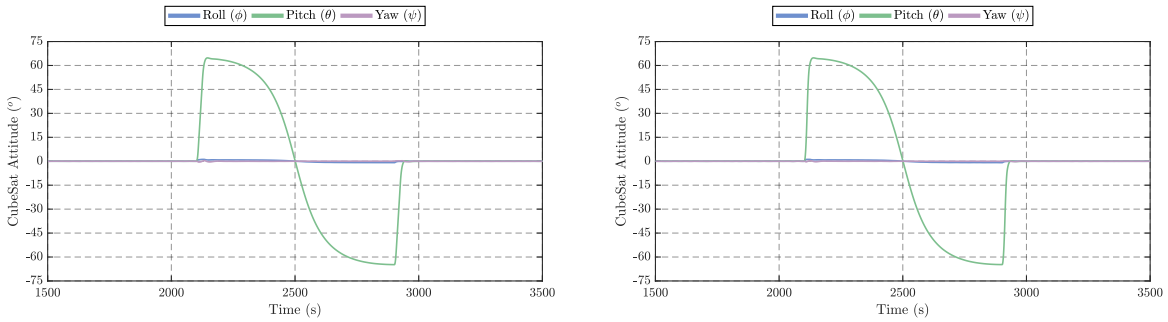

(a) Z3U CubeSat

(b) Z12U CubeSat

Figure 7.19: CubeADCS Target Tracking Manoeuvre for CubeSats in a 650 km SSO

This SSO generally presents the best CubeADCS target tracking results out of the three selected orbits in this section for both CubeSat sizes. This can be attributed to the CubeADCS receiving CT measurements for the majority of the manoeuvres. This is due to the CubeSats being at a much higher altitude than the previous two orbits, which results in the CubeSat holding high pitch angles for shorter periods of time, as well as a smaller Earth disk seen by the CubeSats. As a result, the Earth albedo only enters the CT FOV for a much shorter period. The disturbance torques are also the lowest at this altitude which only helps to improve the results further. The GEKF is still seen to not perform as well as the FEKF, where it once again exhibts a more dampened type response. The 3U CubeSat once again does slightly better than the 12U CubeSat at the time of imaging as well, but on average the 12U CubeSat performs better over the shown period.

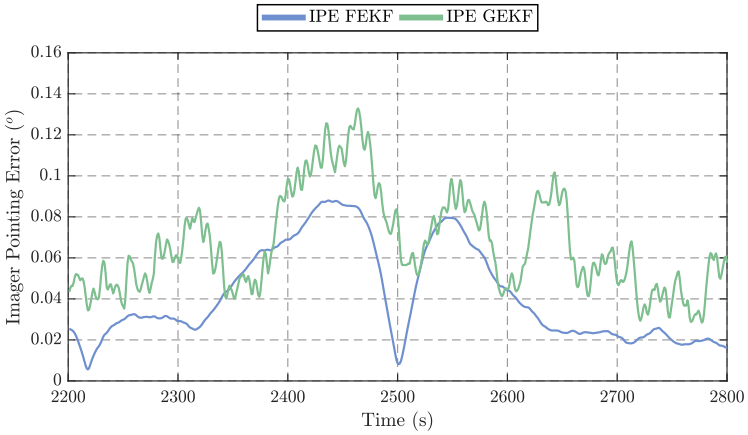

Figure 7.20: Imager Pointing Error During Target Tracking – 3U CubeSat in a 650 km SSO

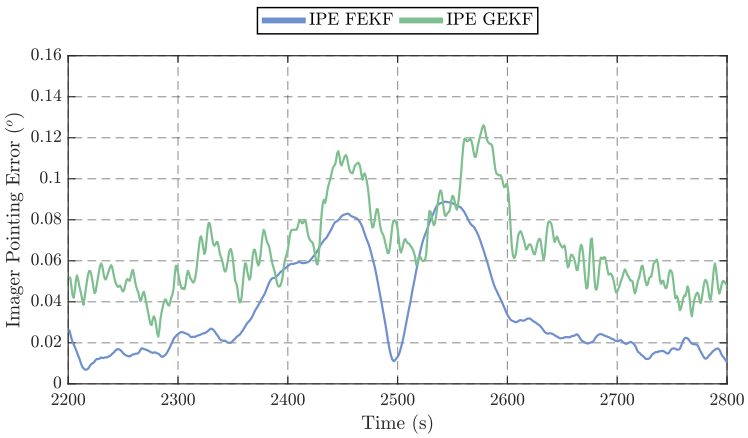

Figure 7.21: Imager Pointing Error During Target Tracking – 12U CubeSat in a 650 km SSO

7.6.4 Overview of the CubeADCS's Target Tracking Performance

The target tracking analysis has revealed that continuous CT measurements are vital to achieving high levels of accuracy during a slew manoeuvre. The effects of not receiving CT measurements are only worsened by extreme external disturbance torques, especially those experienced in LEOs. The worst performance was seen in the ISS orbit, where the external disturbances were highest, and the CT detections were disrupted the most. The best performances are seen in both of the SSOs, which is of the greatest interest in this project.

The GEKF is seen to perform the worst overall, where its response to the changing references appeared to be more dampened than that of the CubeSats using the FEKF, where the errors generally seem to also have a larger offset than that seen from the FEKF. This may be due to the higher levels of noise measured from the gyros. The 12U CubeSats generally perform better over the entire target tracking manoeuvre, but seem to show consistently worse results at the precise times of imaging – at least in the case when the FEKF is used as the estimator. This may be due to the 3U CubeSats having greater agility than the 12U CubeSats where they can respond to changing references at a faster rate with less error.

Overall, the CubeADCS appears to be able to successfully and accurately track Earth based targets to within 100″ in SSOs when using an FEKF, and to within 300″ when using a compensated GEKF. These accuracies translate to a worst case off-target error of less than 1 km at an altitude of 650 km. The best case IPE seen is the incredibly low 30.6″ achieved by the 3U CubeSat using an FEKF in a 650 km SSO, which translates to an off-target error of 96 m.

7.7 Stability

A final analysis was conducted on the stability of the CubeADCS whilst controlling a CubeSat in LEO. The stability of a CubeSat equipped with an imaging payload will have an effect on undesirable factors such as image smearing. The full set of data, including the CubeSats with uncompensated GEKFs with zenith pointing CTs, obtained during the nadir tracking analysis in sec. 7.5 was used to determine the stability, where the same method discussed in sec. 2.5.1 used by the researchers investigating the stability of the XACT ADCS was adopted. To achieve this, the roll, pitch, and yaw errors of all CubeSats from the data, were grouped into bins of 10 s integration periods. The maximum peak-to-peak differences in each bin were then calculated to determine the largest fluctuations in attitude that could be observed over a 10 s integration period. This was done in order to directly compare the results of other known miniaturised ADCSs, such as the XACT ADCS discussed in sec. 2.5.1. In reality, imaging payloads used in EO missions will need a fraction of the integration time used by MinXSS-1.

The best and worst performing CubeSats were determined by observing which CubeSat had the most stability over all three roll, pitch and yaw axes. Tables 7.14 to 7.16 summarise the best and worst performances over each orbit type, where the stability is defined as the magnitude of all three Euler angles' 3σ stabilities. The 3σ stability was determined by calculating which bin contained more than 99.71% of the data. As expected, CubeSats in an ISS orbit generally performed the worst, given the large external disturbance torques the satellites have to endure. It was not expected that for both types of SSOs, that the greatest stability over the 10 s integration period would be exhibited by 3U CubeSats – especially those equipped with DSPs. The change in MoI, however, for a 3U CubeSat with BMSPs to one with DSPs may explain the good stability in this case.

It was additionally found that CubeSat's utilising compensated GEKFs with canted CTs all had similar 3σ stabilities of approximately $0.07°(10s^{-1})$ about each axis, regardless of orbit type and satellite configuration. This once again seems to point to the noise characteristics of the gyros. Although the CubeSats with the best IPAs (Z12U CubeSats) are not listed in the tables below, their stabilities were still close competitors with the best performing Z12U CubeSat showing a stability of 0.0124°, 0.0127° and 0.0234° about the satellite's roll, pitch and yaw axes respectively in a 650 km SSO, using an FEKF

with a canted CT. Despite the large drift in attitude for CubeSats using an uncompensated GEKF with a zenith pointing CT over the sunlit portion of the orbit, the maximum change in attitude over the 10 s integration period was similar to that of the FEKF with the same CT orientation. Although the uncompensated GEKF exhibited the worst stability performances in two of the three orbits, it was only slightly worse than its FEKF counterpart without continuous CT measurements.

Table 7.14: CubeADCS Stability of a CubeSat in an ISS Orbit

	3σ Stability [°(10s^{-1})]	**Estimator**	**CubeSat**	**CT Orientation**	**Solar Panels**
Best	0.0308	FEKF	Z6U	Canted 45°	Deployed
Worst	0.8661	GEKF (Uncompensated)	Z6U	Zenith	Body-mounted

Table 7.15: CubeADCS Stability of a CubeSat in a 500 km SSO

	3σ Stability [°(10s^{-1})]	**Estimator**	**CubeSat**	**CT Orientation**	**Solar Panels**
Best	0.0192	FEKF	Z3U	Canted 45°	Deployed
Worst	0.5945	FEKF	Z3U	Zenith	Deployed

Table 7.16: CubeADCS Stability of a CubeSat in a 650 km SSO

	3σ Stability [°(10s^{-1})]	**Estimator**	**CubeSat**	**CT Orientation**	**Solar Panels**
Best	0.0202	FEKF	Z3U	Canted 45°	Deployed
Worst	0.3480	GEKF (Uncompensated)	Z3U	Zenith	Deployed

The CubeSat with the best performance is the Z3U CubeSat in a 500 km SSO using an FEKF with a canted CT. The roll, pitch and yaw stabilities for this CubeSat can be seen in fig. 7.22 having 3σ accuracies of 0.0081°(10s^{-1}), 0.0114°(10s^{-1}) and 0.0132°(10s^{-1}) respectively. These results compare nicely to the results presented by the researchers discussing the MinXSS-1 mission, where the stability seen in this section will likely be more than adequate for what is required in EO missions.

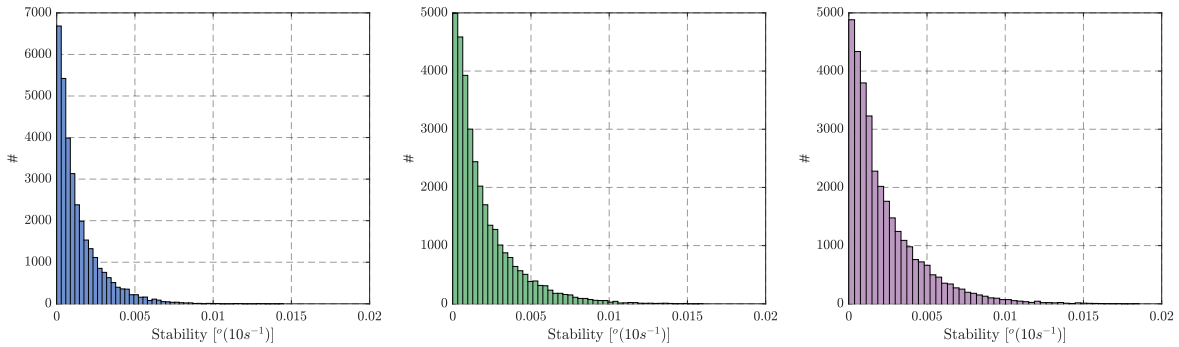

(a) Roll Stability **(b)** Pitch Stability **(c)** Yaw Stability

Figure 7.22: Best CubeADCS Stability of a CubeSat in LEO

7.8 Summary

The simulation investigation set out to determine the IPA and stability of a CubeSat using a CubeADCS in LEO. To achieve this, two types of tracking were investigated, namely: nadir and target tracking. Several different scenarios were investigated to gain a broad understanding of which factors would have the biggest impact on the CubeADCS's performance. These factors included orbit type, CubeSat size

and nominal orientation in its orbit, the type of estimator used, and the orientation of the CT on a CubeSat. Two SSOs were selected for investigation to align with the project scope, where an ISS orbit was additionally examined to include a commonly chosen orbit for missions in the industry.

In the nadir tracking investigation, it was found that CubeSats in ISS orbits had the worst overall IPA, which can be mainly attributed to the extremely harsh environmental disturbance torques experienced in such an orbit. Additionally, CubeSats with their long-body axis aligned with the SBC x-axis generally performed worse than their z-axis aligned counterparts. Those CubeSats which received few CT measurements during the sunlit portions of their orbits also showed significantly worsened performances.

In most cases, CubeSats with deployed solar panels performed worse than those without, except in the cases where the roll axis of a CubeSat was incredibly small and thus harder to control. CubeSats using GEKFs performed consistently within their subcategories, which showed that the major cause of error was predominately due to gyro noise and not from external disturbances. Finally, it was found that without temperature compensation or CT measurements, that the GEKF would cause a drift in attitude that would be too large for missions with a high IPA. The results of the nadir tracking section indicated that the CubeADCS has a potential RMS IPE of less than $32''$, and a worst-case RMS IPE of less than $257''$ for those with continuous CT measurements.

The target tracking investigation revealed that the CubeADCS is able to accurately track targets to within $300''$ for CubeSats in SSOs using a compensated GEKF and to within $100''$ for CubeSats using an FEKF. It was additionally determined that continuous CT measurements play a crucial role in high accuracy target tracking, especially when it comes to rejecting external disturbances in very low orbits. The 3U CubeSats were found to have the best IPEs at times of imaging, but that the 12U CubeSats had the best overall IPE over a larger imaging period. A 3U CubeSat in a 650 km SSO was able to achieve an IPE of as low as $30.6''$.

A final investigation was conducted to determine the stability of a CubeSat equipped with a CubeADCS over an integration period of 10 s in order to compare the results to the performance of the XACT ADCS. This revealed that the most significant change in attitude over the integration period would have a maximum magnitude of $0.8661°(10s^{-1})$ over all three axes and that the best case stability was as low as $0.0192°(10s^{-1})$ in magnitude. High levels of stabilty are shown to only be possible with the CubeADCS receiving continuous CT measurements and for CubeSats having more symmetrical principal MoIs. If the stability of the CubeADCS is shown to be good enough for missions observing distant stars, then the stability is likely to be more than adequate for EO missions.

Chapter 8

Conclusions and Recommendations

8.1 Research Summary and Conclusions

This project sought to investigate the IPA of a CubeADCS aboard a CubeSat in a low-Earth SSO.

In order to achieve this, existing ADCSs currently suited to control CubeSats were investigated. After which, an in-depth investigation into the CubeADCS's underlying subcomponents was performed to gain a better understanding of the theory behind their operation. The underlying theory of satellite orbital dynamics and control were first expanded on to lay the foundation that would allow an accurate simulation model to be constructed and, which would assist in the understanding of the control and operation of the CubeADCS. An accurate simulation model needed to be constructed in order to mimic the space environment experienced by CubeSats in LEO, as well as to replicate the error characteristics and performances of the CubeADCS subsystems. All the above aimed to asses the performances of CubeSpace's attitude control and estimation software algorithms in their ability to perform in the constructed simulation model.

The literature research done in chapter 2 was aimed at investigating CubeSats, trends related to them, and the trends in miniaturised ADCS development, which have allowed CubeSats to achieve good IPAs. In addition to this, three missions were investigated, namely: MinXSS-1, ASTERIA, and the BRITE constellation. These examples provided insight into the types of subcomponents used by ADCSs necessary to achieve a high IPA, as well as the kind of accuracy which has been achieved by CubeSats in real missions. It was found that the miniaturisation of high accuracy ADCS sensors, such as star trackers play a key role in allowing CubeSats to achieve arc-second pointing accuracies and stability. Of the three missions, two of the CubeSats were launched into ISS orbits and were equipped with BCT's XACT ADCS, which has proven to be one of the world's leading manufacturers of miniaturised ADCSs and subcomponents. In both missions (MinXSS and ASTERIA) the XACT ADCS was able to achieve extremely fine 3σ pointing accuracies to within $40''$, which is one of the best known examples of accurate pointing exhibited by CubeSats to date. The last mission (BRITE) used different subcomponents made by different manufacturers. The NanoSats were each launched into SSOs, where UniBRITE was able to achieve an RMS IPA of $53.6''$.

Chapter 3 launched an initial in-depth investigation into the CubeADCS which expanded on the theory behind the operation of the various sensors and actuators implemented. Particular focus was placed on the sensors and actuators crucial to providing CubeSats with a high IPA. These included: the CS fine-sun and nadir sensors, the CL gyroscopes, the CT high accuracy star tracker, and the CWs – precise reaction wheels. Various key performance parameters were identified alongside the possible sources of errors which can effect each sensor in their ability to provide accurate measurements.

The initial analysis revealed that the CS Sun and nadir sensors had a 1σ accuracy of $0.2°$ respectively

over their specified FOVs, and that their greatest sources of errors can be attributed to image sensor noise as well as errors in distortion correction over a large FOV fisheye lens. The investigation into the MEMS gyros revealed that there are multiple sources of errors, which have an impact on their accuracy. It was found that both their scale factor and bias can be heavily affected by temperature gradients and that they are particularly vulnerable to stochastic errors such as angular random walk and bias instability, which cannot be calibrated for. The analysis of the CT proved that it is indeed the most accurate sensor adopted by the CubeADCS, outputting attitude knowledge estimations with a cross-boresight 3σ accuracy of $36''$. The prior research conducted in chapter 2 suggests that an ADCS is only as accurate as its most accurate sensor, which already then theoretically limited the CubeADCS to the same best-case IPA. The primary sources of error pertaining to the CT are similar to that of the CS which are: errors in distortion correction as well as pixel noise of the image sensor. The initial analysis of the CW showed that they are primarily designed to be used in a speed control mode, measuring speeds to within a 0.5 RPM resolution. The largest expected errors are from the small CWs having a 3σ accuracy of 5 RPM. Errors in CW reference tracking can be primarily attributed to encoder noise, the measurement resolution being too coarse, control signal noise, thermal variations, wheel imbalances, and frictional forces.

The aim of chapter 4 was to provide the theoretical knowledge needed to create the various required simulation models, as well as to gain an understanding into the control theory behind an ADCS. Coordinate frames were elaborated on to relate the CubeSats attitude and position in space to locations on Earth. Orbital mechanics and elements were discussed to explain the application of the SGP4 model as well as which elements play a role in defining exactly what a SSO is. ADCS control theory was additionally analysed to gain an understanding of various representations of attitude in space, of which it was found that the most popular method used to propagate a satellite's attitude in space is through the use of quaternions, which provide a solution to three-dimensional rotations in space without any singularities and are convenient to propagate through numerical integration. The discussion of attitude dynamics and kinematics of a satellite were lastly discussed, with the main aim of describing the quaternion feedback control law used to command a satellite to follow various attitude references in space, as well as the theory behind satellite's performing target tracking manoeuvres to point at locations on Earth as they pass over-head.

Chapter 5 was dedicated to constructing the accurate simulation environment experienced by a satellite in space expanding on some of the theory laid out in chapter 4. The SGP4 model was initially discussed, which was found to be the dominant method in industry used to propagate satellite's in LEO along their various orbit trajectories. Examples showing the position and velocity of a modelled CubeSat were presented and shown to accurately mimic the expected ECI referenced satellite vectors for a CubeSat in an SSO. The accuracy of the SGP4 model was briefly analysed to determine just how far the positional model of a satellite can drift from its actual position in space. The simulation of three different CubeSats in three different orbits showed that over a period of 10 days, that the positional knowledge of a CubeSat could drift by nearly 25 km RMS and that the drift is more prominent for CubeSats in very low altitude orbits such as that of the ISS. To protect against this drift in positional knowledge, a solution implementing a hybrid GPS and SGP4 model on an ADCS was discussed which showed promising results which could reduce these errors to a maximum of 1 km. A second solution was also provided which would see even better results, but it was pointed out that the adoption of which could be a high risk as it is a completely new system when compared to the flight proven simple SGP4 stand-alone propagator.

The Sun position and geomagnetic reference models where next defined. These two models served two main purposes: 1) to be used as a basis for the Sun and magnetometer sensor models, 2) to be used to model the solar panel induced magnetic moment disturbance torques acting on a satellite. Following this, the primary disturbance torques affecting CubeSats in LEOs were discussed, which included the satellite induced magnetic moment, gravity gradient, and aerodynamic disturbance torques. It was found through investigation that only the gravity gradient disturbance torques are modelled by ADCS systems and used by their estimators as they are the most predictable type of disturbance. Aerodynamic disturbance

torques are somewhat less predictable and are found to play a significant role of CubeSats operating in very low orbit altitudes such as that of the ISS. It is determined that solar panel induced magnetic disturbances remain fairly consistent regardless of LEO altitude, as the magnetic field strength decreases at a slower rate than atmospheric density (for example) with altitude. This makes it an important source of disturbance to consider for CubeSats in LEO, especially since these torques are most prominent in sun-lit portions of an orbit where imaging usually takes place. The chapter ends by modelling the CubeSat dynamics and kinematics and shows how the attitude and angular rates are propagated.

The crucial investigation into the actual sensor and actuator error characteristics of the subcomponents within the CubeADCS was achieved in chapter 6. Each sensor and actuator implemented on the CubeADCS was investigated and modelled individually based on actual measured data. Primary focus was once again placed on those sensors, which are crucial to the CubeADCS providing a high IPA. A PCB was designed to fit three of the gyros for investigation. The gyros were found to have the largest spectrum of error sources, the most prominent of which is its bias's susceptibility to thermal gradients. The stochastic noise of the gyros was also found to be higher than was expected with peak-to-peak values larger than $0.03\,^{\circ}\,s^{-1}$ when considering both the bias instability and high frequency noise acting together. It was found that temperature bias drift could be modelled and thus compensated for by using techniques such as the soak method. The gyro model was also designed to be able to be used as compensated and uncompensated versions by the simulated CubeADCS. The gyro model was found to accurately resemble the error characteristics measured.

An analysis of the CS followed which sought to determine the actual measured accuracies of both the fine-sun and nadir sensors. CubeSpace provided this author with a functioning CS, where an experiment was set up where the FSS was left to sit and track the position of the Sun as it passed overhead. This revealed that the CS Sun sensor could track the Sun with a 3σ deviation from the mean Sun position of less than 0.25°, far out-performing its stated 1σ accuracy of 0.2°. The nadir sensor was tested by mounting it on a rotation stage and placing a large illuminated ball in front of the camera aligning the ball's centre with its boresight. The camera was then rotated about its boresight, where the error in nadir detections was plotted as the ball moved across the camera's image plane. The nadir sensor errors were found to be well within the stated 1σ accuracy of 0.2° when the entire ball was in the the camera's FOV. As was expected, the errors began to increase significantly as portions of the ball began to leave this FOV, with errors increasing to as much as 9° when less than half the ball was in the FOV. This can be attributed to both the errors in the test setup as the ball appeared to dim as the camera rotated to more extreme angles, as well as errors from the circle fitting algorithm trying to fit a circle to an incomplete image of the ball. Both the CS fine-sun and nadir sensor models mimic the behaviour seen from actual measurements where invalid detections are given when the Sun or Earth vectors indicated that they are outside of each camera's pre-defined acceptable DRs. Both sensors were modelled to show very similar angular error outputs, with the nadir sensor errors increasing as the angle between its boresight and nadir increases.

The last major sensor investigated was the CT star tracker. Unfortunately, this author was not able to perform the investigation on an actual CT sensor, but was instead provided with actual measurement data from field tests conducted by CubeSpace. The data came from a CubeStar which was left over a period of the night to observe the night sky as the stars passed overhead. A log of estimated quaternion data was generated by the device, which was then investigated to determine how much the estimated attitude varied over time. The accuracy was determined to be lower than the stated CT 3σ accuracies with a worst-case cross-boresight RMS error of 0.005 95°. It was determined, however, that the larger measurement errors could be attributed to stray light sources entering the camera's FOV and that possible atmospheric disturbances could impact the results, as on-Earth testing provides a less than ideal environment in which to test such a sensitive device. Nevertheless, the model and error characteristics of the CT were designed to replicate a worst-case scenario and thus used the measured results for the simulation model. Two additional features of the model take into account that the CT will not be able to detect three or more

stars 0.29% of the time and that null detections will also be given if the simulated CubeSat is determined to have an angular rotation rate greater than $0.3\,^{\circ}\,s^{-1}$. The model was thus determined to accurately mimic the CT.

Chapter 6 ended with an analysis of the CW – the high accuracy actuator needed to perform precision pointing. An in-depth investigation was conducted on a medium CW provided to the author by CubeSpace where it was set to track multiple speed references. The errors exhibited at the various reference speeds were determined where the step responses of the wheel at each reference was additionally examined. The observed error characteristics were found to closely resemble the stated error characteristics for speeds less than 2000 RPM. Possible discrepancies in measured versus stated errors could be attributed to the age and usage of the wheel prior to testing by this author. In any case, the CWs are not intended to be run for significantly long periods of time at very high speeds, which indicates that large errors at these speeds should be of relatively low concern. To once again allow for a worst-case scenario, the observed errors were used to model each CW. The step responses of the model were also shown to closely resemble the step response of the actual CW as well.

The final simulations conducted to determine the IPA of the CubeADCS were performed in chapter 7. Several scenarios were investigated to gain a broad understanding of the factors which may influence the performance of the CubeADCS. Such scenarios included: CubeSat size, orbit type, solar panel configuration, long-body axis alignment in the SBC frame, the type of attitude estimator used, and CT orientation within a CubeSat. Two types are attitude reference tracking were assessed, namely: nadir tracking (constant reference) and target tracking (changing reference). The maximum disturbance torques were determined for each orbit type, where the orbits selected were two different altitude SSOs and a single ISS orbit – selected to test the most popular orbit for CubeSats in industry. The CubeADCS was found to be able to track constant references considerably well, provided that CT measurements were available and that the axis with the lowest principle MoI was aligned with the CubeSat yaw axis. CubeSats using the FEKF estimator with continuous CT measurements were able to achieve pointing accuracies with an RMS IPE of between $32''$ and $257''$ over all simulated CubeSat sizes, orbits, and long-body axis alignments, with many CubeSats performing just as well as UniBRITE in sec. 2.5.3. CubeSats in the ISS orbit generally exhibited the largest IPEs with those CubeSats equipped with solar panels having the worst performances.

CubeSats using the temperature compensated GEKF had nearly identical performances regardless of CubeSat orbit type, size, long-body axis alignment, and solar panel configuration. The GEKF does not need to estimate the CubeSat body angular rotation rates, which is the likely reason for the consistent performance. The GEKF was additionally found to reject external disturbances better than the FEKF. Nevertheless, the performance of the compensated GEKF was still limited by the gyro sensor noise, resulting in a best-case RMS IPE of $203''$. The uncompensated GEKF was found to be able to estimate the changing gyro biases with temperature, but not to an accuracy seen with compensation where the errors in bias estimation were prominent in the simulations. In the cases where the GEKF did not have compensation, or continuous CT measurements, the accuracy was found to be too large, with attitude errors drifting by more than 5° over the sunlit portion of each orbit.

The target tracking portion of the investigation proved that the CubeADCS is able to achieve high levels of accuracy when tracking an Earth-based target. The performance of the CubeSats in the ISS orbit was the worst out of the three selected orbits by a large margin. The greater error seen can be directly attributed to the higher external disturbances experienced, where the lack of CT measurements at the time of imaging also contributed to this. The performance of the CubeSats in the SSOs was of the greatest interest in this thesis, however, where it was found that the IPE could be as low as $30.6''$. CubeSats using the compensated GEKF had a worse performance than those using an FEKF, where the smaller 3U CubeSats were actually shown to have the best accuracy at the time of imaging. This is thought to be due to the CubeSat having a greater agility than the 12U CubeSats.

At the end of chapter 7, the data was used from the first nadir tracking investigation to determine the stability of the CubeADCS. The CubeADCS was found to have a good stability about all three of its axes where the best-case stabilities about a CubeSat's roll, pitch and yaw axes was found to be $0.0081°(10s^{-1})$, $0.0114°(10s^{-1})$ and $0.0132°(10s^{-1})$ respectively, and a worst-case combined axes stability magnitude of $0.8661°(10s^{-1})$ over a 10 s integration period. The vast majority of CubeSats having continuous CT measurements had very similar stabilities to the best-case outcome, performing at a level in the same range as the XACT ADCS. A stabilty which is acceptable for stellar observations, is likely to be more than adequate for EO missions.

In conclusion, the outcomes set out in this project were successfully achieved. An accurate simulation environment was setup, accurate subcomponent modelling was conducted to mimic the CubeADCS hardware, and the IPA and stability of the CubeADCS were investigated by testing CubeSpace's estimation on control software algorithms. The results of the simulations show the predicted worst-case performances of the CubeADCS, where all sensor models were set to exhibit the worst possible error characteristics and the environmental disturbances were set to be some of the harshest a CubeSat could experience in LEO. The performance within an ISS orbit was considerably worse than the SSO performances, however, the project set out to determine the performances of the latter, which proved to have great potential for CubeSats using a CubeADCS.

8.2 Improvements and Recommendations

The following section will discuss various improvements which could have been made to improve the research and attempt to provide possible alternative solutions.

8.2.1 Gyroscopes

During the investigation into the gyros implemented on the CubeADCS, it was found that the sensors themselves are prone to several impacting sources of error. The most apparent of which was found to be their high sensitivity to thermal gradients affecting the bias drift. The gyros also seem to have unacceptably large high frequency and bias instability errors which seem to limit to potential performance of the CubeADCS. Investigating different types of MEMS gyros could have been done to determine if there exists better sensors which are perhaps not as error prone as the one used on the CL.

8.2.2 Gyroscope Temperature Compensation

It was found that without any temperature compensation of the gyros, that the bias would not be completely removed and that errors can become significant. It is recommended that temperature compensation should actually be conducted.

8.2.3 Accurate Temperature Modelling

Although it is advised to compensate the gyros for bias drifts caused by thermal variations, a better CubeSat temperature model could have been constructed to more accurately replicate the kind of temperature changes that a CubeSat would experience in LEO. It is a possibility that the simple sinusoidal model could play a role in the reason than the GEKF was not able to completely remove the changing bias.

8.2.4 Magnetometer Testing and Modelling

It could be valuable for future researchers to verify the true effect of alternating current loops on the satellite bus creating magnetic moment disturbances on magnetometer measurements. Reducing these effects would be highly beneficial to improving the accuracy of the magnetic field measurements.

8.2.5 CubeStar Testing and Modelling

The CT was investigated using data provided to the author from CubeSpace. More indepth and accurate testing of the CT could have been achieved and verified if the actual hardware was available to test. Additionally, the effect of having a second CT in the modelled simulations would be useful to determine the absolute limits of the kind of accuracies that could be achieved by the CubeADCS.

8.2.6 CubeWheel Testing and Modelling

Only one CW was tested to gain an understanding of its error characteristics. Investigating more CWs could gain a broader knowledge of the expected CW errors used on different size CubeSats.

8.2.7 Solar Panel Testing and Modelling

The solar panels considered in this simulation were assumed to have certain resultant magnetic moment characteristics. An investigation into an actual solar panel produced by a CubeSat component manufacturer could help to gain a better understanding of their expected impact on a CubeSat, where an accurate model could be constructed.

8.2.8 Mission Data

Although the target tracking performance of the CubeADCS seemed to be poor in comparison to nadir tracking, its performance could not be compared to any other reference from CubeSats performing the same manoeuvre. More data on the accuracies of other CubeSats conducting the same manoeuvres would help to gain a better idea of what can be expected.

8.2.9 Proper SGP4 Error Modelling

A more in-depth investigation could have been conducted into the error of the SGP4 propagator, where noise on the positional knowledge vector matching the actual expected errors in positional knowledge could have been added to test the CubeADCS accuracy in extreme cases when updated TLE data is not available.

8.2.10 Target Tracking Controller Integral Term

It was discovered at the end of this research that the target tracking controller used in the simulations, did not include an integral term gain. The inclusion of such a term in a different controller provided by CubeSpace could show better results, especially with regards to target tracking.

8.2.11 Further Investigation and Optimisation of Estimators

The optimisation of the FEKF and GEKF designs fell out of the scope of this project. An in-depth investigation which seeks to optimise the various weighting parameters per each estimator, could further improve the accuracy of the system as a whole.

References

[1] J. Chin, R. Coelho, J. Foley, A. Johnstone, R. Nugent, D. Pignatelli, S. Pignatelli, N. Powell, and J. Puig-Suari, *CubeSat 101: Basic Concepts and Processes for First-Time CubeSat Developers*, 2017 (cit. on pp. 3, 4).

[2] Nasa, *What are SmallSats and CubeSats?* [Online]. Available: `https://www.nasa.gov/content/what-are-smallsats-and-cubesats` (visited on 06/10/2019) (cit. on pp. 3, 4).

[3] E. Kulu, *Nanosats Database*. [Online]. Available: `https://www.nanosats.eu/` (visited on 08/01/2019) (cit. on pp. 3, 4, 5, 6, 12, 15).

[4] A. Camps, "Nanosatellites and Applications to Commercial and Scientific Missions," *Ionospheric and Atmospheric Threats for GNSS and Satellite Telecommunications Explorer*, 2019. [Online]. Available: `https://www.intechopen.com/books/advanced-biometric-technologies/liveness-detection-in-biometrics` (cit. on pp. 4, 5).

[5] S. G. Anderson, *CubeSats: the Smallest Big Thing in Remote Sensing Sciences*. [Online]. Available: `https://spie.org/news/spie-professional-magazine-archive/2019-july/cubesats?SSO=1` (visited on 09/20/2019) (cit. on p. 4).

[6] European Space Agency, *Low Earth Orbit*, 2020. [Online]. Available: `https://www.esa.int/ESA{\_}Multimedia/Images/2020/03/Low{\_}Earth{\_}orbit{\#}.YARhgWjJTpE.link` (cit. on p. 4).

[7] T. Villela, C. A. Costa, A. M. Brandão, F. T. Bueno, and R. Leonardi, "Towards the Thousandth CubeSat : A Statistical Overview," *International Journal of Aerospace Engineering*, vol. 2019, p. 13, 2019. [Online]. Available: `https://www.hindawi.com/journals/ijae/2019/5063145/` (cit. on pp. 5, 6, 7).

[8] X. Xia, G. Sun, K. Zhang, S. Wu, T. Wang, L. Xia, and S. Liu, "NanoSats/CubeSats ADCS survey," *Proceedings of the 29th Chinese Control and Decision Conference, CCDC 2017*, pp. 5151–5158, 2017 (cit. on pp. 6, 7).

[9] D. Selva and D. Krejci, "A survey and assessment of the capabilities of Cubesats for Earth observation," *Acta Astronautica*, vol. 74, pp. 50–68, 2012, ISSN: 00945765. DOI: `10.1016/j.actaastro.2011.12.014`. [Online]. Available: `http://dx.doi.org/10.1016/j.actaastro.2011.12.014` (cit. on pp. 6, 7, 66).

[10] A. Shah, K. Sarda, C. Grant, S. Eagleson, D. Kekez, and R. E. Zee, "Canadian advanced nanospace experiment 2 orbit operations: One year of pushing the nanosatellite performance envelope," *60th International Astronautical Congress 2009, IAC 2009*, vol. 5, no. December 2009, pp. 3557–3571, 2009 (cit. on p. 7).

[11] B. Johnston-Lemke, K. Sarda, C. C. Grant, and R. E. Zee, "Arc-Minute Attitude Stability on a Nanosatellite: Enabling Stellar Photometry on the Smallest Scale," *Proceedings of the 25th Annual Small Satellite Conference*, pp. 1–13, 2011 (cit. on pp. 7, 14, 15).

[12] J. Guo and C. Han, "Where is the Limit: The Analysis of CubeSat ADCS Performance," *The 4S Symposium*, no. 1, pp. 1–15, 2016 (cit. on pp. 8, 9).

[13] ESA, *Earth Observation Portal Directory*. [Online]. Available: `https://directory.eoportal.org/web/eoportal/satellite-missions/` (cit. on pp. 8, 10, 12).

[14] H. E. Loubser, "The development of Sun and Nadir sensors for a solar sail CubeSat," MSc Thesis, Department of Electrical and Electronic Engineering, Stellenbosch University, 2011 (cit. on pp. 8, 25, 26, 27, 28, 29, 97).

[15] J. Praks, "Aalto-1 Satellite First Months in Orbit (Preprint) IAA-AAS-CU-17 -03-10 AALTO-1 SATELLITE FIRST MONTHS IN ORBIT," no. December, 2017. [Online]. Available: `https://www.researchgate.net/publication/322251534{\_}Aalto-1{\_}Satellite{\_}First{\_}Months{\_}in{\_}Orbit` (cit. on p. 9).

[16] Berlin Space Technology, *iADCS-100*. [Online]. Available: `https://www.berlin-space-tech.com/portfolio/iadcs/` (cit. on p. 9).

[17] J. P. Mason, M. Baumgart, B. Rogler, C. Downs, M. Williams, T. N. Woods, S. Palo, P. C. Chamberlin, S. Solomon, A. Jones, X. Li, R. Kohnert, and A. Caspi, "MinXSS-1 CubeSat On-Orbit Pointing and Power Performance: The First Flight of the Blue Canyon Technologies XACT 3-axis Attitude Determination and Control System," vol. 6, no. 3, pp. 651–662, 2017. [Online]. Available: `http://arxiv.org/abs/1706.06967` (cit. on pp. 10, 11, 12).

[18] J. Mason, *MinXSS CubeSat On-Orbit Performance and the First Flight of the BCT XACT 3-axis ADCS*, Colorado Boulder. [Online]. Available: `http://mstl.atl.calpoly.edu/{~}workshop/archive/2016/Summer/Day2/Session5/3{\_}JamesMason.pdf` (cit. on pp. 10, 11).

[19] Blue Canyon Technologies, *Blue Canyon Technologies - Components*. [Online]. Available: `https://bluecanyontech.com/components` (cit. on p. 10).

[20] R. Hevner, J. Puig-Suari, R. Twiggs, W. Holemans, J. Puig-Suari, and R. Twiggs, "An advanced standard for CubeSats," *25th Annual AIAA/USU Conference on Small Satellites*, Paper SSC11–II–3, 2011 (cit. on p. 12).

[21] NASA, JPL, and California Institute of Technology, *Arcsecond Space Telescope Enabling Research in Astrophysics (ASTERIA)*, 2019. [Online]. Available: `https://www.jpl.nasa.gov/cubesat/missions/asteria.php` (cit. on p. 12).

[22] Nanoracks, *INTERNATIONAL SPACE STATION DEPLOYMENT*. [Online]. Available: `https://nanoracks.com/products/iss-deployment/` (cit. on p. 12).

[23] C. M. Pong, "On-Orbit Performance and Operation of the Attitude and Pointing Control Subsystems on ASTERIA," *AIAA/USU Conference on Small Satellites*, 2018. [Online]. Available: `https://digitalcommons.usu.edu/smallsat/2018/all2018/361/` (cit. on pp. 12, 13, 14).

[24] M. W. Smith, A. Donner, M. Knapp, C. M. Pong, C. Smith, J. Luu, P. D. Pasquale, R. L. Bocchino, B. Campuzano, J. Loveland, C. Colley, A. Babuscia, M. White, J. Krajewski, and S. Seager, "On-Orbit Results and Lessons Learned from the ASTERIA Space Telescope Mission," *32nd Annual AIAA/USU Conference on Small Satellites*, vol. SSC18-I-08, 2018. [Online]. Available: `https://digitalcommons.usu.edu/cgi/viewcontent.cgi?article=4067{\&}context=smallsat` (cit. on pp. 12, 13).

[25] H. Pablo, G. N. Whittaker, A. Popowicz, S. M. Mochnacki, R. Kuschnig, C. C. Grant, A. F. Moffat, S. M. Rucinski, J. M. Matthews, A. Schwarzenberg-Czerny, G. Handler, W. W. Weiss, D. Baade, G. A. Wade, E. Zocłońska, T. Ramiaramanantsoa, M. Unterberger, K. Zwintz, A. Pigulski, J. Rowe, O. Koudelka, P. Orleański, A. Pamyatnykh, C. Neiner, R. Wawrzaszek, G. Marciniszyn, P. Romano, G. Woźniak, T. Zawistowski, and R. E. Zee, "The BRITE constellation nanosatellite mission: Testing, commissioning, and operations," *Publications of the Astronomical Society of the Pacific*, vol. 128, no. 970, 2016 (cit. on pp. 14, 15).

[26] W. W. Weiss, V. M. Passegger, and J. Rowe, "Do have nanosatellites a role in detecting exoplanets ?" *Iaus*, no. 293, pp. 1–5, 2013 (cit. on p. 15).

[27] BRITE-Constellation, *BRITE-Constellation nano-satellites for astrophysics*. [Online]. Available: `https://www.univie.ac.at/brite-constellation/the-constellation/engineering/` (cit. on p. 15).

[28] C. C. Grant, K. Sarda, M. Chaumont, and R. E. Zee, "On-orbit performance of the brite nanosatellite astronomy constellation," *Proceedings of the International Astronautical Congress, IAC*, vol. 5, pp. 3417–3429, 2014 (cit. on pp. 15, 16, 17).

[29] CubeSpace Satellite Systems RF (Pty) Ltd, *CubeADCS User Manual*, 2019 (cit. on pp. 19, 35).

[30] ——, *CubeADCS Y-Momentum*, 2020. [Online]. Available: `https://www.cubespace.co.za/products/integrated-adcs/y-momentum/` (visited on 08/20/2019) (cit. on p. 20).

[31] ——, *CubeADCS 3-Axis*, 2020. [Online]. Available: `https://www.cubespace.co.za/products/integrated-adcs/3-axis/` (visited on 10/07/2020) (cit. on p. 20).

[32] ——, *CubeADCS ICD*, 2019 (cit. on p. 21).

[33] ——, *CubeComputer V4.1 ICD*, 2019 (cit. on p. 21).

[34] Silicon Sensing Systems Ltd., *MEMS Gyroscopes*. [Online]. Available: `https://www.siliconsensing.com/technology/mems-gyroscopes/` (visited on 10/11/2020) (cit. on p. 22).

[35] X. Niu, Y. Li, H. Zhang, Q. Wang, and Y. Ban, "Fast thermal calibration of low-grade inertial sensors and inertial measurement units," *Sensors (Switzerland)*, vol. 13, no. 9, pp. 12 192–12 217, 2013 (cit. on pp. 22, 83).

[36] Novatel, *IMU Errors and Their Effects (Manual)*, 2014 (cit. on p. 22).

[37] Silicon Sensing Systems Ltd., *CRM100 Precision Navigation and Pointing Gyroscope Technical Datasheet*, 2015 (cit. on pp. 23, 77, 83).

[38] Honeywell, "1 , 2 and 3 Axis Magnetic Sensors HMC1051/HMC1052/HMC1053," pp. 1–12, 2006. [Online]. Available: `www.honeywell.com` (cit. on p. 23).

[39] Silonex Inc., *SLCD-61N8 Datasheet*, 2020 (cit. on p. 24).

[40] CubeSpace Satellite Systems RF (Pty) Ltd, *Magnetic Control*, 2019. [Online]. Available: `https://cubespace.co.za/magnetic/` (visited on 08/20/2019) (cit. on p. 25).

[41] ——, *CubeTorquer ICD*, 2019 (cit. on p. 25).

[42] ——, *CubeSense Fine Sun or Earth Sensor*, 2019. [Online]. Available: `https://cubespace.co.za/cubesense/` (visited on 08/20/2019) (cit. on pp. 25, 26).

[43] ——, *CubeADCS Health Check Document*, 2019 (cit. on p. 26).

[44] M. Lee, H. Kim, and J. Paik, "Correction of Barrel Distortion in Fisheye Lens Images Using Image-Based Estimation of Distortion Parameters," *IEEE Access*, vol. 7, pp. 45 723–45 733, 2019 (cit. on p. 28).

[45] S. Licardie and A. Basu, "Proceedings of the 1993 IEEE/JSJ International Conference on Intelligent Robots and Systems," 1993 (cit. on p. 28).

[46] CubeSpace Satellite Systems RF (Pty) Ltd, *CubeSense V2.5 ICD*, 2019 (cit. on p. 29).

[47] A. O. Erlank, "Development of CubeStar A CubeSat-Compatible Star Tracker," MEng Thesis, Department of Electronic and Electrical Engineering, Stellenbosch University, 2013 (cit. on pp. 29, 30, 31, 32, 33).

[48] CubeSpace Satellite Systems RF (Pty) Ltd, *CubeStar V4.2 ICD*, 2019 (cit. on pp. 29, 30, 33, 100, 101).

[49] D Brown, "Decentering Distortion of lenses," D. Brown Associates, Inc, Eau Gallie, Florida, Tech. Rep., 1966 (cit. on p. 31).

[50] M. Kolomenkin, S. Pollak, I. Shimshoni, and M. Lindenbaum, "Geometric voting algorithm for star trackers," *IEEE Transactions on Aerospace and Electronic Systems*, vol. 44, no. 2, pp. 441–456, 2008 (cit. on p. 32).

[51] G. J. Roux, "Augmented Stellar Sensor for a Small Spacecraft," MEng Thesis, Department of Electronic and Electrical Engineering, Stellenbosch University, 2019 (cit. on pp. 32, 33).

[52] CubeSpace Satellite Systems RF (Pty) Ltd, *CubeSpace Satellite Systems Intellectual Property*, 2014 (cit. on pp. 33, 71, 77, 95, 100, 101, 102, 115).

[53] M. Shuster and S. OH, "Three-Axis Attitude Determination from Vector Observations," *Journal of Guidance and Control*, vol. 4, no. 1, pp. 70–77, 1981 (cit. on p. 33).

[54] CubeSpace Satellite Systems RF (Pty) Ltd, *CubeWheel User Manual*, 2019 (cit. on p. 34).

[55] ——, *CubeWheel ICD*, 2019 (cit. on pp. 35, 106).

[56] D. A. Vallado, *Fundamentals of Astrodynamics and Applications*, 1997 (cit. on pp. 37, 39, 40).

[57] W. H. Steyn and M. A. Kearney, "An attitude control system for ZA-aerosat subject to significant aerodynamic disturbances," *IFAC Proceedings Volumes (IFAC-PapersOnline)*, vol. 19, pp. 7929–7934, 2014 (cit. on p. 41).

[58] NASA, *HSF - Orbital Elements*, 2012. [Online]. Available: `https://www.spaceflight.nasa.gov/realdata/elements/graphs.html` (visited on 11/07/2020) (cit. on p. 43).

[59] P. Berlin, *Satellite Platform Design*, February. 2014 (cit. on pp. 43, 44, 45, 65).

[60] J. R. Wertz, D. F. Everett, and J. J. Puschell, *Space Mission Engineering: The New SMAD*. Microcosm Press, 2011 (cit. on pp. 46, 65, 66).

[61] N. Hughes, "Quaternion to and from Euler Angle of Arbitrary Rotation Sequence and Direction Cosine Matrix Conversion Using Geometric Methods," 2017 (cit. on p. 48).

[62] J. Diebel, "Representing attitude: Euler angles, unit quaternions, and rotation vectors," 2006 (cit. on p. 48).

[63] J. B. Kuipers, "Quaternions and Rotation Sequences," *Quaternions and Rotation Sequences*, pp. 127–143, 1999 (cit. on p. 49).

[64] W. H. Steyn, "Near-minimum-time eigenaxis rotation maneuvers using reaction wheels," *Journal of Guidance, Control, and Dynamics*, vol. 18, no. 5, pp. 1184–1189, 1995 (cit. on pp. 50, 52).

[65] X. Chen, W. Steyn, and Y. Hashida, "Ground-target tracking control of Earth-pointing satellites," 2000 (cit. on p. 54).

[66] G. H. Janse van Vuuren, "The Design and Simulation Analysis of an Attitude Determination and Control System for a Small Earth Observation Satellite," MEng Thesis, 2015 (cit. on pp. 55, 65, 66).

[67] F. R. Hoots and R. L. Roehrich, "Spacetrack Report No. 3–Models for Propagation of NORAD Elements Sets," *Spacetrack Report*, vol. 3, no. 3, pp. 1–91, 1980 (cit. on pp. 56, 57).

[68] J. Andres Fraire, P. Ferreyra, and C. Marques, "OpenCL-Accelerated Simplified General Perturbations 4 Algorithm," in *14th Argentine Symposium on Technology*, 2013, pp. 57–68 (cit. on p. 56).

[69] N. C. Rossouw, "A GPS-based On-board Orbit Propagator for Low Earth-Orbiting CubeSats," MEng Thesis, Department of Electrical and Electronic Engineering, Stellenbosch University, 2015 (cit. on p. 59).

[70] ——, "A GPS-based On-board Orbit Propagator for Low Earth-Orbiting CubeSats," no. December, pp. 1–6, 2015 (cit. on pp. 59, 60).

[71] J. Meeus, *Astronomical Algorithms*, 1st. Willmann-Bell, Inc., 1991 (cit. on p. 60).

[72] C. C. Finlay, S. Maus, C. D. Beggan, T. N. Bondar, A. Chambodut, T. A. Chernova, A. Chulliat, V. P. Golovkov, B. Hamilton, M. Hamoudi, R. Holme, G. Hulot, W. Kuang, B. Langlais, V. Lesur, F. J. Lowes, H. Lühr, S. Macmillan, M. Mandea, S. McLean, C. Manoj, M. Menvielle, I. Michaelis, N. Olsen, J. Rauberg, M. Rother, T. J. Sabaka, A. Tangborn, L. Tøffner-Clausen, E. Thébault, A. W. Thomson, I. Wardinski, Z. Wei, and T. I. Zvereva, "International Geomagnetic Reference Field: The eleventh generation," *Geophysical Journal International*, vol. 183, no. 3, pp. 1216–1230, 2010 (cit. on pp. 63, 64).

[73] NASA - Glenn Research Center, *Center of Pressure - CP*, 2015. [Online]. Available: `https://www.grc.nasa.gov/www/k-12/airplane/cp.html` (cit. on p. 65).

[74] W. H. Steyn and V. Lappas, "Cubesat solar sail 3-axis stabilization using panel translation and magnetic torquing," *Aerospace Science and Technology*, vol. 15, no. 6, pp. 476–485, 2011 (cit. on pp. 65, 66).

[75] A. Lassakeur and C. Underwood, "Magnetic Cleanliness Program on CubeSats For Improved Attitude Stability," in *2019 9th International Conference on Recent Advances in Space Technologies (RAST)*, 2019, pp. 123–129 (cit. on pp. 66, 67).

[76] C Shaffer, "A Study on the Usage of TASC and UTJ Solar Cells in the Design of a Magnetically Clean CubeSa," in *27th Annual AIAA/USU Conference on Small Satellites*, 2013 (cit. on p. 66).

[77] CubeSpace Satellite Systems RF (Pty) Ltd and SCS Space (Pty) Ltd, *nSight-1 In-Orbit Calibration Results of the 3-axis Honeywell HMC1053 Magnetometer*, 2017 (cit. on pp. 71, 72).

[78] J. Gerber, "A 3-Axis Attitude Control System Hardware Design for a CubeSat," MEng Thesis, Department of Electronic and Electrical Engineering, Stellenbosch University, 2014 (cit. on pp. 74, 75).

[79] A. Panel and E. S. Society, *IEEE Std 952-1997 (R2003) Standard Specification Format Guide and Test Procedure for Single-Axis Interferometric Fiber Optic Gyros*. IEEE, 2003, ISBN: 1559379618. [Online]. Available: `https://ieeexplore.ieee.org/document/7862718` (cit. on p. 78).

[80] NXP Freescale Semiconductor, *Allan Variance: Noise Analysis for Gyroscopes (Manual)*, 2015 (cit. on p. 78).

[81] M. SOTÁK, F. KMEC, and V. KRÁLÍK, "the Allan Variance Method for Mems Inertial Sensors," in *Proceedings of the International Scientific Conference Modern Safety Technologies in Transportation*, 2009, pp. 272–277 (cit. on p. 79).

[82] A. A. Hussen and I. N. Jleta, "Low-Cost Inertial Sensors Modeling Using Allan Variance," *International Scholarly and Scientific Research & Innovation*, vol. 9, no. 5, pp. 1069–1074, 2015 (cit. on p. 79).

[83] O. J. Woodman, "An introduction to inertial navigation," Tech. Rep. 696, 2007 (cit. on p. 79).

[84] Silicon Sensing Systems Ltd., *PinPoint Precision Navigation and Pointing Gyroscope*, 2013 (cit. on p. 80).

[85] A. Maio, R. Knight, and W. Nothwang, "Microelectromechanical System (MEMS) Gyroscope Noise Analysis and Scale Factor Characterization over Temperature Variation," US Army Research Laboratory, Adelphi, Tech. Rep., 2016 (cit. on p. 85).

[86] CubeSpace Satellite Systems RF (Pty) Ltd, *CubeSense V2.5 User Manual*, 2019 (cit. on p. 88).

[87] Faulhaber, "Brushless Flat DC-Micromotors," Tech. Rep., 2012. [Online]. Available: `https:/www.faulhaber.com` (cit. on pp. 105, 107, 108).

Appendix A

TLE Data Sets

The following TLE datasets are used throughout chapters 5 to 7:

A.1 ISS Orbit

```
1 43549U 98067NX  19079.80889842  .00010024  00000-0  44056-4 0  9997
2 43549  51.6372  75.0213 0005440 149.9450 210.1856 15.59182522 38604
```

Figure A.1: ISS TLE Dataset

A.2 Sun-Synchronous 500 km Orbit

```
1 43138U 18004AD  19079.88923238 +.00001642 +00000-0  44056-4 0  9997
2 43138 097.4981  30.0000 0008590 202.3540 157.7324 15.23770662065847
```

Figure A.2: 500 km SSO TLE Dataset

A.3 Sun-Synchronous 650 km Orbit

```
1 39161U 13021C   19079.66625617  .00000186  00000-0  44056-4 0  9990
2 39161  97.9909  30.0000 0008051 254.3460 105.6870 14.72170270315122
```

Figure A.3: 650 km SSO TLE Dataset

Appendix B

MEMS Sensor PCB Design

The following development board was designed to test the CRM100 MEMS gyro sensors in chapter 6. The device had an XBEE wireless sensor mounting for possible cases when wireless comunication was needed, as well as an SPI interface to each gyro sensor, which was communicated to via an Arduino.

Eagle PCB design software was used to design the board.

B.1 Schematics

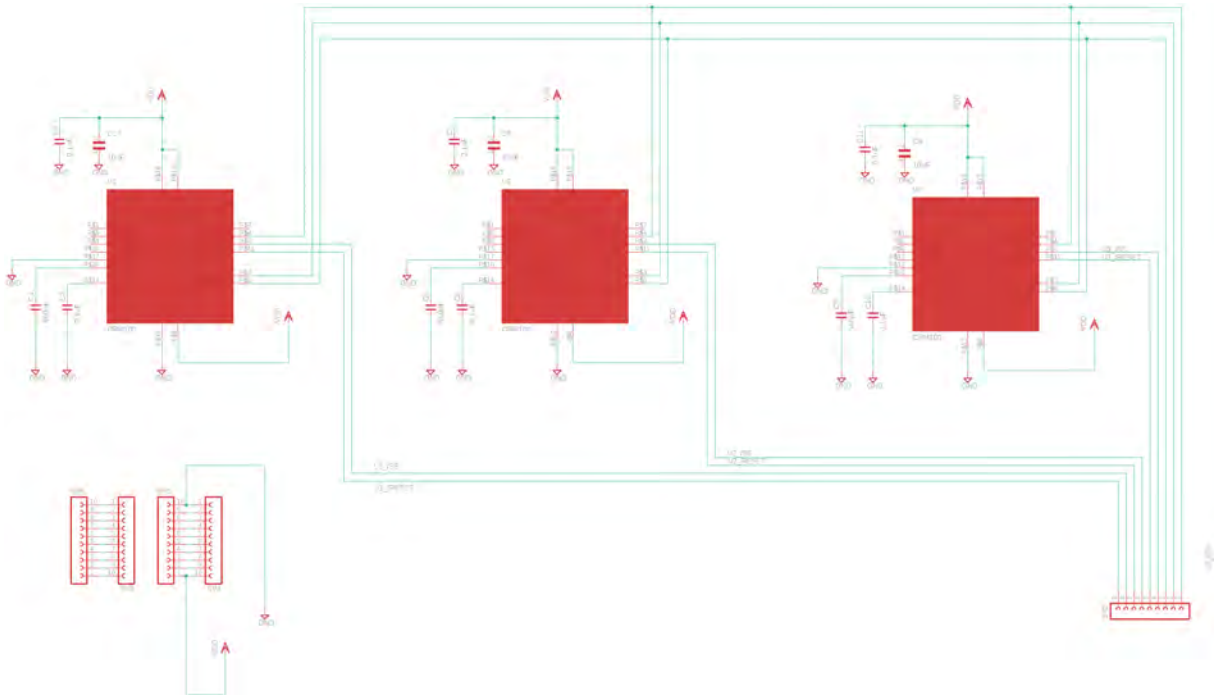

Figure B.1: CRM100 Gryo Interface Schematics

B.2 PCB

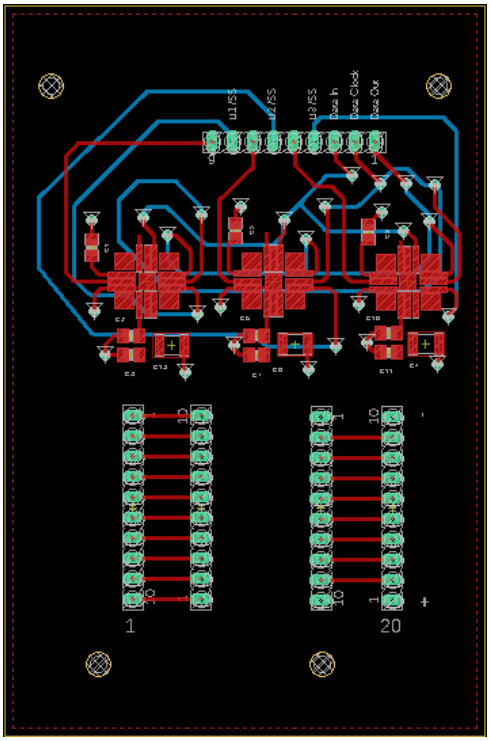

Figure B.2: CRM100 Gryo Interface PCB Layout

Appendix C

Simulated CubeSat Solar Panel Configurations

The following section shows the visual representations and typical CubeSat MoIs used as the simulated CubeSats in the simulations throughout chapter 7. The convention representing the MoIs in the subsections that follow show principle moment of inertia, J_{zz}, to be aligned with the long-body axis of the CubeSat (nominal nadir pointing). In the case of the CubeSat long-body axis pointing in the ram direction, J_{xx} swaps with J_{zz}.

C.1 3U CubeSats

The simulated 3U CubeSats MoIs are shown below.

$$\mathbf{J}_{3U_{BMSP}} = \begin{bmatrix} 0.0361 & 0 & 0 \\ 0 & 0.0365 & 0 \\ 0 & 0 & 0.0075 \end{bmatrix} \text{ kg m}^2$$

$$\mathbf{J}_{3U_{DSP}} = \begin{bmatrix} 0.0476 & 0 & 0 \\ 0 & 0.0485 & 0 \\ 0 & 0 & 0.0105 \end{bmatrix} \text{ kg m}^2$$

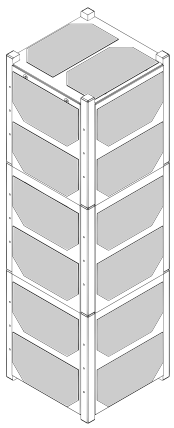

(a) 3U CubeSat with Body Mounted Solar Panels

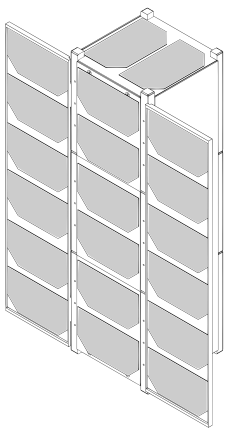

(b) 3U CubeSat with Two 3U Deployed Solar Panels (-Y Facet)

Figure C.1: 3U CubeSat Solar Panel Configurations

C.2 6U CubeSats

The simulated 6U CubeSats MoIs are shown below.

$$\mathbf{J}_{6U_{BMSP}} = \begin{bmatrix} 0.065 & 0 & 0 \\ 0 & 0.08 & 0 \\ 0 & 0 & 0.026 \end{bmatrix} \text{ kg m}^2$$

$$\mathbf{J}_{6U_{DSP}} = \begin{bmatrix} 0.071 & 0 & 0 \\ 0 & 0.104 & 0 \\ 0 & 0 & 0.048 \end{bmatrix} \text{ kg m}^2$$

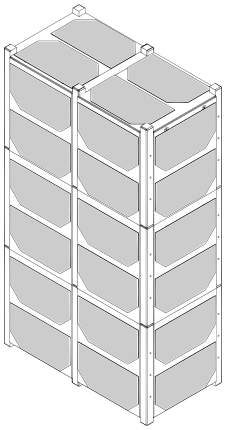

(a) 6U CubeSat with Body Mounted Solar Panels

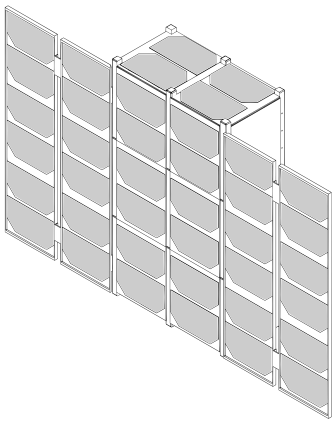

(b) 6U CubeSat with Four 3U Deployed Solar Panels (-Y Facet)

Figure C.2: 6U CubeSat Solar Panel Configurations

C.3 12U CubeSat

The simulated 12U CubeSats MoI is shown below.

$$\mathbf{J}_{12U_{BMSP}} = \begin{bmatrix} 0.26 & 0 & 0 \\ 0 & 0.265 & 0 \\ 0 & 0 & 0.16 \end{bmatrix} \text{ kg m}^2$$

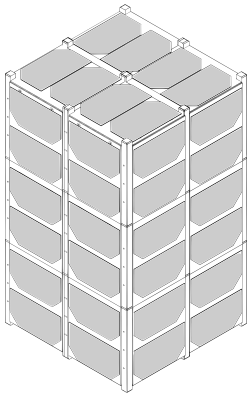

Figure C.3: 12U CubeSat with Body Mounted Solar Panels